Experimental studies of nuclear structure and shape phenomena around the N=Z line

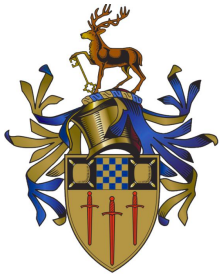

Carmine Kevin Belvedere

Department of Physics

University of Surrey

A thesis submitted in fulfilment of the requirements for the degree of

Doctor of Philosophy

Faculty of Engineering and Physical Sciences

July 2022

Abstract

The low-energy Coulomb excitation of ^{72}Se experiment was conducted using the Miniball/CD detector setup to detect prompt gamma rays in coincidence with scattered particles at the HIE-ISOLDE facility at CERN. The quadrupole moment (QM), hereafter always recorded in units of eb, was deduced to be $Q_s(2_1^+) = -0.24^{+0.13}_{-0.22}$, implying a prolate configuration; this first independent measure is in agreement with the only other experimentally reported value, which was published during this thesis project. The prolate shape of this state confirms that shape inversion to oblate configurations near the ground state does not occur until at least ^{70}Se. The QM for the 2_1^+ state in the beam contaminant ^{68}Ge is found to be $Q_s(2_1^+) = -0.39^{+0.33}_{-0.17}$, implying prolate configuration; this is the first experimentally deduced value of this QM and represents the first post-acceleration of a radioactive neutron-deficient Ge isotope at an ISOL facility. Gamma-ray spectroscopy of ^{60}Zn was conducted at Argonne National Laboratory (ANL) using the ATLAS accelerator for the production of a ^{3}He beam directed onto an enriched ^{58}Ni target. This induced the ^{58}Ni(^{3}He,n) light-ion fusion-evaporation reaction and the Gammasphere detector array was used for detection of prompt gamma-rays following the reaction. A firm assignment for the 2_2^+ state is made, as well as previously unknown structures built above the 2_2^+ state and 3_1^+ state being discovered. Several new states with transitions decaying to the 4_1^+ state are also observed. Some states potentially corresponding to resonances in the astrophysical ^{59}Cu(p,γ) reaction are identified. First observation of these states provides critical information for follow-up work to obtain the reaction rate. The level density deduced is in agreement with the recent work of Soltesz et al. using no gamma-decay information.

Acknowledgements

My first words of thanks must go to my supervisor, Dr Daniel Doherty, for sticking by me despite my early issues and for encouraging me to produce my best throughout my Ph.D. Without his consistent advice, guidance and the sharing of his personally developed resources, this thesis and my research outputs could not have been completed to the standard that I can proudly display today. I also extend a special thanks to fellow doctoral researcher Lisa Morrison for her patience and kindness in voluntarily giving up her time to help me get to grips with GOSIA.

I would also like to dedicate part of this section to Dr Malcolm Harris and his wonderful family. Firstly for giving me the opportunity to work for their business and sustain myself financially in Guildford when the start of my degree was delayed on multiple occasions with administrative issues linked to funding. But furthermore, for treating me like a part of their family, for engaging in stimulating conversations with me, for sharing their life experiences with me and for allowing me to express myself and feel heard at a time when I felt nothing else was going my way.

I can take great pleasure acknowledging all the brilliant, indefatigable academics and scientists involved with the two experiments I speak about in this thesis, those working at the HIE-ISOLDE facility at CERN and at Argonne National Laboratory. Moreover, those whose computer codes I was able to take advantage of to make my analysis infinitely easier; especially Dr Liam Gaffney and his MiniballCoulexSort and Chisqsurface codes.

I am eternally grateful for those who I am lucky to call my friends, those who have pushed me, questioned me and just gone on the ride with me; whether that be by watching football matches, duelling on peggle, playing squash, allowing me to stay in your home, transporting all my stuff from storage, dropping incessantly into risky reels, talking fpl, spinning to win, stealing my sheep, poaching my draft pick, irrationally invading my territories, making ludicrous meals, triggering unnecessary safety cars..these are the insane things that have kept me sane throughout.

Nothing that I have achieved and will achieve, this thesis being no exception, would have been or will be possible without the nurture and support I have received throughout my life my loving parents. Their unwavering faith in me and my decisions allows me to live my life confidently without fear of judgement or failure, something that is likely to bring the best out of anyone and undoubtedly does so out of me.

Finally, and most importantly, I write and dedicate these closing words to my companion, my biggest fan, my person. Without her, I could not possibly be half of the person I am today, the person to have turned the corner from a darker period, the person to face the challenges I have been presented with and take them in my stride, the person to vindicate my parents faith in me, the person to enjoy the extra things in life, the person to be aware enough to be able acknowledge all the wonderful support I have received and referred to here, and the person to submit this thesis and complete this degree with pride and satisfaction.

Declaration

The two experiments described in this thesis were performed by fellow members of the University of Surrey Nuclear Physics Group and our collaborators at various international facilities. The data analysis and interpretation of results are entirely my own work, and this thesis has been written entirely by me. Any ideas, data, images or text resulting from the work of others (whether published or unpublished) are fully identified as such within the work and attributed to their originator in the text or bibliography. No portion of the work referred to in this thesis has been submitted in support of an application for another degree qualification at this university or any other academic institution.

Carmine Kevin Belvedere

July 2022

Lay Summary

The atomic nucleus comprises of protons and neutrons, known as the nucleons. Nuclear structure theories are used to try and understand the way nucleons are arranged in the nucleus, how they interact with each other and how this affects properties such as the shape of the nucleus. Many theoretical models have been developed which look to best describe the behaviour of the nucleons in different areas of the nuclear chart. Results from nuclear structure physics experiments are key in pointing these models in the right direction. The shape of the nucleus is of particular interest when looking to constrain theoretical models and nuclei that have roughly equal numbers of protons and neutrons are known to have interesting shape characteristics. This thesis reports results from two experiments which look to find out about the shape of these type of nuclei. The first is the Coulomb excitation of ^{72}Se, with many modern theories making differing predictions for the shapes of exotic selenium isotopes. The first independent measure of the shape of the first excited state is reported here, which strengthens the use of a particular type of theoretical model in this area of the nuclear chart. The first experimentally deduced description of the shape of the first excited state in ^{68}Ge is also reported. The second study, the gamma-ray spectroscopy of ^{60}Zn, a nucleus which theoretical models predict to have a combination of shapes, has yielded the first firm assignment for multiple levels of importance for testing theoretical predictions. This assignment will allow for future experimental studies to deduce the shapes of the states which will further test theoretical predictions. Previously unknown excited states and decays are also discovered - some states potentially being relevant to the ^{59}Cu(p,γ) reaction, which plays a key role in the shape of X-ray burst light curves.

Table of contents

List of figures

List of tables

Chapter 1

General Introduction

Atoms are the building blocks of everything we see around us. They are made up of electrons bound to and orbiting a nucleus. The atomic nucleus constitutes over 99% of the atom's mass and comprises of a combination of protons and neutrons; the nucleons. The theory of nuclear structure is used to try and understand the way these nucleons are arranged in the nucleus, how they interact with each other and how this affects macroscopic properties such as the shape of the nucleus. One of the first attempts to explain nuclear structure in the early 20th century was the Liquid Drop Model [1, 2], but this had its limitations. In modern times the most widely accepted theory is the shell model. This model uses quantum physics principles to describe the nucleus in terms of energy levels, in an analogous way to electrons filling shells in the atomic shell model, but with no central potential in the nuclear shell model as opposed to in the atomic shell model where the nucleus acts as a central potential of positive charge, attracting the negatively charged electrons.

The shell model assumes the nucleus to take a spherical shape [3], but this does not tend to be the case for nuclei with open shells (i.e. partially filled shells). The shell model thus tends to break down in these regions of the nuclear chart. A variation of the shell model developed by S. G. Nilsson [4], known as the deformed shell model, or Nilsson model, can be used to model nuclei with deformed shapes.

Excited states in nuclei, especially far from closed shells, can also be described by collective motion of the nucleons, as if the nucleus were one body which can undergo certain types of motion; either vibrational or rotational motion. One can distinguish between these motions by observing the properties of excited states (such as the energies, and spin-parity quantum numbers) [5]. This idea first stemmed from the liquid drop model and was then brought forward and adapted following the discovery of the shell model. Rotational motion tends to be observed experimentally in high-A nuclei (A ~ 150 and above), as well as in highly-deformed structures in lighter nuclei far from closed shells. Collective motions outside this range are dominated by vibrational modes, where the nucleus oscillates about its equilibrium shape.

In more recent times, various, more complex models have been developed by theorists which attempt to better predict and describe specific phenomena in certain areas of the nuclear chart, such as the Adiabatic Self-Consistent Coordinate (ASCC) method [6] and methods based on Hartree-Fock-Bogoliubov (HFB) calculations [7–10]. Experimental nuclear physics research seeks to benchmark state-of-the-art nuclear theories both by seeking to push out to the limits of stability at both the proton and neutron driplines and by measuring important properties of nuclei such as the matrix elements connecting nuclear states. These probes can be employed using a variety of experimental setups, many of which are extremely complex and can only be conducted at select institutions and facilities globally.

The shape of the nucleus is of particular interest, since this is an important and sensitive prediction from a number of theoretical calculations and models. Coulomb excitation, having originally been conducted with stable light-ion beams in the 1950s and 1960s, has undergone a renaissance in recent times with the advent of new radioactive ion beam (RIB) facilities. It has emerged as a fantastic method to explore low-lying states in radioactive isotopes of interest, owing to the large cross sections involved. It is a highly efficient experimental technique, providing high yields and very good resolution when used in conjunction with high-quality arrays of germanium detectors, such as Miniball at HIE-ISOLDE, CERN. The typical setup for

these experiments involves a beam which is accelerated toward the deliberately chosen target. Gamma rays emitted from the de-excitation of excited nuclei then detected by detectors such as the one mentioned above. The scattered beam and/or target nuclei are registered in coincidence with a particle detector close to the target position.

Low-energy Coulomb-excitation experiments must be designed carefully so that the interaction between the beam and target nuclei is a purely electromagnetic one, i.e. the influence of the short-ranged strong nuclear force is minimised. This can be achieved through the choice of beam energy. As the excited states of the chosen nucleus de-excite, gamma rays with energy equal to the difference between the excited states are emitted. A wide variety of transitions can be measured, some which cannot be observed with other experimental techniques, meaning new transitions can be identified and new excited states discovered. As well as this, it is possible to obtain electromagnetic matrix elements connecting low-lying states and to measure spectroscopic quadrupole moments. With the appropriate set of electromagnetic matrix elements, it is possible to provide a model-independent measurement of the nuclear shape.

Nuclei in the mass region A ~ 70 close to the N = Z line are known to exhibit a variety of nuclear shapes. These were predicted in the 1970s and can be attributed to large shell gaps at both prolate and oblate deformation, which are most pronounced for proton and neutron numbers 34 and 36 [11]. The first part of this thesis will look at a radioactive isotope of selenium, which has proton number Z = 34. Numerous theoretical predictions [12, 13] indicate the possibility of shape coexistence in the N=38 radioactive isotope ^{72}Se.

The low-energy Coulomb excitation of ^{72}Se was conducted using the Miniball/CD detector setup to detect prompt gamma rays and scattered particles at the HIE-ISOLDE facility at CERN. At this facility, state-of-the-art RIBs are available at sufficient intensities which allow for rich sets of matrix elements connecting states to be obtained, including those required to determine the intrinsic shapes in the nuclei of interest. The experimentally deduced shapes of these states can then be compared with theoretical predictions in order to benchmark and test these

calculations. One such way this is achieved is to answer the currently open question of where the shape transition from prolate to oblate shapes happens along the selenium isotopic chain.

The charge-independent nature of the strong nuclear force means both protons and neutrons can be treated identically, as nucleons. Around the N = Z line, mirror pairs, nuclei which have the same nucleon number but have their proton and neutron number interchanged, are a great display of this as their structures tend to be remarkably similar. Protons and neutrons in these nuclei typically occupy the same shell-model orbitals which makes the nuclear structure more intriguing with respect to other areas of the nuclear chart. One can gain further information into the likely structure of a given nucleus by looking at its mirror partner. Conversely, constraining the nuclear properties of a given nucleus can shed light on the properties of its mirror partner. Studies into self-conjugate nuclei which lie on the N = Z line, such as ^{60}Zn, are not able to call upon this technique to gain further information on properties and structure, thus information in such cases tends to be more limited. This makes experimentally constrained results more valuable when it comes to furthering the understanding of these nuclei.

There is considerable nuclear structure interest in the low-lying structure of ^{60}Zn, with information on bound levels still relatively scarce. Information on the location of important low-lying levels such as the 0_2^+ or 2_2^+ is sought as theoretical calculations in this key region for shape changes predict the coexistence of prolate- and oblate-deformed structures [14]. Light-ion–induced fusion-evaporation reactions are a powerful tool for the production of neutron-deficient nuclides closer to the valley of β stability, such as ^{60}Zn. These reactions also result in a more favourable population of low-spin states in the final nuclei [15].

Since ^{60}Zn lies on the rp-process path and is important for understanding X-ray burst events, the favourable population of low-spin states leads to a greater probability of observing the key states above the proton emission threshold relevant to the astrophysical ^{59}Cu(p,γ) reaction, which plays an important role in the shape of X-ray burst light curves.

Fusion-evaporation reactions occur when a projectile is accelerated with such energy to allow it to fuse with the target nucleus to form a highly excited compound nucleus, which then de-excites via the "evaporation" of light particles. This reaction mechanism is ideal for gamma-ray spectroscopy as once the excitation energy of the system is near the particle separation energy, de-excitation continues mostly via gamma decay, allowing for the detection and discovery of a great number of transitions (and thus excited states). These kind of experiments can be conducted at facilities with particle accelerators powerful enough to generate the energy required for the fusion process and with high-quality germanium gamma-ray detector arrays for gamma-ray detection.

The gamma-ray spectroscopy of ^{60}Zn was conducted at Argonne National Laboratory (ANL) using the ATLAS accelerator for the production of ^{3}He beams fired at a high-purity ^{58}Ni target to induce the ^{58}Ni(^{3}He,n) light-ion fusion-evaporation reaction. The Gammasphere detector array was used for the detection of prompt gamma rays following the reaction, allowing for the analysis of gamma-gamma coincidence relationships with previously-identified transitions in ^{60}Zn. This analysis was conducted with a view to gaining further information on the low-lying structure of this nucleus, as well as identifying resonant states of the ^{59}Cu(p,γ) reaction.

The following chapters will present the following: the underlying theory that is necessary knowledge for contextualising the purpose of these experiments and their results is discussed in further detail in Chapter 2. The experimental methodologies for the two experiments are presented in Chapters 3 and 5 for the low-energy Coulomb excitation experiment and fusion-evaporation experiment, respectively. The results from these experiments are displayed and analysed in the subsequent chapters, 4 and 6. Chapter 7 provides a summary and some outlook beyond the work in this thesis.

Chapter 2

Nuclear Structure Theory

2.1 Overview

The nucleus of an atom forms 99% of its mass and is comprised of two of the three particles found in the atom: the proton and the neutron. The nucleus of most atoms has a diameter in the order of 10^{-15}m [16], meaning that the vast majority of the mass of the atom (diameter in order of 10^{-10}m [17]) is contained within a tiny fraction of its volume. The mass of the proton and neutron are almost identical (both being 1.67×10^{-27} kg to 2 decimal places) and act very similarly within the nucleus. Intuitively, they are grouped together as the "nucleons" [18–20]. The third particle, the electron, is found on the outer edge of the atom, has charge of -1e (where $e \approx 1.6 \times 10^{-19}$ C) and has a mass much lighter than the nucleons (approximately 5.5×10^{-4} times the mass of a nucleon) [21, 22]. The total number of nucleons is referred to as the mass number (A number) of the atom. However, there are fundamental differences that allow distinction between the two nucleons. The proton has charge +1e, for example [18], whereas the neutron is neutral and has no charge [20]. With this in mind, an non-ionised atom will have the same number of electrons as protons, balancing the charges. In addition, the neutron has a marginally larger mass than the proton [23].

The framework in which any physics is understood is in that of the fundamental interactions. There are four known fundamental interactions: the gravitational, weak, electromagnetic and strong interactions. The attraction between negatively charged electrons in orbit of the positively charged nucleus is attributed to the electric and magnetic fields created by the electromagnetic interaction. The electromagnetic interaction acts between charged particles, is effective at a vast range of distances and has infinite range [24]. This interaction is comprised of the electrostatic force, known as Coulomb's law (shown in equation 2.1 which acts on particles with signed charges q_1 and q_2 at rest separated by distance r with k_e, Coulomb's constant, = 9×10^9 $\mathrm{Nm^2C^{-2}}$) [25], and magnetic and electric forces acting as particles move relative to each other.

$$F = \frac{k_e q_1 q_2}{r^2} \tag{2.1}$$

The electromagnetic interaction is significantly stronger than the gravitational interaction, but the forces it creates tend to cancel out for large bodies. Therefore in many contexts, such as in astrophysics, gravity is the dominant interaction despite being fundamentally weaker. Our present understanding of the gravitational interaction stems from the General Theory of Relativity [26]. It is experienced by all particles and acts on any body with mass, energy or momentum and has infinite range. It produces strong long-range forces but is very weak compared to the other forces and is negligible on the scale of the atomic nucleus. The electromagnetic interaction is now often coupled with one of the other fundamental interactions, the weak interaction. The weak interaction acts at very small distances ~ 10^{-18} m and is the interaction that is responsible for beta decay [27]. These two interactions have been successfully unified to form the electroweak interaction [28–30].

While the electromagnetic interaction is responsible for binding the atom together, it repels the identically-charged protons in the nucleus from each other. These only remain bound together alongside the neutrons due to another fundamental interaction, the strong interaction,

being far stronger than the electromagnetic interaction at nuclear distances. At these distances (~10^{-15} m), the strong interaction is the strongest of the four fundamental interactions: roughly 10^2 times stronger than the electromagnetic interaction, 10^6 times stronger than the weak interaction and 10^{38} times stronger than the gravitational interaction.

The strong interaction is only observable at two distinct ranges where it performs two distinct roles. Firstly, on a smaller scale, at distances smaller than the radius of a nucleon, where it is the interaction responsible for holding fundamental particles called quarks together in order to form protons and neutrons, amongst other hadron-type particles. This interaction is carried by a particle called the gluon [31–33]. Secondly, on a larger scale of around 1 to 3 fm (10^{-15} m = 1 fm), the strong interaction is what binds the nucleons together to form the nucleus of an atom. This is in fact the residuum of the interaction at smaller scales between the quarks and diminishes rapidly with distance. It is for this reason that there are constraints on how large a nucleus can be (nuclei beyond Z = 82 are largely unstable). It is mediated by π, ρ and ω mesons, particles predicted by Hideki Yukawa in 1935 [34], with the Pion first discovered experimentally in 1947 [35]. About 99% of the mass a proton is attributed to the energy field formed by the strong interaction, with the rest formed by its actual constituents [36].

The way in which different nuclear bodies (known as nuclides) are defined are dependent on their A, Z and N numbers. Every nuclide has a distinct combination of protons and neutrons. The A number is the total of both protons and neutrons in the nuclide and is usually the number seen when nuclides are referred to in literature. For example, ^{72}Se has A number 72 - this notation is used throughout this thesis work. Any nuclides with the same A number are referred to as "isobars" e.g. ^{72}Se and ^{72}Kr are isobars, with ratio of N and Z different. The Z number indicates the element, for example, any nucleus with Z = 1 is a hydrogen nucleus, any with Z = 34 is selenium, any with Z = 92 is uranium etc. All nuclides with the same Z number are called isotopes, e.g. any nuclide with Z = 34 with differing N number such as ^{74}Se (N=40),

^{72}Se (N=38) etc. Three isotopes of hydrogen are shown in Figure **??**. Nuclides with the same N but differing Z are referred to as isotones.

Study into nuclear structure attempts to better understand how these nucleons behave within the nucleus of the atom and how changing properties of the nucleus (and consequently the atom), such as proton number (Z number) or neutron number (N number), affects the way these nucleons interact. There have been several models developed attempting to explain the structure of the nucleus, and some of these are elaborated on in later sections of this chapter.

2.2 Nuclear Properties

2.2.1 Nuclear Radius and Size

If one models the nucleus as a sphere in a simplified way, there must be an associated radius to describe this nucleus. Electron scattering experiments [37, 38] have produced results which indicate that the distribution of nucleons is fairly consistent throughout the nucleus [39] i.e. the number of nucleons per unit volume is roughly constant. This is shown by equation 2.2 where R is the nuclear radius and A is the mass number of the nucleon.

$$\frac{A}{\frac{4}{3}\pi R^3} \sim constant \tag{2.2}$$

Therefore the radius R must be proportional to $A^{1/3}$ ($R \propto A^{1/3}$) and once introducing a proportionality constant, say R_0, the familiar equation for nuclear radius (equation 2.3) is reached.

$$R = R_0 A^{1/3} \tag{2.3}$$

R_0 has been experimentally deduced to be approximately 1.2 fm, although this value can vary by around 0.2 fm, depending on the nucleus in question. [39–42].

2.2.2 Nuclear Excitations and Excited States

If one takes the nucleus as a finite quantum system with angular momentum **J** and angular momentum quantum number j equal to some multiple of $1/2$, providing $j \neq 0$, the nucleus will have a magnetic dipole moment and most likely an electric quadrupole moment as well. The nuclear angular momentum and magnetic moment manifest themselves most immediately in atomic spectroscopy, where the interaction between the nuclear magnetic moments and the electron moments gives rise to the electronic energy levels that can be observed in experiment. This supports the idea of a simple quantum-mechanical model of the nucleus, with quantum number n and angular momentum components l (orbital) and s (spin).

Modelling the nucleus in this way means that nuclei have excited states at discrete energy levels, varying for each different nucleus. These excited states can be characterised by their angular momentum, J, and parity, π, where the parity of the state dictates what the structure of the nucleus would be if the spatial coordinates of all the nucleons were reversed. A positive parity state will have a wavefunction that looks identical if the spacial coordinates are reversed whereas a negative parity state will look different if reversed. The J^{π} notation is thus used to label nuclear excited states. Often, one will see the J^{π}_{x} notation, where x is represents the order of excited states with the same J^{π} in the same nucleus starting from the lowest energy. For example, if there are two or more 2^{+} states in a given nucleus, the one found at lowest energy will have notation 2^{+}_{1} and the state at higher energy 2^{+}_{2} and so on. An example of this is in the ^{60}Zn nucleus where the excited states at 1004 keV and 2559 keV both have $J^{\pi} = 2^{+}$ [43], but the state at 1004 keV is labelled as 2^{+}_{1} or the "first" 2^{+} state and the state at 2559 keV is labelled as 2^{+}_{2} or the "second" 2^{+} state.

The lifetime of a nuclear state is the mean amount of time a nucleus will remain in the given state before decaying to another state of lower energy [44]. The final state will depend on the gamma-decay branching ratios of the state. For example, for many low-lying 2^{+}_{1} states, such as the 2^{+}_{1} state in ^{72}Se and ^{60}Zn, there is only one state it can gamma decay to (the 0^{+}_{1} ground

state). This is the case for most even-even nuclei, though there are instances where the 0_2^+ can be the first excited state of a nucleus, such as in ^{72}Ge [45]. For states which have fragmented gamma-ray decays, such as the 2_2^+ state in ^{60}Zn, the state will decay to each of the possible final states according to the gamma-ray branching ratio for each transition, where the ratios are compared to the most dominant transition which will always have branching ratio 100. In the case of the 2_2^+ state in ^{60}Zn, the dominant gamma decay path is the 2559-keV transition to the ground state (therefore with branching ratio 100) and the other decay via a gamma-ray from this state is the 1555-keV transition to the 2_1^+ state at 1004 keV, which has gamma branching ratio 92 [43], implying that for every 100 gamma decays via the 2555-keV transition, there are 92 decays via the 1555-keV transition. This information allows us to infer the relative strength of different transitions from the same state.

The lifetime of the state, τ, is related to the width of the state, Γ, by the relation $\Gamma\tau = \hbar$ [46]. The probability of the state decaying to a lower state is proportional to τ and is determined by the matrix element describing the mode of decay joining the initial and final states. This spectroscopic knowledge serves as a vital constraint when performing analysis of Coulomb-excitation data.

2.2.3 Matrix Elements and Transition Probabilities

The matrix element of a transition describes the mode of excitation or decay of the transition and provides insight on whether the wavefunctions of the two states overlap significantly enough to imply some sort of structural connection between the states. For example, the $\langle 2_1^+ | E2 | 0_1^+ \rangle$ matrix element where $\langle 2_1^+ |$ and $| 0_1^+ \rangle$ are the wavefunctions for those states and $E2$ is the electric quadrupole operator describes the decay of the 2_1^+ state to the 0_1^+ by an $E2$ transition. The notation used here is known as Dirac notation [47] and is used throughout this thesis.

In the case of an $E2$ transition, its reduced transition probability, known as the $B(E2)$ value, is related to the matrix element $\langle\Psi_f|E2|\Psi_i\rangle$ by the relation in equation 2.4 where J is the angular momentum and Ψ is the wavefunction of the state.

$$B(E2;J_i \rightarrow J_f) = \frac{1}{2J_i+1}\langle\Psi_f|E2|\Psi_i\rangle^2 \tag{2.4}$$

These quantities can be difficult to contextualise as their orders of magnitude can vary significantly. In order to better understand these values, one can express them in W.u. (Weisskopf units). Weisskopf units are calculated using the Weisskopf estimates [48], with transition rates calculated in the particular scenario where the transition is occurring due to the effects of a single nucleon outside of a closed shell. Given this definition, one would expect values of ~ 1 W.u. for transitions in nuclei near closed shells exhibiting single-particle behaviour (described in Section 2.7), and values $\gg 1$ W.u. for nuclei far from closed shells exhibiting collective behaviour (described in Section 2.8). This applies for matrix elements between two states in the same band. For matrix elements between states in different bands, such as the $\langle 0_2^+|E2|2_1^+\rangle$ matrix element, a large $B(E2)$ value implies significant structural similarity between the states between the states. Small values indicate the states have distinct underlying structures.

2.3 Cross Section

The probability of any nuclear reaction occurring is represented by its cross section. This can be thought of as the area in which the two particles have to hit each other for the reaction to successfully take place. Therefore, the higher the cross section, the more likely the reaction. Given that this measure is for the nuclear scale, the unit used is the "barn", which is 10^{-28} m^2 (the square of general order of magnitude for the radius of a nucleus, 10^{-14}m).

The cross section is proportional to the products of matrix elements involved in the transitions which occur due to a reaction, so can be calculated with the knowledge of matrix elements

in a semi-classical way [49]. Thus, if the reaction cross sections are well known, these can be used to better obtain matrix elements and this is an approach often adopted in Coulomb excitation experiments.

2.4 Gamma Decay

Gamma decay is an electromagnetic process [50] that occurs when a nucleus in an excited state decays towards a less energetic state. For example, as a nucleus goes from the first excited state to the ground state, a gamma ray is emitted equal to the energy difference between the two states. The gamma ray, discovered in the early 20th century [51–53], is a form of electromagnetic radiation. It is the highest energy (shortest wavelength) type of electromagnetic radiation [54] and gamma rays emitted from decaying nuclei tend to be in the order of a few keV to a few MeV. Gamma rays are ionising and highly penetrating [55], travelling easily through the body and therefore extremely hazardous to humans. They can cause serious internal organ damage and comprehensive shielding is required when running experiments with this type of radiation. Materials such as lead and concrete blocks are typically used for shielding purposes.

A gamma ray passing through any matter can interact with an electron and transfer all or some its energy to it. Provided the energy the gamma-ray photon imparts to the electron is greater than that of the binding energy of the electron, the electron is ejected from the atom and the atom is ionised (i.e. it no longer has a net charge of 0, as a negatively charged electron has been removed). The electron will travel with a kinetic energy equal to the difference between the energy the photon has imparted and electron's binding energy.

When the photon transfers all its energy to the bound electron and is absorbed, the process is called the photoelectric effect [56–58]; this is most seen at low energy. When the gamma ray imparts only part of its energy to the electron, it scatters off at an angle and at a lower energy, depending on the amount of energy imparted the electron. This process is called Compton scattering [59]. The way in which this angle, θ, and new energy, E', relate to the initial energy,

E, of the photon can be described by equation 2.5, where m_e is the electron rest mass ≈ 511 keV.

$$E' = \frac{E}{1 + (\frac{E}{m_e c^2})(1 - cos\theta)} \tag{2.5}$$

.

Compton scattering is the dominant absorption mechanism for gamma rays at energies below 10 MeV. This is usually reflected in a typical energy spectra by a feature known as the "Compton edge", corresponding to the largest energy transfer in Compton scattering, when the photon backscatters (i.e. scatters at an angle of 180°) off an atomic electron. At gamma-ray photon energies above 2 m_e (~ 1.022 MeV), the energy of the photon can be converted into an electron-positron pair, in a process known as pair production [60, 61]. This process is dominant at gamma-ray energies above 10 MeV. The energy of the photon emitted from the de-excitation of nucleus is directly converted within its own electromagnetic field (specifically, the electric field) and forms an electron-positron pair. The positron eventually annihilates with a free electron and two identical gamma rays are released of 511 keV (or more, depending on kinetic energy of the pair). The different ways a gamma ray can interact with matter are shown in Figure **??**

Gamma rays emitted from the de-excitation of nuclei are approximately equal to the difference between the energy level the nucleus was initially in and the one it has de-excited to. Consequently, the gamma rays that can be emitted are quantised. This means that the gamma rays will also have a spin and parity, which can be used to describe the transition that has occurred. They are a form of "multipole radiation" and the multipole order is determined by 2^l (for example, if a gamma ray has angular momentum $l = 1$, it is dipole radiation, $l = 2$ quadrupole radiation and so on). The multipolarity of these gamma quanta can give information on the spins and parities of the excited states [62, 63].

Selection Rules in Gamma Decay

As per conservation of angular momentum, the gamma ray must take angular momentum equal to the difference in angular momentum of the initial and final state of the nucleus. Therefore, quantum number l, angular momentum, of the gamma ray must satisfy the rule as in equation 2.6 where J_i is the total angular momentum of the initial nuclear state and J_f is the total angular momentum of the final nuclear state [62, 63].

$$|J_\mathrm{i} - J_\mathrm{f}| \leq l \leq J_\mathrm{i} + J_\mathrm{f} \tag{2.6}$$

The parity, π, of the gamma ray, depending on whether it is an electric (E) or magnetic (M) type gamma ray, can be determined using the selection rules in equations 2.7 and 2.8 [62, 63].

$$\pi(El) = (-1)^l \tag{2.7}$$

$$\pi(Ml) = (-1)^{l+1} \tag{2.8}$$

This means that for electric gamma quanta, the parity will not change for even l and change for odd l, and vice versa for the magnetic case [62, 63]. In transitions where the change in angular momentum between the initial and final states makes several multipole radiations possible, the lowest order multipole tends to be the most prominent. The transition rate decreases by a factor of about 1000 from one multipole to the next one, so the lowest multipole transitions are most likely to occur [64]. In fact, in experiments such as the ones looked at in this thesis work, the transitions that are focused on are the $E1$, $E2$ and $M1$ transitions. Monopole $l = 0$ transitions are forbidden as gamma rays are photons, meaning that their angular momentum must be equal to or greater 1. In the following subsection, a method by which these transitions can occur, called internal conversion, is introduced and explained.

Internal Conversion

The de-excitation energy emitted from a nucleus can be directly transferred to electrons in the same atom, causing the ejection of an electron [65]. Internal conversion can be viewed as analogous to the photoelectric effect, with a "virtual" gamma ray emitted and its energy transferred to an electron within the same atom. The wavefunction of an inner shell electron penetrates the nucleus and the electron couples to an excited state of the nucleus, absorbing the energy of the transition directly without the emission of a gamma ray. What is observed is an electron with an energy equal to the energy difference between the two states minus the binding energy of the electron.

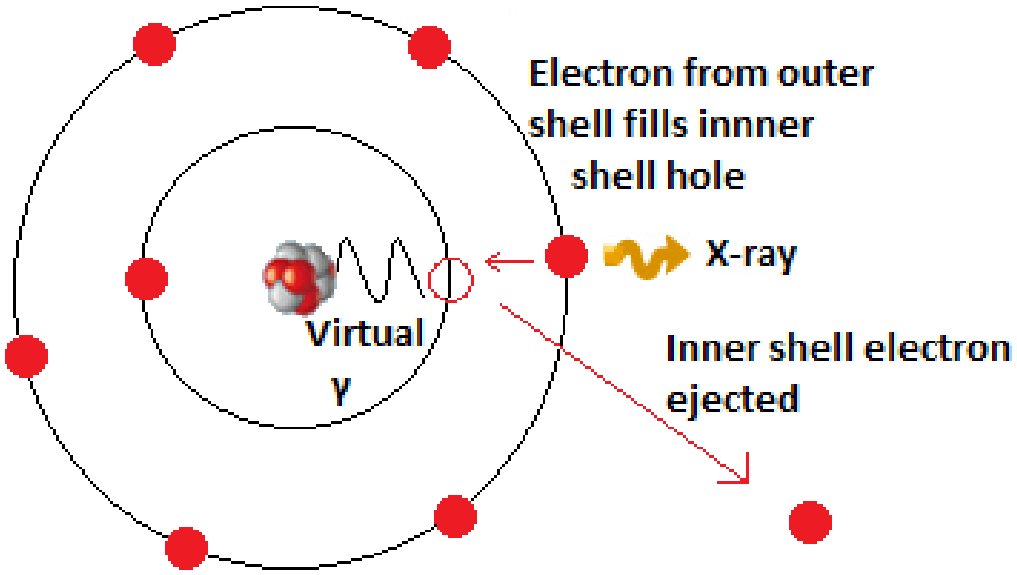

Fig. 2.1 A visulisation of the internal conversion process; energy from the nuclear transition is transferred to an inner electron which is ejected, causing an outer shell electron to fall into its place. An X-ray equal to the energy difference between the two shells is released as this happens.

Once an electron, usually from an inner shell, is removed from the atom, an electron from a higher energy shell moves down to fill the gap in the inner shell [65]; hence "internal (electron) conversion". An X-ray equal to the energy difference of the two shells is emitted

and this process repeats itself until all gaps in lowest energy shells have been filled. A visual representation of this process can be seen in Figure 2.1.

2.5 The Liquid Drop Model

One of the initial theories for nuclear structure was the Liquid Drop Model, put forward by George Gamow around 1930 [1]. It was first used to approximate the mass and other properties of the nucleus by Weizsäcker [2] using the semi-empirical mass formula (SEMF). The mass, m, can be calculated using equation 2.9 where m_{n} and m_{p} are the rest mass of the neutron and proton, respectively, c is the speed of light $\approx 3\times10^{8}$ ms^{-1} and E_{B} is the binding energy of the nucleus, which takes the form shown in equation 2.10 as per the SEMF [2]. The unknown coefficients (a, b, s, d and δ) are constrained by using known experimentally-determined binding energies with equation 2.10.

$$m = Nm_{\mathrm{n}} + Zm_{\mathrm{z}} + \frac{E_{\mathrm{B}}}{c^2} \tag{2.9}$$

$$E_{\mathrm{B}} = aA - bA^{\frac{2}{3}} - s\frac{(N-Z)^2}{A} - d\frac{Z^2}{A^{\frac{1}{3}}} - \frac{\delta}{A^{\frac{1}{2}}} \tag{2.10}$$

This model describes the nucleus as an incompressible nuclear fluid, with the nucleons acting similar to the molecules in a drop of water. Though it has obvious limitations, it gives a good explanation for the spherical shape of nuclei and gives good approximations for some properties of the nucleus, such as the binding energy and shape variables and deviations from uniformity of neutron and proton densities [66]. It provided a great starting point for our understanding of the nucleus and is still used, for example, in predicting alpha-decay half-lives of heavy and super-heavy elements [67].

2.6 Mean Field Theory Overview

Mean field theories attempts to simplify large and complex stochastic and quantum mechanical models by reducing many-body problems to multiple one-body problems. The idea is to approximate the effect of the many components on any one component by formulating a universal averaged effect (hence "mean field"). These can then be used to better understand how components in a system, such as nucleons in a nucleus, interact with each other, and to better understand the behaviour of the system.

In terms of describing nuclear structure, the main obstacle for mean field theories is usually calculating the potential of the mean field. It can be said that there are two methods of doing this. One can be classed as a more phenomenological approach, where the nuclear potential is modelled by a mathematical function and parametrized - a good example of such potential being the Woods-Saxon potential discussed in section 2.7.1. The Nilsson Model described in section 2.7.2 uses this procedure to great success, for example. The other is known as a self-consistent or "Hartree-Fock" type approach, described in section 2.9, which attempts to use effective interaction between nucleons to mathematically predict nuclear potentials. The key to these Hartree-Fock type approaches, rather than accurately describing the nuclear potential, is finding a model which best represents the interaction between nucleons, as unlike in the atomic case, this is not known analytically.

2.7 Single Particle Models

2.7.1 The Nuclear Shell Model

From experiments, certain nuclei with special values for proton and neutron number (the so-called "magic numbers") proved to be much more tightly bound than other models such as the liquid drop model predicted. This suggested the possible existence of a shell structure within the nucleus [68]. These magic numbers were found to be 2, 8, 20, 28, 50, 82 and 126,

evidence for which can be seen in plots such as the one seen in Figure 2.2. The idea of a shell structure was theorised in the 1930s [69, 70] and the first shell models discovered in 1949 [71–74] successfully reproduced and explained the magic numbers.

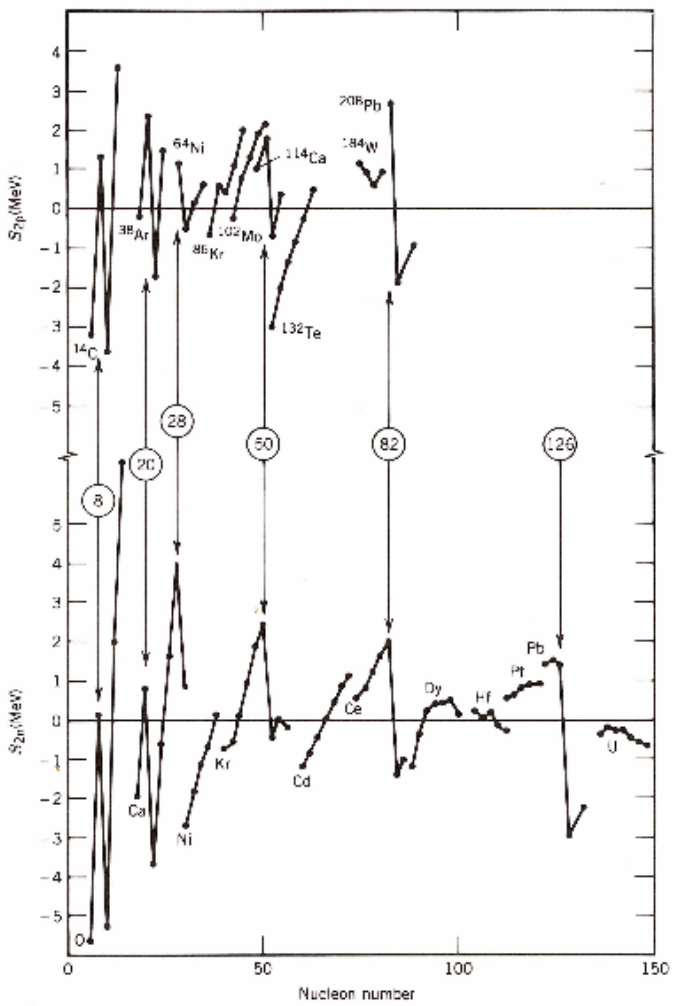

Fig. 2.2 Two nucleon separation energies for series of isotopes (top; two proton separation energy) and isotones (bottom; two neutron separation). The lowest Z / A number nuclei is noted for each sequence. The data plotted is the difference between the predictions from the SEMF mentioned in section 2.5 and measured values [75]. The abrupt changes around the so-called "magic numbers" is apparent. Figure scanned from [40].

The nuclear shell model suggests that the nucleons can be treated in such a way that they fill "shells", analogous to how electrons fill shells orbiting the nucleus in the atomic shell model, with lower energy shells favoured according to the Pauli exclusion principle [76, 77],

but without a central potential. In this model, each neutron moves independently in a common potential well that is the spherical average of the nuclear potential produced by all the other nucleons, while each proton moves independently in a common potential well that is the spherical average of the nuclear potential of all the other nucleons, together with the Coulomb potential of the other protons [78] (i.e. protons and neutrons fill their own seperate shells, independent of each other).

An important factor in explaining the extra binding energy and stability associated with nuclei at these magic numbers lies in how one models the potential in which the nucleons sit. Figure 2.3a shows at what nucleon numbers the extra stability is predicted if nucleons were acted on by the infinite square well and harmonic oscillator, early models for this nuclear potential [79]. The degeneracy, i.e. the number of nucleons that can be contained at each energy level is $2(2l+1)$ ('Pauli exclusion principle' - cannot have same set of quantum numbers [76, 77]). While quite close (correct for the first three numbers), neither potential successfully reproduces the magic numbers.

A spherically symmetric central mean field potential called the Woods-Saxon potential [80] can be used as the potential in which the nucleons lie and takes the form of the equation shown in equation 2.11, where $R = r_0 A^{\frac{1}{3}}$, known as the nuclear radius. In this equation $r_0 = 1.25$ fm and A is the mass number. Typical values for the parameters are: $V_0 \approx 50$ MeV and $a \approx 0.5$ fm [81].

$$V(r) = -\frac{V_0}{1 + exp(\frac{r-R}{a})} \tag{2.11}$$

This potential is a good approximation as it well represents the nature of the strong interaction at short distances; it rapidly approaches zero as r goes to infinity $((r-R) \gg a)$ and nucleons at $r \approx R$ within a distance of order a near the surface of the nucleus experience a large force towards the center. Its predictions for the magic numbers can be seen in Figure 2.3b. Even using this modified potential, the magic numbers cannot be accurately reproduced. It is

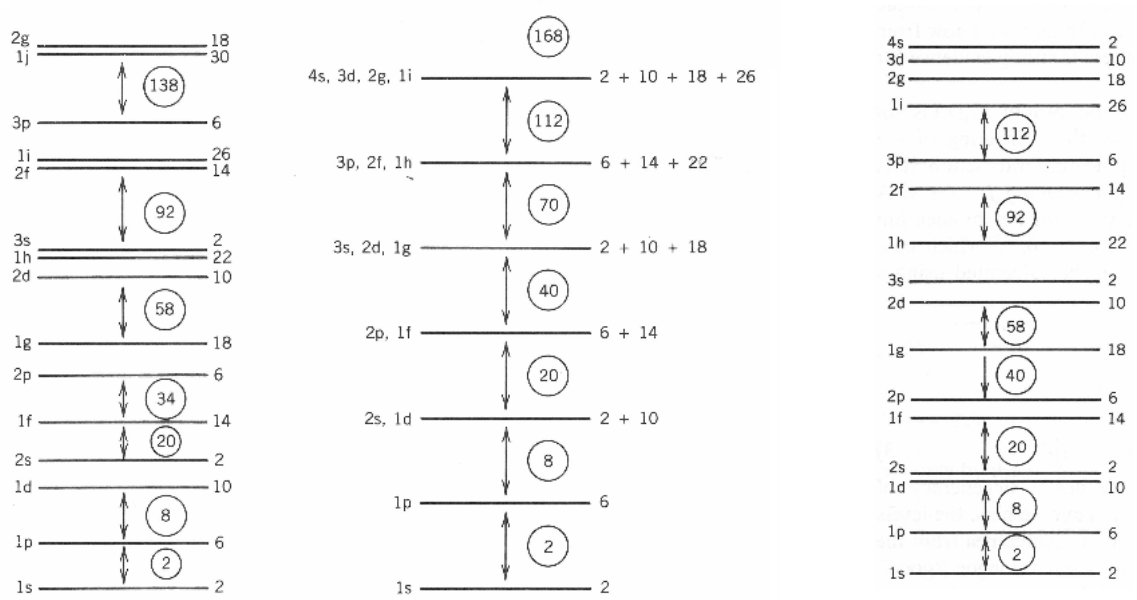

(a) Infinite square well (left) / harmonic oscillator (right) (b) Woods-Saxon

Fig. 2.3 Splitting of the nucleons with predictions for the nucleon numbers at which "closed shells" appear; where the nucleons are acted on by the infinite square well, harmonic oscillator and Woods-Saxon potentials, respectively. Figure scanned from [40].

not sufficient to solely model the nucleons as moving within a common potential well. The spin-orbit interaction must also be taken into account, given the quantum-mechanical model of the nucleus being considered. This can be done using equation 2.12, where $V_c(r)$ is a central potential such as the Woods-Saxon potential and $V_{so}(r)\vec{L}.\vec{S}$ is the term representing spin-orbit component [73]. This splits the levels into their different j values.

$$V(r) = V_c(r) + V_{so}(r)\vec{L}.\vec{S} \tag{2.12}$$

$$\vec{L}.\vec{S} = \frac{1}{2}[\vec{J}^2 - \vec{L}^2 - \vec{S}^2] \tag{2.13}$$

Recalling that protons and neutrons are fermions, they must obey the 'Pauli exclusion principle' and must have half integer spin [76, 77]. Equation 2.13 can be obtained by remembering that $\vec{J} = \vec{L} + \vec{S}$. With this in mind, for a single nucleon, the quantum number $j = l \pm \frac{1}{2}$.

Using the equations and principles mentioned, the magic numbers are successfully predicted. Figure 2.4 displays how taking into account the spin-orbit interaction changes the energy levels and the degeneracy of each level.

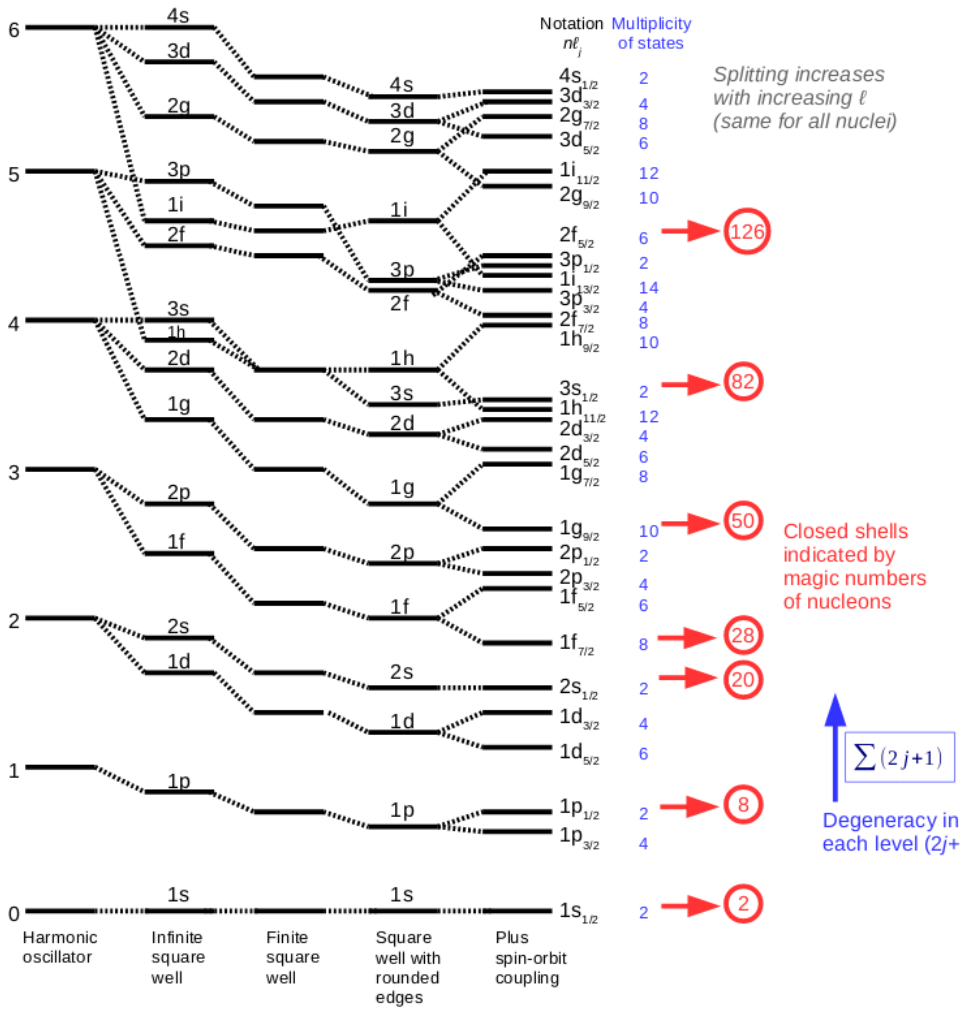

Fig. 2.4 Splitting of the nucleons with predictions for the nucleon numbers at which "closed shells" appear for several different potential types and for when the spin-orbit potential is included, and how these compare and change. Figure reproduced from [82].

The shell model can be used to predict the spin and parity of the ground state of nuclei. All nucleons in a complete shell have total angular momenta zero has they cancel each other out and all nucleons in the same energy level have the same parity, therefore with an even number of nucleons, the parity will always be positive. This means that all nucleons from closed shells

contribute positive parity and zero angular momentum, allowing for the prediction of spin and parity for the ground state of nuclei via any nucleons outside closed shells.

In the case of even-even nuclei (nuclei with an even number of protons and an even number of neutrons) such as ^{60}Zn and ^{72}Se, this will always be 0^+, as two of the same nucleon outside of a closed shell will always be paired (left-most example in Figure 2.5). This is because once one considers the relation between the strong interaction and angular momentum, it can be assumed that nucleons in the same energy level tend to form pairs of opposite angular momenta. It is implied there is a paring interaction which makes this configuration more energetically favourable [83].

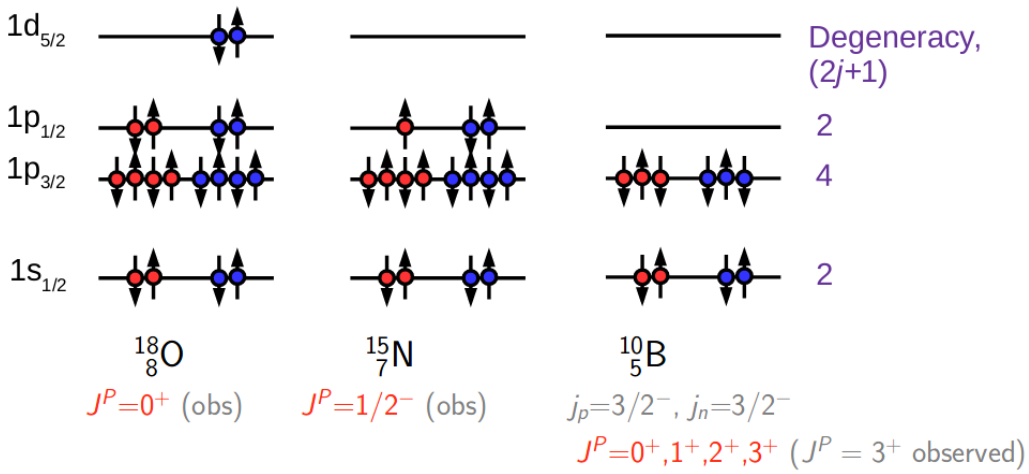

Fig. 2.5 Examples of how the shell model can be used to predict the spin and parity of the ground state of nuclei. Figure reproduced from [82].

The shell model is problematic, however, with isotopes far from closed shells. The assumption made based on this model is that nucleons within bound shells do not contribute to nuclear properties. By consequence, this model is less effective at N and Z far from closed shells as there are a great number of valence particles outside of the core of bound shells.

2.7.2 The Deformed Shell Model

An issue presented by the shell model is its assumption of a spherical nuclear shape [3], with its ability to predict nuclear properties, such as the spin and parity of states, breaking down for nuclei with significant deformations from spherical shape (e.g. nuclei far from closed shells). A generalisation of the shell model for deformed shapes was developed by S. G. Nilsson [4] and is known as the deformed shell model, or Nilsson model.

The principle behind this model is to alter the oscillator constants in the various spatial directions. Take the case of the simple harmonic oscillator, where the potential $V(r)$ becomes:

$$V(r) = \frac{m}{2}(\omega_{\mathrm{x}}{}^2 x^2 + \omega_{\mathrm{y}}{}^2 y^2 + \omega_{\mathrm{z}}{}^2 z^2) \tag{2.14}$$

where m is the mass of the particle, $\omega_{\mathrm{x,y,z}}$ are the angular frequencies in the respective axes and x, y and z are the distances from the centre along the respective axes. This potential can be substituted into equation 2.12 as $V_{\mathrm{c}}(r)$. This new total potential creates its own energy level splitting which takes into account the deformation of nuclei.

Many states which are seperate in the spherical shell model are found to mix in the deformed shell model, such as the $1\mathrm{d}_{3/2}$ and the $1\mathrm{f}_{7/2}$ states. As a consequence, the total angular momentum does not have a well defined value in this model, especially in the case of non-axially symmetric nuclei, for which the Nilsson model was extended for by Newton [84, 85]. For axially symmetric deformation, however, there is a well defined quantum number, Ω, which is the projection of the total angular momentum on the symmetry axis. This principle is displayed in Figure 2.6. Consider the valence nucleon in orbit of the deformed potential as in Figure 2.6. It will have lower energy if its orbit lies closer to the rest of the nuclear matter than if it lies at larger distances from it [86]. From this, it is obvious the that a particle following the orbit on the left of Figure 2.6 will have lower energy than the other in that case i.e. the energy depends on the orientation with respect to the symmetry axis.

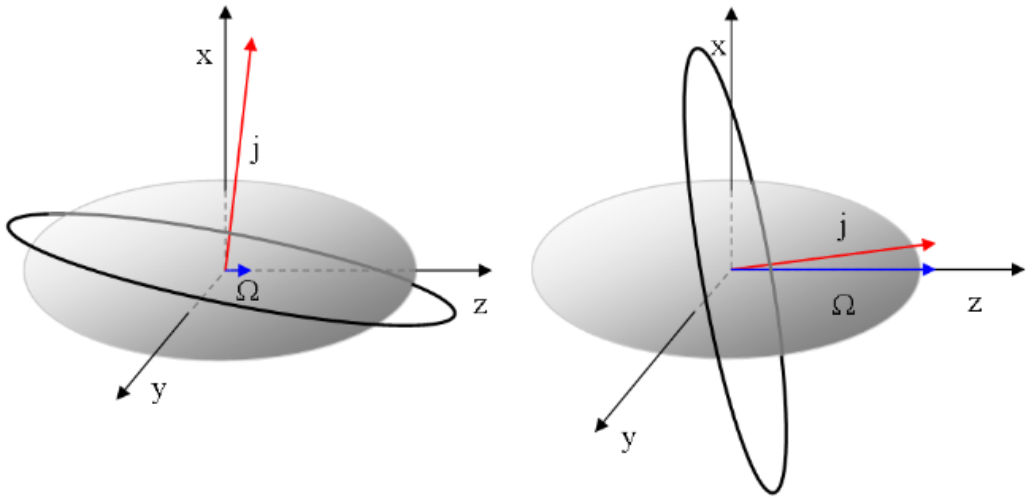

Fig. 2.6 Visual representation of Ω, the projection of the total angular momentum on the symmetry axis. Figured reproduced from [87].

Figure 2.7 shows a "Nilsson diagram" where single particle energies are plotted against a deformation parameter, in this case ε, which indicates if deformation is prolate ($\varepsilon > 0$) or oblate ($\varepsilon < 0$) for axially symmetric nuclei. The quantum number, Ω, is visible for each individual level, displayed as the number on the lines outside of the square brackets, with the numbers in the square brackets representing the quantum numbers $[Nn_z m_l]$. For more detailed information on the Nilsson notation please refer to the original paper by Nilsson [4]. The equivalent spherical shell model notation also indicated on the Nilsson diagram. This type of diagram visualises well how this model is an extension of the shell model, as at $\varepsilon = 0$ for no deformation (i.e. a spherical shape), the individual levels for each shell merge into one and form the structure predicted by the shell model. It also displays clearly the idea that the energy of the state will depend on its orientation, with the energy for any given level with specific quantum number Ω varying with changing deformation parameter. These diagrams also effectively display the shell splitting and shell mixing described previously.

This model can be used to predict the shapes of nuclei in a given state with known energy, as one can calculate the deformation parameter which fits the model for the given nucleus with specific nucleon number and known energy level. Large shell gaps at both prolate and

oblate deformation can tell us that a wide variety of shapes may be exhibited in this nucleon number region. An example of this is for nucleon number = 34, which is marked and visible on Figure 2.7.

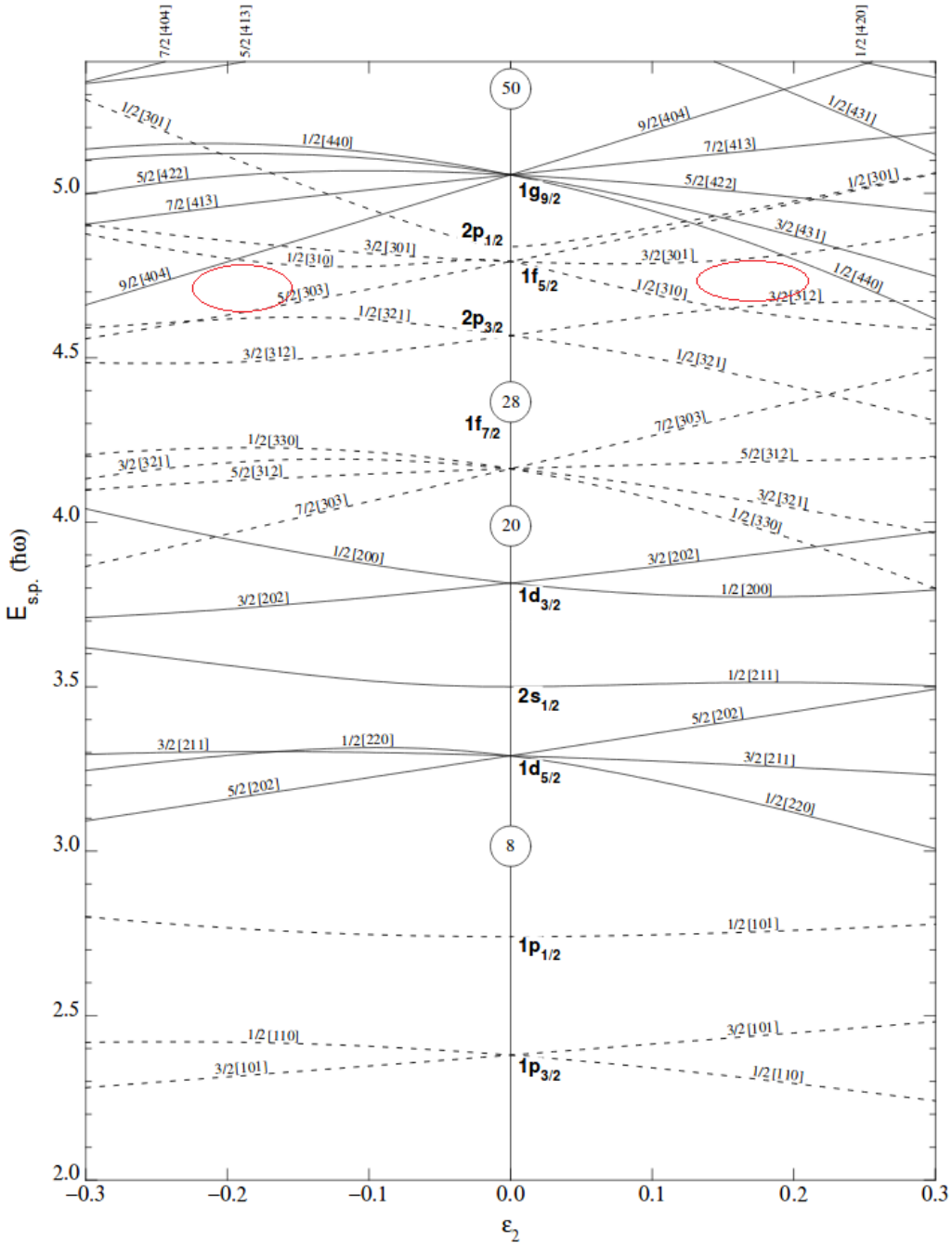

Fig. 2.7 Nilsson diagram for protons or neutrons, Z or N $\leq$ 50. Shell gaps at both prolate and oblate deformation are indicated for Z = 34. Figure adapted from [88].

.

2.8 Collective Motion of the Nucleus

The nucleus, as discussed previously, can be seen as a quantum mechanical system with discrete energy levels, with these levels differing for each nucleus. These energetic states can occur due to the collective motion of the nucleons, which can be split into two categories: vibrational motion and rotational motion. The type of collective motion can be distinguished by looking at the energy levels of the excited states in a given nucleus [5]. The principle of collective motion is that one takes the nucleus as a single body which can undergo these types of motion, an idea first stemming from the liquid drop model of the nucleus described in section 2.5 [89]. With the discovery and implementation of the shell model in 1949, the theory of nuclear collectivity was brought forward and adapted to take into account the new model of the nucleus [3, 90–92].

Nuclear rotations tend to be observed experimentally in high-A nuclei (A ~ 150 and above), as well as in nuclei with non-spherical equilibrium shapes far from closed shells. These motions are much tougher to observe outside this range and are dominated by vibrational states, with some exceptions such as the superderformed states of ^{36}Ar [93]. The Hamiltonian of a nucleus while undergoing rotational motion has the form [91]

$$H_{\text{rot}} = \sum_{k} \frac{L^2}{2I_{\text{k}}} \tag{2.15}$$

where k represents the three axes in the reference frame, L is the rotational angular momentum and I_{k} is the moment of inertia with respect to the k-th axis. If one takes the case of an even-even nucleus such as ^{72}Se, it can be assumed the ground state of any band is $J^{\pi} = 0^{+}$. The first rotational band of such a nucleus built on such a state will have angular momentum arising solely from rotational motion ($J = L$) with its projection along the symmetry axis, K, equal to 0 for an axially symmetric nucleus [94]. As a consequence, the motion of rotation must be about an axis perpendicular to that of the one of symmetry. The energies for this band can thus be represented by equation 2.16, for even integer values of J.

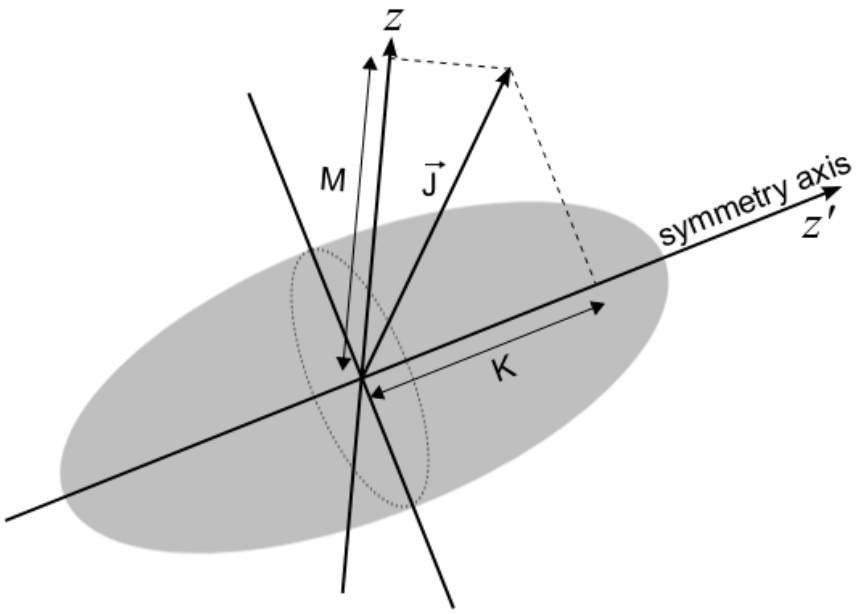

Fig. 2.8 A cylindrically symmetric rotator. The symmetry axis is z'. The projection of the angular momentum upon this axis is K, and upon the z-axis in the laboratory frame is M. Figure reproduced from [95].

$$E_{\text{rot}} = \frac{\hbar^2}{2I} J(J+1) \tag{2.16}$$

With the assumption that the moment of inertia is constant for low-spin states, one can simply calculate the energies for these states and thus transition energy ratios. The energies for the 0^+, 2^+ and 4^+ are shown in equations 2.17 2.18 and 2.19, with the ratio of the 4^+ to 2^+ shown in equation 2.20.

$$E_{\text{rot}}(0^+) = 0 \tag{2.17}$$

$$E_{\text{rot}}(2^+) = 6\frac{\hbar^2}{2I} \tag{2.18}$$

$$E_{\text{rot}}(4^+) = 20\frac{\hbar^2}{2I} \tag{2.19}$$

$$R_{4/2} = \frac{20}{6} \approx 3.33 \tag{2.20}$$

Therefore one can deduce that the first rotational band of a nucleus exhibiting perfectly rotational motion should have an $R_{4/2}$ of 3.33. However, it must be considered that this is an idealised situation; centrifugal stretching will vary I, especially at higher spin [96]. The ground-state rotational band of ^{160}Dy, for example, has a ratio $R_{4/2}$ of 3.27 [97]. $R_{4/2}$ values like this show that the nucleus in question does not rotate like a rigid body as in the idealised scenario; only some of its nucleons are in collective motion. Nonetheless, this can be a useful tool for identifying rotational bands in nuclei.

Nuclear vibrations occur when a nucleus oscillates about its equilibrium shape. These vibrations can be represented by multipole radiation as shown in Figure 2.9. The nuclear shape can be modelled mathematically and will change based on a parameter from this model, λ, as seen in equation 2.22 in section 2.10. λ represents the type of multipole radiation by which the vibration is occurring, such that the multipole is a 2^λ-pole i.e. $\lambda = 0$ is a monopole, $\lambda = 1$ is a dipole etc. as can be seen in Figure 2.9. This vibrational energy is carried by the phonon, comparable to how the photon is the carrier for the electromagnetic interaction. The respective 2^λ-pole radiation is carried by its corresponding phonon i.e. quadrupole radiation carried by $\lambda = 2$ quadrupole phonon and carries two units of angular momentum etc.

Monopole vibrations are accounted for by calculations of the average radius of the nucleus in the nuclear shape, while dipole vibration cannot occur due to the effect of internal nuclear forces as it involves a net displacement of the centre of mass of the nucleus [40]. The quadrupole vibration is thus considered. In the case of an even-even nucleus with ground state 0^+, adding a single quadrupole phonon carrying 2 units of angular momentum (and by proxy, even parity) will always give a first excited state of 2^+. Adding another quadrupole phonon gives rise to a

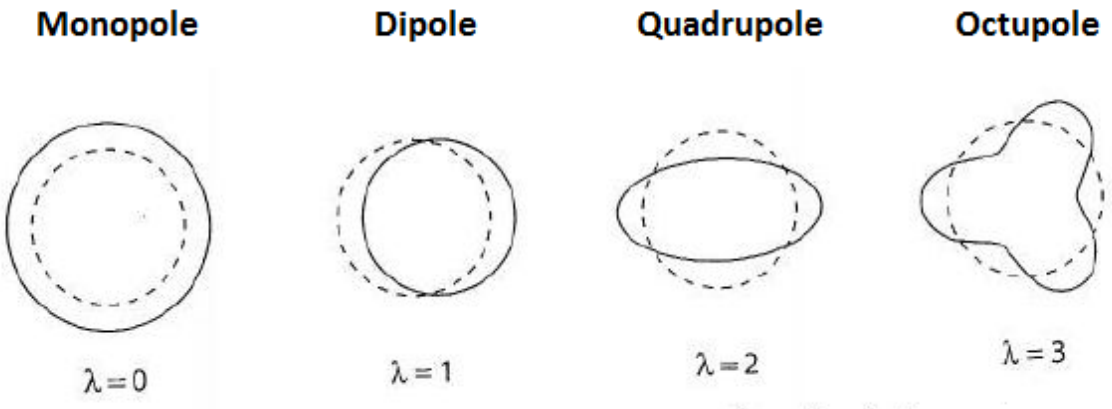

Fig. 2.9 The first vibration modes of the nuclear surface, showing the form of the nucleus for each mode (solid line) in comparison to the original spherical nucleus. The dotted line represents the original "fixed volume" sphere. Figure taken from [98].

.

triplet of 0^+, 2^+ and 4^+ states, though the degeneracy of the triplet tends to break down given the simplified nature of this model [40, 94]. Clusters of these three states at similar energy can be seen in vibrational even-even nuclei, such as in ^{120}Te [99, 100].

If one approximates these vibrations with a quadrupole harmonic oscillator, the energy spectrum will follow equation 2.21 with $n = 0, 1, 2, 3...$ for the number of phonons for the state, ω the oscillation frequency and $\hbar$ the reduced Planck's constant as previously.

$$E_{\mathrm{n}} = \hbar\omega\left(n + \frac{5}{2}\right) \tag{2.21}$$

Given the energy spectrum dictated by equation 2.21 and the fact each phonon carries the same amount of energy, the energy levels in a nucleus of this kind should be equally spaced, meaning a ratio $R_{4/2}$ of 2. This can be seen in even-even nuclei, such as the example nucleus used previously, ^{120}Te [99, 100].

Vibrational nuclei can also exhibit octupole collectivity with $\lambda = 3$, which transfers 3 units of angular momentum and negative parity. As a result, the first excited states of such modes are 3^- and these tend to be found at energies above the two-phonon states.

2.9 Hartree–Fock Theory and "Self-Consistent" Methods

The problem with finding a model which best represents the interaction between nucleons lies in the fact that while the strong force is relatively well understood on the quark binding level, the residual force which binds together the nucleons is not. There is no currently established connection between the quark-quark interaction and the nucleon-nucleon interaction which gives any insight into the latter, though chiral effective field theory has had successes in recent times for microscopic calculations of nuclear reactions and structure [101–103], being applied in few-nucleon reactions [104] and predicting structure of lighter mass nuclei [105].

One has to consider that the interactions between nucleons in the nucleus are far more complex than a simple two-body problem, thus this issue could be better solved numerically. The idea of the Hartree-Fock approach is to find an approximation to the ground-state, starting with a Hamiltonian with N kinetic energy terms (N.B. not neutron number N, but some variable N) and potential terms taking into account all possible two-body interactions in the set of n fermions. This approximation of the N-body problem minimizes the total-energy wave-function "functional", allowing only N-body Slater determinants [106] of one-particle spin-orbitals as variational functions. This method leads to a set of unknowns in the Hartree–Fock equations [7–9]. The individual energy levels (and wave-functions) of nucleons can be established once these are solved.

When the Hartree solution of the Schrödinger equation (basis for the Hartree-Fock method) was derived, it was noted that the eventual field computed had to be "self-consistent" with the initial assumed field [107]. In addition, it is normal for the solutions of the Hartree-Fock equations to have nucleons subject to the mean field created by other nucleons. For this reason, this type of method was also referred to as the self-consistent field method (SCF) [108, 109].

While Hartree-Fock equations are obtained analytically, they are commonly solved numerically. In practice, one starts with a set of reasonable guesses for the individual wave-functions e.g. eigenfunctions of a harmonic oscillator, which can be used to compute a Hartree–Fock

potential. The Schrödinger equation is then solved again and the process repeats until the difference between the new and previous wave-functions (or energy levels) is below a given value, as in any iterative numerical method. The equations are almost universally solved by means of an iterative method, although a fixed-point iteration algorithm does not always converge [110]. In this way, the mean-field potential is defined and the Hartree-Fock equations at this point are treated as the standard Schrödinger equations for the system. The corresponding Hamiltonian is called the Hartree-Fock Hamiltonian. The Bogoliubov transformation is often used to diagonalize the Hamiltonians, which yields the stationary solutions of the corresponding Schrödinger equation [10]. This method, known the HFB (Hartree–Fock–Bogoliubov) method, has the ability of more accurately predicting certain properties of nuclei, especially away from closed shells [111, 112]. Other modern nuclear structure theories, such as the Adiabatic Self-Consistent Coordinate (ASCC) method, are also derived via this method.

2.10 Nuclear Shapes, Deformation and Shape Coexistence

The shape of a nucleus can be described using the multipole parameter, λ, defined in section 2.8. The radius of this deformed nucleus, $R(\theta,\phi)$, defined as the distance between a point on the nuclear surface and the origin, can be written as seen in equation 2.22 [92] where R_s is the nuclear radius in a spherical configuration equal to the nuclear radius defined in section 2.2.1, μ is the projection of λ on the z-axis and $\alpha_{\lambda,\mu}$ and $Y_{\lambda,\mu}$ are the expansion coefficients for deformation and spherical harmonics, respectively.

$$R(\theta,\phi) = R_s\left(1+\sum_{\lambda\mu}\alpha_{\lambda,\mu}Y_{\lambda,\mu}(\theta,\phi)\right) \tag{2.22}$$

If one considers the quadrupole deformation, found commonly in nuclei far from closed shells [86], the equation seen in (2.22) can be reduced for $\lambda = 2$ leading to definition of parameters known as β and γ, representing the deformation of the nucleus in this mode [92, 113].

The β parameter defines the stretching or compression in a reference direction e.g. the symmetry axis for axially symmetric nuclei, while the γ parameter is an angle which defines this reference axis. For γ values which are a multiple of 60° , the β parameter refers to stretching or compression along the symmetry axis and thus defines a prolate, spherical or oblate axially symmetric shape. For γ values $\neq$ n $\cdot$ 60°, all 3 axes are different and thus the nucleus is described as having a non-axially symmetric deformation. The way these parameters describes the shape is well displayed in Figure 2.10.

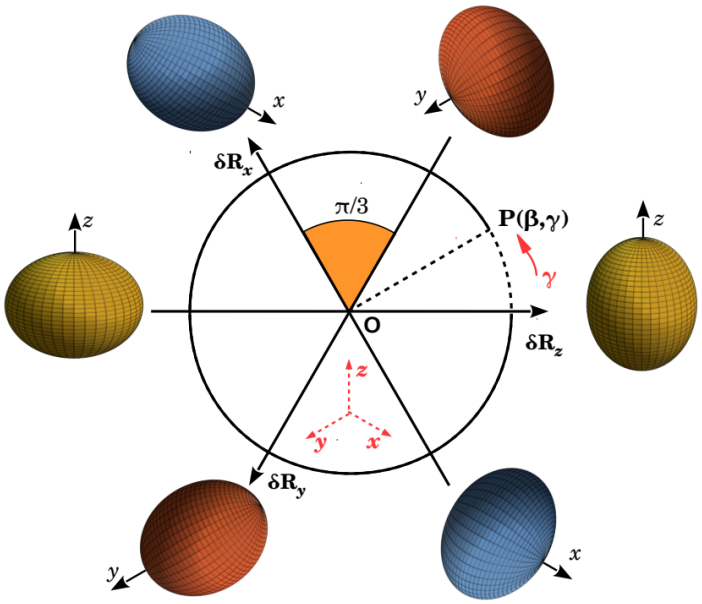

Fig. 2.10 Visual representation of quadrupole deformation with β-γ coordinates. The origin O represents the spherical configuration. If one takes a deformed nucleus represented by point P, β is given by the length of the segment OP and γ is given by the angle subtended from the horizontal axis. Figure reproduced from [114].

As one can see, if nucleus is axially symmetric and falls on one of the solid lines in Figure 2.10, the shape can be described purely by the sign and magnitude of the β parameter, with the sign defining if it is prolate or oblate and the magnitude expressing the extent to which this shape has this type of deformation. So for nuclei with γ = n $\cdot$ 120°, the shape is described with β going from perfectly oblate at β = -1 through to perfectly prolate at β = +1. For γ = n $\cdot$

120 + 60°, it is similar but with the sign convention reversed, where β = -1 describes a perfectly prolate shape and β = +1 describes a perfectly oblate shape.

With this in mind, rather than normalizing the γ parameter to 0 and looking at the β parameter deformation, typically done for axially symmetric nuclei, one can look at the absolute magnitude of β in conjunction with γ to understand more about shape configuration. For example, with an absolute magnitude of $\beta = 0.7$, if $\gamma = 0°$ then the shape is axially symmetric and extremely prolate, if $\gamma = 60°$ then the shape is axially symmetric and significantly oblate and if γ is in between these values then the shape is non-axially symmetric. Using this convention, one arrives at the classic potential energy surface contour diagrams which describe nuclear shape seen often in literature, such as the one for ^{72}Se displayed in Figure 2.11 and thus these predictions can be used not only to study the quadrupole deformation of a nucleus but also its triaxiality.

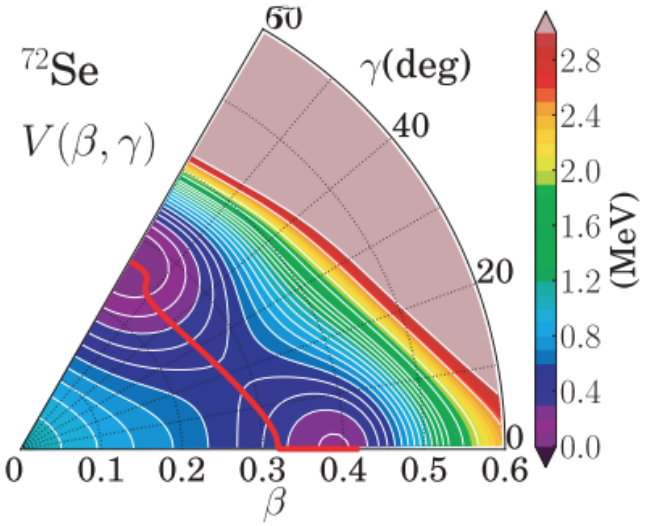

Fig. 2.11 A β-γ contour plot for the ^{72}Se nucleus. Purple areas represent the deepest minima in the potential energy surface predicted for this nucleus, seen at both prolate and oblate axial deformation (around β 0-3 - 0.4), using a constrained Hartree-Fock-Bogoliubov (CHFB) method. This is an indicator of shape coexistence. Figure taken from [115].

As a consequence of this deformation, the nucleus must have an electric quadrupole moment that is non-zero, as described in section 2.7.1, due to the shift in charge distribution. This is defined in equation 2.23 as

$$Q_0 = \langle \Psi_{\mathrm{J\,M\,K}} | Q_2 | \Psi^*{}_{\mathrm{J\,M\,K}} \rangle \tag{2.23}$$

which is the diagonal matrix element where Ψ_J is the state of the nucleus with some total angular momentum J, magnetic quantum number M and quantum number K representing the projection of J on the symmetry axis for axially symmetric nuclei, Ψ^*_{JMK} is it's conjugate and Q_2 is the quadrupole moment operator. If one holds the assumption of an axially symmetric nucleus with even charge distribution, the intrinsic quadrupole moment, Q_0, can be expressed by equation 2.24 where Z is the proton number of the nucleus, R_{x} is the radius one of the two identical axis and R_{z} is the radius of the symmetry axis.

$$Q_0 = \frac{2}{5} Z \left({R_{\mathrm{z}}}^2 - {R_{\mathrm{x}}}^2 \right) \tag{2.24}$$

One can see from this equation that the shape of the nucleus will determine the sign of the quadrupole moment where a prolate shape will give a positive Q_0, an oblate shape a negative Q_0 and $Q_0 = 0$ is a spherical shape. This physical quantity gives a similar insight into the shape of a nucleus as the β parameter when considering nuclei which are axially symmetric. In fact, these can be related as seen in equation 2.25 [116], which considers up to the second-order term of the expansion.

$$Q_0 = \frac{3}{\sqrt{5\pi}} Z \beta {R_{\mathrm{s}}}^2 \left(1 + \frac{2}{7} \sqrt{\frac{5}{\pi}} \beta \right) \tag{2.25}$$

If one can find the quadrupole moments of different states, information can be inferred on how the shape of the nucleus develops as it changes state. Spectroscopic quadrupole moments represent the most direct measure of the charge distribution of nuclei and hence

of the nuclear shape [117]. One can relate the spectroscopic quadrupole moment, Q_s to the intrinsic quadrupole moment Q_0 using equation 2.26 where K is the projection of the angular momentum I onto the symmetry axis of the nucleus.

$$Q_s(I) = \frac{3K^2 - I(I+1)}{(I+1)(2I+3)} Q_0 \tag{2.26}$$

Q_s does not guarantee a model-independent measure of the intrinsic shape of the nucleus, however. If one takes the example of a non-axial nucleus, for states with $K = 0$, Q_s and Q_0 have differing signs, implying the shape observed in the laboratory frame is not the intrinsic shape. Furthermore, the spectroscopic quadrupole moment for quantum states with angular momentum 0 or $\frac{1}{2}$ cannot be observed. Therefore, quantifying this observable only allows for the deduction of shapes of higher spin states such as 2^+ and 4^+ states. In some cases, the spectroscopic quadrupole moment vanishes, such as in cases of shape coexistence where prolate and oblate shapes are mixed and equally probable, or for certain non-axial shapes [117].

If one can obtain a sufficient number of matrix elements, the β and γ parameters for the lowest-lying states of different bands can be obtained using the Kumar-Cline quadrupole sum rules [118, 119]. This method is particularly helpful for 0^+ states, given the lack of observable quadrupole moment as mentioned previously. They provide a bridge between the matrix elements and the intrinsic shape of the nucleus and involve evaluating so-called rotationally invariant scalar products of the electric quadrupole operator, E2, implying that the results will be the same, independent of the reference frame used: be it the laboratory frame or the frame centered on the principal axis of the nucleus [120]. A greater scope of discussion and derivation of these invariants and the sum rule methodology is beyond the scope of this work and the reader is pointed to the original references references [118, 119] for this.

In Figure 2.11, the contour map shows predictions for shapes at both prolate and oblate shapes, implying there are eigenstates with different shapes coexisting at the same time. This is a typical way of identifying of shape coexistence in nuclear physics. Certain nuclei can

exhibit eigenstates with different shapes and this appears to be a unique type of behavior in finite many-body quantum systems [121]. This means that a nucleus can have certain shape configuration in its ground state coexisting with some different shape configuration in another band of states. This phenomenon is known as shape coexistence. A classic signature of shape coexistence is where a ground state of a given nucleus in one shape configuration, with a low-lying second 0^+ state in a differing shape configuration.

Shape coexistence can be predicted in theory with the HF method described in section 2.9 constraining the nuclear density to different multipole deformation (e.g. quadrupole and octupole). Single particle states are obtained in this way and result in an energy surface with a minimum energy that most often corresponds to a non- spherical density distribution. One can also include pairing interactions using the HFB method to simultaneously optimize both the mean single-particle field and the pairing properties in nuclei. As a result, coexisting shapes may appear for certain proton and neutron numbers [121].

Shape coexistence in nuclei was first observed in doubly closed shell ^{16}O and ^{40}Ca [121–123] and was initially seen as an an exotic rarity that exhibits “islands of occurrence”, say around N = Z or near doubly closed shells. A famous instance of shape coexistence in nuclear phyics is that of the Hoyle state [124], a shape co-existing excited state of ^{12}C essential for the nucleosynthesis of carbon in helium-burning stars. There is a reasonable possibility that it may be observed in almost all nuclei and could explain the apparent disappearance or "collapse" of the shell structure in nuclei [121]. Deformation of nuclei can also exhibited via octupole deformation, with $\lambda = 3$. For some combinations of Z and N the nucleus can further lower its energy through octupole-octupole interactions, and the nucleus no longer retains reflection symmetry [125], such as for nucleon numbers 34, 56, 88 and 134. Octupole deformations are not investigated in this work, but are relevant to the broader scope, with an example of an "octupole magic" nucleus being ^{68}Se, which is predicted to have large octupole deformation [126].

2.11 Mirror Nuclei and Structure Around the N = Z Line

Mirror nuclei are pairs of nuclei which have the same nucleon number but have their proton and neutron number interchanged. For example, the mirror nucleus for ^{58}Ni, which has Z = 28 and N = 30, is ^{58}Zn, which has Z = 30 and N = 28. Given the charge-independent nature of the strong interaction, both protons and neutrons can be treated identically, as nucleons, with nucleons having isospin t = 1/2. Total isospin of a nuclear system, T, can take a half-integer value between $|N-Z|/2$ and $(N+Z)/2$. Under this isospin formulation, neutrons and protons have isospin projection $t_z(n)$ = +1/2 and $t_z(p)$ = -1/2, respectively. One can couple the projections of the isospin to give the total isospin projection, t_z, as described in Equation 2.27, where where N is the neutron number Z is the proton number the nucleus of interest.

$$T_z = \frac{1}{2}(N-Z) \tag{2.27}$$

Under this description, one would expect nuclei with the same nucleon number A and isospin T to have very similar structure. Mirror pairs are a great display of this isospin symmetry as, were it not for isospin-breaking and Coulomb effects, they would have exactly the same structure. This is well presented visually in Figure 2.12 for the ^{70}Kr/^{70}Se mirror pair.

Protons and neutrons in these nuclei typically occupy the same orbitals which makes the nuclear structure more intriguing with respect to other areas of the nuclear chart. For example, N = Z nuclei are important for the understanding of the proton-neutron pairing interaction and the so-called "Wigner" effect. The latter, manifesting as an excess binding in self-conjugate systems, is still treated as an empirical correction even in the most advanced microscopic mass models [128].

N = Z nuclei also of interest when looking for so-called 'superallowed' beta decays. These special decays are particularly sensitive to theoretical analysis and precise experimental measurements of superallowed beta decays provide fantastic tests of the Standard Model of

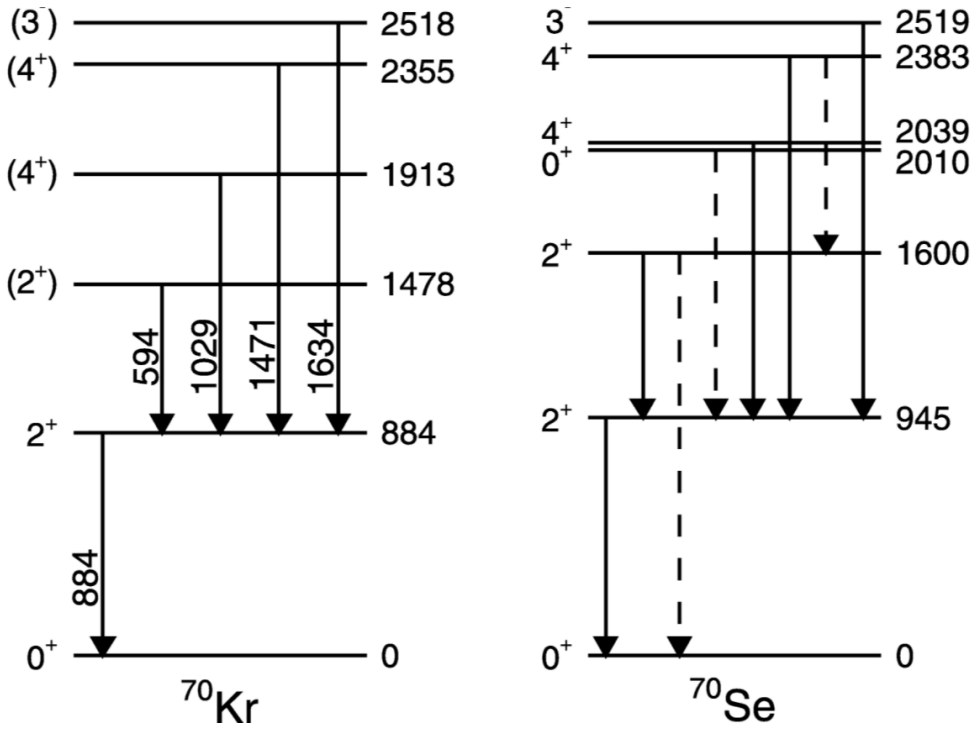

Fig. 2.12 Level scheme of ^{70}Kr and its mirror nucleus ^{70}Se as reported by Wimmer et al. and figure adapted from [127].

Particle Physics, specifically its description of electroweak interactions. For example, the recent paper discussing the properties of the currently known superallowed $0^+ \rightarrow 0^+$ decays [129], confirming the Conserved Vector Current (CVC) hypothesis [130] of the Standard Model to high degree of precision.

Furthermore, one can investigate possible alpha cluster states along the N = Z line, for example ^{60}Zn = ^{56}Ni + ^{4}He or clustering in the ^{12}C + ^{12}C as seen in Ref [131]. Clustering in nuclei is a long-standing topic in nuclear physics. While it has attracted much experimental and theoretical attention over the years, it is a model which is still controversial in terms of whether such clustering can be clearly delineated and separated from the complexity of nuclear structure described within more conventional nuclear models. In this sense, there is still ambiguity in terms of the uniqueness and relevance of the clustering description [131].

Alpha-clustering, superallowed beta decays and the Wigner effect are not discussed in the main body of this thesis but give insight into why phenomena around the N = Z line are

of interest to the nuclear structure field. In addition, N = Z nuclei lie along the explosive rp-process nuclear synthesis pathway and their low-lying structure may be of interest in determining astrophysical reaction rates, such as in the case of ^{60}Zn.

Around the N = Z line where these similarities in mirror nuclei are most visible, one can gain further information into the likely structure of a given nucleus by looking at its mirror partner. Conversely, constraining the nuclear properties of a given nucleus can shed light on the properties of its mirror partner. Studies into self-conjugate nuclei which lie on the N = Z line, such as ^{60}Zn, are not able to call upon this technique to gain further information on properties and structure, thus information in such cases tends to be more limited. Therefore, one has to call upon either theoretical calculations and/or angular-distribution measurements from experiment to determine the spins and parities of the excited states of interest, making experimentally constrained results more valuable when it comes to furthering the understanding of these nuclei.

Chapter 3

Low-Energy Coulomb Excitation of ^{72}Se

3.1 Introduction and Motivation

Low-energy Coulomb excitation is a process where the nucleus can be excited to higher energy levels in a solely electromagnetic way and was first used as an experimental probe in the 1950s, typically with light projectiles incident on heavy targets. The key pieces of information that can be obtained from these experiments are associated with transition probabilities between different energy levels, as well as identifying excited states and properties which give important information on nuclear shape, such as the quadrupole moment of a state [132].

The idea of exciting the nucleus in this way was first conceived as early as 1921 [133], but was not successfully reported as an excitation mechanism until heavy ions underwent single-step excitation using proton beams in 1953 [134]. In the years after this, with the availability of heavy-ion beams, multi-step Coulomb excitation would also be observed [135, 136]. This technique would proceed to be used as a tool for the model-independent measurement of properties of excited states in stable nuclei (spin-parity, energy, lifetime) and the multipolarity of the gamma decay between these states, as well as for the measure of static electric quadrupole moments in the region of nuclear chart where rotational collective motion was predicted.

Other measurements which can be made to obtain information about the quadrupole moment and quadrupole shape deformation. These include laser spectroscopy, an recent example being the recent laser-spectroscopy studies of the nuclear structure of neutron-rich radium [137], where model-independent values of quadrupole moments and mean-square charge radii gives information on quadrupole deformation. Furthermore, lifetime measurements can be used, via some model, to find information about the quadrupole shape of the nucleus. A recent example of this technique is seen from the lifetime measurements of short-lived excited states in ^{69}As and ^{66}Ge nuclei [138], where deformation and shape evolution of these nuclei is discussed. Coulomb excitation stands out from these techniques in its ability to measure higher order deformations beyond quadrupole shapes, such as octupole and hexadecapole deformations, such as in the study of isotopes of Neodymium [139].

The development of radioactive beam facilities (RIBs) using the ISOL (Isotope mass Separator On-Line) technique [140] has allowed for the production of beams of radioactive isotopes at high intensity. With this technology available, low-energy Coulomb excitation underwent a renaissance, given its ability to deduce nuclear properties in a model-independent fashion and the large cross sections associated with the Coulomb-excitation process. In parallel, theoretical work began to point towards the importance of shape coexistence and Coulomb excitation proved to be an ideal tool to probe these phenomena.

The first experiments using RIBs for low-energy Coulomb excitation were performed in the early 2000's, such as the Coulomb excitation of radioactive Te isotopes [141] and the low-energy Coulomb excitation of ^{30}Mg [142] at the ISOLDE facility at CERN in Switzerland. A pioneering study of the neutron deficient Kr isotopes was also conducted around this time at GANIL in France [143], results from which acted as motivation for study into the neighbouring Se isotopes. This is because nuclei with mass A ~ 70 close to the N = Z line have been known to exhibit different nuclear shapes, with coexistence of prolate and oblate shapes predicted over three decades ago [11]. This can be linked to large shell gaps at both prolate and oblate

deformation, with these gaps most pronounced for proton and neutron numbers 34 and 36, as seen in the previous chapter in Figure 2.7.

The low-energy Coulomb excitation experiments of neutron-deficient krypton (Z=36) isotopes, ^{74}Kr and ^{76}Kr [143], have allowed for the determination of the intrinsic shapes for several low-lying states in these isotopes. There is strong evidence for a prolate ground-state band coexisting with an excited oblate band built on the low-lying 0_2^+ state, supported by the discovery of the highly oblate 0_2^+ shape isomer in ^{74}Kr [144]. Studies into the properties of the 0_2^+ shape isomer in ^{72}Kr indicate an oblate ground state for the N = Z nucleus [145], implying that shape inversion occurs at this point along the isotopic chain. Furthermore, Hartree-Fock-Bogoliubov (HFB) calculations using the Gogny D1S interaction and the configuration-mixing method (GCM/GOA) successfully predict the shape inversion below A=74 [143].

For the neutron-deficient selenium (Z=34) isotopes the shape coexistence scenario is not as well established as in the krypton isotopes and is likely to be even more complex. The structure of ^{72}Se has been shown to be similar to that of the N = 38 isotone ^{74}Kr, with an isomeric 0_2^+ state located just above the 2_1^+ level [11]. Theoretical calculations predict oblate ground states for Se isotopes with N ~ Z [12, 115, 146], which is of considerable interest as oblate ground states are extremely rare, particularly in the middle of a shell where prolate deformation usually prevails. The position along the isotopic chain of the shape transition is also of particular interest, with this still being an open question following studies giving contrasting results for ^{70}Se [147, 148] and a further study claiming the transitional nucleus to be ^{68}Se [149].

It has also been indicated that in order to fully understand the underlying nuclear structure properties in this mass region, one should also allow for triaxial (i.e. not axially symmetric) degrees of freedom. Adiabatic Self-consistent Coordinate (ASCC) calculations for ^{72}Se, the results of which have been shown previously via the contour map in Figure 2.11, show the ground state wave function to be widely spread over the triaxial region; a maximum is expected at oblate deformation, but with the wave function extending to the prolate region [13].

Figure 3.1 shows how the prolate nature of this ground state band is expected to develop with increasing angular momentum, according to both the GCM(GOA) and ASCC calculations, while the excited state band appears to be generally weakly oblate. This result is in contrast to calculations performed for more neutron deficient ^{68}Se and ^{70}Se which utilised the same approach [13]. For the excited band built upon the known 0_2^+ level, the various theoretical approaches are in disagreement. ASCC calculations predict a weakly deformed, oblate excited band, whereas the more recent GCM(GOA) calculations predict that mixing is present for the low-lying 0_2^+ and 2_1^+ states before giving way to purer configurations at larger excitation energy.

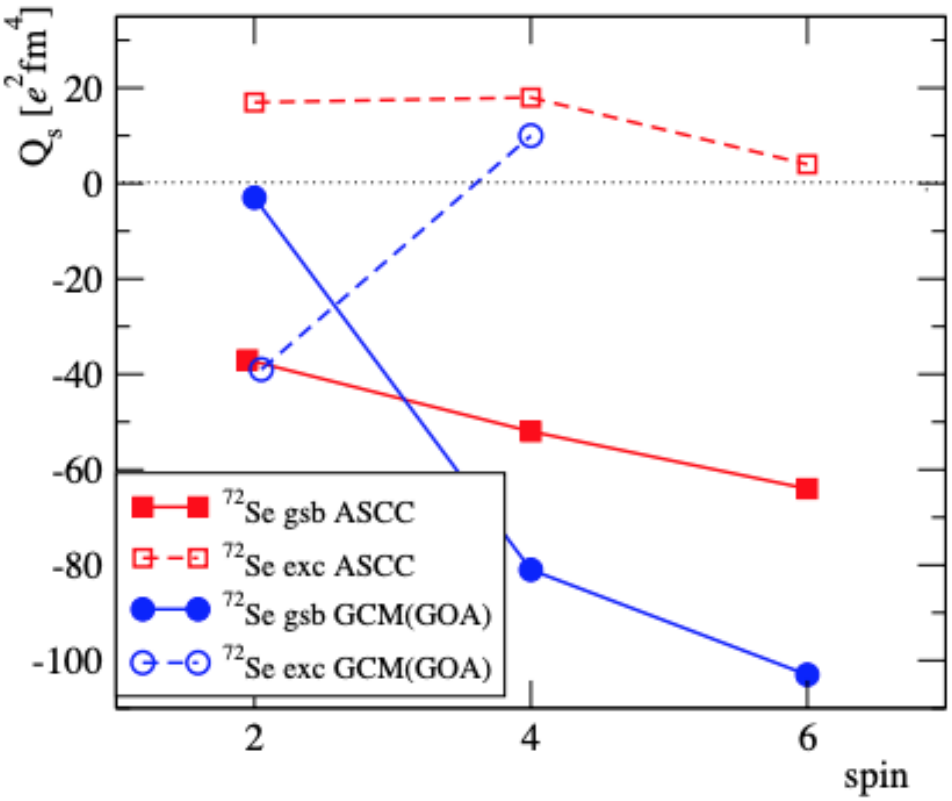

Fig. 3.1 Theoretical predictions for the quadrupole moments of states in the ground-state and excited band in ^{72}Se. The GCM(GOA) calculations [12] are represented by blue circles, while ASCC calculations from the work of Hinohara et al. [13] are represented by red squares.

Figure 3.2b) and Figure 3.2c) display the results of GCM(GOA) [12] and ASCC [13] calculations, respectively for states at low excitation energy. When compared to the experimental results, the GCM(GOA) calculations better describe collectivity present in the excited band as well as the mixing between the excited and ground state bands, but both theoretical models underestimate the strength of the inter-band transitions and generally the mixing between these two structures is still not well understood.

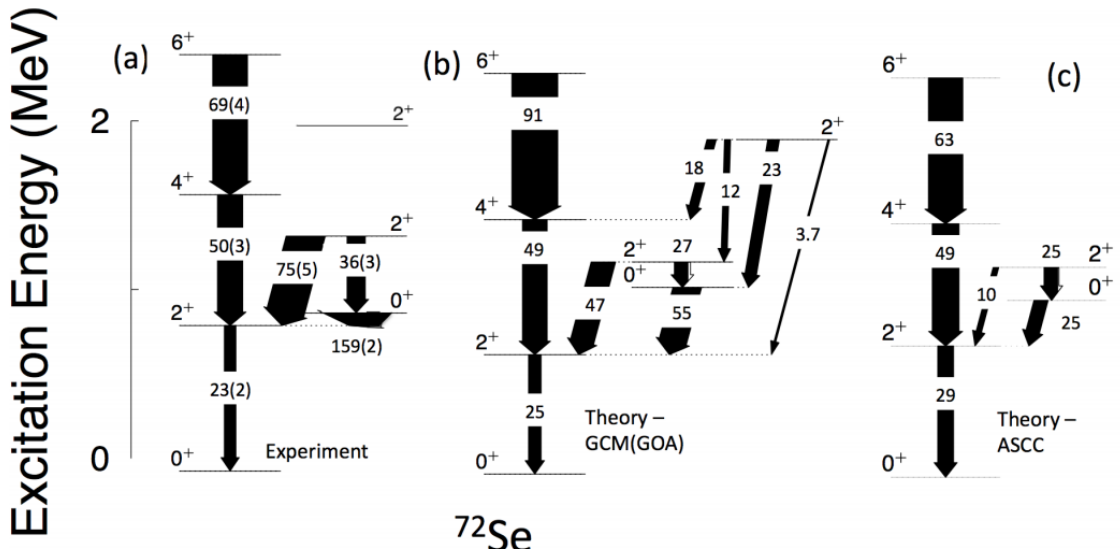

Fig. 3.2 Comparison of reduced transition probabilities, B(E2), between low-lying states in ^{72}Se between (a) Experimentally determined from ref [150]; (b) Theoretical prediction utilising the GCM(GOA) configuration-mixing method [12]; (c) Theoretical prediction using Adiabatic Self-Consistent Coordinate (ASCC) method [13]. The numbers and the widths of the arrows in each of the figures represent the B(E2) values in Weisskopf units (W.u).

The main drive for this low-energy Coulomb excitation work is to test these theoretical predictions via the measurement of E2 matrix elements connecting the states and QMs of the levels, as shapes of these states can only be inferred from their quadrupole moments. Coulomb excitation experiments are sensitive to the QM of excited states through the angular distribution of the cross section via 'reorientation' effect, which enhances or reduces the cross section depending on the size and sign of the QM. Nuclei with non-spherical charge distributions undergo reorientation in the presence of the large electric field gradient of the target nucleus,

inducing a second-order angular dependence to the cross section [151]. An example of this effect is visible in Figure 3.3, where the calculated intensity ratio of the $6_1^+ \rightarrow 4_1^+$ and $4_1^+ \rightarrow 2_1^+$ transitions for two choices of a QM corresponding to the prolate and oblate configurations are shown.

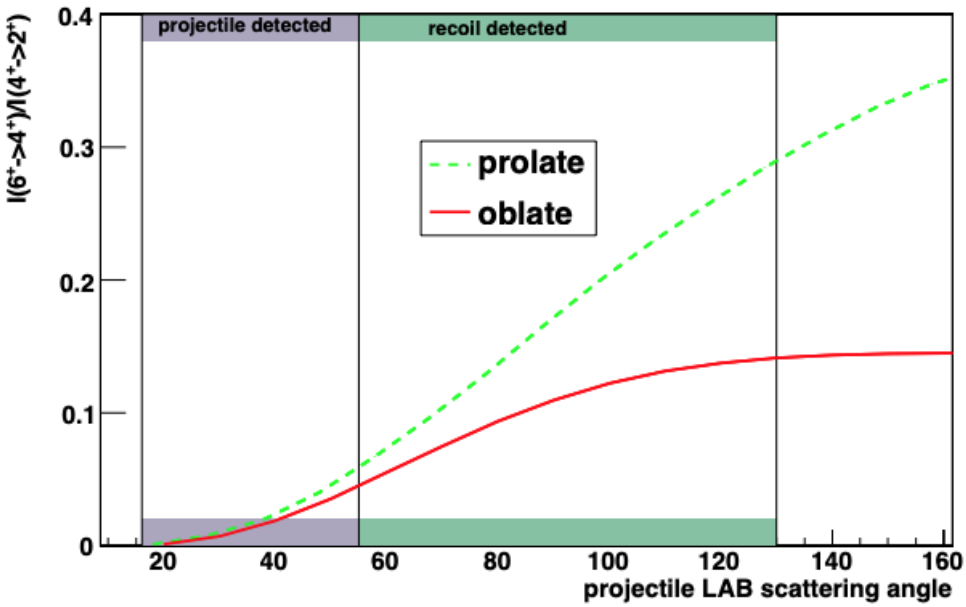

Fig. 3.3 Intensity ratio of the $6_1^+ \rightarrow 4_1^+$ transition to the $4_1^+ \rightarrow 2_1^+$ transition as a function of projectile scattering angle. Calculations were performed with the GOSIA code for different extreme assumptions of the quadrupole moment of the 4_1^+ state (corresponding to the rotational limits). The shaded areas represent the angular coverage of the particle detector for the detection of both projectiles and recoils. [152]

The low-energy Coulomb excitation experiment of ^{72}Se discussed in this work was conducted using the Miniball/CD detector setup (described further in Sections 3.5,3.6) at the HIE-ISOLDE facility at CERN. At this facility (described further in Section 3.3), state-of-the-art setups provide beams of unstable ^{72}Se with sufficient intensities which allow for the study of intrinsic shapes of a number of levels, including the critical 2_1^+, 2_2^+ and 4_1^+ states. For excited states with $J \neq 0$, assignment of the nuclear shape is achievable by measuring the static QM. The intrinsic shape of $J = 0$ states is not observable in the laboratory system but can be deduced by employing the "quadrupole sum rules" method [118, 119] from a complete

set of E2 matrix elements connecting these states, as mentioned previously in Section 2.10. This method also allows for the extraction of the /*gamma* deformation parameter which gives information on the triaxiality of the nucleus, though it should be noted that triaxiality of the nucleus is not investigated in this work and thus is not mentioned in great detail in this thesis. The approach discussed was used successfully in the analysis of the previously mentioned Coulomb excitation experiments involving the light krypton isotopes [143], as well as for the even-even Hg isotopes [153].

3.2 Low-Energy Coulomb Excitation Theory

Low-energy Coulomb excitation is a type of reaction where the nucleus can be excited to higher energy levels purely due to the time-varying Coulomb interaction. This happens due to the inelastic scattering of charged particles, usually in the form of a charged beam incident on a carefully selected nucleus target, which transmit energy through the electromagnetic field between them [49]. The excited nucleus will then de-excite via gamma decay as described in section 2.4. The intensities of these gamma rays are the main observables from experiments performed in this way, as the process itself is not directly observable.

For this reaction to occur in a purely electromagnetic way, there must be a minimum distance that the two nuclei are separated by, so that the interaction is not affected by any nuclear forces. This is defined by "Cline's safe distance" [154–157], D_{min}, which is shown in Equation 3.1, where A_{b} and A_{t} are the mass numbers of the projectile and target, respectively.

$$D_{\mathrm{min}} = 1.25(A_{\mathrm{b}}{}^{\frac{1}{3}} + A_{\mathrm{t}}{}^{\frac{1}{3}}) + 5.0fm \tag{3.1}$$

This can then be used to calculate a "safe" maximum beam energy, E_{max}, that will assure this safe distance is maintained. This is calculated using equation 3.2, where Z_1 and Z_2 are the respective charges (proton numbers) of the beam and target.

$$E_{\max} = 1.44 \frac{A_b + A_t}{A_t} \frac{Z_1 Z_2}{D_{\min}} \tag{3.2}$$

Beam and/or target nuclei must be carefully chosen depending on which nucleus is of interest. As a general rule, the two chosen nuclei should have no overlapping gamma rays, or it would be impossible to distinguish between them in the gamma-ray spectra. In the cases when the beam nuclide is of interest, such as for the experiment discussed in this thesis, a target nuclide with high energy excited states is favourable, as it makes it highly unlikely that there is an overlap of energy states. These tend to be very stable magic or doubly-magic nuclei, such as ^{208}Pb [119]. Furthermore, its high Z number increases the reaction cross section because it increases the Coulomb interaction between the two nuclei, which is measured by the Sommerfeld parameter, η, shown in equation 3.3, where v is the relative velocity between the two nuclei [49]. This is an especially important consideration when using radioactive beams, as beam intensities are much lower.

$$\eta = \frac{Z_1 Z_2 e^2}{\hbar v} \tag{3.3}$$

The cross section for the reaction is maximized when the optimal beam and target are chosen, as well as having a beam energy close to the maximum safe allowed energy and as great a beam intensity as possible [49]. In most low-energy Coulomb excitation experiments with high enough cross section and beam intensity, it is possible to detect the target nucleus at forward angles and the projectile in both forward and backward angles in the lab reference frame. When the projectile is scattered at backward angles, as shown in Figure 3.4, it accelerates to the point of closest approach and then reverses direction. While undertaking this hyperbolic trajectory, it spends more time in the area in which excitation occurs. This means that more excitations should occur and thus excited states at much higher energy level attained. In addition, it increases the sensitivity to second order effects, allowing for the measurement of quadrupole moments which give more information about the nuclear shape.

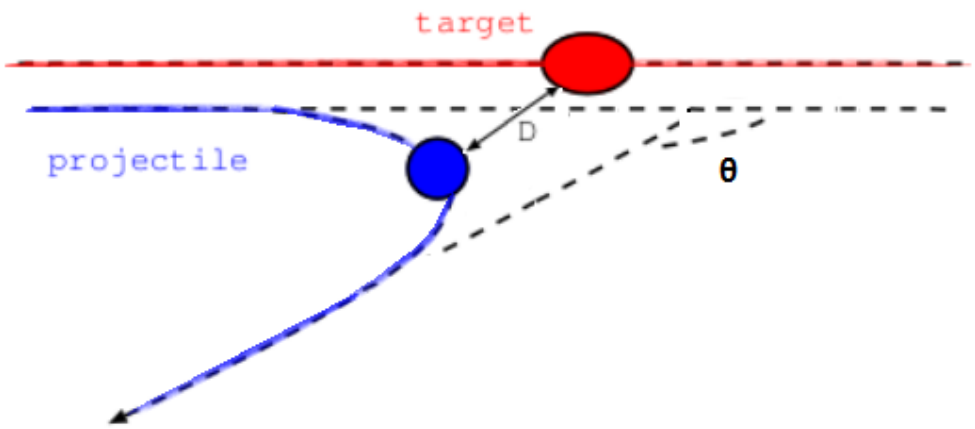

Fig. 3.4 A schematic of a projectile being scattered at backward angles during low-energy Coulomb excitation. D is the closest distance of approach for the projectile on the target and θ is the angle at which the projectile is scattered.

Low-energy Coulomb excitation at backward angles is favoured for the reasons mentioned above, but is still also conducted at forward angles with certain experimental setups. This usually happens when radioactive beams are used, such as in the case of ^{72}Se. The nature in which these radioactive beams have to be made limits the beam intensity in experiments such as these, which in turn limits the yield. More often than not, the yield at backward angles is far too low for any kind of meaningful result to be obtained, so the experiment is performed at forward angles. The picture in this case is similar to that seen in Figure 3.4, with the projectile accelerating from the target after having been accelerated to the point of closest approach. However, instead of being detected when undergoing a hyperbolic trajectory, the projectile is detected when the angle of its trajectory with respect to the beam axis does not exceed 90°. The number of excitations in these experiments is thus limited as the projectile no longer follows the trajectory which keeps it in an area where it can be excited for longer. The excitation energies and number of different states which can be attained is lower, but good insight can still be obtained for the transitions between the first few states (which can include the 0_2^+, from which evidence for shape coexistence can be obtained).

3.3 Beam Production with HIE-ISOLDE

The beam in this experiment was formed at the HIE-ISOLDE (High-Intensity and Energy Isotope Separator Online DEtector) at CERN in Geneva, Switzerland. Radioactive nuclides are produced via spallation, fission, or fragmentation reactions of high-energy protons from the proton synchrotron booster (PSB) on thick targets. The synchrotron accelerates the protons around a path of fixed radius where magnetic fields are constantly increasing the energy of the proton beam. The PSB has four individual superimposed synchrotron rings, (with radius 25m) and these collectively accelerate the protons to an energy of 1.4 GeV and intensity of up to 2 μA. Following the proton bombardment onto a thick target, the products are directed into a given ion source via chemically selective processes and extracted as a radioactive ion beam. The target material is kept at high temperatures so that the produced radioactive atoms diffuse out of the target into the dedicated ion sources, such as an Electron Beam Ion Source (EBIS). Ionisation can take place in a hot plasma, on a hot surface or by laser excitation. Laser ionisation for selected chemical elements allows for further selection and in some cases can provide a beam prepared in a particular isomeric state. Ions are swept out of the ion-source by an applied voltage, accelerated and directed into an electro-magnet where they are separated by powerful mass separators. Beams extracted are high intensity radioactive beams of high isotopic and often isobaric purity, which in many cases reach the highest intensities available worldwide. More than 1000 isotopes with half-lives down to milliseconds of 74 elements (Z=2 to 89) have been produced at intensities up to 10^{11} atoms per μA of proton beam [158].

In this experiment, a pure ^{72}Se beam was attained by extracting selenium isotopes as SeCO molecules (A = 100) [159] via the bombardment of protons on a ZrO_2 target which were then directed into and broken apart inside an EBIS charge breeder. This beam removes the problems associated with other A~70 contaminants such as abundantly produced Ga isotopes and is what opens up the possibility of using Coulomb excitation at so-called safe energies below the Coulomb barrier. It should be noted that the beam also contains small amounts of carbon, neon

and other light gases from the EBIS charge breeder. These are present in very small amounts, however, and excitation of the target due to these light nuclei is much less than for the heavier ^{72}Se beam, making the presence of these 'contaminants' negligible when it comes to analysing the results.

A beam energy of 305 MeV (4.2 MeV/u) was chosen to enhance the population of higher-lying states and with a view to constrain a more precise measurement of the QMs made via the reorientation effect. This beam energy was not possible at the ISOLDE facility where only 3.1 MeV/u was achievable. The present experiment run with beam energy 4.2 MeV/u is only possible with the upgrade to HIE-ISOLDE providing beams up to 10 MeV/u.

3.4 Target Selection

As mentioned in Section 3.2, when one is interested in the excitation of the beam, a target nuclide with high energy excited states is favourable, such as the stable and doubly-magic ^{208}Pb. This target is also favourable as it has high Z number thus increasing the reaction cross section, which is an especially important factor when using limited intensity RIBs. With this in mind, ^{208}Pb was chosen as the target for this experiment, with a view to maximising the number of excitations of ^{72}Se observable at forward angles. This target also has no overlapping transitions with ^{72}Se. Its first excited state, a 3^- state at 2614.5 keV, decays via greatly suppressed E3 transitions.

A second experiment was performed with a ^{196}Pt target with a view to collecting sufficient statistics for the $0_2^+ \rightarrow 2_1^+$ transition as this low-energy transition (75 keV) is approximately degenerate with the Pb K_α X-rays at 72, 73 and 75 keV and is thus likely unobservable with the ^{208}Pb target. Furthermore, spectroscopic data for ^{196}Pt is well-known, so running an experiment with this target is sensible as a "backup" experiment in case of low statistics, as one can normalise to the target data to constrain matrix elements (further explained in Section 4.2).

3.5 Miniball

The high-resolution Miniball germanium detector array was used to measure gamma ray yields in this experiment and is made up of of 24 six-fold segmented, tapered, encapsulated high-purity germanium crystals. It has been operational at the ISOLDE facility at CERN for over 10 years [160] and is shown in Figure 3.5. It is usually based at CERN but is mobile and can be transported for use at several selected state-of-the-art facilities worldwide, such as at Orsay's tandem facility and, more recently, in RIKEN, Japan, as part of the HICARI project.

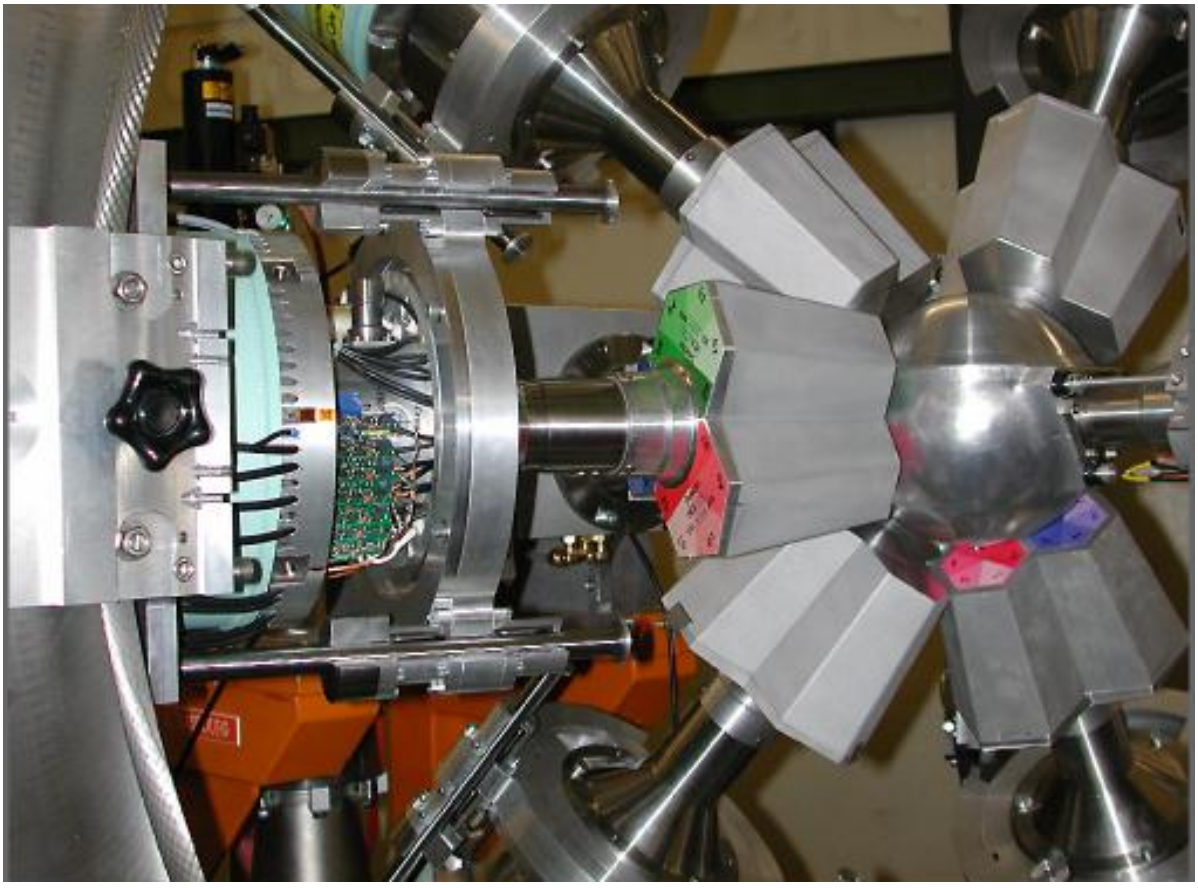

Fig. 3.5 A target chamber for a gamma-ray spectroscopy experiment surrounded by Miniball cluster detectors [160]

Each detector has a quasi-cylindrical shape with diameter 70 mm and height 78 mm. They are hexagonally tapered allowing for six-fold segmentation. High granularity and high efficiency were achieved by the segmentation of the charge-collection electrodes of the Ge

detectors and the use of pulse-shape analysis to determine the position of the first interaction of the γ ray within the Ge crystal, giving a spatial resolution significantly finer than the dimensions of the crystal [160].

The Miniball detectors are housed and sealed inside a thin aluminium can which allows them to be in the open and handled for transportation and maintenance purposes. A typical Miniball HPGe detector can be seen in Figure 3.6. There is a slight loss of efficiency at low energy due to the aluminium can, but this effect is negligible for realistic applications [161].

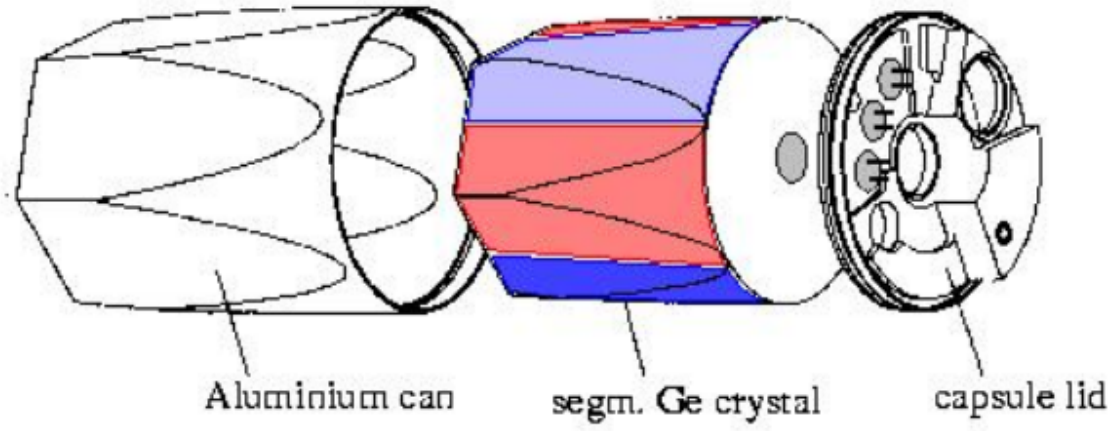

Fig. 3.6 Schematic of a Miniball HPGe detector [161]

These semiconductor gamma-ray detectors consist of solid material in which electrons and holes are produced when a gamma ray is absorbed. Germanium is the most commonly used semiconductor detector as its relatively high atomic number (Z = 32) allows for a good detection efficiency for photons. Electrons and holes are collected by an electric field in the material to provide an electric signal that is a direct measure of the energy of the gamma ray [162]. In order for a germanium crystals to act as a spectrometer in the way that has been described, it needs to be highly purified as impurities in the crystal can trap electrons and holes, severely reducing its efficiency as a detector. Germanium crystals used in this detector array

are "high-purity", (HPGe), purified to a level which enables them to be used as spectroscopy detectors.

The resolution which can be achieved from such detectors in gamma-ray spectroscopy experiments is limited not just by the intrinsic resolution of the semiconductor but also by Doppler broadening, caused by the high velocities involved in these types of experiments (around 10% speed of light in low-energy Coulomb-excitation experiments), the angular spread and the finite opening angles of the detectors. The lead cause for the Doppler broadening of peaks tends to be from the detector opening angles and is most prominent at larger angles with respect to the beam axis, i.e. worst at $\theta = 90°$. The concept of Doppler broadening and how this is corrected for is further explained in Section 3.8.5.

The detectors must also be cooled to temperatures below 77 K or too much electrical noise is produced, rendering them useless as spectrometers. Below these temperatures, thermal excitations of valence electrons are drastically reduced, meaning that only a gamma ray can feasibly cause the detector to register a hit. Cooling to this temperature is one slight drawback of this detector array, as it takes a lot of time for it to cool and must not be allowed to warm while in use. This is, however, a small inconvenience with respect to the greatly improved accuracy and precision of the results it can produce.

3.6 Particle Detection

The scattered ions from the low-energy Coulomb excitation process were detected by a double-sided silicon strip detector (DSSSD), known as a CD detector (QQQ2) [163], placed at forward angles spanning and angular range of 20° to 59°. This range at forward angles is chosen given the use of a radioactive beam with limited intensity; the cross section at backward angles would be far too low for any kind of meaningful result to be obtained, as mentioned in Section 3.2. The detector being placed at forward angles does allow for the detection of the heavy nucleus target as well, however, meaning an even greater range of angles can be covered for the lighter nucleus

beam (^{72}Se), as per conservation of momentum calculations (relation between projectile and target scattering angle for the experimental setup in this work shown in the following chapter in Figure 4.7).

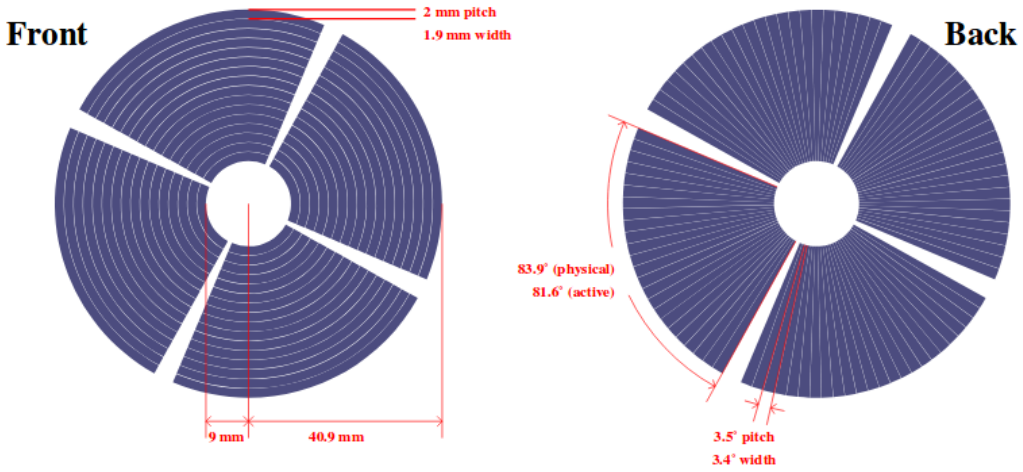

Fig. 3.7 A diagram of both sides of the "CD" detector used in this experiment

As can be seen in Figure 3.7, a detector of this type is created by carefully fitting 4 quadrants of around 0.5 mm thickness together. The front side of the detector is comprised of 16 annular rings of silicon with 1.9 mm width, with the first ring sitting at a radius of 9 mm. The back of the detector is divided into 24 sectors of silicon spanning 3.4° each. These sectors are grouped together in pairs in order to reduce the total number of electronic channels, whilst not overly compromising the physics involved (this is because ϕ has a smaller impact than θ in the Doppler-correction calculations). De-excitation gamma rays were measured in coincidence with scattered particles detected by the DSSSD allowing for an event-by-event Doppler correction (process explained in section 3.8.5). In addition, particle gating reduces the gamma-ray background from the beta decay of beam particles implanted into the CD detector.

3.7 Simulation of the Kinematics Involved in the Coulomb Excitation of ^{72}Se on a ^{208}Pb Target

In the low-energy Coulomb excitation of ^{72}Se described in this chapter, one of the targets chosen was ^{208}Pb. The kinematics of this reaction are simulated using a computer code and the energies at which the beam and target hit the particle detector, as well as the angle that these hit in the lab reference frame, are shown in Figure 3.8. These simulations incorporate the appropriate physics and geometry and can be used to both plan experiments and aid in understanding the collected data, for example, by determining the correct beam and target location.

This data will also clarify whether beam and target is distinguishable at forward angles. If this is the case, it provides a platform for experiments with detectors at forward angles to cover a larger range of angles. If one isotope goes off at a certain angle, the other must go at a given angle according to the conservation of momentum.

^{72}Se is a radioactive isotope, with half life of 8.40±0.08 days [164], thus the beam intensity in this experiment is lower than in stable beam cases. As mentioned previously, this experiment will need to be performed with particle detectors at forward angles as the cross section for the reaction is too low at backward angles. Looking at the area representing forward angles in Figure 3.8, detector hits at a wide range of energies can be expected, due to hits represented by both beam and target. The spread of energies detected for both beam and target across this area are quite consistent throughout the visible angular range.

The plot in Figure 3.8 produced from this simulation gives an indication of at what angles the two can be resolved. It appears slightly difficult to resolve in energy between beam and target hits between 0°and 30°, becoming increasingly easier with greater lab angle up to around 80°. Detectors could still, however, be placed at the angles where the two solutions appear difficult to resolve as the points which overlap are outliers and will form a very small proportion

of the total data recorded. This simulation study confirms that energy resolution should not be a significant obstacle and that the beam and target groups are clearly distinguishable and as mentioned in Section 3.6, the angular coverage chosen for the particle detector in this experiment was 20°to 59°.

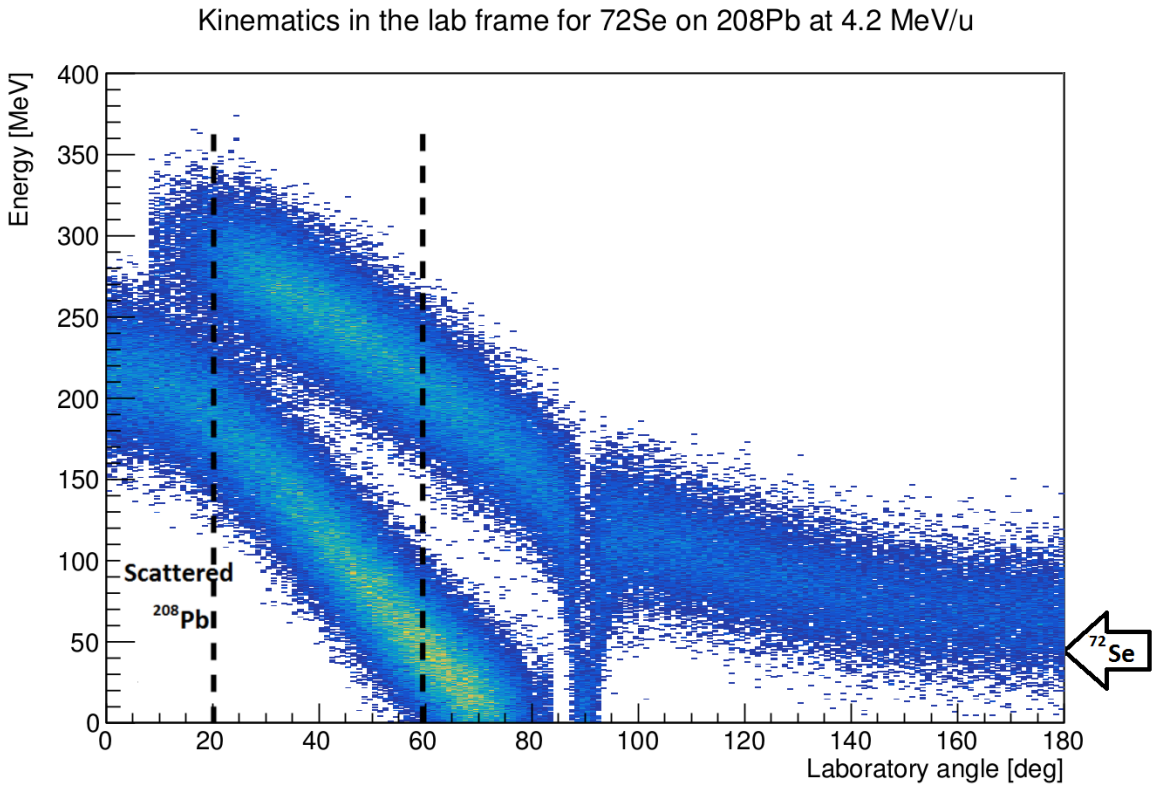

Fig. 3.8 The energies and angles (in the lab frame) at which hits are expected at a detector for this particular experimental setup with a radioactive ^{72}Se beam. Areas with more frequent hits are where the histogram is a yellow-green colour, with blue areas representing less counts. The section of the plot between the dotted lines shows the lab angles which the particle detector covered in the conducted experiment.

3.8 Preliminary Data Analysis

3.8.1 Data "Sorting"

Data from these experiments is collected in a non-readable binary format and thus must be "sorted" in order to create histograms for analysis. This can be done using various computer programs known as "sort codes"; in the case of this experiment, Miniball's own sort code, "MiniballCoulexSort" [165]. This code creates histograms from raw data in two steps, first creating trees from the binary data which are then used to create and fill the histograms used for data analysis.

3.8.2 Energy Calibration

Energy calibrations are necessary to relate the size of the signal in each detector channel to a "physical" energy value. This is accomplished by placing radioactive sources (nuclei with gamma decays that have well-established energy and intensity) at the target position for the experimental run. For this experiment, ^{152}Eu and ^{133}Ba sources were chosen, as these well cover the energy regions which are relevant for this work (for both the ^{208}Pb and ^{196}Pt target experiments) of 0 - 1500 keV. Data from the source gamma decays are related to the known energy and intensities using the "ENCAL" program which forms part of the Radware software package [166].

3.8.3 Efficiency Calibration

The data from the "sources" just mentioned are also used to establish the efficiency of a gamma-ray detector array. These detectors do not detect every γ ray that is emitted from a given nuclide and the level of detection varies with the energy of the gamma ray. One can use the program 'EFFIT' from the RadWare software package [166] to perform an efficiency calibration, where the efficiency, ε, is dependent on the energy of the gamma ray, E_γ, as shown in Equation 3.4.

The parameters A, B and C in Equation 3.4 are constants which describe the lower energy region and similarly parameters D, E and F define the higher energy region. G is a parameter which is related to the point and sharpness if turnover of the curve and x and y are as defined in Equation 3.5.

$$\varepsilon = \exp\left\{\left[(A+Bx+Cx^2)^{-G}+(D+Ey+Fy^2)^{-\frac{1}{G}}\right]\right\} \tag{3.4}$$

$$x = \ln\frac{E_\gamma}{100}\ ;\ y = \ln\frac{E_\gamma}{1000} \tag{3.5}$$

This calibration allows for an "efficiency curve" to be plotted, displaying the relative efficiency of the detector over a given energy range. The efficiency curve for this experiment is shown in Figure 3.9. Using this calibration, the area of peaks representing particular transitions seen in the gamma-ray spectra can be corrected to their true value, known as the "yield" of the transition or gamma ray.

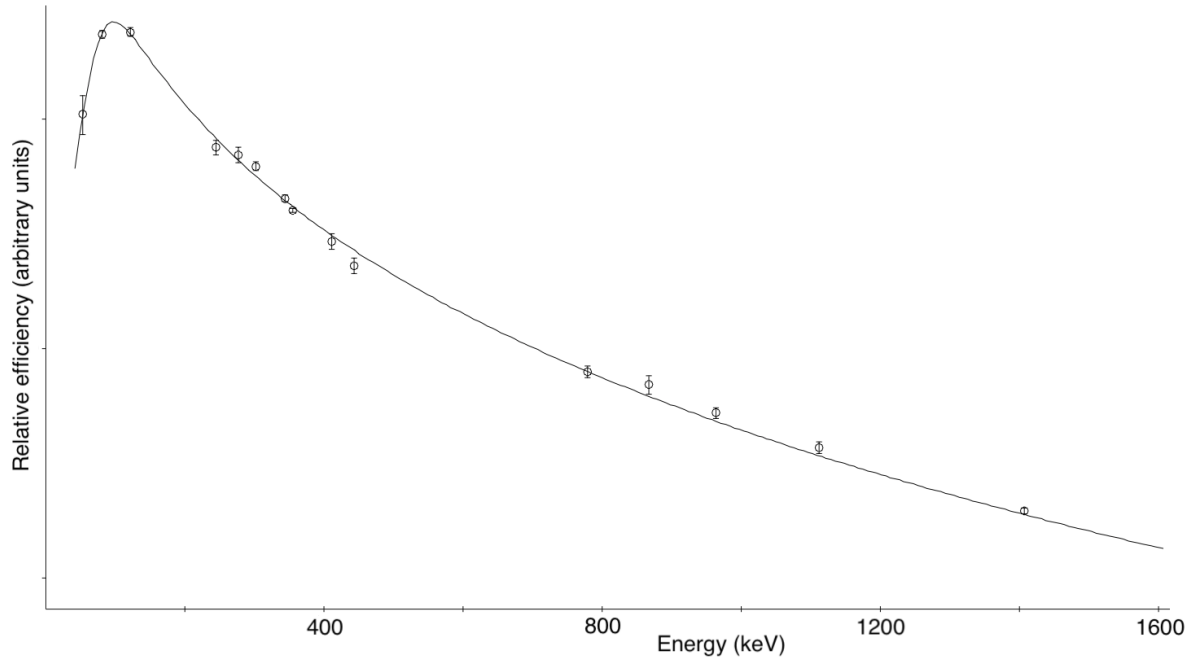

Fig. 3.9 A relative efficiency curve for the Miniball detector array used in the Coulomb excitation of ^{72}Se, where sources of ^{152}Eu and ^{133}Ba sources were used.

3.8.4 Time Gating

Before the gamma ray spectra from an experiment can be properly scrutinised, one must select the prompt particle-gamma coincidence events by "time gating" in order to remove background events that are not of interest - this can be done in multiple ways depending on the experiment type. For this analysis, the time difference between particle and gamma ray events can be plotted as particles are detected in this experiment type. The particle-gamma time coincidence plot is shown in figure 3.10. Here, the time difference between detectors is plotted on the horizontal axis, with the number of counts on the vertical axis. As one would expect, one clear peak corresponding to the prompt events of interest is visible. The data is then gated on this peak, with only gamma rays within the range of the "gate" being recorded. This vastly reduces the background from non-prompt room background and beta-decay events which were registered by the particle detector.

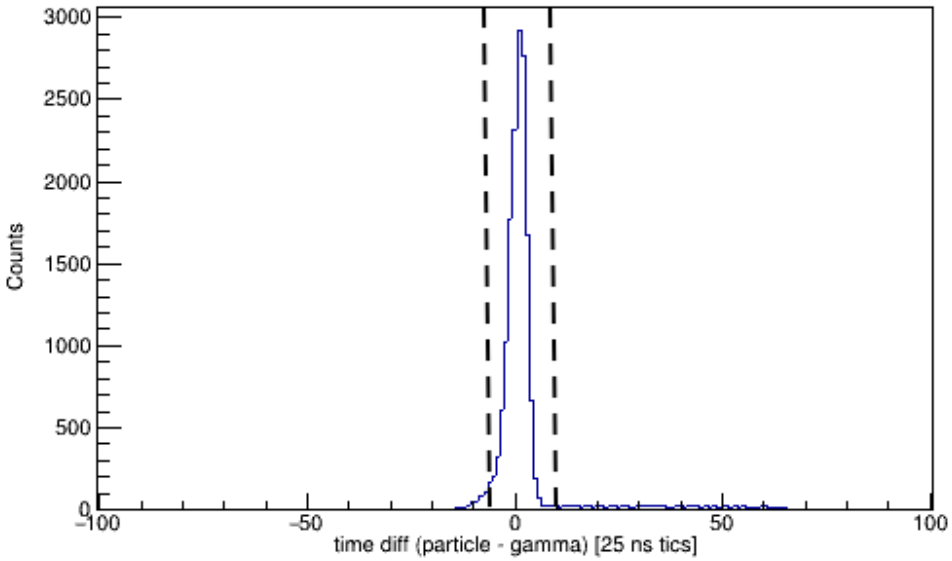

Fig. 3.10 Spectrum obtained for hits on the miniball detector array gated on the EBIS signal, with only data from "beam on" periods recorded. One can set a gate around the central peak, representing gamma events which occur in coincidence with a particle detection and thus events of interest, rejecting the random events which fall outside of this peak. The gate chosen for this data is shown as the area between the dotted lines.

3.8.5 Doppler Correction

Beam particles in this experiment travelled at $\frac{v}{c}$ values of ~10%, meaning that the energy of the gamma rays detected were slightly different depending on what part of the detector the gamma ray hit. Not accounted for, this would cause the eventual energy spectrum to be very unclear, making it very difficult to draw any meaningful results and conclusions from the experiment. Detected gamma-ray energy can be Doppler corrected using the non-relativistic Doppler shift relation shown in Equation 3.7. This approximation of the relativistic Doppler shift relation (shown in Equation 3.6) can be used given that $\frac{v}{c}$ does not greatly exceed 10% in this experiment. For these equations, $E_\gamma^{'}$ is the measured gamma-ray energy, E_γ^0 is the true gamma-ray energy, $\beta = \frac{v}{c}$ (v is the recoil velocity) and θ is the angle at which the gamma ray is emitted respect to the recoiling nucleus.

$$E_\gamma^{'} = \frac{E_\gamma^0\sqrt{(1-\beta^2)}}{1-\beta\cos(\theta)} \tag{3.6}$$

$$E_\gamma^{'} = E_\gamma^0(1+\beta\cos(\theta)) \tag{3.7}$$

The $\cos(\theta)$ in Equation 3.7 is deduced for Coulomb excitation using the relation seen in Equation 3.8, where the angle at which the gamma ray hits the detector with respect to the beam axis is defined by θ_γ and ϕ_γ, and the angle at which the particle is travelling with respect to the beam axis is defined by θ_p and ϕ_p.

$$\cos(\theta) = \sin(\theta_p)\sin\big(\theta_\gamma\big)\cos\big(\phi_p-\phi_\gamma\big)+\cos(\theta_p)\cos\big(\theta_\gamma\big) \tag{3.8}$$

Thus if one knows precisely the angle at which the gamma ray hits the detector (precisely determined by Miniball) and the angle at which the particle is travelling with respect to the beam axis (determined by the DSSSD), as well as the energy at which the gamma-ray is detected, it is possible to successfully execute Doppler correction calculations.

Chapter 4

Analysis, Results and Discussion of the Low-Energy Coulomb Excitation of ^{72}Se

4.1 Overview

This chapter presents results from the analysis of the Coulomb Excitation of ^{72}Se, performed at the HIE-ISOLDE facility at CERN using the Miniball detector array to detect gamma rays and a DSSSD for particle detection. This experiment was run in two parts utilising two different targets, ^{208}Pb and ^{196}Pt, carefully chosen for the reasons explained in Section 3.4.

The main focus of this experiment was designed to be the excitation from the ^{208}Pb target, given its larger reaction cross section, but technical issues with the RIB at the HIE-ISOLDE facility when this experiment was run meant that not enough data was collected to allow for any other transition in ^{72}Se aside from the 862-keV $2_1^+ \rightarrow 0_1^+$ to be visible in the gamma-ray spectrum. While it is clear that values for many of the properties which acted as motivation for this experiment can no longer be extracted (such as the spectroscopic quadrupole moment (QM) of the 2_2^+ and 4_1^+ states or the B(E2; $0_2^+ \rightarrow 2_1^+$)), it is still possible to deduce the QM of the 2_1^+ state from just the yield of the 862-keV $2_1^+ \rightarrow 0_1^+$ transition. This value is of significance as it will contribute to answering the currently open question of where the shape transition

from prolate to oblate shapes happens along the selenium isotopic chain. Different theoretical approaches referred to in the previous chapter do not agree on the position of this shape transition, thus establishing its occurrence experimentally is a key test of theory in this region.

For observed gamma-ray yields to be translated into absolute cross-section, a previously reported value of a matrix element connected to the ground state is required. A value of this kind is in fact known for ^{72}Se. Extraction of the QM using just a single transition was successfully accomplished in the study reporting the only other experimentally deduced value for the QM of the 2_1^+ state in ^{72}Se [167]. It is impossible, however, to obtain an independent measure of the QM and B(E2) value from just a single observed transition. Where transitions from the target are also observed, it is possible to obtain an independent measure of the QM and B(E2) value by normalising to target spectroscopic data instead. The second target used in this experiment, ^{196}Pt, has well-established low-lying structure and spectroscopic data, making it ideal for this kind of analysis technique. The extraction of matrix elements (MEs), including diagonal MEs related to the QM, from γ-ray yields is realised using the GOSIA/GOSIA2 code and this process is described further in Section 4.2. The benefits and drawbacks of the two target choices are discussed in detail in Section 3.4.

The data from the experiment run with the ^{208}Pb target is shown for completeness in Section 4.3. Analysis techniques applied to optimise the γ-ray spectra utilised for the extraction of γ-ray yields are also described in this section. Section 4.4 shows the results from the experiment run with the ^{196}Pt target, detailing the technique used to extract the QM of the 2_1^+ state by normalising to the known matrix elements in the well-studied ^{196}Pt target nucleus. From the spectra presented in these sections, it is made clear that an additional radioactive beam contaminant, ^{68}Ge, is present and also undergoes Coulomb excitation, with its $2_1^+ \rightarrow 0_1^+$ transition visible at an energy of 1015 keV. The QM for the 2_1^+ state in this nucleus is extracted similarly to that of ^{72}Se and these results is presented in Section 4.5. Finally, the values presented in Sections 4.4 and 4.5 are compared with previous work in Section 4.6.

4.2 Extraction of Matrix Elements from Experimental Data using GOSIA

As mentioned in Section 3.1, low-energy Coulomb excitation allows measurement of E2 matrix elements, as well as QMs of levels via the angular distribution of the cross section due to the 'reorientation' effect, which enhances or reduces the cross section depending on the size and sign of the QM. The experimental observable which relates to this is the gamma-ray yield measured, for different angular ranges of the scattered particle.

In order to use this observable to exploit the angular dependence to the cross section and extract matrix elements, one can use the semiclassical coupled-channel least-squares search code GOSIA [168]. GOSIA was first written and used in 1979 by collaborators at the University of Rochester and can be used as a Coulex analysis tool as well as a Coulex simulation tool for prospective experiments. It has been regularly and consistently updated since its inception and matrix elements are currently extracted via a multidimensional fit to the data.

A plethora of input data is required as parameters for the fit. This list includes the key experimental observable, the gamma-ray yields at several scattered particle angular ranges. Further requirements include experimental conditions such as beam energy, mass and atomic number of both the projectile and target and whether the projectile or target is detected for that particular angular range. Properties of the gamma-ray detector including size, efficiency and geometry are also defined. Finally, known spectroscopic data of the nucleus of interest, such as the energetic level scheme around the matrix elements of interest, spin-parity quantum numbers, lifetimes, gamma-ray branching ratios, E2/M1 mixing ratios and internal electron conversion coefficients, is equally necessary input for the code. The input codes used for this experiment are shown in Appendix B.

GOSIA uses a normalisation process in order for the fit to converge, allowing for the extraction of the matrix elements. Normalisation constants are introduced by the code, related

to the χ^2 as per Equation 4.1, where C_{global} is the global normalisation constant, C_m is the normalisation constant for the m-th experiment (GOSIA takes each angular range as a seperate "experiment" when asking for input), I_i^c is the gamma-ray intensity calculated by GOSIA for the i-th transition, I_i^e is the experimental gamma ray intensity for the i-th transition and σ_i is the experimental uncertainty of the i-th gamma ray intensity.

$$\chi^2 = \sum_m \sum_i \frac{(C_{global} C_m (I_i^c - I_i^e))^2}{\sigma_i^2} \tag{4.1}$$

Matrix elements which best represent the experimental data are extracted at the minimisation step where C_m values are fitted to find a minimum χ^2 value for a certain set of matrix elements.

One of the projectile or target will always be the nucleus of interest in a Coulex experiment, but both are excited during the experiment. The number of gamma rays emitted by both the projectile, N_p, and target, N_t, when excited by the other can both be precisely computed and thus the ratio, $\frac{N_p}{N_t}$, is also known. This ratio is expressed in Equation 4.2, where $b_{p/t}$ is the branching ratio for the transition, $E^{\gamma}_{p/t}$ is the energy of the transition gamma ray and $\sigma_{p/t}$ is the integrated cross-section, for the projectile and target with respective flags, subscripts p and t.

$$\frac{N_p}{N_t} = \frac{b_p E_p^{\gamma} \sigma_p}{b_t E_t^{\gamma} \sigma_t} \tag{4.2}$$

If matrix elements for the target are known, σ_t can be calculated and thus σ_p can be determined, allowing for the extraction of projectile matrix elements. An extension of the GOSIA code, GOSIA2, uses this key relation to allow for the extraction of projectile matrix elements when normalising to the target. In this case, the input data specified previously is required for the both beam and target. The χ^2 minimum is found for the target data and the set of normalisation factors deduced is used to minimise the beam data. GOSIA2 is a powerful tool for analysis when there are a low number of counts but is limited to one combination of beam and target and can only be used when attempting to extract values for 2 matrix elements.

4.3 Analysis and Results from the ^{208}Pb Target Experiment

Data from the low-energy Coulomb excitation of ^{72}Se experiment run with the ^{208}Pb target is presented in this section. Figure 4.1 shows 2D histograms which display the energy of detected particles in this experiment, as well as the angle at which these particles hit the detector. With the angles covered by the present experimental setup, it is expected that both scattered target and projectile particles would be detected. By looking at Figure 4.1a, which shows the energies and angles of all detected particles in the experiment, and by using two-body kinematics combined with simulations such as those described in Section 3.7, one can approximately "cut" the histograms to contain just the detected projectile or target particles. These histogram "cuts" are seen in Figures 4.1b and 4.1c for detected projectile and target particles, respectively.

These "cuts" in the data allow for γ-ray spectra to be "gated" on beam or target particle detection i.e. forming a 1D γ-ray spectrum incremented when a γ-ray is detected in coincidence with the beam or target. This method gives a vast reduction in γ-ray background, removing gamma rays associated with the beta decay of the RIB as well as background present within the laboratory. Furthermore, analysing solely beam or target data allows for the exploitation of the cross section angular dependence for the constraint of matrix elements.

Figures 4.2 and 4.3 show the individual gated spectra following Doppler correction for the beam and target, respectively. The effect of the Doppler correction technique described in 3.8.5 is best seen when comparing Figures 4.2 and 4.3 and Figures 4.4 and 4.5. Figures 4.2a and 4.3a show all gamma rays detected in coincidence with a beam particle detection, with the peak arising due the $2_1^+ \rightarrow 0_1^+$ at 862 keV well observed when Doppler correction corresponding to the beam particle detection in the CD detector is conducted in Figure 4.2a. As one would expect, when Doppler correction corresponding to the target particle detection in the CD detector is conducted as in Figure 4.3a, this peak is broadened, while the peak attributed to X-rays emitted from the target is more sharply observed. These effects are similarly seen in the target gated spectra in Figures 4.2b and 4.3b.

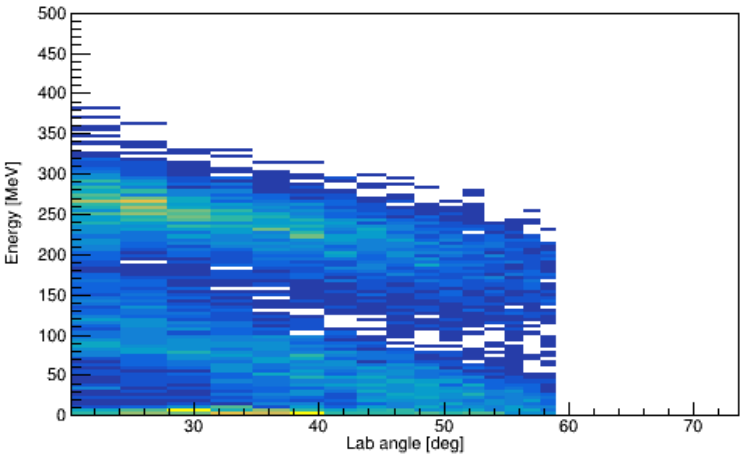

(a) All particle hits

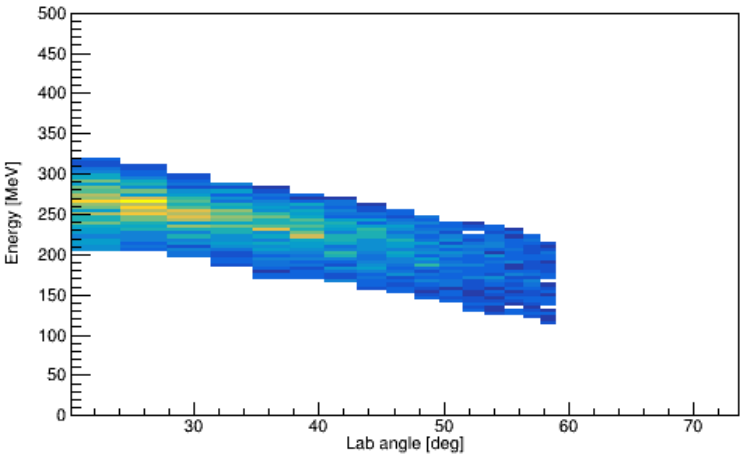

(b) ^{72}Se beam hits

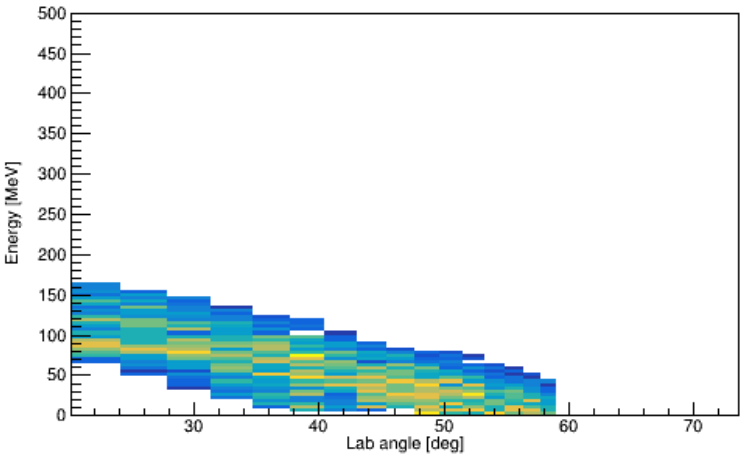

(c) ^{208}Pb target hits

Fig. 4.1 The energies and angles (in the lab frame) at which hits are recorded at the DSSSD particle detector for this particular experiment. Areas with more frequent hits are where the histogram is a yellow-green colour, with blue areas representing less counts.

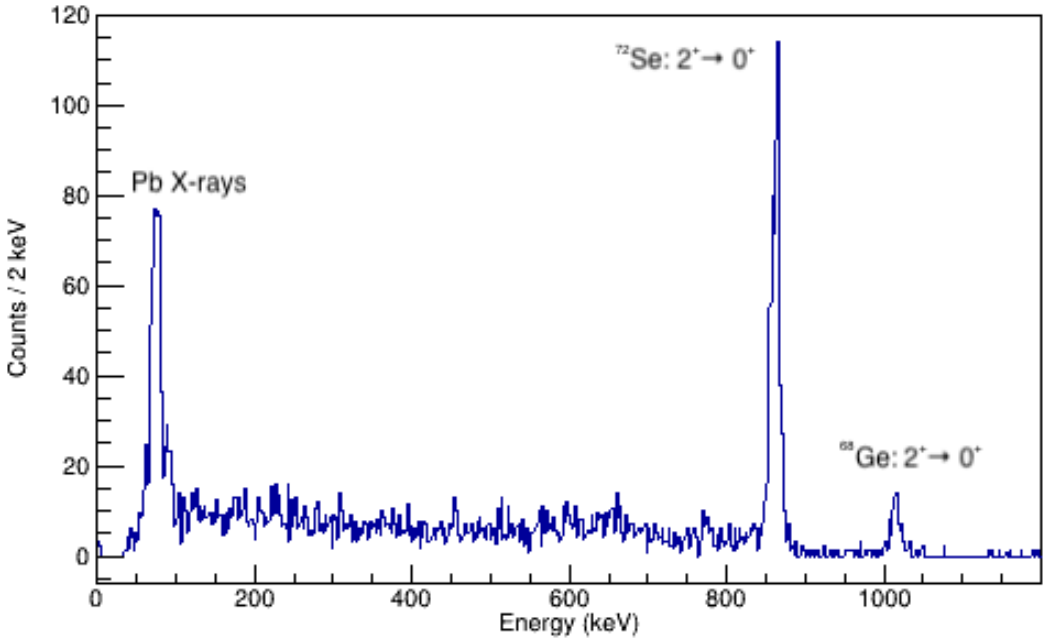

(a) Gated on detected beam particles.

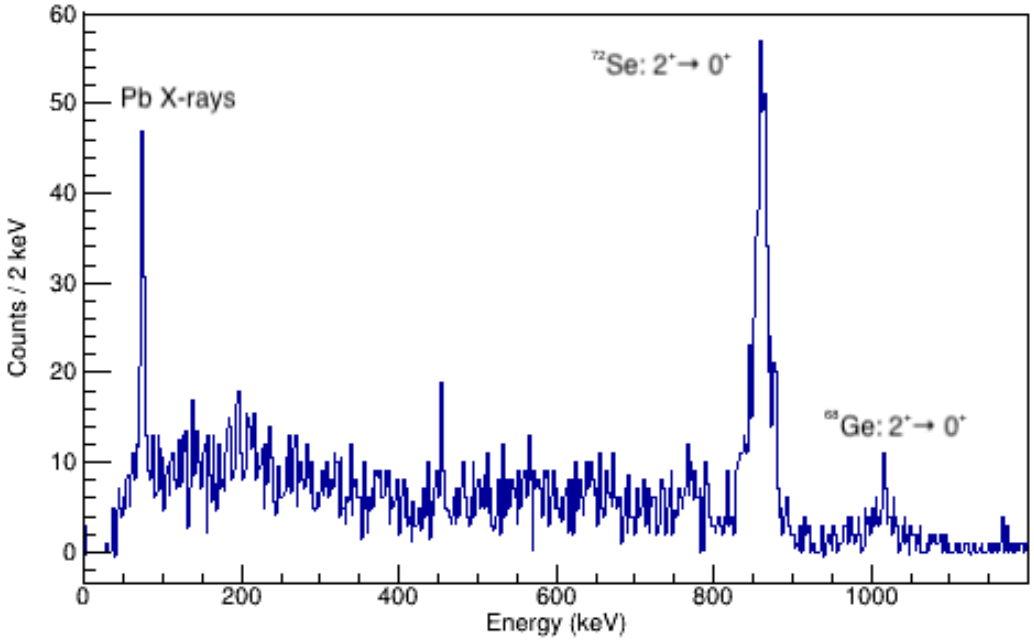

(b) Gated on detected target particles.

Fig. 4.2 Background-subtracted γ-ray spectra produced from the Coulomb Excitation of a ^{72}Se beam by a ^{208}Pb target when Doppler corrected for the beam nuclide.

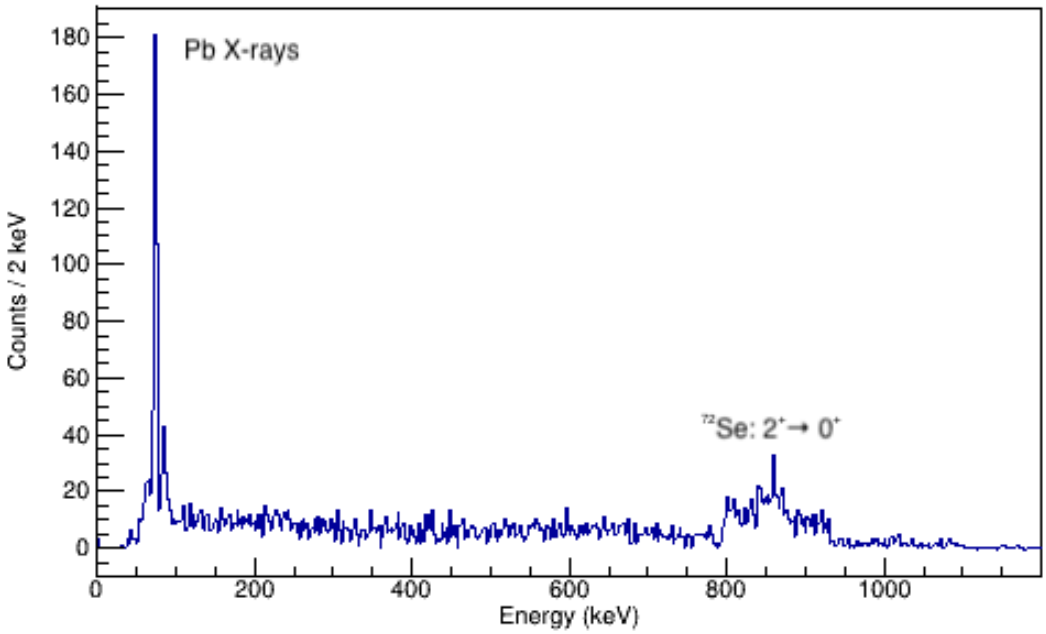

(a) Gated on detected beam particles.

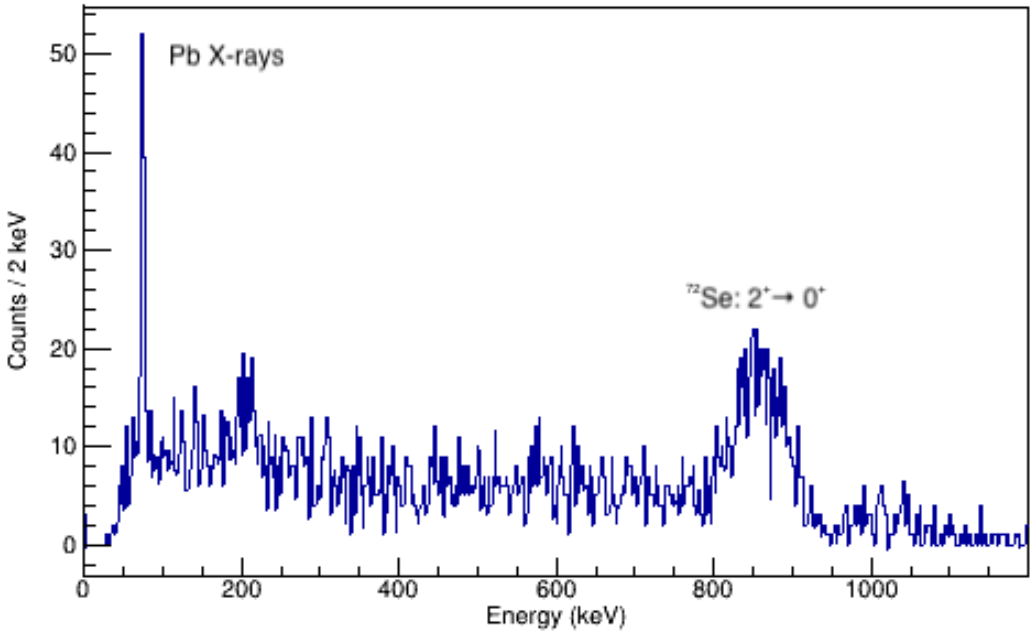

(b) Gated on detected target particles.

Fig. 4.3 Background-subtracted γ-ray spectra produced from the Coulomb Excitation of a ^{72}Se beam by a ^{208}Pb target when Doppler corrected for the target nuclide.

Figure 4.3 provides confirmation that no transitions from the target are visible in the experiment, owing to the small Coulomb excitation cross sections for target excitation. No peaks are visible in either of the target Doppler-corrected spectra apart from the Doppler broadened $2_1^+ \rightarrow 0_1^+$ in ^{72}Se and a peak from K_α X-rays emitted from ^{208}Pb. It is thus not possible to extract a QM value for the 2_1^+ state in ^{72}Se which is independent of the B(E2) value for the $2_1^+ \rightarrow 0_1^+$ transition using this data.

A third slightly broadened peak is observed, however, in the beam Doppler-corrected spectra in Figure 4.2 at ~ 1000 keV. This has been attributed to the 1015-keV $2_1^+ \rightarrow 0_1^+$ in the neutron-deficient nucleus ^{68}Ge, a likely contaminant in the beam. This conclusion is reached given the proximity of the peak energy to the transition energy, as well as the fact that one would expect this peak to be associated to an isotope of similar mass given the minimal Doppler broadening. ^{68}Ge is also a feasible beam contaminant due to the nature of the formation of ^{72}Se from a ^{72}SeCO molecule (A=100). ^{68}Ge is likely produced as a ^{68}GeS molecule (also A=100) which is similarly broken apart in the EBIS. The formation of the ^{68}Ge in this way is a point of interest, as Ge beams were hitherto thought to be very tricky to form at ISOL facilities. The formation of ^{68}Ge in this way represents the first post-acceleration of a radioactive neutron-deficient Ge isotope at an ISOL facility.

4.4 Analysis and Results from the ^{196}Pt Target Experiment

A second target was used in this experiment, ^{196}Pt, initially chosen as a reserve, with much less beam time dedicated to this setup. Given the practical complications when conducting the experiment, the data collected from the runs with this target is in fact what is used for analysis and to draw results and is presented in this section. Once again, the $2_1^+ \rightarrow 0_1^+$ transitions in the beam and beam contaminant, ^{68}Ge are observed, seen clearly in the beam Doppler-corrected spectra in Figure 4.4.

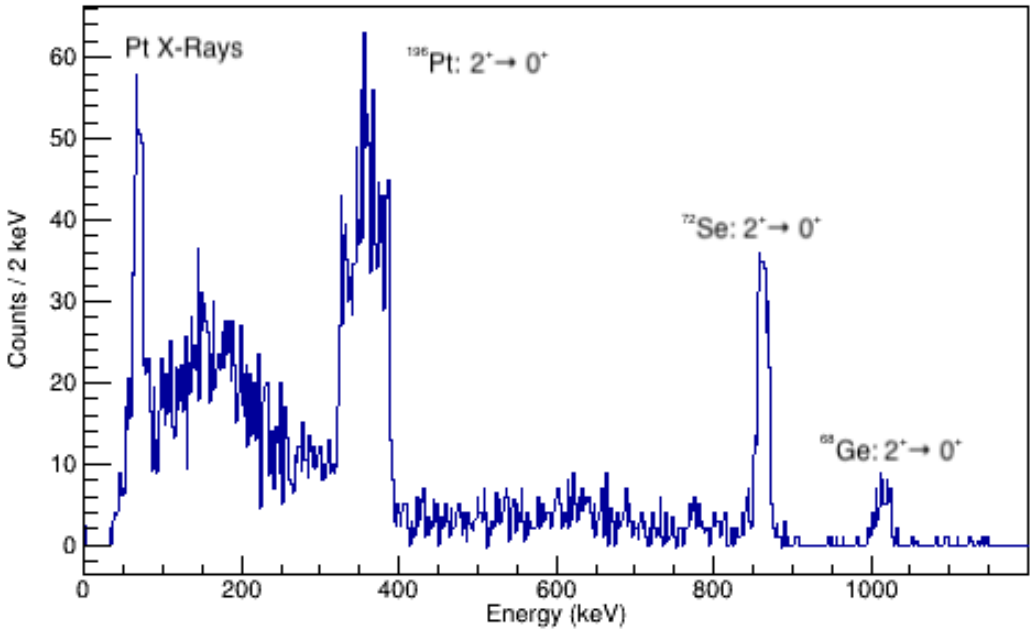

(a) Gated on detected beam particles.

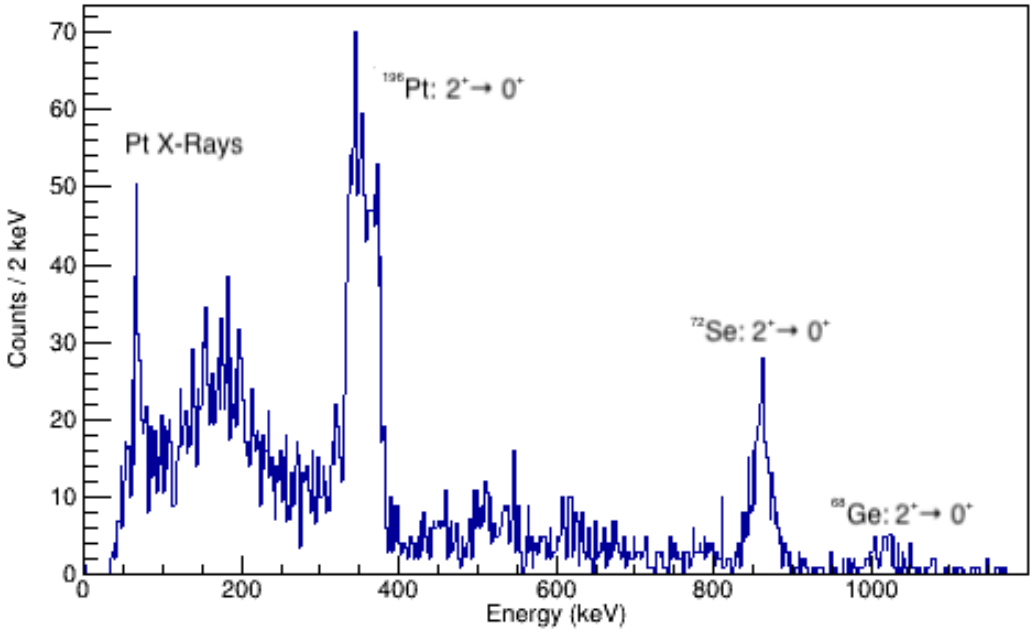

(b) Gated on detected target particles.

Fig. 4.4 Background-subtracted γ-ray spectra produced from the Coulomb Excitation of a ^{72}Se beam by a ^{196}Pt target when Doppler corrected for the beam nuclide.

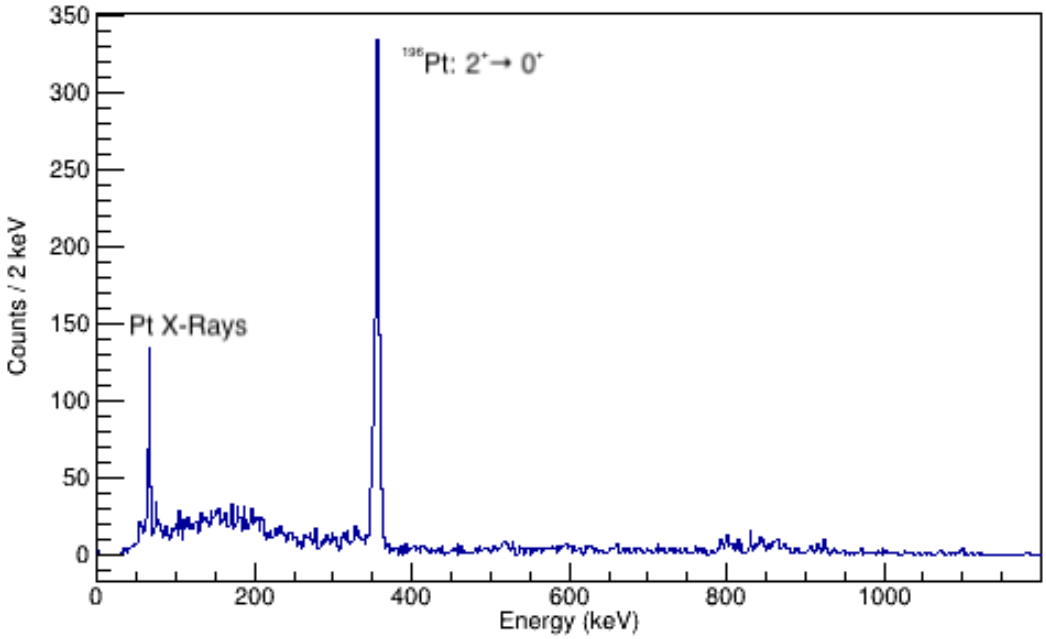

(a) Gated on detected beam particles.

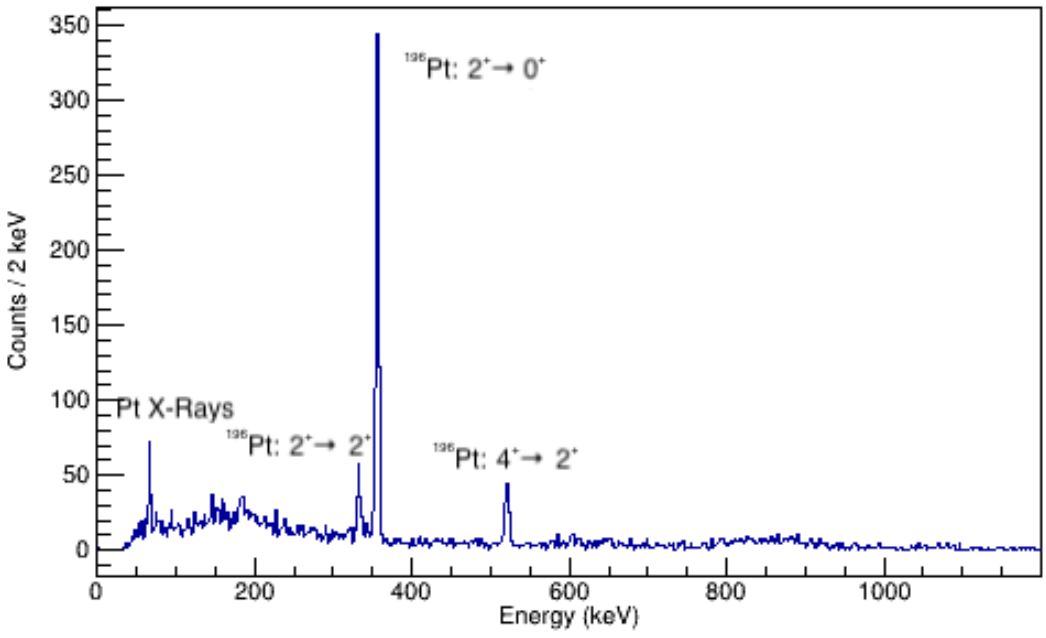

(b) Gated on detected target particles.

Fig. 4.5 Background-subtracted γ-ray spectra produced from the Coulomb Excitation of a ^{72}Se beam by a ^{196}Pt target when Doppler corrected for the target nuclide.

As expected, transitions from ^{196}Pt are also observed, with the lowest-lying 356-keV $2_1^+ \rightarrow 0_1^+$ transition observed strongly and seen in both target-gated and beam-gated spectra, best observed when Doppler-corrected for the target as seen in Figure 4.5. Furthermore, in Figure 4.5b, which shows the target-gated spectrum when Doppler-corrected for the target, two other peaks are visible. These represent the $2_2^+ \rightarrow 2_1^+$ and $4_1^+ \rightarrow 2_1^+$ transitions in ^{196}Pt at 333 keV and 521 keV, respectively. A simplified level scheme for ^{196}Pt in Figure 4.6 visually displays the transitions from this nucleus observed in the experiment.

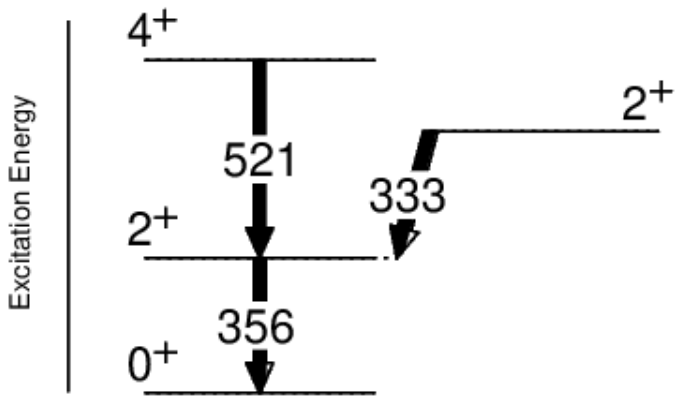

Fig. 4.6 Simplified level scheme of the target nucleus ^{196}Pt showing the transitions between low-lying states observed in this experiment. All energies are in keV.

As the particle detector was placed at forward angles, specifically spanning the range 20° to 59°, the heavy nucleus target ^{196}Pt is detected as well as the light projectile nucleus ^{72}Se. Using conservation of momentum, a greater range of projectile scattering angle is accessible for analysis. Results of these calculations for this specific experimental setup are shown in Figure 4.7. One can see from Figure 4.7b that it is possible to obtain gamma-ray yield for projectile scattering angles up to 121.810° in this experiment.

The annular rings of the particle detector used with this setup (as described in Section 3.6) allows for total gamma-ray yield to be split and measured for different angular ranges of the scattered particles as each of the 16 rings represents a small angular range between the overall range of 20° to 59°. Splitting the data in this way allows for the extraction of matrix

elements constrained by the angular dependence to the cross section. As one would expect, the more angular ranges can be used, the more accurate the extracted matrix elements would be. However, one cannot just split the data into the maximum possible angular ranges as there would not be enough counts in each range to produce a worthwhile result, especially in an experiment with a low number of counts such as the one discussed here. The ideal number of angular ranges are such that maximises the angular sensitivity to the cross section without compromising the level of statistics and level of uncertainty on the yield in each range.

Theta CM	Theta Projectile	Theta Target
61.000	45.745	59.500
62.000	46.536	59.000
63.000	47.330	58.500
64.000	48.126	58.000
65.000	48.924	57.500
66.000	49.724	57.000
67.000	50.527	56.500
68.000	51.332	56.000
69.000	52.140	55.500
70.000	52.951	55.000
71.000	53.764	54.500
72.000	54.581	54.000
73.000	55.400	53.500
74.000	56.222	53.000
75.000	57.046	52.500
76.000	57.874	52.000
77.000	58.706	51.500
78.000	59.540	51.000

(a) Centre of mass angular range where both beam and target are detected in this experiment.

Theta CM	Theta Projectile	Theta Target
123.000	101.936	28.500
124.000	103.029	28.000
125.000	104.131	27.500
126.000	105.242	27.000
127.000	106.361	26.500
128.000	107.490	26.000
129.000	108.629	25.500
130.000	109.777	25.000
131.000	110.934	24.500
132.000	112.102	24.000
133.000	113.279	23.500
134.000	114.466	23.000
135.000	115.664	22.500
136.000	116.872	22.000
137.000	118.090	21.500
138.000	119.319	21.000
139.000	120.559	20.500
140.000	121.810	20.000

(b) Equivalent projectile scattering angle for lowest target detection angles in this experiment.

Fig. 4.7 Equivalent centre of mass, projectile and target angles for this specific experimental setup, as per conservation of momentum calculations. Areas highlighted in yellow are angles at which the projectile can be detected in this experiment and areas highlighted in green are angles at which the target can be detected.

For this experiment, there is an obvious limitation due to the level of statistics that were obtained. An attempt was made to split the data into 4 angular ranges, but the number of counts in each range was not sufficient and led to statistical uncertainty on the extracted angular yields which significantly limited the errors in any extracted matrix element values. Splitting the

data into 2 angular ranges would not sufficiently harness the sensitivity of the cross section to projectile scattering angle, therefore, the data was split into 3 angular ranges, despite the level of uncertainty for the yields.

The gamma-ray yields for the 3 angular ranges for all transitions in both the projectile and target observed in this experiment, alongside their uncertainties, are listed in Tables 4.1 and 4.2, respectively. All yields reported are calculated using the peak areas extracted from the respective spectra formed after the data was split according to the chosen angular ranges, with these values corrected for efficiency; this part of the analysis was completed using the appropriate programs within the RadWare software package [166]. This correction for efficiency is what causes the uncertainties on the yield to be higher than one would expect, as both the computed peak area and its statistical uncertainty are multiplied by the same factor to correct for efficiency.

Table 4.1 Gamma-ray yields for transitions in ^{72}Se observed in this experiment over 3 ranges for the projectile scattering angle. Data from ranges marked * are from gamma rays seen in coincidence with target particle detection, with equivalent projectile scattering angle calculated using conservation of momentum calculations.

Projectile scattering angular range (degrees)	Transition	Yield (arb. units)	Uncertainty
20 - 45.5	$2_1^+ \rightarrow 0_1^+$	5500	900
46.5 - 73.2*	$2_1^+ \rightarrow 0_1^+$	3200	500
73.2 - 121.8*	$2_1^+ \rightarrow 0_1^+$	2900	400

Table 4.2 Gamma-ray yields for transitions in ^{196}Pt observed in this experiment over 3 ranges for the projectile scattering angle. Data from ranges marked * are from gamma rays seen in coincidence with target particle detection, with equivalent projectile scattering angle calculated using conservation of momentum calculations.

Projectile scattering angular range (degrees)	Transition	Yield (arb. units)	Uncertainty
20 - 45.5	$2_1^+ \rightarrow 0_1^+$	10000	700
46.5 - 73.2*	$2_1^+ \rightarrow 0_1^+$	7000	400
	$4_1^+ \rightarrow 2_1^+$	1000	300
	$2_2^+ \rightarrow 2_1^+$	900	300
73.2 - 121.8*	$2_1^+ \rightarrow 0_1^+$	5000	400
	$4_1^+ \rightarrow 2_1^+$	1400	400
	$2_2^+ \rightarrow 2_1^+$	800	300

Given the measured yields for all observed transitions for the chosen angular ranges, it is possible to perform a GOSIA2 analysis in order to extract the $\langle 2_1^+ | E2 | 0_1^+ \rangle$ and $\langle 2_1^+ | E2 | 2_1^+ \rangle$ matrix elements in ^{72}Se as described in Section 4.2, when all relevant input data is prepared alongside the yields. The unobserved 4_1^+ level at 1637 keV, 0_2^+ level at 937 keV and 2_2^+ level at 1317 keV were also added to the GOSIA input files to act as "buffer" states, negating the possibility of obtaining an artificially large value for the $2_1^+ \rightarrow 0_1^+$ transition probability. It should be noted that in this work, analysis was conducted with and without buffer states and the results were not significantly different.

For this particular type of analysis, another code can be used in conjunction with GOSIA2, known as the "chisqsurface" code, which takes a GOSIA or GOSIA2 input file with the minimisation command and calculates the 2-dimensional χ^2 surface for a given range and number of transitional and diagonal matrix elements [169]. For this work, a range of 0.3 - 0.8 was chosen for the transitional matrix element $\langle 2_1^+ | E2 | 0_1^+ \rangle$, given its previously reported value from literature of 0.46(2), obtained from lifetime measurements [170]. For the diagonal matrix element $\langle 2_1^+ | E2 | 2_1^+ \rangle$, an arbitrary range of -1.5 - 1.5 was chosen. The chisqsurface code was run across these ranges with the number of different combinations of matrix element values chosen in such a way to produce a 0.025 step increment for both matrix elements. The visual output of this analysis is seen in Figure 4.8.

The reported values for the transitional $\langle 2_1^+ | E2 | 0_1^+ \rangle$ and the diagonal $\langle 2_1^+ | E2 | 2_1^+ \rangle$ matrix elements in ^{72}Se at the 1σ and 2σ level are presented in Table 4.3. It should be noted that the quoted uncertainties on these values are formed from not just the uncertainty on the yield but also the uncertainties in the other inputs specified previously. This includes uncertainties on the previous reported spectroscopic data of ^{196}Pt, uncertainty in the target thickness (thus the stopping power) and uncertainty in the beam energy. The statistical uncertainties quoted are deemed appropriate even with the presence of the Ge contaminant as the contribution of this

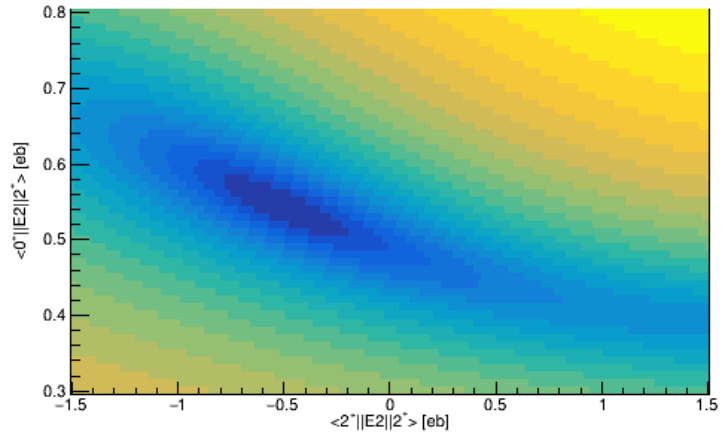

(a) Full result produced by the "chisqsurface" code across the ranges seen for the given matrix elements.

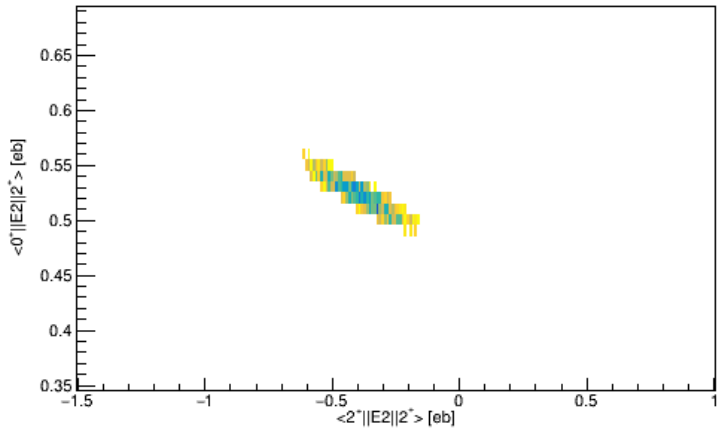

(b) Values of matrix elements within 1σ of the χ^2 minimum.

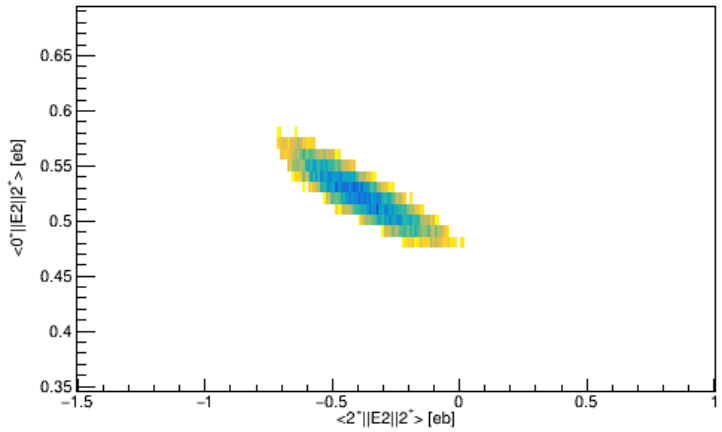

(c) Values of matrix elements within 2σ of the χ^2 minimum.

Fig. 4.8 Output from the "chisqsurface" code run with GOSIA2 focused on the $\langle 2_1^+ | E2 | 0_1^+ \rangle$ and $\langle 2_1^+ | E2 | 2_1^+ \rangle$ matrix elements in ^{72}Se. The Z axis represents the χ^2 value for the given pair of matrix element values, with dark blue areas being where the lowest χ^2 values are found.

isotope to the beam was $< 10\%$, thus any uncertainty due to its presence is likely covered in the quoted uncertainty.

One can use the diagonal matrix element of a state to find its QM (and thus gain information about its charge distribution and therefore its shape) using the relation seen in Equation 4.3, where $Q_s(J_i^\pi)$ is the QM for the J_i^π state, CG is the Clebsch–Gordan coefficient and $\langle J_i^\pi | E2 | J_i^\pi \rangle$ is the diagonal matrix element for the J_i^π state.

$$Q_s(J_i^\pi) = \sqrt{\frac{16\pi}{5(2J+1)}} * CG * \langle J_i^\pi | E2 | J_i^\pi \rangle \tag{4.3}$$

$$Q_s(2_1^+) = \sqrt{\frac{16\pi}{25}} * \sqrt{\frac{2}{7}} * \langle 2_1^+ | E2 | 2_1^+ \rangle \tag{4.4}$$

This equation for the specific case of a 2_1^+ state is shown in Equation 4.4, for which the Clebsch–Gordan coefficient is $\sqrt{\frac{2}{7}}$. Thus the QM of the 2_1^+ state in ^{72}Se is also reported in Table 4.3.

Table 4.3 Reported values for matrix elements at the 1σ and 2σ level and the QM of the 2_1^+ state in ^{72}Se from the analysis of the experiment discussed in this work.

Matrix element / QM	Reported value (eb)	Uncertainty limit
$\langle 2_1^+ \| E2 \| 0_1^+ \rangle$	$0.510^{+0.055}_{-0.025}$	1σ
	$0.510^{+0.075}_{-0.035}$	2σ
$\langle 2_1^+ \| E2 \| 2_1^+ \rangle$	$-0.320^{+0.165}_{-0.295}$	1σ
	$-0.320^{+0.345}_{-0.395}$	2σ
$Q_s(2_1^+)$	$-0.24^{+0.13}_{-0.22}$	1σ

4.5 Analysis and Results for the ^{68}Ge Beam Contaminant

As mentioned in the previous section, a contaminant peak is attributed to the 1015-keV $2_1^+ \rightarrow 0_1^+$ in the neutron-deficient nucleus ^{68}Ge. The transitional $\langle 2_1^+ | E2 | 0_1^+ \rangle$ and diagonal $\langle 2_1^+ | E2 | 2_1^+ \rangle$ matrix elements can thus be extracted in a similar way as is done for ^{72}Se. Some preliminary analysis procedures are conducted again in order to increase the precision of the eventual yield for the ^{68}Ge transition, with Doppler correction of the data run again, taking ^{68}Ge as the "beam" nucleus. Similarly, the histogram "cut" is performed again for the new "beam".

Gamma-ray yields are once again recorded for 3 angular ranges (equivalent scattering projectile scattering angle beyond 59° determined using conservation of momentum calculations with ^{68}Ge as the "beam") for all transitions in both the projectile and target observed in this experiment. The reason for this number of angular ranges is the same as was described for ^{72}Se in the previous section. These yields, alongside their uncertainties, are listed in Tables 4.4 and 4.5 for projectile and target, respectively. As before, all yields reported are calculated using the peak areas extracted from the respective spectra formed after the data was split according to the chosen angular ranges, with these values corrected for energy and efficiency calibrations (completed with RadWare package [166]). Uncertainties quoted here are much higher with respect to the ^{72}Se due to the very low number of counts observed for the transition in ^{68}Ge, with a 'peak' in the histogram being quite difficult to establish precisely.

Table 4.4 Gamma-ray yields for transitions in ^{68}Ge observed in this experiment over 3 ranges for the projectile scattering angle. Data from ranges marked * are from gamma rays seen in coincidence with target particle detection, with equivalent projectile scattering angle calculated using conservation of momentum calculations.

Projectile scattering angular range (degrees)	Transition	Yield (arb. units)	Uncertainty
20 - 37.7	$2_1^+ \rightarrow 0_1^+$	1100	400
37.7 - 56.4	$2_1^+ \rightarrow 0_1^+$	1000	400
56.5 - 123.1*	$2_1^+ \rightarrow 0_1^+$	1700	600

Table 4.5 Gamma-ray yields for transitions in ^{196}Pt observed in this experiment over 3 ranges for the projectile scattering angle. Data from ranges marked * are from gamma rays seen in coincidence with target particle detection, with equivalent projectile scattering angle calculated using conservation of momentum calculations.

Projectile scattering angular range (degrees)	Transition	Yield (arb. units)	Uncertainty
20 - 37.7	$2_1^+ \rightarrow 0_1^+$	6900	600
37.7 - 56.4	$2_1^+ \rightarrow 0_1^+$	6600	600
56.5 - 123.1*	$2_1^+ \rightarrow 0_1^+$	9500	700
	$4_1^+ \rightarrow 2_1^+$	2100	300
	$2_2^+ \rightarrow 2_1^+$	1400	400

Given the measured yields for all observed transitions for the chosen angular ranges, it is possible to perform the GOSIA2/chisqsurface analysis in the exact same way as in the ^{72}Se case. For this nucleus, a range of 0.1 - 0.6 was chosen for the transitional matrix element $\langle 2_1^+ | E2 | 0_1^+ \rangle$, given its previously reported value from literature of 0.36(2) [171]. For the diagonal matrix element $\langle 2_1^+ | E2 | 2_1^+ \rangle$, an arbitrary range of -2 - 1.5 was chosen. The chisqsurface code was run across these ranges with the number of different combinations of matrix element values chosen in such a way to produce a 0.01 step increment for both matrix elements. The visual output of this analysis is seen in Figure 4.9.

The reported values for the transitional $\langle 2_1^+ | E2 | 0_1^+ \rangle$ and the diagonal $\langle 2_1^+ | E2 | 2_1^+ \rangle$ matrix elements in ^{68}Ge at the 1σ and 2σ level are presented in Table 4.6. One can use the relation to the $\langle 2_1^+ | E2 | 2_1^+ \rangle$ diagonal matrix element as seen in Equation 4.4 to find the QM of the state, thus the experimentally deduced QM for the 2_1^+ state in ^{68}Ge can be constrained and is also reported in Table 4.6. It should be noted that the uncertainties on the diagonal matrix element and QM for the 2_1^+ state are likely larger than the statistical ones quoted here, due to the fact the vast majority of the beam composition is in fact ^{72}Se and not ^{68}Ge, which could not be corrected for in the analysis. The value quoted is a first estimate which should be used as a basis for the analysis of a further experiment looking to better constrain the QM.

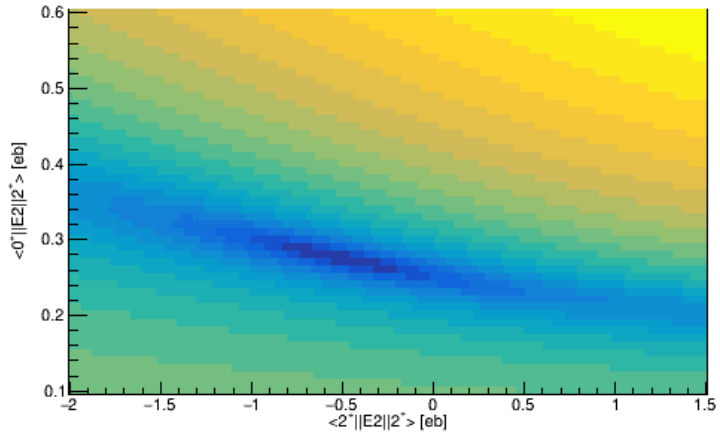

(a) Full result produced by the "chisqsurface" code across the ranges seen for the given matrix elements.

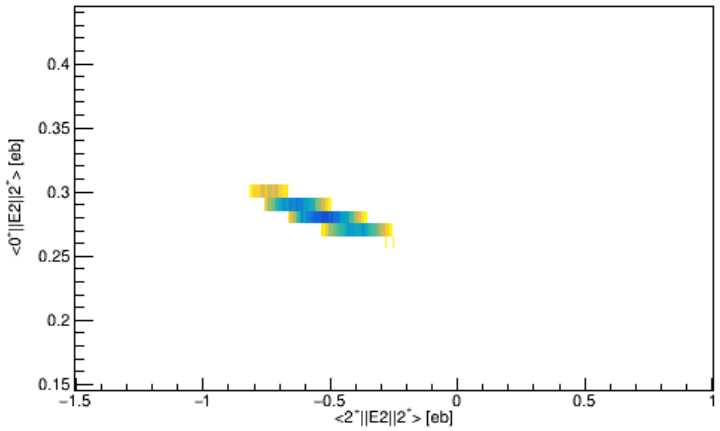

(b) Values of matrix elements within 1σ of the χ^2 minimum.

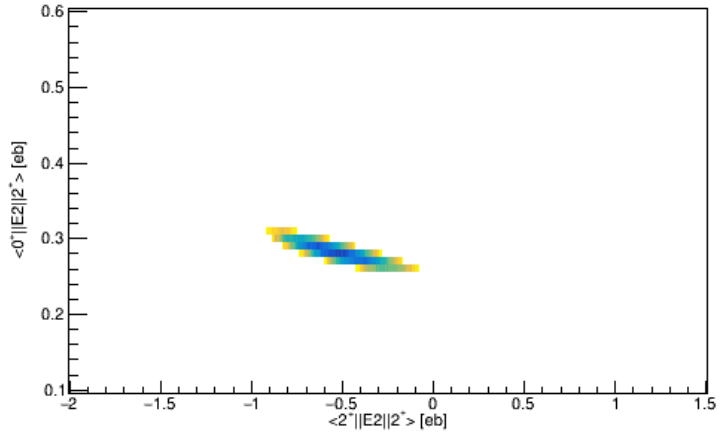

(c) Values of matrix elements within 2σ of the χ^2 minimum.

Fig. 4.9 Output from the "chisqsurface" code run with GOSIA2 focused on the $\langle 2_1^+ | E2 | 0_1^+ \rangle$ and $\langle 2_1^+ | E2 | 2_1^+ \rangle$ matrix elements in ^{68}Ge. The Z axis represents the χ^2 value for the given pair of matrix element values, with dark blue areas being where the lowest χ^2 values are found.

Table 4.6 Reported values for matrix elements at the 1σ and 2σ level and the QM of the 2_1^+ state in ^{68}Ge from the analysis of the experiment discussed in this work.

Matrix element / QM	Reported value (eb)	Uncertainty limit
$\langle 2_1^+ \vert E2 \vert 0_1^+ \rangle$	$0.280^{+0.025}_{-0.025}$	1σ
	$0.280^{+0.035}_{-0.025}$	2σ
$\langle 2_1^+ \vert E2 \vert 2_1^+ \rangle$	$-0.510^{+0.265}_{-0.305}$	1σ
	$-0.510^{+0.435}_{-0.405}$	2σ
$Q_s(2_1^+)$	$-0.39^{+0.33}_{-0.17}$	1σ

4.6 Discussion and Comparison to Previous Work

The initial goal of this experiment was to obtain a large set of E2 matrix elements connecting multiple states and QMs of multiple levels and while this was not possible, important values were still reported from the limited data collected. All values for matrix elements and QMs reported in this work are in units of eb. In ^{72}Se, the QM for the 2_1^+ state was deduced to be $Q_s(2_1^+) = -0.24^{+0.13}_{-0.22}$, implying a prolate configuration. The sign of the QM is in agreement with the only other experimentally reported value by Henderson et al. of $-0.57^{+0.29}_{-0.29}$ [167], while the magnitudes of the two reported values are within each others 1σ limit, with vastly reduced uncertainty on this value reported here. Furthermore, the reported transitional matrix element from this experiment $\langle 2_1^+ \vert E2 \vert 0_1^+ \rangle = 0.510^{+0.055}_{-0.025}$ for ^{72}Se is within the 1σ limit of the literature value of $0.46^{+0.02}_{-0.02}$ [170], giving greater credibility to the $Q_s(2_1^+)$ result reported. The $Q_s(2_1^+)$ value reported here is also important confirmation that the shape transition from prolate to oblate shapes in the selenium isotopic chain does not occur until at least ^{70}Se.

Multiple theoretical predictions have been made for the QM for the 2_1^+ state in ^{72}Se. As displayed in Figure 3.1 from Section 3.1, the GCM(GOA) calculations [12] and ASCC calculations [13] both predict a negative $Q_s(2_1^+)$, which is in agreement with the result reported in this work, though the value predicted by GCM(GOA) calculations is very weakly prolate. Similar work from Hinohara et al. [115] using a constrained Hartree–Fock–Bogoliubov (CHFB)

method with both a local quasi-particle random phase approximation (LQRPA) and Inglis-Balyaev (IB) defined normal modes produce approximately the same results, again in good agreement with value quoted in this work. CHFB/Gogny based theoretical models appear to disagree with the prolate-dominated configuration implied by this work, with CHFB Gogny-D1M mapped interacting boson model (IBM) [172] and CHFB Gogny-D1S models [173] both predicting a positive $Q_s(2_1^+)$ value in ^{72}Se, though they disagree significantly on the magnitude. Similarly, another theoretical model based on the PMMU shell-model Hamiltonian [174] predicts a positive $Q_s(2_1^+)$, although no magnitude is reported.

One can see from the various theoretical models that even for an individual state in one isotope of selenium, the picture is unclear. The fact that the angular distribution of the cross section in this experiment represents a QM for the 2_1^+ state that is negative at close to the 2σ level, and that this implied prolate configuration is in agreement with the previous experimental value, implies theoretical models predicting a negative $Q_s(2_1^+)$ appear to be more accurate. However, these models attempt to predict far more than just one QM, looking to understand shape configurations for multiple bands across the isotopic chain.

Given the apparent level of sensitivity of the available models, with minor variations in model parameters being potentially significant [174], it is still greatly important to further test the current models. More experimental data is needed, such as a greater set of E2 matrix elements connecting low-lying states in selenium isotopes, attainable via similar Coulex experimental setups as the one used in this work - a follow-up Coulomb-excitation experiment proposal has recently been accepted with a view to achieving this. Two-neutron transfer experiments to determine the intrinsic shape evolution for the 0^+ states across the isotopic chain could also provide significant evidence with which to probe theoretical predictions and a feasibility study into such an experiment is discussed in Appendix A.

A bonus measurement is also reported from this experiment, with the QM for the 2_1^+ state in the beam contaminant ^{68}Ge found to be $Q_s(2_1^+) = -0.39^{+0.33}_{-0.17}$, implying prolate configuration

as in the ^{72}Se case. This is the first experimentally deduced value for the QM for the 2_1^+ state in ^{68}Ge. The reported transitional matrix element $\langle 2_1^+ | E2 | 0_1^+ \rangle = 0.280^{+0.025}_{-0.025}$ for ^{68}Ge is within the 2σ limit of the literature value $0.36^{+0.02}_{-0.02}$ [171]. The formation of ^{68}Ge in this experiment also represents the first post-acceleration of a radioactive neutron-deficient Ge isotope at an ISOL facility. Germanium isotopes are another important testing ground for beyond-mean-field type theoretical calculations, such as those discussed previously, but experimental results on QM values were previously even more lacking than for the selenium isotopes. In particular, a shape transition from prolate to oblate ground states is predicted but the location of this transition point is uncertain; a situation similar to the neutron-rich Ge isotopes, close to N=50, where a shape transition is also thought to occur [172]. Similar to the ^{72}Se case, it is vitally important to further test these theoretical models with follow-up experiments performed with similar setups to the one discussed in this thesis, focusing specifically on the neutron-deficient germanium isotopes. This is now feasible given the newly discovered method for producing radioactive germanium beams from this experiment. Given that the uncertainties on the diagonal matrix element and QM for the 2_1^+ state are likely larger than the statistical ones quoted here, for the reasons mentioned previously, a further experiment looking to more precisely compute the QM for the 2_1^+ state in ^{68}Ge would be the perfect place to start.

Chapter 5

Gamma-Ray Spectroscopy of ^{60}Zn

5.1 Introduction and Motivation

Fusion-evaporation is a type of nuclear reaction which can be experimentally induced by accelerating a projectile nucleus with enough energy such that it fuses with a target nucleus, overcoming the Coulomb barrier between them and forming a highly excited compound nucleus. This compound nucleus then de-excites via the "evaporation" of light particles (e.g. protons, neutrons, alphas), hence referred to as "fusion-evaporation". It is a useful reaction mechanism for the gamma-ray spectroscopy of specific nuclei as once the excitation energy of the system is roughly equal to the nuclide particle separation energy, de-excitation continues predominantly via gamma decay. The detection of these gamma rays allows for the constraint of nuclear structure properties via transition energies and coincidence relationships, which give information about the level structure, or via angular correlations, which allow for the deduction of the spin and parity of a state. The full fusion-evaporation process is displayed schematically in Figure 5.1.

Fusion-evaporation can be induced by both heavy-ion and light-ion beams. Heavy-ion–induced fusion-evaporation reactions are typically used to produce and study nuclei far out towards the proton drip line and were first used in this way to study heavy nuclei [175],

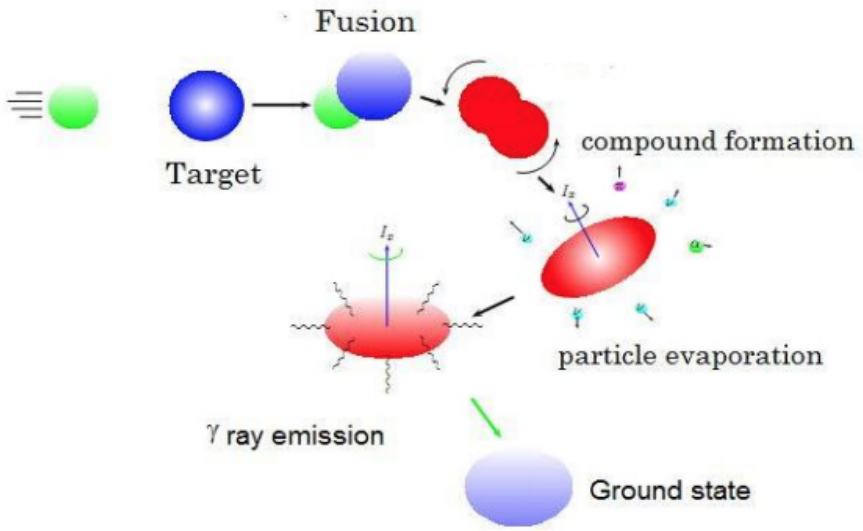

Fig. 5.1 A simple diagram displaying the fusion-evaporation process and its decay to the ground state of a compound nucleus.

with lighter nuclei studied later in the 1970s, such as in the fusion-evaporation reactions forming nuclei with mass 32≤A≤46 [176]. Light-ion–induced fusion reactions are optimal for the production of neutron-deficient nuclides closer to the valley of β stability. Furthermore, light-ion–induced reactions result in a more favourable population of low-spin states in the final nuclei with respect to heavy-ion induced fusion-evaporation [15]. This is because the low mass of the projectile will mean that the total angular momentum in the compound nucleus system formed after fusion is lower, thus lower angular momentum excited states is more likely to be populated. The development of the IGISOL ("Ion-Guide Isotope Separator On-Line") technique in the early 1980s allowed for light-ion fusion-evaporation reactions to work with short-lived and rare radioactive isotopes [177] and has allowed for a lot of modern studies such as the one conducted in [15].

There is considerable nuclear structure interest in the low-lying states in ^{60}Zn and information on bound levels is still relatively scarce. In particular, no firm assignment has yet been made for either the 0_2^+ or 2_2^+ states. Information on the location of these levels is critical as theoretical calculations in this key region for shape changes predict the coexistence of prolate-

and oblate-deformed structures [14]. Establishing the location of levels associated with both structures will, therefore, provide valuable information to test these predictions, albeit in an indirect way which is complementary to investigations using direct techniques such as Coulomb excitation. There is also astrophysical motivation, as studying the properties of resonant states of the ^{59}Cu(p,γ) reaction can shed light on the impact of this reaction rate on the shape and structure of X-ray burst light curves.

Excited states in ^{60}Zn have been studied with heavy-ion fusion-evaporation previously, where the ^{40}Ca(^{28}Si,2α) and ^{40}Ca(^{32}S,3α) channels were used to strongly populate high-spin states belonging to a proposed super-deformed band [178]. No information about low-lying non-yrast states was reported, nor were any proposed resonances for the ^{59}Cu(p,γ) reaction, corresponding to low-l proton captures on the ^{59}Cu ground state ($J^{\pi} = \frac{3}{2}^{-}$). The ^{58}Ni(^{3}He,$n$) light-ion fusion-evaporation reaction can be used to more strongly populate low-spin states in ^{60}Zn, as the use of a light projectile reduces the amount of angular momentum in the compound system compared to in the heavy-ion case. This leads to the population of excited states in the low-lying structure of ^{60}Zn, as well as low-spin states of relevance to the astrophysical ^{59}Cu(p,γ) reaction above the proton emission threshold at 5105 keV [179], which correspond to low-l proton captures on the ground state of ^{59}Cu. This was shown to be a successful approach by Doherty et al. [180, 181] where states corresponding to low-l proton captures were identified that had not been reported in reactions with heavier projectiles [182].

The gamma-ray spectroscopy of ^{60}Zn was conducted at Argonne National Laboratory (ANL) using the ATLAS accelerator for the production of low energy ^{3}He beams which were fired at an enriched ^{58}Ni target, with the Gammasphere detector array utilised for the detection of prompt gamma rays following the induced ^{58}Ni(^{3}He,n) light-ion fusion-evaporation reaction. This study aims to to investigate the level structure of ^{60}Zn and to give first experimental insight into the astrophysical ^{59}Cu(p,γ) reaction rate. This is done by identifying new states and transitions and by confirming or refuting the existence of previously reported structures,

possibly re-assigning transitions and states tentatively reported by other studies. With sufficient statistics, spin-parity assignments for states connected by these transitions can also be made.

5.2 Fusion-Evaporation Theory

Fusion-evaporation reactions involve the bombardment of a given projectile onto an appropriate target with sufficient energy such that the two nuclei fuse to form a compound system, as displayed in Figure 5.1. The energy required for this to occur needs to be sufficient so that the Coulomb repulsion caused by the electromagnetic interaction between the two nuclei can be overcome, or that a significant probability of tunnelling through the Coulomb barrier is realised. The excitation energy of this system can be described by equation 5.1, where $E_x{}^{CN}$ is the energy of the compound nucleus, Q is the Q-value of the reaction, E_p is the energy of the projectile, M_p is the mass of the projectile and M_t is the mass of the target.

$$E_x{}^{CN} = Q + E_p(1 - \frac{M_p}{M_p + M_t}) \tag{5.1}$$

The resulting compound nucleus will have lifetime in the order of ~10^{-19}s, time long enough for it to no longer recognise its production mode and thus decay in a way which will give information about the nuclear structure independent of the initial nuclei [183]. This compound system first de-excites via "evaporation" of light particles, such as in the case of ^{58}Ni(^{3}He,n) where a neutron evaporates from the compound ^{61}Zn to form ^{60}Zn, and this remains the dominant mode of decay until the energy of the system approaches that of the particle separation energy, around ~10^{-15}s after fusion, where the system begins to mostly decay via gamma rays. This process is visible in Figure 5.1 but is best seen schematically in Figure 5.2.

The evaporating light particle carries away some energy and angular momentum, de-exciting the system and reducing its total angular momentum; what is apparent from Figure 5.2 is that

particle evaporation removes a large amount of energy from the system while only removing a small amount of angular momentum. Due to the effects of the centrifugal barrier, the emission of particles with high angular momentum is greatly suppressed in reactions such as these, thus particles mostly with small angular momentum are emitted. Gamma rays emitted after the evaporation of particles are from excited states of a certain nucleus, cascading down to the ground state (as is also shown in Figure 5.2). These nuclei are the potential evaporation channels of the compund nucleus (such as ^{60}Zn in the case of this work).

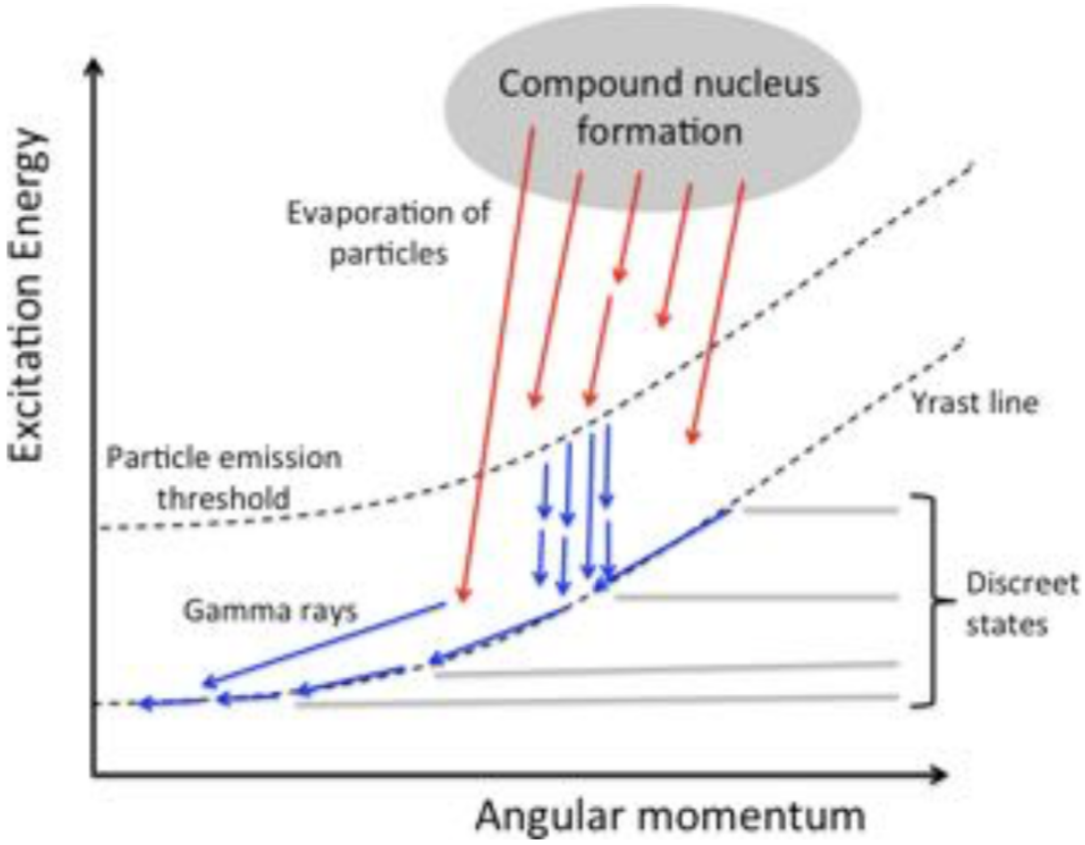

Fig. 5.2 A schematic representation of the decay of a compound nucleus produced in a typical fusion-evaporation reaction. The emission of particles is represented with red arrows whereas γ rays are shown in blue From [184].

5.3 Beam Production with ATLAS Accelerator System

The Argonne Tandem-Linac Accelerator System, known as ATLAS, is one of the world's leading linear accelerators for heavy ions at energies in the vicinity of the Coulomb barrier, the energy domain best suited to study the properties of the nucleus. ATLAS can provide beams of all stable isotopes from hydrogen to uranium up to 17 MeV per nucleon and these can be delivered to multiple experimental areas [185].

"Tandem" is the name given to a particular type of electrostatic particle accelerator and forms a part of the ATLAS accelerator used for this experiment. An outline of this kind of accelerator can be seen in Figure **??**. These produce the highly positively ionised particles of the material of interest. This accelerator is made up of two accelerator tubes connected by a high voltage terminal. The material is negatively ionised forming a negative ion source and is then "pre-accelerated" towards the first acceleration tube. The negative ions are then accelerated towards the high voltage terminal by the first low energy accelerator tube. When entering the high voltage terminal, the particles go through an "electron stripper" (such as a carbon foil), losing a great proportion of electrons. The now strongly positively ionised particles are accelerated away from the high voltage terminal by a high energy accelerator tube and then sent towards a target.

The ATLAS accelerator used in this experiment makes use of this "Tandem" type accelerator in conjunction with a "linac" type accelerator, a particle accelerator where ionised particles are accelerated in a straight line, shown in Figure **??**. These kinds of accelerators are generally housed in a straight and hollow vacuum pipe, where multiple cylindrical electrodes with increasing length further from the source are placed. A particle source is placed at the start of the pipe, say an ion source for positively charged nuclei as in the case for ATLAS, and the particles are sent from the source through the electrodes, accelerated by a radio-frequency oscillating electric field, created in the gap between each electrode which has an oscillating voltage applied such that adjacent electrodes have opposite polarity.

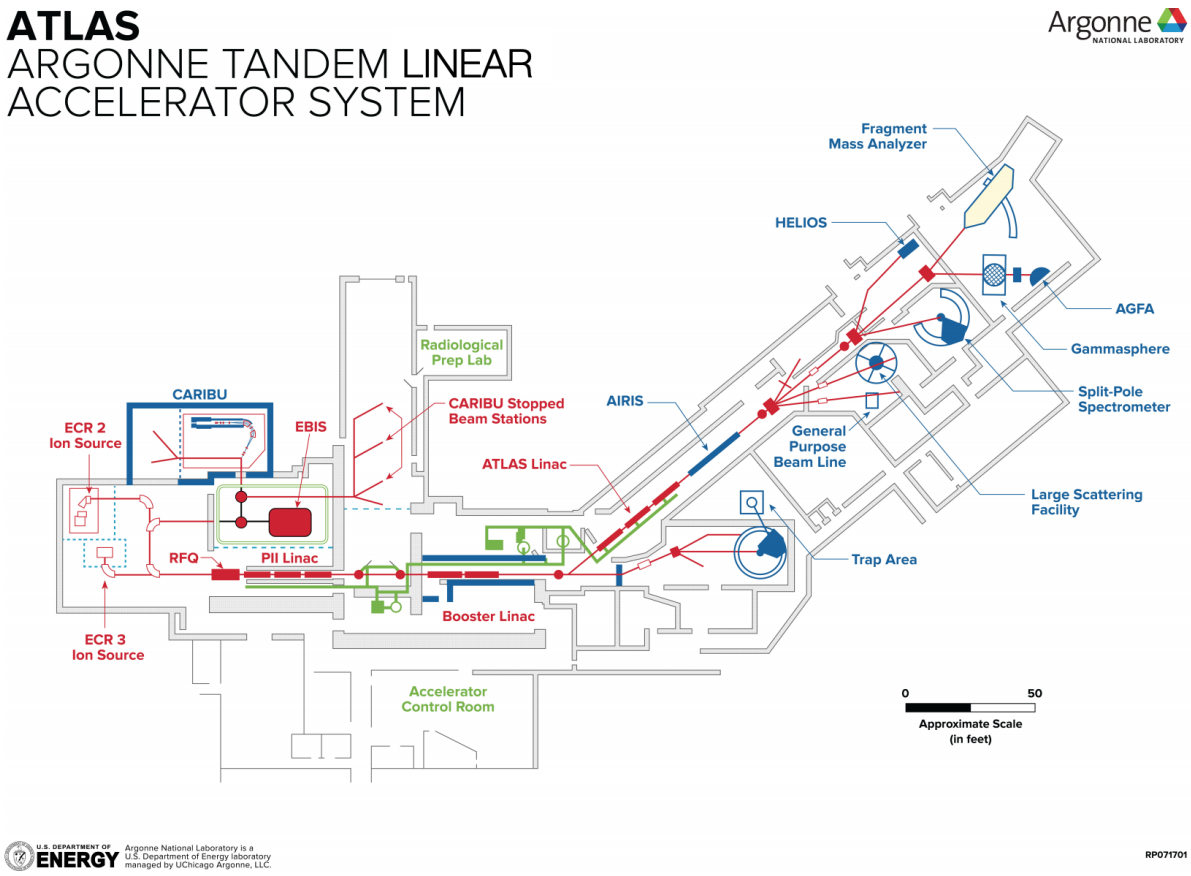

Fig. 5.3 A recent floor plan of the ATLAS accelerator [185]

The ATLAS accelerator consists of multiple acceleration sections, as seen in Figure 5.3, with each the energy increase escalating with each section the particles pass through. Pre-accelerators are used as the source for the main linac; these include a 9 MV electrostatic tandem Van de Graaf accelerator and an electron cyclotron resonance (ECR) ion source. Ions produced here are then sent through the "booster" linac for further acceleration before entering the main "ATLAS" linac, where ions are accelerated using superconducting split-ring resonators which can each have their relative radio-frequency phases varied (this permits a wide variety of ions to be accelerated). In the experiment discussed in this work, the ATLAS linac acted simply as a vacuum pipe, as the beam energy required was achieved using solely the tandem accelerator, thus the superconducting cavities of the linac weren't used.

The accelerated beam of ions is sent to a specific experimental area with dedicated experimental setup. In the case of the ^{58}Ni(^{3}He,n) reaction experiment discussed in this work, the 10 MeV ^{3}He beam was sent to the experimental area where Gammasphere is kept (seen in Figure 5.3) to be impinged onto a ^{58}Ni target to induce the fusion-evaporation reaction desired, forming the ^{60}Zn nucleus of interest. A beam energy of 10 MeV was chosen for the ^{3}He, large enough to overcome the Coulomb barrier of 8.9 MeV but low enough to limit the number of open evaporation channels, which are shown in Table 5.1.

Table 5.1 Predicted cross sections, obtained with the LISE++ code "PACE4", for the dominant evaporation channels following the ^{3}He + ^{58}Ni fusion reaction; total fusion cross section = 160 mb at 10 MeV beam energy.

Nucleus	Z	N	Cross Section (mb)	Evaporation Channel
^{60}Zn	30	30	13	1n
^{60}Cu	29	31	104	1p
^{59}Cu	29	30	2	1p1n
^{59}Ni	28	31	13	2p
^{57}Ni	28	29	29	1α

It is important to limit the number of evaporation channels as no ancillary detectors were used in the study (such as neutron detectors or charged-particle detectors to veto channels that produce protons and alphas). At this beam energy, the compound formation will have energy 20.560 MeV as per Equation 5.1 in Section 5.2 (visual representation in Figure 5.4).

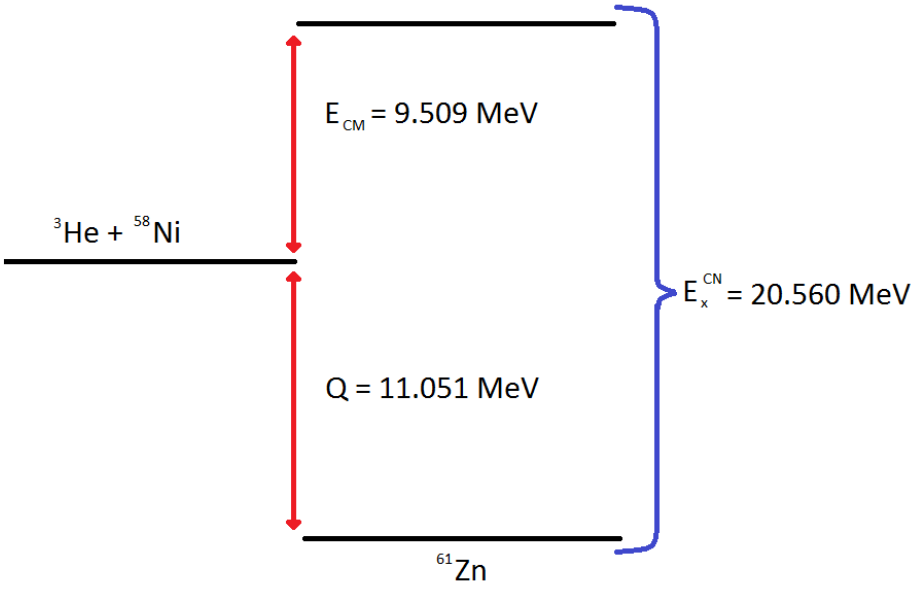

Fig. 5.4 Visual representation of the excitation energy of the compound nucleus formation after the ^{3}He + ^{58}Ni fusion reaction

.

5.4 Target Nucleus

A 750 μg/cm^2 thickness target of enriched ^{58}Ni, formed at the Argonne National Laboratory Physics Division Target Lab, was used for this experiment. As is standard procedure for these type of gamma-ray spectroscopy experiments, thin films of the material, produced by the bombardment of the powder form of the material by an electron beam, are placed in frames which are attached to a target holder which is positioned in the centre of the the Gammasphere detector array. The target material used in this experiment was enriched to to over 99% purity, vastly decreasing the likelihood of contaminants being produced.

5.5 Gammasphere

Gammasphere is a gamma-ray detector array which consists of up to 110 high-purity germanium (HPGe) detectors, each about the size of a coffee cup, in a spherical arrangement. Gammasphere is as a semiconductor gamma-ray detector in the same way as Miniball described in Section 3.5. Each germanium detector is surrounded by a BGO shield which allows for the suppression of background resulting from Compton scattering gamma-ray events [186]. This is important as in a spectrum dominated by Compton background, obtaining reliable peak areas, especially for weak transitions, is difficult. The detectors are also attached to both a liquid nitrogen Dewar for cooling and to electronic modules which allow for data acquisition. The full combination of all these parts is classed as a "module" and a diagram of this can be seen in Figure 5.5.

Using its full 110 detector module capacity, Gammasphere has around ~0.45 solid angle coverage. It can also make use of detectors in the ring at polar angles of 90 degrees which are electronically segmented to reduce the Doppler broadening effect caused by the opening angle of the detector (reduces this opening angle by a factor of 2). It is also possible to correct for the Doppler broadening due to the well defined ring layout of the Gammasphere detectors. The detectors in the Gammasphere array are placed in 17 rings, with each detector ring having a known angle with respect to the beam axis, accurate to 0.01°.

The Gammasphere array makes use of a bismuth germanate (BGO) shield around its HPGe detectors. These shields veto Compton scattered events which help to create cleaner peaks in spectra corresponding to useful gamma-ray hits. This is done by having extra high-efficiency but low resolution detectors in order detect Compton scattered gamma rays, as shown in Figure **??**, thus vetoing events which Compton scatter out of the Ge crystal. Bismuth germanate is perfect for this purpose as its low resolution is not an issue but the high atomic number of Bismuth (Z = 83) means its detection efficiency is very high. Gammasphere also has a BGO suppressor "plug" which sits behind the detector in order to detect photons scattered through angles near 0°; this setup is shown in Figure 5.5.

Fig. 5.5 A typical Gammasphere detector module [187]

.

The method in which Compton scattered gamma rays are rejected in the Gammasphere array allows for them to be vetoed by more than one BGO detector. A gamma ray scattered from either of two adjacent HPGe detectors can be dismissed, as neighbouring segments in the BGO detectors for each one are combined, allowing for gamma rays to be vetoed as per the logic diagram seen in the right of Figure 5.6. False vetoes from direct gamma-ray hits upon the BGO detectors are avoided via the use of hevy metal ("hevimet") shields as seen in Figure 5.5. This Compton suppression method allows for an near three-fold increase in peak-to-total ratio compared to no suppression, with photo-peak area roughly equal in both cases [188].

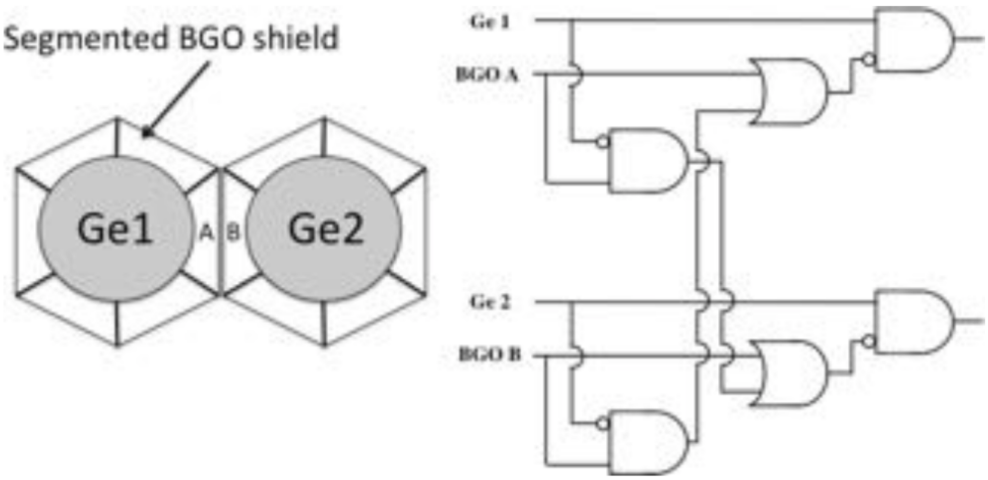

Fig. 5.6 Left: Visualisation of the "honeycomb" formation of two adjacent gammasphere modules. Right: Logic diagram representing how gamma rays are vetoed in gammasphere. Adapted from [184] and [189].

As mentioned previously, the nuclei that are formed from this reaction will undergo gamma decay and it is the detection and measurement of these gamma rays which are the key observable from this reaction. The data acquisition trigger for this experiment was set for when two coincident gamma rays were registered, i.e. where two 'clean' Ge signals (no BGO signals, just Ge) from two of the HPGe detectors are needed to trigger data acquisition. While this means it is not possible to observe direct high-energy transitions to the ground state, it was

not feasible to run this experiment requiring a single gamma ray as the data rate would be too high. This is due to the number of open evaporation channels for this particular reaction and their associated cross sections, as seen in Table 5.1. The vast majority of the 110 high-purity germanium detectors from Gammasphere were used for this experiment, giving close to the full solid angle coverage available. This detection setup is ideal for detecting gamma rays being emitted from weaker transitions at higher energies (close to or above the proton separation energy), as well as allowing for more precise angular distribution measurements used for the spin assignments of new or previously discovered spin-uncertain states.

5.6 Preliminary Analysis

During this experiment, data acquisition was conducted in multiple "runs" of approximately 2 hours, leading to multiple binary files being created to store the data from each run. Each file containing data from the experiment is then "sorted" using a sort code (computer program) made for Gammasphere experiments "GSSort" [190], which creates histograms populated by all the data collected in each file from the experiment. GSSort also allows for users to form their own histograms and analysis depending on the type of experiment; for example, the angular correlation analysis in this work that is discussed in Section 6.2 was conducted using user-defined histograms.

Similar to with the data from the Coulomb excitation of ^{72}Se, one can time gate gamma-ray data from a fusion-evaporation experiment. For this experiment, the spectrum used for this purpose shows the time difference between two gamma rays, as seen in Figure 5.7. One can set a gate around the main peak in this spectrum, which encompasses the data representing prompt coincidences we are interested in, and reject all events outside this peak which represent random events. As can be seen in Figure 5.7., there is one clearly visible main peak which contains the majority of the data and contains the data of interest. Data that falls in this peak is

taken forward for analysis whereas the rest of the events are rejected. The range chosen for this purpose was between channels 3860 and 4090 as seen in Figure 5.7.

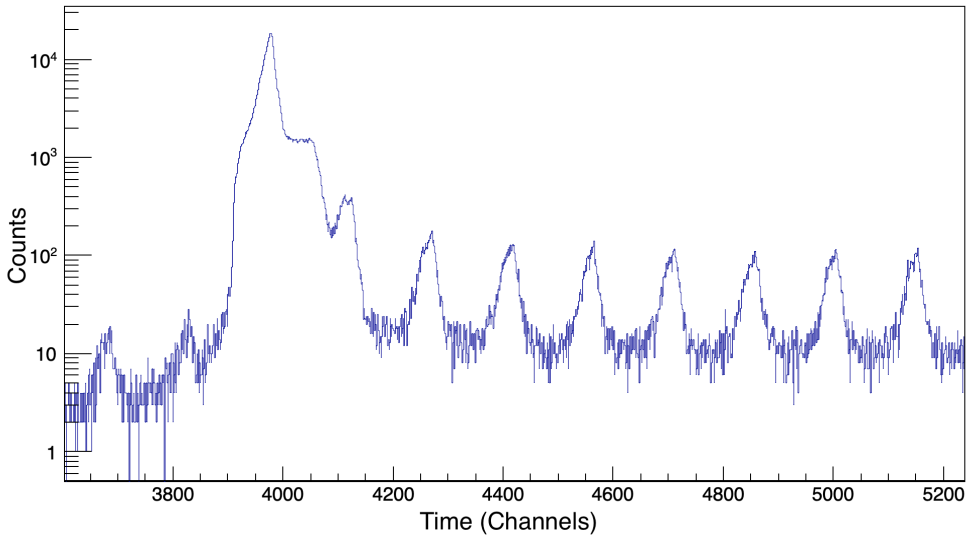

Fig. 5.7 Time spectrum obtained for one of the germanium detectors of the GAMMASPHERE array from this experiment. One can set a gate may around the central peak, rejecting the random events which fall outside of this peak. Smaller peaks correspond to the beam RF, caused by the pulsed nature of the beam "packets" from the Linac accelerator.

Energy and efficiency calibrations are conducted in a similar way to the previous experiment. Gamma-ray decay data from ^{152}Eu and ^{56}Co sources are utilised for this purpose. Doppler correction is again required for data from this experiment and given the light ion beam used in this experiment, recoils move non-relativistically therefore the non-relativistic Doppler shift relation may be used as per Equation 3.7.

The velocity at which the nucleus recoils is dependent on experimental conditions including beam energy, evaporation channel and kinematics. A mean value of β can be taken from classical calculations given that a narrow distribution of recoils is expected for each isotope. Assuming a narrow angular set of recoils around the beam axis at $\theta = 0°$, the emission angle of the gamma ray may be assumed to be the Gammasphere detector angle. By plotting $E_\gamma{}'$ as a function of detector angle, one can find a β value which can be used in the data sort for Doppler correction.

Chapter 6

Level Structure of ^{60}Zn and Potential Implications of the Astrophysical ^{59}Cu(p,γ) Reaction Rate in X-ray Burst Environments

6.1 Overview

This chapter presents the results from the Gamma-ray Spectroscopy of ^{60}Zn, which was populated in the ^{58}Ni(^{3}He,n) fusion-evaporation reaction, performed at the ATLAS facility at Argonne National Laboratory using the Gammasphere detector array.

Knowledge of this self-conjugate nucleus is limited, as can be seen by Figure 6.1, which shows a level scheme for this nucleus up to ~7 MeV based on previous experimental work. This is due to the fact that populating states in this nucleus via fusion-evaporation will either require a 2 neutron evaporation channel (which will likely have small cross section) or the use of a ^{3}He beam, which is not as readily accessible for an experiment of this type, with very few

facilities worldwide currently having the ability to produce this beam in conjunction with an array of HPGe detectors which has the required efficiency and resolution for measuring gamma rays from such a weakly produced reaction channel. Very few states have firm spin-parity assignments and there are very few known transitions in this energy range compared to other, less-exotic, nuclei in this region. A superdeformed band at large excitation energy has already been established from the heavy-ion fusion evaporation work of Svensson et al. [178]; this study also identified the 2^+, 4^+, 6^+ and 8^+ states of the yrast band seen in Figure 6.1, which the super-deformed band feeds into.

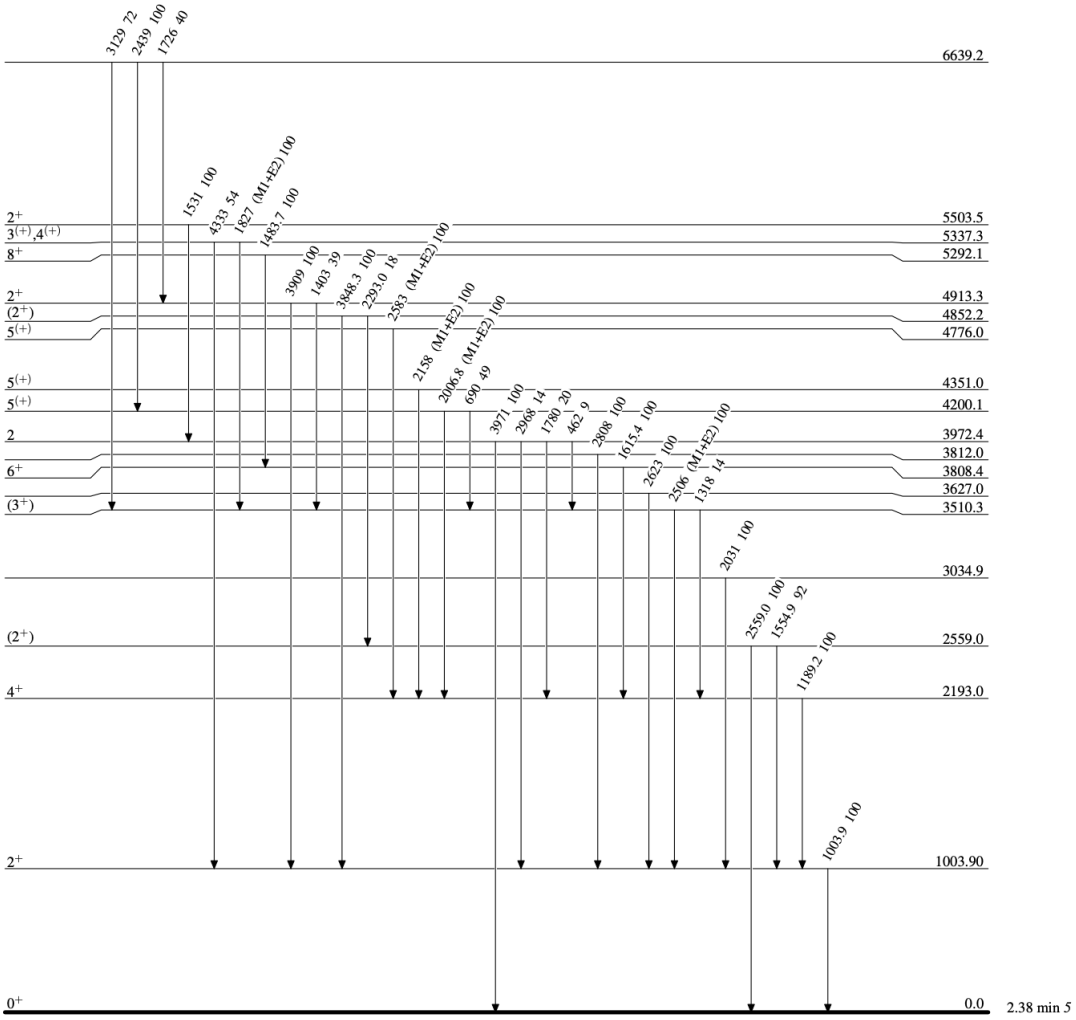

Fig. 6.1 Level scheme for ^{60}Zn at low energy (<7 MeV) based on previous experimental work [191].

In this work, a level scheme is constructed based on the analysis of gamma-gamma coincidence relationships with previously-identified transitions in ^{60}Zn in order to extend the knowledge of the poorly known structure of this nucleus. This work will also shed light on its low-lying spin structure with a particular focus on identifying levels indicative of shape-coexistence phenomena. Spin-parity assignments for states with transitions observed in this experiment can be made due to the well-defined geometry of the Gammasphere array, with precisely known detector angles with respect to the beam axis. The expanded knowledge on the low-lying structure of ^{60}Zn is presented in Section 6.2.

The results extracted from the analysis of this experiment are compared with previous studies and shell-model calculations in Section 6.3. As mentioned in Section 5.1, there is also astrophysical motivation for this experiment, with resonant states of the ^{59}Cu(p,γ) reaction able to shed light on the impact of this reaction rate on the shape and structure of X-ray burst light curves - these states are further looked at and their implications discussed in Section 6.4.

6.2 Low-Lying Level Structure of ^{60}Zn

In this section, an expanded level scheme for the self-conjugate nucleus ^{60}Zn at energy up to ~6 MeV is created based on data seen in gamma-ray spectra formed from the detection of gamma rays following the ^{58}Ni(^{3}He,n) fusion-evaporation reaction. These one-dimensional spectra, such as the one seen in Figure 6.2, are formed by "gating" two-dimensional gamma-gamma coincidence matrices on a particular transition energy by projecting the data within this energy gate on one axis of the matrix onto the other. The one-dimensional spectrum formed from this will display the number of counts coincident with the gate energy across all energies. Peaks in these spectra represent transitions occurring in coincidence with the gate transition. In the case of the spectrum seen in Figure 6.2, the "gate" is set as the entire energy range, which acts as if no gate is set, displaying number of counts coincident with any other gamma ray in the experiment across all energies.

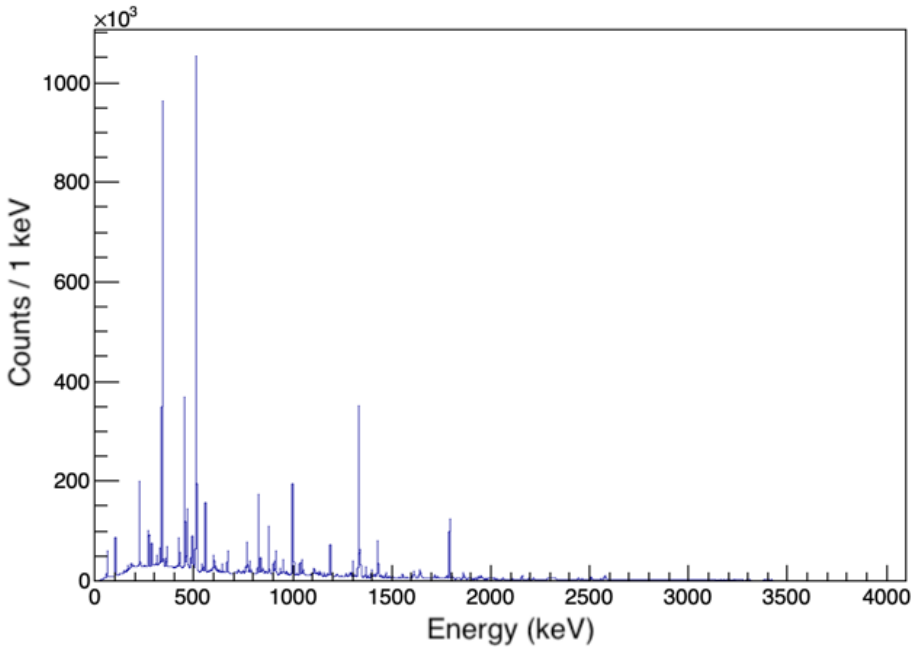

Fig. 6.2 Total projection of the γ-γ matrix.

The two-dimensional gamma-gamma coincidence matrices are created by incrementing the matrix for each pair of coincident gamma rays i.e. two gamma rays are detected at energies $E_{\gamma 1}$ and $E_{\gamma 2}$, both of which occur within the time window set around the prompt peak in the time spectrum seen in Figure 5.7 in Section 3.8.4, thus a count is logged in the matrix at the points ($E_{\gamma 1}$,$E_{\gamma 2}$) and ($E_{\gamma 2}$,$E_{\gamma 1}$). It should also be noted that since a trigger condition of two coincident gamma rays was used in this work, transitions which are not fed by or feed another visible transition (such as a higher energy, low-spin state decaying to the ground state, for example) will not be seen in any of these spectra. As discussed in Section 5.6, this trigger condition was required to keep the data rate to a manageable level.

Before going into the analysis of these spectra, one has to remember that the nucleus of interest in this case, ^{60}Zn, will not be the only nucleus formed and decaying via gamma decay in this experiment (see Table 5.1). Peaks in single-gated spectra may show coincidences with other evaporation channels containing transitions of similar energy. To better understand the other evaporation channels, the 1D projection of the γ-γ matrix with no gate set, displaying

coincidences with any other gamma ray in the experiment across all energies (Figure 6.2) is analysed. In this spectrum, several peaks are visible which can readily attributed to other strong evaporation channels.

It is possible to attribute the peaks in this spectrum to specific transitions in other evaporation channels based on the prediction evaporation cross section in Table 5.1. Based on these cross sections, one would expect to see the most intense gamma-ray transitions observed in the spectrum arise from transitions in ^{60}Cu and ^{59}Ni, with contributions also possible from the formation of ^{59}Cu and ^{57}Ni. Figure 6.3 highlights the largest visible peaks in the 1D projection of the γ-γ matrix with no gate. As one can see from Figure 6.3a and Table 6.1, the most significant peaks can be attributed to transitions in ^{60}Cu and ^{59}Ni.

Table 6.1 Energies, E_γ, at which most visible peaks are seen in the 1D projection of the γ-γ matrix with no gate set (Figure 6.3a). Using the most recent Nuclear Data Evaluations for the nuclei believed to be produced in this experiment, peaks are associated to transitions which closely match in energy. Peaks listed with two transitions were doublet peaks very close in energy, such as that seen around ~1000 keV shown more clearly in Figure 6.3b.

Peak No.	E_γ (keV)	Associated transition
1	62.9(1)	^{60}Cu: $1^+ \rightarrow 2^+$
2	104.3(1)	^{60}Cu: $(3^+) \rightarrow 2^+$
3	225.2(1)	^{60}Cu: $2^+ \rightarrow 1^+$
4	339.6(1)	^{59}Ni: $5/2^- \rightarrow 3/2^-$
5	454.2(1)	^{60}Cu: $(3^+) \rightarrow 2^+$
	466.0(2)	^{59}Ni: $1/2^- \rightarrow 3/2^-$
6	511.24(7)	Pair production (as described in Section 2.4).
7	557.9(1)	^{60}Cu: $(4^+) \rightarrow 2^+$
8	826.4(1)	^{60}Ni: $2^+ \rightarrow 2^+$
9	998.9(1)	^{59}Ni: $7/2^- \rightarrow 5/2^-$
	1003.9(1)	^{60}Zn: $2^+ \rightarrow 0^+$
10	1333.28(8)	^{60}Ni: $2^+ \rightarrow 0^+$
11	1792.3(1)	^{60}Ni: $2^+ \rightarrow 2^+$
(i)	491.7(2)	^{59}Cu: $1/2^- \rightarrow 3/2^-$
(ii)	768.9(2)	^{57}Ni: $5/2^- \rightarrow 3/2^-$

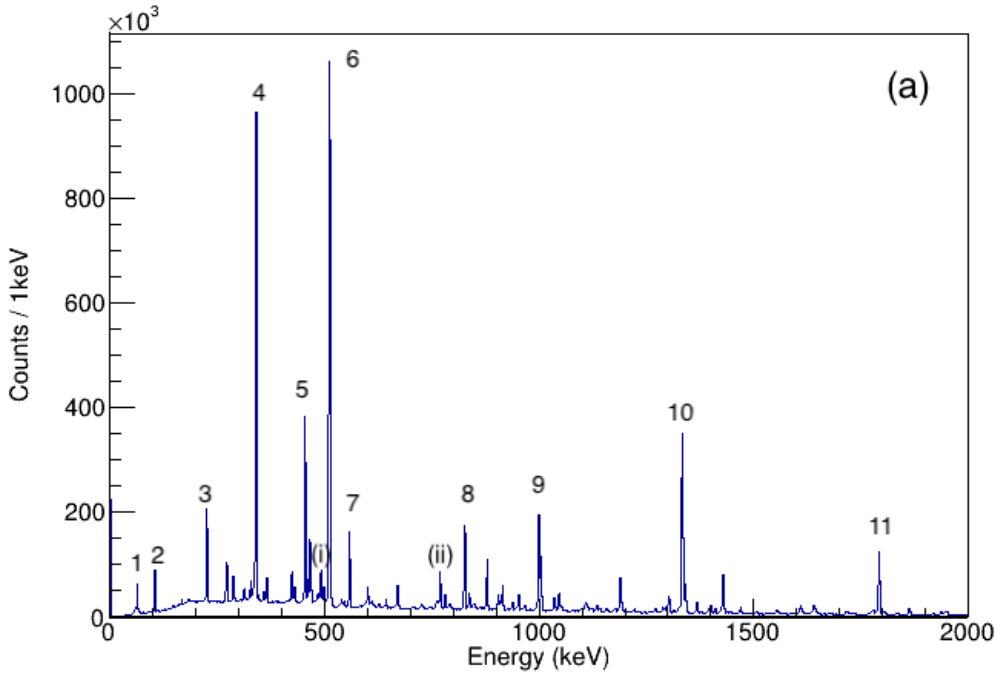

(a) Projection of the γ-γ matrix with no gate set for the energy range 0 - 2000 keV, with largest peaks labelled. Two smaller peaks are highlighted, (i) - the largest peak seen from a transition in ^{59}Cu and (ii) - the largest peak seen from a transition in ^{57}Ni.

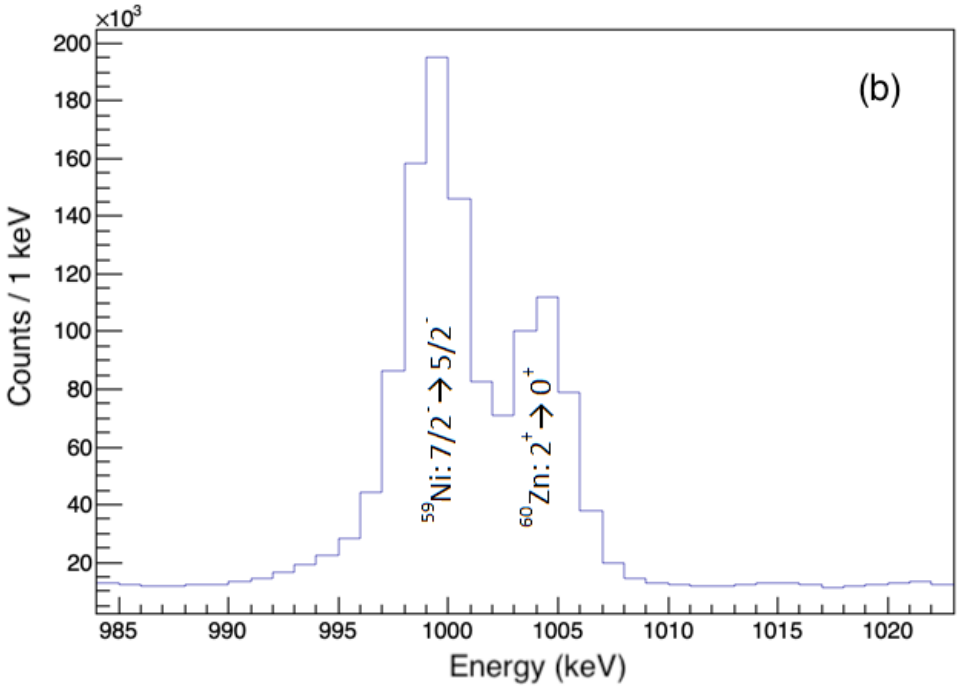

(b) Projection of the γ-γ matrix with no gate set focused on the 1004-keV transition in ^{60}Zn and the 998-keV transition in ^{59}Ni.

Fig. 6.3 Spectra displaying the projection of the γ-γ matrix with no gate set highlighting peaks relating to other channels from the fusion-evaporation reaction.

Three of the peaks listed in Table 6.1, however, are attributed to ^{60}Ni, which is not one of the nuclei seen in Table 5.1 given it is not a viable fusion-evaporation channel in this experiment. Due to the light-ion low-energy beam and substantial target thickness used in this experiment, it is feasible that reaction products may end up being stopped within the target. Furthermore, the largest reaction channel in this experiment is that for the production of ^{60}Cu (as per Table 5.1), which is an unstable nucleus with half-life 24 minutes [192]. The appearance of ^{60}Ni is therefore explained by ^{60}Cu stopping in the target and then β-decaying to ^{60}Ni. With ^{60}Cu abundantly produced and having a relatively short half life, β-decays occur at a large enough rate such that gamma decays from ^{60}Ni are observed.

A peak of particular interest is that around 1000 keV, marked as the $7/2^- \rightarrow 5/2^-$ in ^{59}Ni, which appears to form a doublet peak with the key 1004-keV $2^+ \rightarrow 0^+$ transition in ^{60}Zn. This is focused on in Figure 6.3b, which confirms this doublet peak with the ^{59}Ni $7/2^- \rightarrow 5/2^-$ at 998 keV and the ^{60}Zn $2^+ \rightarrow 0^+$ at 1004 keV. Given the close proximity in energy of these transitions, one would expected the peaks from transitions in ^{59}Ni which are in coincidence with the 998-keV transition to be visible in the spectra gated solely on the 1004-keV $2^+ \rightarrow 0^+$ transition in ^{60}Zn.

A peak is also seen near 1190 keV (not labelled in Figure 6.3a), which is close to the energy of the 1189-keV $4^+ \rightarrow 2^+$ transition in ^{60}Zn. This energy also corresponds to the $5/2^- \rightarrow 3/2^-$ transition in ^{59}Ni, thus, with no gate set, one cannot determine which of these transitions this peak represents (or, the most likely outcome, that it is a mix of both). To ensure the 1189-keV $4^+ \rightarrow 2^+$ transition in ^{60}Zn is observed, one can look at the 1D spectrum formed when gating on the 1004-keV $2^+ \rightarrow 0^+$ transition in ^{60}Zn. While this gate may contain some contamination from ^{59}Ni as discussed previously, it should not contain the 1189-keV transition in ^{59}Ni as it does not fall in coincidence with the 998-keV transition. Part of the 1D spectrum formed when gating on the 1004-keV $2^+ \rightarrow 0^+$ transition in ^{60}Zn, between the energies of 1000 and 3000 keV, is shown in Figure 6.4. A large peak can indeed be seen at 1189-keV, representing the

$4^+ \rightarrow 2^+$ transition in ^{60}Zn. Moreover, given the number of counts in this peak, one can be confident to use this transition in order to analyse coincidences in ^{60}Zn. Using Figure 6.4, it can also be determined that the known 1555-keV $(2^+) \rightarrow 2^+$ and the 2506-keV $(3^+) \rightarrow 2^+$ seen in Figure 6.1 are appropriate transitions for analysing coincidences.

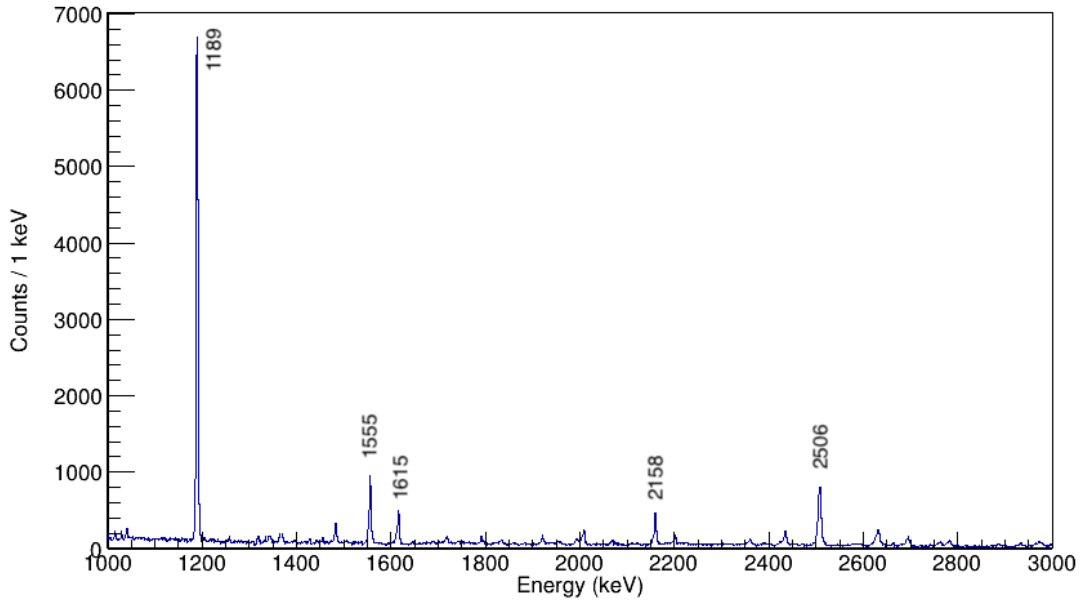

Fig. 6.4 Projection of the γ-γ matrix gated on the 1004-keV transition in ^{60}Zn. - energy range 1000 - 3000 keV

Figure 6.4 shows two other prominent peaks, at 1615 keV and 2158 keV, both of which correspond to transitions in ^{60}Zn: the $6^+ \rightarrow 4^+$ and the $5^{(+)} \rightarrow 4^+$ transitions, respectively. As these both decay to the 4^+ state at 2193-keV, which decays via the 1189-keV $4^+ \rightarrow 2^+$ transition, a simple way to confirm that these peaks correspond to these transitions is to look at the spectrum formed when gating on the 1189-keV transition. Figure 6.5 shows this spectrum an energy range of 1500 - 2200 keV and peaks at both 1615 keV and 2158 keV are both clearly visible, indicating that the transitions at these energies in ^{60}Zn are indeed well observed in this experiment. Other peaks visible in this spectrum are not discussed here and is addressed later

in this section when coincidence analysis is presented; this spectrum is only presented here to reinforce the observation of the aforementioned known transitions in ^{60}Zn.

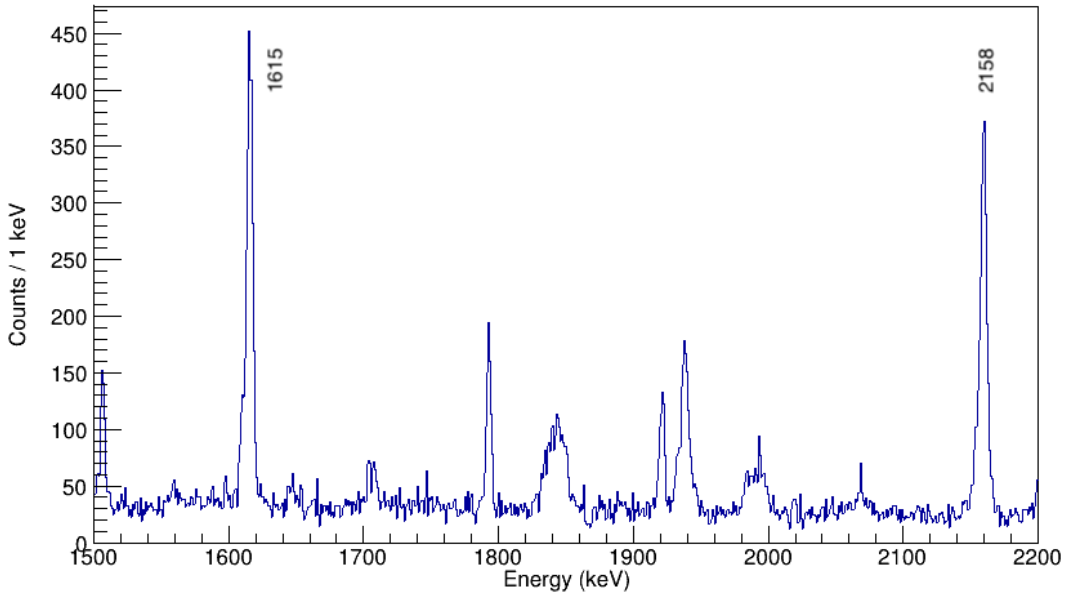

Fig. 6.5 Projection of the γ-γ matrix gated on the 1189-keV transition in ^{60}Zn. - energy range 1500 - 2200 keV

Based on the evidence presented, a list of known transitions in ^{60}Zn appropriate for use as coincidence gates is displayed in Table 6.2. 2D γ-γ matrices can then be gated on these transitions, allowing for the visulisation of the number of gamma rays observed in coincidence with these transitions. The 1615-keV transition was not used as a gate in the final analysis following preliminary analysis of the results seen when gating on this transition. Other transitions seen in Figure 6.1 are seen with low statistics or are not observed in this experiment and are thus not used as gating transitions.

Transitions from other evaporation channels mentioned previously will not be the only ones to fall within the gate energy ranges chosen. In fact, there are transitions in ^{59}Ni that occur at energies which fall in the chosen ranges for all of the gating transitions. Given the high likelihood of transitions from other evaporation channels being present in spectra formed

Table 6.2 Previously reported transitions in ^{60}Zn observed in this experiment chosen as gating transitions. E_γ, is the transition energy as reported in previous work. The "energy range used for gate" is the energy range which is used to represent the transition on one axis of the γ-γ matrix to project onto the other when gating. Superscripts 1, 2 and 3 correspond to the works in references [43], [178] and [193], respectively.

Transition	E_γ (keV)	Energy range used for gate (keV)
$2^+ \rightarrow 0^+$	1003.7(2) [1]	1002-1010
$4^+ \rightarrow 2^+$	1189.2(4) [2]	1185-1193
$(2^+) \rightarrow 2^+$	1554.9(6) [1]	1548-1563
$(3^+) \rightarrow 2^+$	2506(1) [3]	2498-2514
$5^{(+)} \rightarrow 4^+$	2158(1) [3]	2150-2165

with just one gate, it is possible to gate on two different transitions at once to ensure that the peaks observed are indeed attributed to the nucleus of interest. 2D gamma-gamma coincidence matrices are formed in a similar way as before, but in this case the matrix is only incremented when the pair of coincident gamma rays are both detected in coincidence with a gamma ray within a set energy gate, thus forming an already gated matrix, known as a "cube". When this is projected for another energy gate, the 1D spectrum formed will display the number of gamma rays observed across all energies which fall coincident with both of these gates.

Using 2D gamma-gamma coincidence matrices is a powerful method of analysing coincidences with drastically reduced counts from transitions in other evaporation channels, as it requires two of these transitions to fall within the given energy gates and also for these to be in time coincidence with each other. For example, as mentioned previously, the 1189-keV transition in ^{59}Ni does not fall in coincidence with the 998-keV transition, thus the chance that a spectrum gated on both 1004-keV and 1189-keV transitions in ^{60}Zn would see peaks from ^{59}Ni is vastly reduced. Counts from transitions of the desired evaporation channel are also reduced to a lesser degree, therefore significant levels of statistics are required when using this analysis method.

Figure 6.6 displays three 1D spectra across the same energy range, produced when the gamma-gamma matrix is gated on just the 1004-keV transition (Figure 6.6a), just the 1189-keV

transition (Figure 6.6b) and both the 1004- and 1189-keV transitions (Figure 6.6c). These figures neatly display the effect gating twice has on the peaks that are visible in the spectrum. Several peaks which are visible in both single-gated spectra are also visible in the dual-gated spectrum and these peaks can be confidently taken as representing transitions to the 2193-keV 4^+ state. The only exception is the peak at 1483 keV, which is the $8^+ \rightarrow 6^+$ transition that sits above the 1615-keV $6^+ \rightarrow 4^+$ transition that decays to the 2193-keV 4^+ state.

Several peaks which are visible in Figure 6.6b are not seen in Figure 6.6a or the double-gated spectrum in Figure 6.6c and these peaks are generally attributed to transitions from other evaporation channels. Peaks solely seen in the 1004-keV gated spectrum, such as in Figure 6.6a, can also be taken to represent transitions to the 1004-keV 2^+ state. Examples of this are seen in Figure 6.7a, which displays the same spectrum as Figure 6.6a but for a different energy range. Peaks here at 2008 keV, 2435 keV, 2631 keV and 2695 keV are seen with a high level of statistics and cannot be attributed to any known transitions falling in coincidence with the 998-keV transition in ^{59}Ni. These are therefore taken to represent newly discovered transitions to the 1004-keV 2^+ state in ^{60}Zn, just as the 2508 keV and 2971 keV peaks represent known transitions to the 1004-keV 2^+ state. Figures 6.7 and 6.8 display the same spectra as Figure 6.6 but for different energy ranges, with all peaks relating to observed transitions in ^{60}Zn marked accordingly.

Figure 6.9 shows the 1D spectra formed when gating on just the 1555-keV transition (Figure 6.9a) and both the 1004-keV and 1555-keV transitions (Figure 6.9b). It should be noted that the number of counts seen from the transitions of the remaining energy gates are far lower than that of the 1004-keV transition and even the 1189-keV transition. Transitions feeding these states are not expected to be visible in the spectra formed when gating on just the second transition in the cascade (such as the 1004 keV in this case) as they were for the 1189-keV $4^+ \rightarrow 2^+$ to the 1004-keV $2^+ \rightarrow 0^+$ transition cascade, hence these spectra are no longer shown.

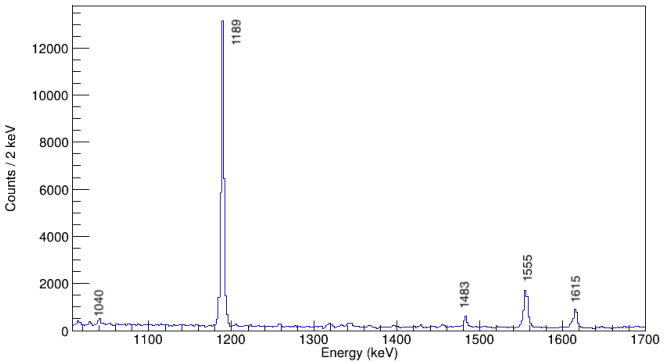

(a) Projection of the γ-γ matrix gated on the 1004-keV transition in ^{60}Zn.

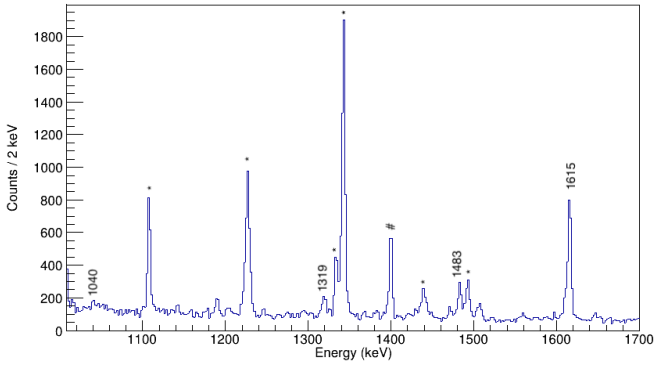

(b) Projection of the γ-γ matrix gated on the 1189-keV transition in ^{60}Zn.

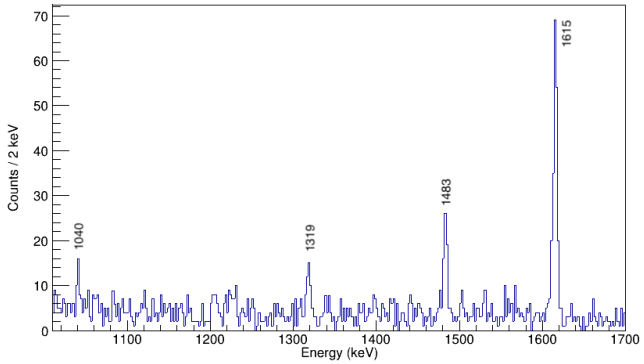

(c) Projection of the γ-γ-γ cube gated on both the 1004- and 1189-keV transitions in ^{60}Zn.

Fig. 6.6 Gamma-ray spectra highlighting peaks corresponding to observed transitions to the 2193-keV 4^+ state in ^{60}Zn, which decays to the 2^+ state at 1004 keV via a 11189-keV transition - energy range 1010 - 1700 keV. Peaks marked * are transitions from ^{59}Ni which fall in coincidence with the 1189-keV $5/2^- \rightarrow 3/2^-$ transition. Peak marked # is the 1399-keV decay in ^{59}Cu, from the $7/2^-$ state (which has a transition at 1188-keV feeding it) to the ground state.

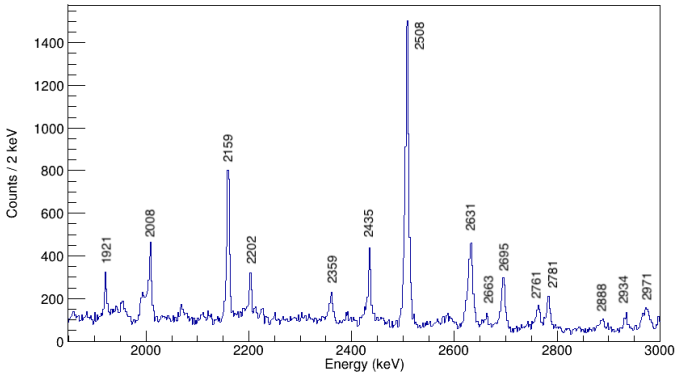

(a) Projection of the γ-γ matrix gated on the 1004-keV transition in ^{60}Zn.

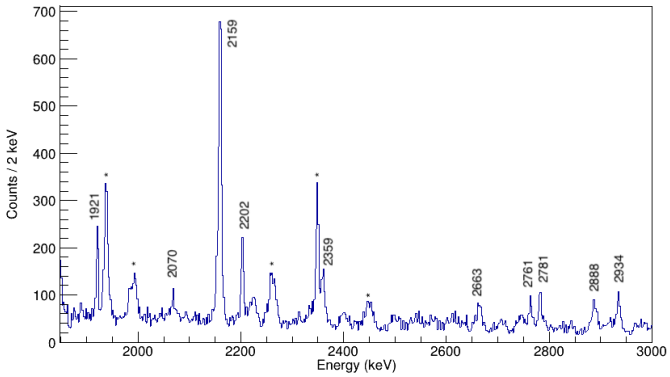

(b) Projection of the γ-γ matrix gated on the 1189-keV transition in ^{60}Zn.

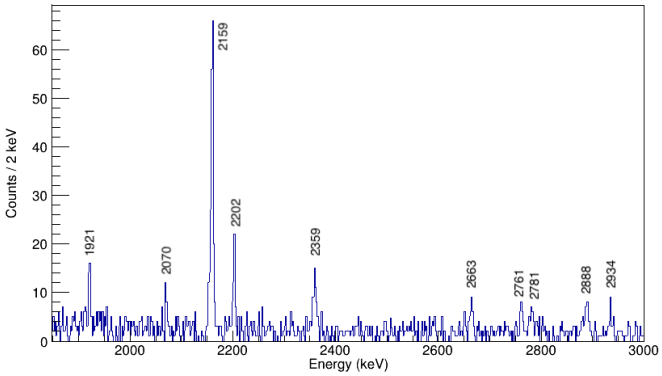

(c) Projection of the γ-γ-γ cube gated on both the 1004- and 1189-keV transitions in ^{60}Zn.

Fig. 6.7 Gamma-ray spectra highlighting peaks corresponding to observed transitions to the 2193-keV 4^+ state in ^{60}Zn, which decays to the 2^+ state at 1004 keV via a 11189-keV transition - energy range 1850 - 3000 keV. Peaks marked * are transitions from ^{59}Ni which fall in coincidence with the 1189-keV $5/2^- \rightarrow 3/2^-$ transition.

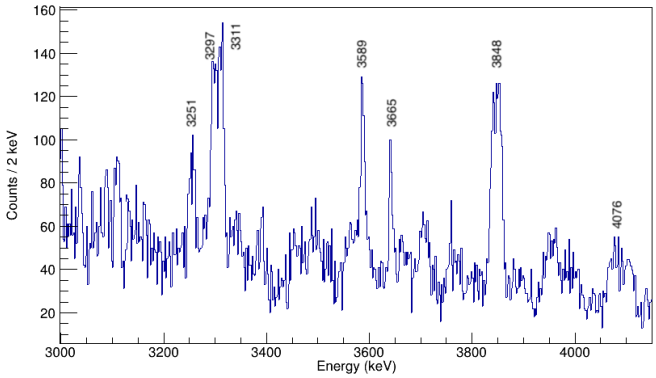

(a) Projection of the γ-γ matrix gated on the 1004-keV transition in ^{60}Zn.

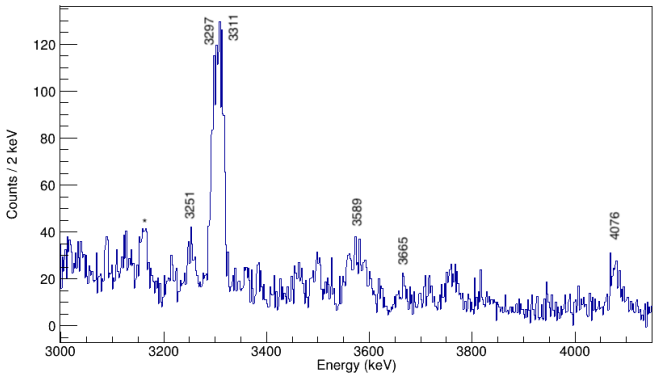

(b) Projection of the γ-γ matrix gated on the 1189-keV transition in ^{60}Zn.

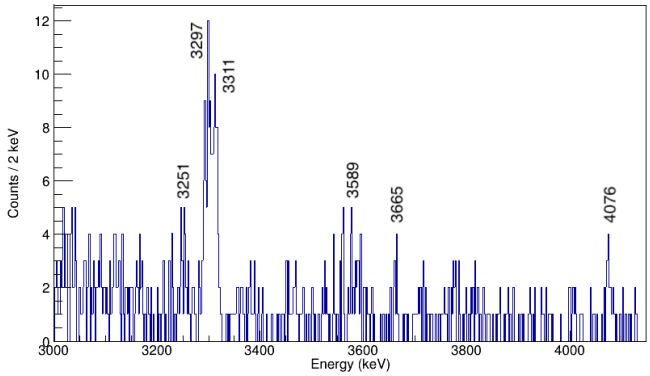

(c) Projection of the γ-γ-γ cube gated on both the 1004- and 1189-keV transitions in ^{60}Zn.

Fig. 6.8 Gamma-ray spectra highlighting peaks corresponding to observed transitions to the 2193-keV 4^+ state in ^{60}Zn, which decays to the 2^+ state at 1004 keV via a 11189-keV transition - energy range 3000 - 4150 keV. Peaks marked * are transitions from ^{59}Ni which fall in coincidence with the 1189-keV $5/2^- \rightarrow 3/2^-$ transition.

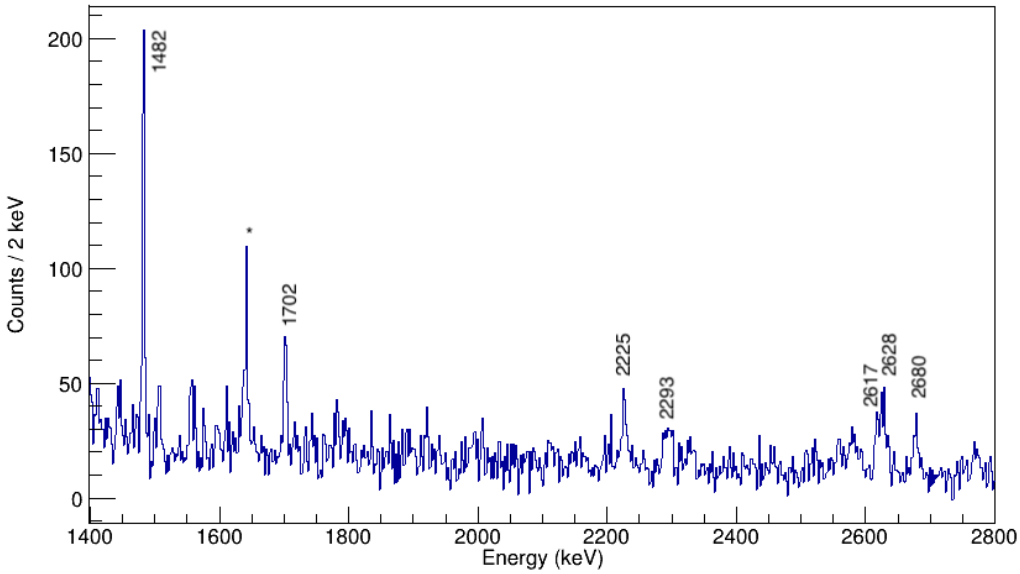

(a) Projection of the γ-γ matrix gated on the 1555-keV transition in ^{60}Zn.

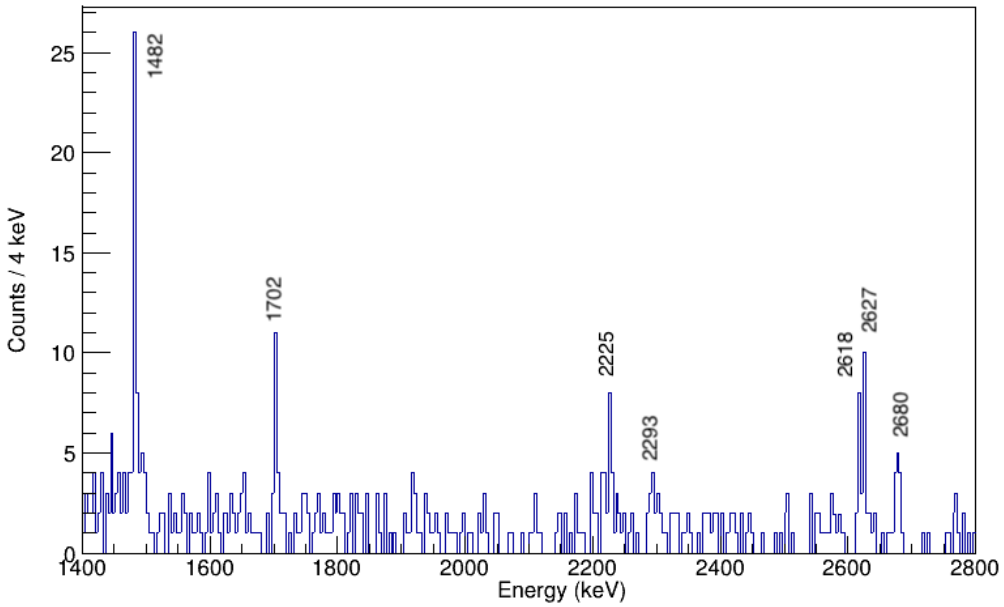

(b) Projection of the γ-γ-γ cube gated on both the 1004- and 1555-keV transitions in ^{60}Zn.

Fig. 6.9 Gamma-ray spectra highlighting peaks corresponding to observed transitions to the 2559-keV (2^+) state in ^{60}Zn, which decays to the 2^+ state at 1004 keV via a 1555-keV transition - energy range 1400 - 2800 keV. Peaks marked * are transitions from ^{60}Cu which fall in coincidence with the 1552-keV $6^- \rightarrow 5^+$ transition.

Figures 6.10 and 6.11 display appropriate spectra for the 2506- and 2158-keV gating transitions, respectively. Figures 6.10a and 6.11a show the chunks of the spectra which highlight the peaks of interest as these peaks would not be as visually clear if a larger range for these spectra were presented. Peak energies for all transitions in ^{60}Zn observed in this experiment are listed in Table 6.3.

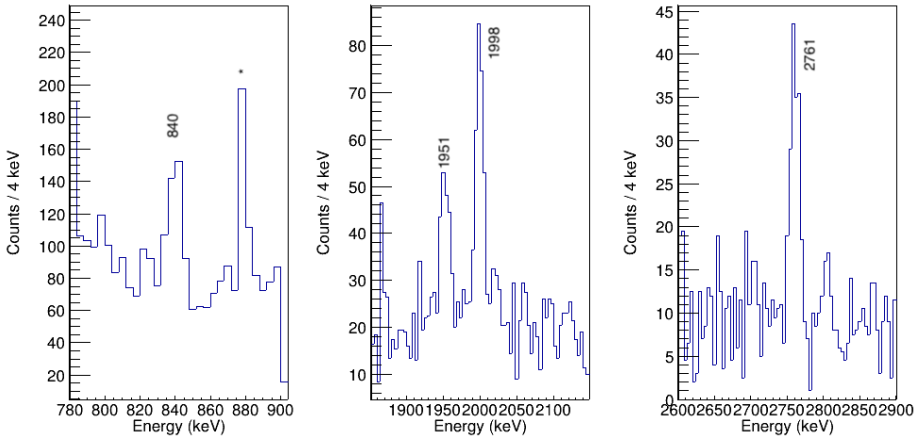

(a) Projection of the γ-γ matrix gated on the 2506-keV transition in ^{60}Zn.

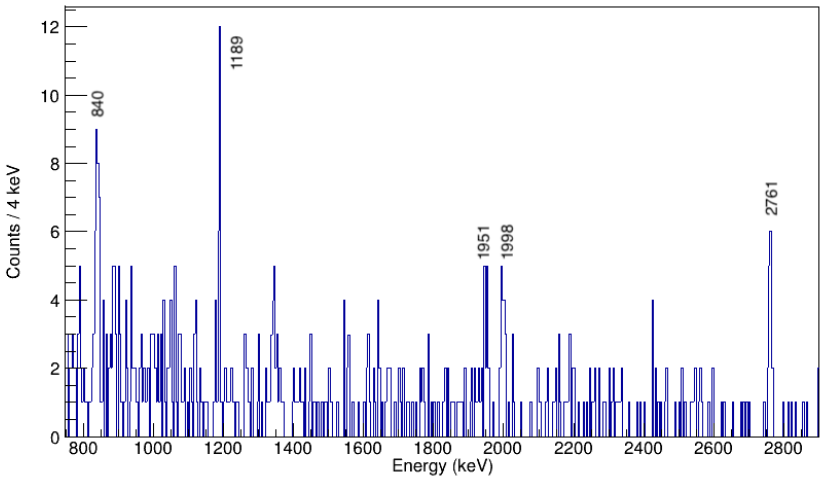

(b) Projection of the γ-γ-γ cube gated on both the 1004- and 2506-keV transitions in ^{60}Zn.

Fig. 6.10 Gamma-ray spectra highlighting peaks corresponding to observed transitions to the 3510-keV (3^+) state in ^{60}Zn, which decays to the 2^+ state at 1004 keV via a 2506-keV transition - energy range 780 - 2900 keV. The peak marked * is the $3/2^- \rightarrow 3/2^-$ transition from ^{59}Ni which falls in coincidence with the 2505-keV $1/2^+ \rightarrow 3/2^-$ transition.

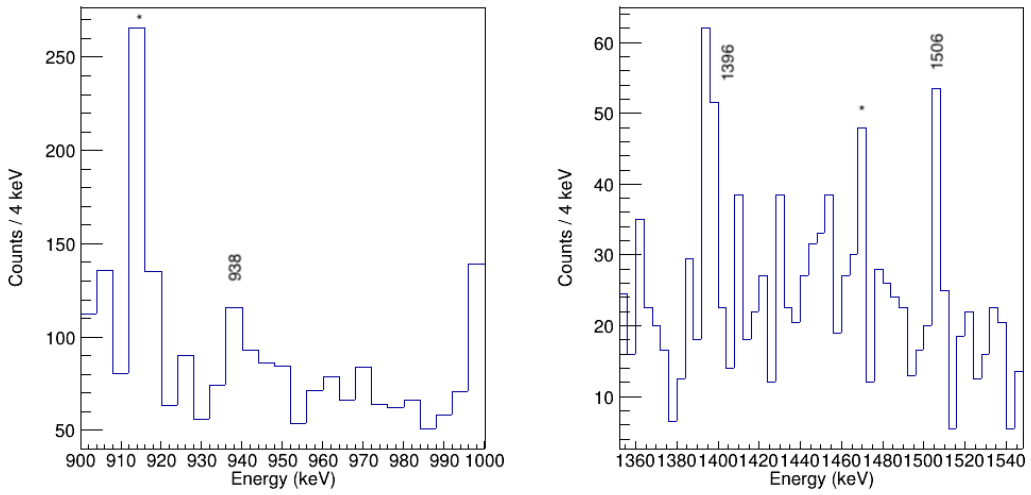

(a) Projection of the γ-γ matrix gated on the 2158-keV transition in ^{60}Zn.

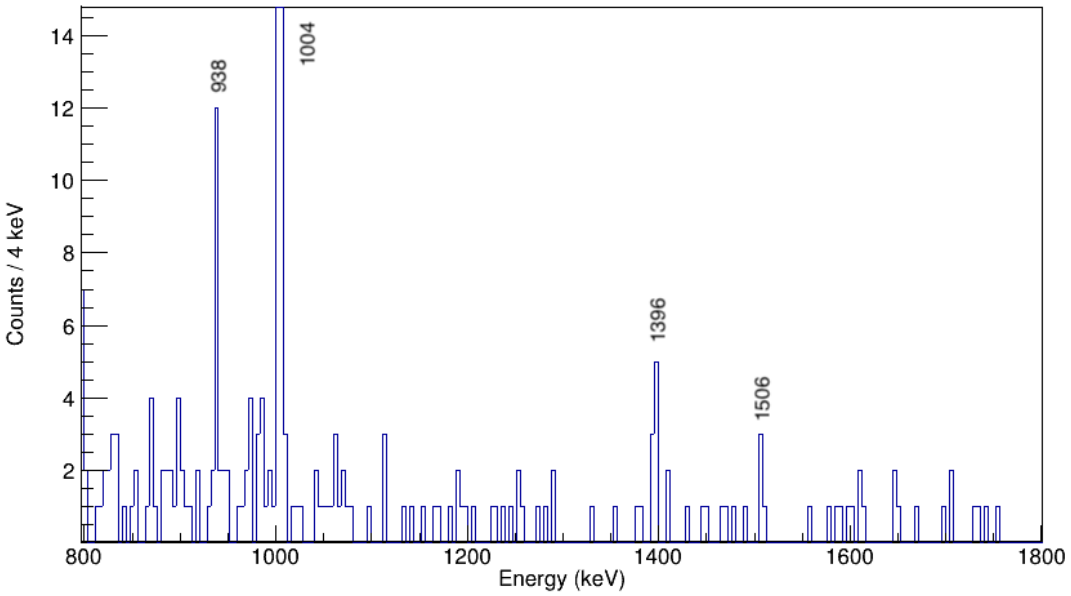

(b) Projection of the γ-γ-γ cube gated on both the 1189- and 2158-keV transitions in ^{60}Zn.

Fig. 6.11 Gamma-ray spectra highlighting peaks corresponding to observed transitions to the 4352-keV $5^{(+)}$ state in ^{60}Zn, which decays to the 4^+ state at 2193 keV via a 2158-keV transition - energy range 900 - 1800 keV. Peaks marked * are transitions from ^{60}Cu.

Table 6.3 Gamma-ray energies, E_γ, for transitions in ^{60}Zn observed in this experiment. E_x is the excitation energy of the state which the transition decays from. Transitions written on the same line are known decays from the same state.

E_x (keV)	E_γ (keV)	E_γ (keV)	E_γ (keV)	E_γ (keV)	E_γ (keV)
2192.6(2)	1188.7(1)				
2559.2(2)	1555.3(1)				
3011.4(3)	2007.5(2)				
3232.8(8)		1040.2(6)			
3438.4(3)	2434.5(2)				
3511.6(2)	2507.7(1)	1318.6(6)			
3634.8.7(4)	2631.0(3)				
3698.7(3)	2694.8(2)				
3807.5(4)		1614.9(2)			
3975(2)	2971(2)				
4041.4(6)			1482.2(4)		
4113.7(7)		1921.1(5)			
4261.1(14)			1701.9(12)		
4262.2(19)		2069.6(17)			
4351.6(8)				840.0(6)	
4352.0(6)		2159.4(4)			
4394.8(9)		2202.2(7)			
4551.7(13)		2359.1(11)			
4784(2)			2225(2)		
4851.4(7)	3847.5(5)		2294(3)		
4856.0(17)		2663.4(15)			
4973.5(16)		2780.9(14)			
5080.5(13)		2887.9(11)			
5127.0(16)		2934.4(14)			
5177(2)			2618(2)		
5186(2)			2627(2)		
5239(3)			2680(3)		
5289.5(21)					937.5(15)
5444(3)		3251(3)			
5462(3)				1951(3)	
5489.6(17)		3297.0(15)			
5504.0(17)		3311.4(15)			
5510(2)				1998(2)	
5748(3)					1396(2)
5782(3)		3589(3)			
5858(3)					1506(2)
5858(5)		3665(5)			
6269.0(21)		4076.4(19)			
6273.0(19)				2761.4(17)	
Decays to:	2^+	4^+	(2^+)	(3^+)	$5^{(+)}$

In order to better understand the low-lying structure of ^{60}Zn, it is important not only to determine transitions and energy levels but also the spin-parity (J^{π}) of these levels. The only energy levels with established J^{π} are those in the ground state band up to a J^{π} of 8^{+}, with a few other low-lying levels tentatively assigned, as well as those found in the high-energy superdeformed band.

New and existing levels which have transitions decaying from them observed in this experiment can be assigned a J^{π} by making use of the conservation of angular momentum. The angular momentum carried away when a transition occurs between two states must be equal to the difference in spin between those two states, and this angular momentum can be experimentally determined by performing angular distribution analysis of the observed gamma rays. Gammasphere, the gamma-ray detector array used in this experiment, is perfect for this type of analysis with its large number of detectors and well established ring layout as mentioned in Section 5.5.

Two methods are commonly used for this kind of analysis, one of which involves obtaining the intensity of the observed gamma rays at a given angle with respect to a fixed axis. The recoiling nuclei in fusion-evaporation reactions such as the type described in this work can be taken to move in a narrow cone along the beam axis, thus one can plot the intensity of the observed gamma rays as a function of detector angle, with the beam axis taken as the "fixed axis". This intensity, $W(\theta)$, as a function of detector angle, is defined in Equation 6.1, where a_k are the angular distribution coefficients, $P_k(cos\theta)$ are the Legendre polynomials and L_{max} is the largest multipolarity that contributes towards the decay.

$$W(\theta) = \sum_{k=even}^{2L_{max}} a_k P_k(cos\theta) \tag{6.1}$$

As mentioned in Section 2.4, transition strength rapidly diminishes with increasing L, thus only the $L = 1$ and $L = 2$ multipoles are taken as relevant to the decay, represented by the

a_2 and a_4 coefficients, respectively. These coefficients can be computed when a transition facilitates a change in spin between two states of 0, 1 or 2 [194].

This type of analysis can be done easily with arrays which have well-defined geometries such as Gammasphere. With Gammasphere, one can look at the spectra formed for each ring and then plot the intensities seen in each of these spectra as a function of the well-known angle of each detector ring. This method, however, is not employed for angular distribution analysis in this work as it requires a high level of statistics which is not the present for the dataset analysed here. A second method, which looks at the ratio of counts seen for a particular transition at the most forward and the most backward angles with respect to angles around 90°, is chosen for this work. This ratio, R_{DCO}, is defined in Equation 6.2, where I is the intensity measured at a given angle θ with respect to the beam axis,

$$R_{\mathrm{DCO}} = \frac{I(\sim 0^{\circ}) + I(\sim 180^{\circ})}{I(\sim 90^{\circ})} \tag{6.2}$$

In order to deduce the change in spin, ΔJ, brought about by a transition using this method, one must first perform an internal calibration by finding the $\mathrm{R_{DCO}}$ value for well-known transitions in the nuclei formed from other evaporation channels. This calibration will yield what $\mathrm{R_{DCO}}$ value corresponds to each ΔJ, meaning that it is possible to understand the ΔJ of observed transitions in ^{60}Zn by finding their $\mathrm{R_{DCO}}$ ratio.

An internal calibration is necessary because these $\mathrm{R_{DCO}}$ values are different for different experimental setups, dependent on factors such as geometry and number of detectors as well as the spin of the initial and final states. Therefore, one cannot directly compare these values from reaction to reaction. For example, in the recent study done with Gammasphere looking at single-particle and collective excitations in the N = 28 isotones ^{54}Fe and ^{53}Mn [195], $\mathrm{R_{DCO}}$ values are all seen up to ~1.3, whereas in this work, values are seen up to ~2.5, with values ~1.3 equating to ΔJ = 2 in that work but ΔJ = 1 in this work.

In this work, two 2D gamma-gamma matrices are formed for coincident gamma rays seen between 0° and 40° and 140° and 180° and for those seen between 75° and 105°. These matrices are used to form 1D spectra in the same way as described for analysing coincidences previously, either by projecting the entire contents of one axis onto the other (i.e. with no gate) or by setting gates on transitions which fall in coincidence with the transitions of interest. The number of counts seen in a peak of a 1D spectrum formed from the matrix filled with coincident gamma rays between 0° and 40° and 140° and 180° is taken to represent $I(\sim 0^\circ) + I(\sim 180^\circ)$ and similarly anything in the 75° to 105° range is taken for $I(\sim 90^\circ)$.

An internal calibration was conducted using known transitions with $\Delta J = 0,1,2$ in abundantly produced 1p and 2p evaporation channels ^{60}Cu and ^{59}Ni, respectively. The R_{DCO} for each of these is shown in Figure 6.12. It is clear from this plot that transitions with $\Delta J = 1$ and $\Delta J = 2$ are discernible, with $R_{DCO} = 0.6\text{-}1.6$ for $\Delta J = 1$ and $R_{DCO} = 1.8\text{-}2.8$ for $\Delta J = 2$. $\Delta J = 0$ transitions are somewhat identifiable at $R_{DCO} = 1.7\text{-}1.9$, but relatively large uncertainties make concrete spin-parity assignment challenging. In principle, it is also possible to establish different R_{DCO} which represent E1 and M1/E2 $\Delta J = 1$ transitions, however, with the statistics available here that was not found to be the case. $\Delta J = 1$ transitions marked with * in Figure 6.12 are E1 transitions and these fall in the middle of the $\Delta J = 1$ R_{DCO} range and at similar R_{DCO} values to many M1/E2 $\Delta J = 1$ transitions.

As mentioned above, one can gate the gamma-gamma matrices when trying to obtain the R_{DCO} for a given transition, as long as the matrices for both angular ranges are gated in the same way. In most cases, when performing an internal calibration, one must take note of the multipolarity of the gate transition as well as that of the transition seen in the spectrum, as the same transition can give vastly different R_{DCO} ratios when gated on transitions of differing multipolarity. However, this effect is not seen and does not need to be accounted for in this work due to the large solid angle coverage and symmetry of the Gammasphere array. This is well displayed in Figure 6.13 where multiple R_{DCO} values are plotted for each transition,

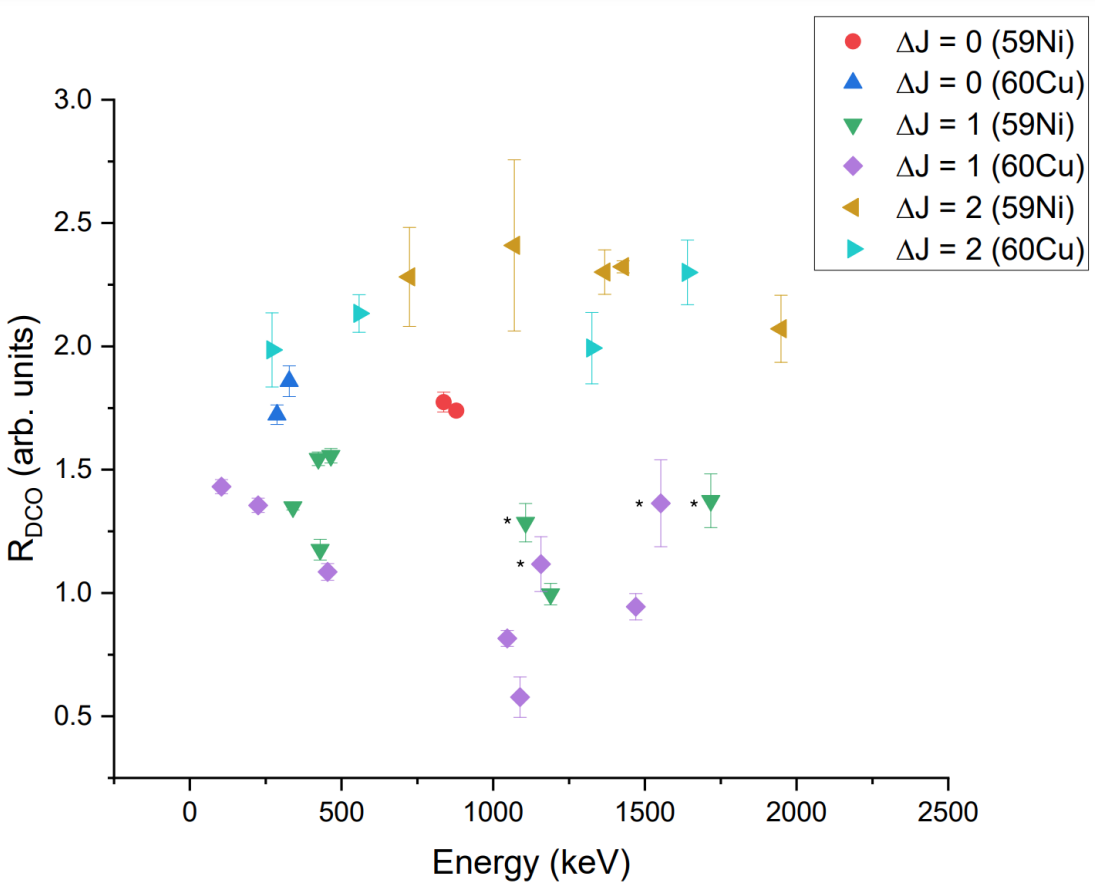

Fig. 6.12 R_{DCO} ratios for known transitions with $\Delta J = 0,1,2$ in ^{60}Cu and ^{59}Ni observed in this experiment. $\Delta J = 1$ data points marked with * are E1 transitions as opposed to M1/E2. Error bars seen correspond to 1σ statistical uncertainties.

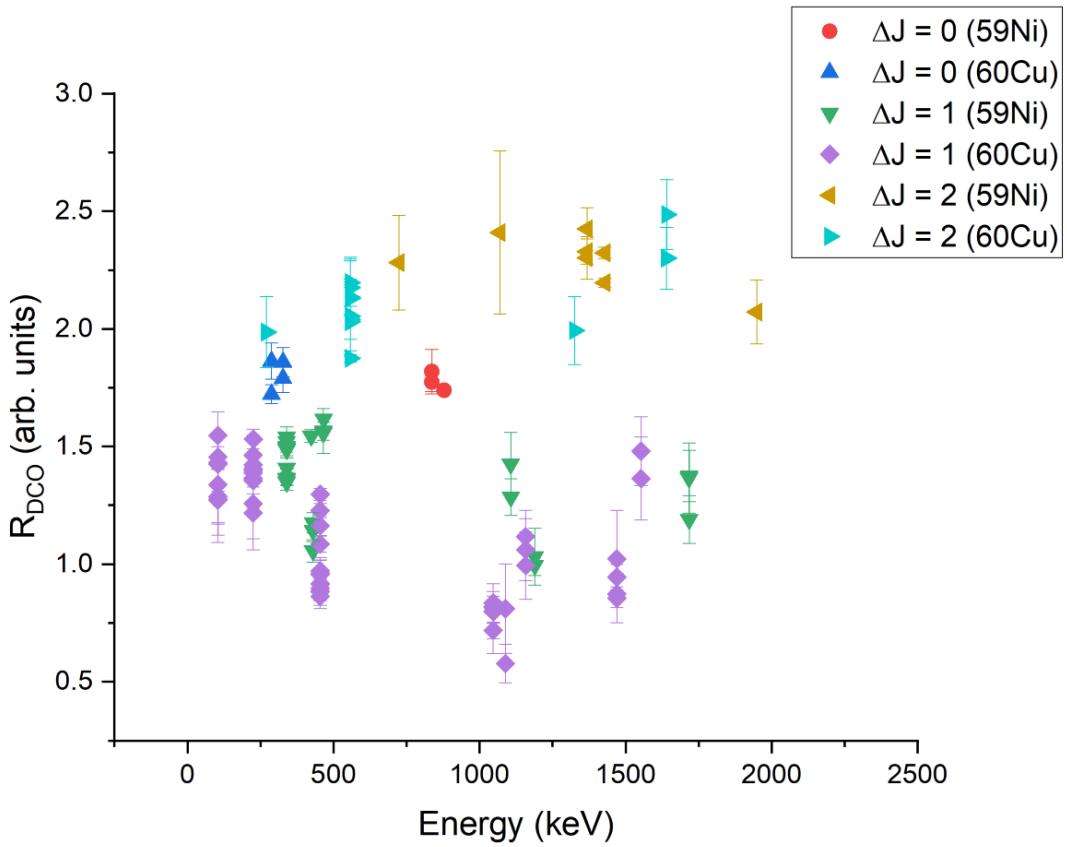

Fig. 6.13 R_{DCO} ratios for known transitions with ΔJ = 0,1,2 in ^{60}Cu and ^{59}Ni observed in this experiment. Multiple values are plotted for each transition, obtained using gates of coincident transitions with differing multipolarity. Error bars seen correspond to 1σ statistical uncertainties.

calculated from peaks in the 1D projection of the gamma-gamma matrices gated on coincident transitions with differing multipolarity. All of the data points for transitions with multiple points are seen to cluster at R_{DCO} values quite close together.

The values from the internal calibration can now be used to assign ΔJ to the transitions in ^{60}Zn observed in this experiment. R_{DCO} values and the implied ΔJ for all transitions in ^{60}Zn observed in this experiment are listed in Table 6.4 and displayed visually in Figure 6.14.

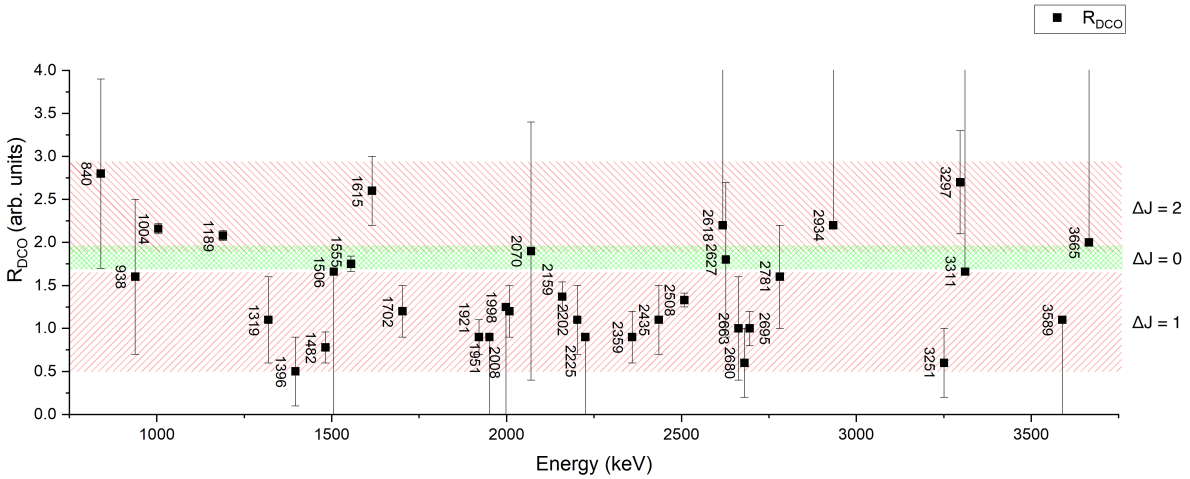

Fig. 6.14 R_{DCO} ratios for transitions in ^{60}Zn observed in this work. Shaded regions are labelled with their the respective ΔJ based on internal calibrations. Error bars seen correspond to 1σ statistical uncertainties.

A provisional assignment for the spin-parity of the initial and final states for each transition is given based on the ΔJ deduced from its respective R_{DCO} ratio and spin-parity assignments seen in Figure 6.1. For some transitions, statistics were too low to obtain R_{DCO} values to adequate precision so limits are reported and in some cases, no value can be reported at all. For transitions where no R_{DCO} is reported, ΔJ is taken to be between 0 and 2, as it is assumed that transitions with ΔJ>2 cannot be observed in this experiment as transitions with multipolarities of M2/E3 and above are too slow to compete with the faster transitions at lower multipolarities.

Transitions decaying from bound states below the proton separation energy are assigned the higher of the two possible spin values possible where a precise ΔJ value can be reported,

as this is the most likely assignment in this region. Proton unbound states are assigned with all possible spin-parity assignments possible based on the ΔJ reported, aside from the state at 5291.2 keV, which is taken as the 8^+ state in the ground state band as its only decay is to the 6^+ state in the GS band.

Table 6.4 Angular distribution ratios, R_{DCO}, implied change of spin, ΔJ, and assignments of all transitions in ^{60}Zn observed in this experiment. E_γ is the energy of the transitions and E_x is the excitation energy of the state which the transition decays from. States below the dashed line are proton-unbound states which lie above the proton separation energy at 5105 keV [179].

E_x (keV)	E_γ (keV)	R_{DCO}	ΔJ	Assignment
1003.9(1)	1003.9(1)	2.16(6)	2	$2^+ \rightarrow 0^+$
2192.6(2)	1188.7(1)	2.08(6)	2	$4^+ \rightarrow 2^+$
2559.2(2)	1555.3(1)	1.75(9)	0	$2^+ \rightarrow 2^+$
	2559(2)	–	0-2	$2^+ \rightarrow 0^+$
3011.4(3)	2007.5(2)	1.2(3)	1	$3 \rightarrow 2^+$
3232.8(8)	1040.2(6)	–	0-2	2-6 $\rightarrow 4^+$
3438.4(3)	2434.5(2)	1.1(4)	1	$3 \rightarrow 2^+$
3511.6(2)	1318.6(6)	1.1(5)	1	$3^+ \rightarrow 4^+$
	2507.7(1)	1.33(8)	1	$3^+ \rightarrow 2^+$
3634.8.7(4)	2631.0(3)	–	0-2	0-4 $\rightarrow 2^+$
3698.7(3)	2694.8(2)	1.0(2)	1	$3 \rightarrow 2^+$
3807.5(4)	1614.9(2)	2.6(4)	2	$6^+ \rightarrow 4^+$
3975(2)	2971(2)	–	0-2	$2 \rightarrow 2^+$
4041.4(6)	1482.2(4)	0.78(18)	1	$3 \rightarrow 2^+$
4113.7(7)	1921.1(5)	0.9(2)	1	$5 \rightarrow 4^+$
4261.6(19)	1701.9(12)	1.2(3)	1	$(3^+) \rightarrow 2^+$
	2069.6(17)	1.9(15)	0-2	$(3^+) \rightarrow 4^+$

Continued on next page

Table 6.4 – *Continued from previous page*

E_x (keV)	E_γ (keV)	R_{DCO}	ΔJ	Assignment
4352.0(6)	840.0(6)	2.8(11)	2	$5^+ \rightarrow 3^+$
	2159.4(4)	1.37(17)	1	$5^+ \rightarrow 4^+$
4394.8(9)	2202.2(7)	1.1(4)	1	$5 \rightarrow 4^+$
4551.7(13)	2359.1(11)	0.9(3)	1	$5 \rightarrow 4^+$
4784(2)	2225(2)	<0.9	1	$3 \rightarrow 2^+$
4851.4(7)	2294(3)	–	0-2	$(2^+) \rightarrow 2^+$
	3847.5(5)	–	0-2	$(2^+) \rightarrow 2^+$
4856.0(17)	2663.4(15)	1.0(6)	1	$5 \rightarrow 4^+$
4973.5(16)	2780.9(14)	1.6(6)	0-2	$2\text{-}6 \rightarrow 4^+$
5080.5(13)	2887.9(11)	–	0-2	$2\text{-}6 \rightarrow 4^+$
5127.0(16)	2934.4(14)	>2.2	2	$2^+,6^+ \rightarrow 4^+$
5177(2)	2618(2)	>2.2	2	$0^+,4^+ \rightarrow 2^+$
5186(2)	2627(2)	1.8(9)	0-2	$0\text{-}4 \rightarrow 2^+$
5239(3)	2680(3)	0.6(4)	1	$1,3 \rightarrow 2^+$
5289.5(21)	937.5(15)	1.6(9)	0-2	$3\text{-}7 \rightarrow 5^+$
5291.2(15)	1482.8(8)	-	0-2	$8^+ \rightarrow 6^+$
5462(3)	1951(3)	<0.9	1	$2,4 \rightarrow 3^+$
5489.6(17)	3297.0(15)	2.7(6)	2	$2^+,6^+ \rightarrow 4^+$
5504.0(17)	3311.4(15)	>1.66	0,2	$2^+,4^+,6^+ \rightarrow 4^+$
5510(2)	1998(2)	<1.25	1	$2,4 \rightarrow 3^+$
5748(3)	1396(2)	0.5(4)	1	$4,6 \rightarrow 5^+$
5782(3)	3589(3)	<1.1	1	$3,5 \rightarrow 4^+$

Continued on next page

Table 6.4 – *Continued from previous page*

E_x (keV)	E_γ (keV)	R_{DCO}	ΔJ	Assignment
5858(3)	1506(2)	<1.66	1	$6^+ \rightarrow 5^+$
	3665(5)	>2.0	2	$6^+ \rightarrow 4^+$
6273.0(21)	2761.4(17)	1.6(7)	0-2	$(5^+) \rightarrow 3^+$
	4076.3(19)	–	0-2	$(5^+) \rightarrow 4^+$

Certain transitions are taken to decay from the same state if the proposed E_x of the levels which they decay from in Table 6.3 fall within each others uncertainty range. The placement of these transitions is verified in most cases by the ΔJ of the transitions implied from the R_{DCO} ratio; this is the case for transitions that decay from the proposed excited states at 3511.6 keV, 4352 keV and 5858 keV. It is also possible to make a more precise spin-parity assignment for these states e.g. for the 5858 keV state, a spin assignment of 6 is in agreement with the ΔJ values for both transitions, but this state can only be a 6^+ state given that transitions with ΔJ=2, such as the 3665-keV transition decaying from this state, are assumed to be E2 transitions.

The proposed state at 4261.6 keV has 1702- and 2070-keV transitions decaying from it to 2^+ and 4^+ states, respectively. The 1702-keV transition has ΔJ=1, implying a spin assignment of 1 or 3 for this state, but the 2070-keV transition has an R_{DCO} value which cannot determine a precise ΔJ value, making any spin assignment between 2 and 6 possible. The transitions are still taken to decay from the same state, with this state tentatively assigned (3^+), as 3 is the only spin assignment in agreement with the possible ΔJ values for both transitions. The 1555-keV transition decaying from the 2559-keV state is strongly observed and thus the state can be assigned confidently solely on this despite no precise ΔJ for the transition to the ground state.

The states at 4851.3 keV and 6273.0 keV also have multiple transitions proposed to decay from them but these assignments are tentative as no precise spin-parity assignment was possible for any of these transitions from angular distribution analysis. The state at 6273.0 keV is

tentatively assigned a spin-parity of (5^+) as its two transitions decay to 4^+ and 3^+ states, making a (5^+) is the most likely spin-parity for this state. The state at 4851.3 keV and its decays are taken as analogous to those seen in Figure 6.1 decaying from the (2^+) state at 4852.2 keV and thus are assigned accordingly in Table 6.4. The 2971-keV transition is assigned without a precise ΔJ in a similar way, being taken as analogous to the 2968-keV transition in Figure 6.1.

Using all experimental outputs presented in this section, a level scheme up to ~6 MeV above the ground state is constructed for ^{60}Zn and is displayed in Figure 6.15.

Fig. 6.15 Full level scheme for ^{60}Zn based on observed gamma decays in this work. All gamma energies are in keV.

6.3 Comparison with Theoretical Calculations and Previous Work

Results obtained from this experiment presented in Section 6.2 are now compared first with known information from previous work and then with theoretical predictions made based on shell-model calculations. This is done with a view to validate the conclusions made from this work but also to produce an enhanced level scheme for ^{60}Zn by using the results seen in this experiment in conjunction with previously known information and theoretical predictions. The nucleus ^{60}Zn is self-conjugate so, in the absence of a well-studied mirror partner, we rely on solely on previous information and shell-model calculations to aid in the interpretation of its structure from experimental results.

6.3.1 Comparison to Previous Work

Table 6.5 presents known information for states below 6 MeV in excitation energy alongside the equivalent information deduced from this work. Newly-observed levels and transitions are marked in **bold** and those observed in previous works but not this work are marked in *italics*. Excited states which are newly discovered by transitions observed here and which cannot be taken as analogous to any previously known state are assigned J^π as per the assignments seen in Table 6.4. Those states which are observed in this work and can be assumed as analogous to previously known states are not automatically assigned J^π based on this work. An interpretive combination of J^π deduced in this work and any J^π assignment of the previously known level is used. These states and their interpretation are discussed below.

Table 6.5 Previously known information about the energetic structure of ^{60}Zn compared to the results seen in this work. The spin-parity (J^π) and energy level (E_x) of the states are presented alongside gamma-ray energies, E_γ, of any transitions decaying from them. [1]: From the work of Mazzocchi et al. [43]. [2]: From the work of Svensson et al. [178]. [3]: From the work of Schubank et al. [193]. [4]: From the work of Pougheon et al. [196]. [5]: From the work of Boucenna et al. [197]. [6]: From the work of Evers et al. [198].

(Previous work)			(Current work)		
J^π	E_x (keV)	E_γ (keV)	J^π	E_x (keV)	E_γ (keV)
2^+ [1]	1003.7(2) [1]	1003.7(2) [1]	2^+	1003.9(1)	1003.9(1)
4^+ [2]	2193.0(5) [2]	1189.2(4) [2]	4^+	2192.6(2)	1188.7(1)
(2^+) [1]	2559.0(5) [1]	1554.9(6) [1]	2^+	2559.2(2)	1555.3(1)
		2559.0(8) [1]		2559(2)	
–	–	–	**3**	**3011.4(3)**	**2007.5(2)**
–	*3034.9(11)* [3]	*2031(1)* [3]	–	–	–
–	3200(100) [4]	–	**2-6**	3232.8(8)	**1040.2(6)**
–	–	–	**3**	**3438.4(3)**	**2434.5(2)**
$2^{(+)}$,$4^{(+)}$ [3] / 3 [6]	3510.3(6) [3]	1318(1) [3]	3^+	3511.6(2)	1318.6(6)
		2506(1) [3]			2507.7(1)
–	*3627.0(11)* [3]	2623(1) [3]	–	–	–
–	–	–	**0-4**	**3634.8.7(4)**	**2631.0(3)**
–	–	–	**3**	**3698.7(3)**	**2694.8(2)**
(4^+) [5]	*3710(50)* [5]	–	–	–	–
6^+ [2]	3808.4(7) [2]	1615.4(5) [2]	6^+	3807.5(4)	1614.9(2)
–	*3812.0(11)* [3]	*2808(1)* [3]	–	–	–
2 [3]	3972.4(8) [3]	462(1) [3]	2	3975(2)	–
		1780(1) [3]			–
		2968(2) [3]			2971(2)

Continued on next page

Table 6.5 – *Continued from previous page*

(Previous work)			(Current work)		
J^π	E_x (keV)	E_γ (keV)	J^π	E_x (keV)	E_γ (keV)
		3971(2) [3]			–
–	–	–	**3**	**4041.4(6)**	**1482.2(4)**
–	–	–	**5**	**4113.7(7)**	**1921.1(5)**
$(0^+),(2^+)$ [6]	*4180(30)* [6]	–	–	–	–
$5^{(+)}$ [3]	*4200.1(8)* [3]	*690(1)* [3]	–	–	–
		2006.8(10) [3]			–
–	–	–	**(3^+)**	**4261.6(19)**	**1701.9(12)**
		–			**2069.6(17)**
$5^{(+)}$ [3]	4351.0(11) [3]	–	5^+	4352.0(6)	**840.0(6)**
		2158(1) [3]			2159.4(4)
(5^-) [5]	4400(50) [5]	–	$5^{(-)}$	4394.8(9)	**2202.2(7)**
–	–	–	**5**	**4551.7(13)**	**2359.1(11)**
$5^{(+)}$ [3]	*4776.0(11)* [3]	2583(1) [3]	–	–	–
–	–	–	**3**	**4784(2)**	**2225(2)**
(2^+) [1]	4852.2(7) [1]	2293.0(10) [1]	(2^+)	4851.4(7)	2294(3)
		3848.3(7) [1]			3847.5(5)
–	–	–	**5**	**4856.0(17)**	**2663.4(15)**
2 [6]	*4913.3(9)* [3]	*1403(1)* [3]	–	–	–
		3909(2) [3]			–
–	–	–	**2-6**	**4973.5(16)**	**2780.9(14)**
–	–	–	**2-6**	**5080.5(13)**	**2887.9(11)**
–	–	–	**$2^+,6^+$**	**5127.0(16)**	**2934.4(14)**

Continued on next page

Table 6.5 – *Continued from previous page*

(Previous work)			(Current work)		
J^{π}	E_x (keV)	E_γ (keV)	J^{π}	E_x (keV)	E_γ (keV)
–	–	–	**0^+,4^+**	**5177(2)**	**2618(2)**
2 [6]	5200(60) [6]	–	(2^+)	5186(2)	**2627(2)**
–	–	–	**1,3**	**5239(3)**	**2680(3)**
8^+ [2]	5292.1(9) [2]	1483.7(6) [2]	8^+	5291.2(15)	1482.8(8)
(7^-) [5]	5300(50) [5]	–	(7^+)	5289.5(21)	**937.5(15)**
$3^{(+)}$,$4^{(+)}$ [3]	*5337.3(11)* [3]	*1827(1)* [3]	–	–	–
		4333(2) [3]			–
–	–	–	**3,5**	**5444(3)**	**3251(3)**
–	–	–	**2,4**	**5462(3)**	**1951(3)**
–	–	–	**2^+,6^+**	**5489.6(17)**	**3297.0(15)**
2 [6]	5503.8(14) [3]	*1531(1)* [3]	2^+	5504.0(17)	–
		–			**3311.4(15)**
–	–	–	**2,4**	**5510(2)**	**1998(2)**
–	–	–	**4,6**	**5748(3)**	**1396(2)**
–	–	–	**3,5**	**5782(3)**	**3589(3)**
–	–	–	**6^+**	**5858(3)**	**1506(2)**
		–			**3665(5)**
–	–	–	**(5^+)**	**6273.0(21)**	**2761.4(17)**
		–			**4076.3(19)**

Ground state band

States up to a J^{π} of 8^{+} are observed in this work in line with the work of Svensson et al [178]. The information for the 2^{+} state is taken from Mazzocchi et al. [43] as it is the most recent, but is also seen by Svensson et al. [178]. The J^{π} assignments made in this work are in agreement with previous work, strengthening their respective assignments, though the spin measurement for the 8^{+} state is not made here.

Structure built upon second 2^{+} state

The tentatively assigned second (2^{+}) state observed by Mazzocchi et al. [43] at 2559 keV is strongly observed in this work via the transition to the 2^{+} state in the GS band. This transition is assigned with $\Delta J=0$ in this work, confirming the tentative (2^{+}) assignment. A weaker transition, direct to the ground state, is also observed in this work. As mentioned previously in Section 5.1, structure built upon this state is important for investigating possible shape coexistence in this nucleus suggested by theory.

As well as new states and transitions decaying to this state, the transitions decaying from the 4852-keV (2^{+}) seen by Mazzocchi et al are observed. No precise spin-parity assignment was possible for this state in this work and remains as the tentative (2^{+}) previously reported. One of the new transitions reported with E_{γ}=2627 keV is taken to decay from the state seen by Evers et al. [198] at 5200 keV, with the energy level of this state detailed in this work consistent with this value and its large uncertainty. In this work, no precise assignment was possible for this state, yielding a possible range of 0-4, while Evers et al. [198] reports a spin of 2, thus this state is tentatively assigned a J^{π} of (2^{+}). The (2^{+}) assignment is favoured as a change of parity is far more unlikely for a low spin $\Delta J=0$ transition such as this.

Structure built upon state at 3510 keV

The state reported at 3510.6 keV by Schubank et al. [193] (at 3520 keV by Evers et al. [198]) is seen in this study (at 3511.6 keV) via the well observed 2507.7-keV transition to the 2^+ state in the GS band, with the transition decaying to the 4^+ state reported by Schubank et al. [193] also seen in this study at 1318.6 keV. Schubank et al. [193] and Evers et al. [198] disagree on the spin-parity of this state, with claims of $2^{(+)}$,$4^{(+)}$ and 3 made by the respective studies. In this work, both transitions decaying out of this state are taken to have $\Delta J=1$, consistent with a 3^+ assignment in agreement with Evers et al. [198], and thus 3^+ quantum numbers for this state are adopted accordingly.

Among the 4 new transitions decaying to this state observed in this work is the 840.0-keV transition taken to decay from the state at 4352.0 keV. This state is previously reported by Schubank et al. [193] along with a transition to the yrast 4^+ state. This transition is also strongly observed in this work (E_γ=2159.4 keV), with $\Delta J=1$ from angular distribution analysis indicating a spin of 5 for this state consistent with the work of Schubank et al. [193]. The 840.0-keV transition decaying to the 3^+ mentioned previously facilitates a $\Delta J=2$ decay, implying a 5^+ assignment for the state which it decays from. This evidence coupled with the energy of this transition falling within 1σ of the energy difference between the two states justifies its placement and the 5^+ assignment given to the state at 4352.0 keV.

Furthermore, 3 new transitions are observed in this work decaying to the 5^+ state at 4352.0 keV. The 937.5-keV transition appears to decay from the (7^-) state seen by Boucenna et al. [197], with the state energy of 5289.5 keV presented in this work well within the large uncertainty bounds from the previously known value. No precise spin-parity assignment was possible for this transition in this work, with any spin assignment from 3-7 possible for the state, based solely on the observation of the gamma rays. Given that the previously reported spin assignment for this state of 7 falls within the range of assignments reported in this experiment, the state is tentatively assigned (7^+). The change to the previously reported negative parity is made

because an assignment of (7^-) would imply an M2/E3 decay, which is usually very unlikely to be observed in in-beam experiments such as this, where lower multipolarity decays dominate.

Other transitions decaying to the 2193 keV 4^+ state

In addition to the previously known transitions already discussed which decay to the 2193.0-keV 4^+ state, 15 new transitions are observed decaying to this state in this work. The 1040.2-keV transition observed in this work is taken to facilitate a decay from a state at 3232.8 keV. This state is taken as analogous to the 3200 keV state seen by Pougheon et al. [196], although no spin-parity is reported by this study and no precise assignment is possible from this work, meaning this state can only be given a spin range between 2 and 6.

A state at 4394.8 keV seen in this work via a newly discovered 2202.2-keV transition to the 4^+ state appears consistent with the (5^-) reported by Boucenna et al. [197]. An angular distribution analysis in this work indicates the 2202.2-keV transition to facilitate a $\Delta J=1$ decay, yielding a spin value consistent with that previously reported. The parity of this state cannot be obtained from this work and thus a spin-parity of $5^{(-)}$ is adopted for this state, with the tentative negative parity assignment taken from Boucenna et al. [197].

Another state observed in this work appearing to be previously known is that seen at 5504.0 keV decaying via a 3311.4-keV transition to the 4^+ state at an excitation energy of 2193.0 keV. This state is observed at 5503.8 keV by Schubank et al. [193] with no spin-parity assignment and at 5520 keV by Evers et al. [198] with a spin of 2. In this work, the 3311.4-keV transition is taken to have $\Delta J=0,2$, implying a spin-parity assignment of 2^+,4^+ or 6^+. Given the previous spin assignment of 2, a spin parity of 2^+ is adopted for this state.

Previously reported states and transitions not observed in this work

While several previously known transitions were observed in this experiment, one can see from Table 6.5 that some transitions and states are not observed in this work. All but two are

reported from the ^{58}Ni(^{3}He,$n\gamma$) study by Schubank et al. [193]. Given the similarity between the experimental setups of that study and this work, this discrepancy would at first be unexpected, but can be explained by the type of target used in the respective experiments. The experiment conducted by Schubank et al. [193] used a natural Ni target, containing only 68% ^{58}Ni, as well as 26% ^{60}Ni, 4% ^{62}Ni and 1% of both ^{61,64}Ni. The target used in this work, on the other hand, was one enriched in ^{58}Ni to over 99% purity. Therefore, it is reasonable to assume that the target used in the work of Schubank et al. [193] was of a significantly lower purity, making it more likely for several other contaminants to be produced, in turn increasing the likelihood of mis-assigned gamma rays.

Figure 6.16 displays the level scheme constructed from the conclusions made in the discussion presented in this section combined with the results reported in Section 6.2.

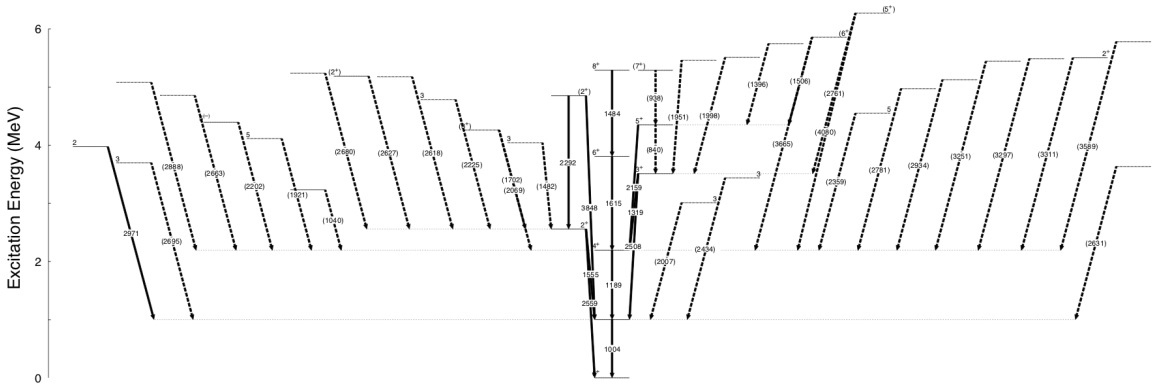

Fig. 6.16 Full level scheme for ^{60}Zn based on observed gamma decays with adopted spin-parity assignments in the present work, supported by previous work. Levels and transitions newly observed in this work are represented by dotted lines and those which were previously known are in solid lines. All gamma energies are in keV.

6.3.2 Comparison to Shell-Model Predictions

In the case of a self-conjugate nucleus, such as ^{60}Zn, comparison to a mirror nucleus is not possible. Therefore, appealing to theoretical models is important when looking to draw firm conclusions about low-lying structures. The shell model is chosen as the theoretical basis for these predictions as opposed to mean-field models referred to in the Coulex experiment previously discussed in this work. The reason for this choice is because here we are interested in higher-lying states close to the proton emission threshold, which are not accessible with mean-field techniques, which are better utilised for low-lying structure. Furthermore, there is interest in the suitability of a ^{56}Ni core for ^{60}Zn.

In this section, the results presented in this work are compared with shell-model calculations performed with the NuShellX code in the jj44pn model space (^{56}Ni core) and using the jj44pna interaction with effective charges of 1.5 and 0.5 for protons and neutrons, respectively. These calculations were performed specifically to be included in this thesis work by another member of the Department of Physics.

A partial level scheme displaying the results of these calculations for levels which can unambiguously be related to experimental counterparts is shown in Figure 6.17a. These can be compared with their experimental counterparts, seen in Figure 6.17b. An immediately obvious difference in the structures from these calculations with respect to the experimental results is the yrast band decaying to the second 2^+ state. It is assumed that the shell model does not predict the correct energy ordering for the two lowest-lying 2^+ states. This is an assumption supported by the structure built upon these two states. The structure predicted by the shell model to be built upon the "first" 2^+ state at 1709 keV is similar to that in experiment built upon the second 2^+ state at 2559 keV and the structure above the predicted "second" 2^+ state at 1898 keV is similar to that above the experimental first 2^+ state at 1004 keV.

The shell-model predictions also reproduce the first 3^+ state, decaying to the 2^+ and 4^+ states in the ground state band, and this can be taken as analogous to the state observed at

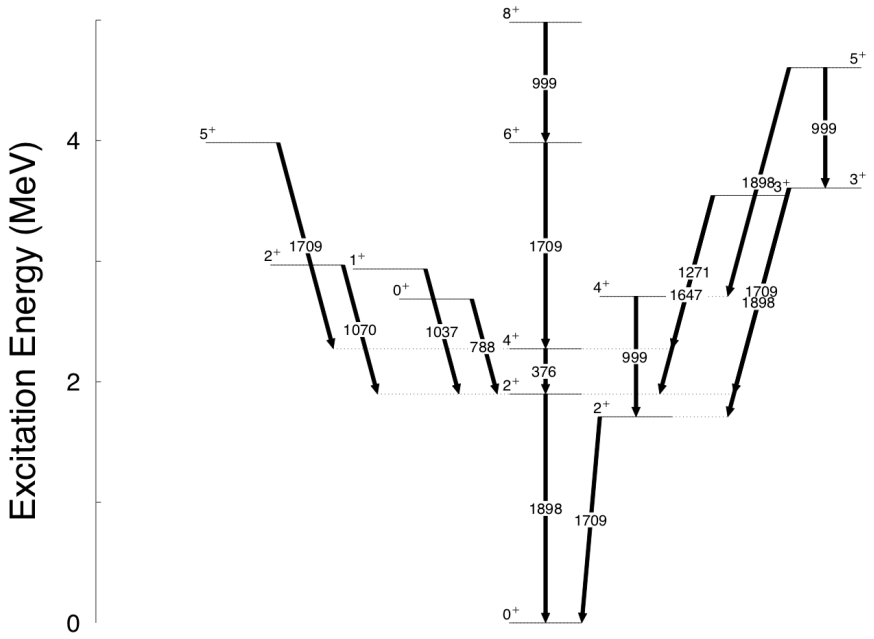

(a) Partial level scheme for ^{60}Zn based on NuShellX shell-model calculations. All transition energies are in keV.

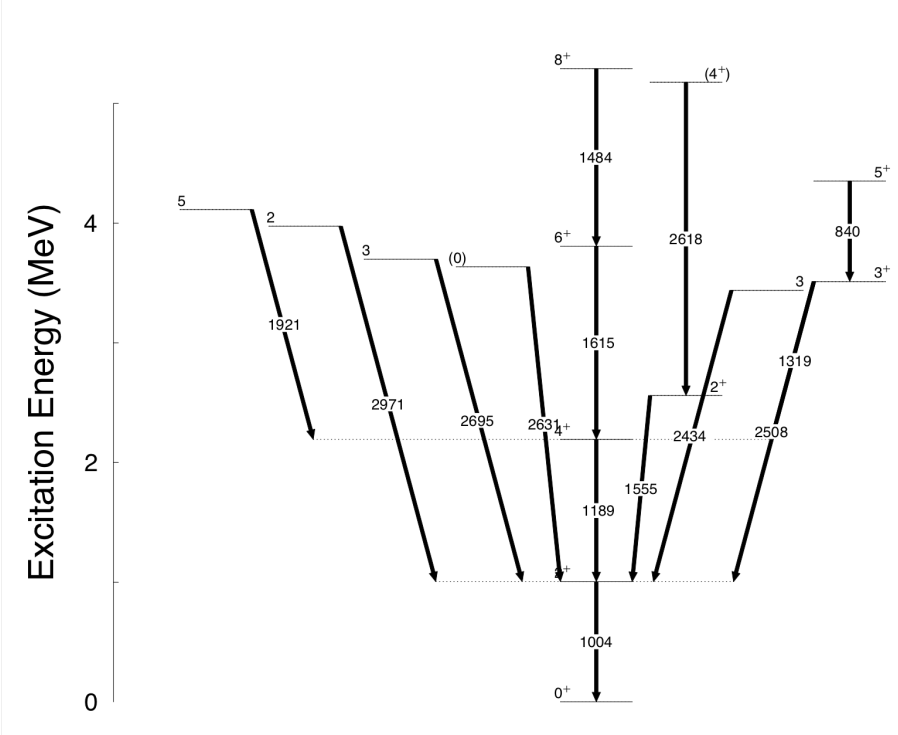

(b) Partial level scheme for ^{60}Zn based on experimental work. All transition energies are in keV.

Fig. 6.17 Partial level schemes displaying states which can be seen in both the theoretical predictions and experimental results.

3511.6 keV. Similar to the case of the first and second 2^+ states, it appears that the shell model also incorrectly predicts the energy ordering for the similar energy 3^+ states, with the higher lying 5^+ state (taken as analogous to the experimentally observed 4352-keV state) decaying to the higher energy 3^+ state which decays to both 2^+ states as opposed to the first 3^+ state as observed in experiment. This second 3^+ state is more difficult to pair with an experimental counterpart as no states which could have this spin are observed to decay to both 2^+ states; it could feasibly be paired with the state experimentally observed at 3438.4 keV, with the transition to the second 2^+ possibly too weak to be observed in this experiment.

States predicted by these shell-model calculations are successfully paired with experimentally observed states at similar energies, spin parity and gamma-decay branches. However, the energy difference between the levels generally disagree. This discrepancy stems from the overestimation of the excitation energy of ground state band 2^+ state (predicted at 1898 keV but observed at 1004 keV) and the underestimation of side-band 2^+ state (predicted at 1709 keV but observed at 2559 keV).

The shell-model predictions using the parameters mentioned previously are somewhat able to describe of the low-lying structure of the self-conjugate nucleus ^{60}Zn, with some newly observed states predicted reasonably well. These calculations are not fully in agreement with experiment, due to the use of the relatively soft ^{56}Ni core for nuclei in this region. It should be noted that calculations in this region using an alternative core, such as ^{40}Ca, may be more appropriate. These will, however, require a significantly larger model space and, therefore, computational time.

6.4 Astrophysical ^{59}Cu(p,γ) Reaction Rate

Although not the primary goal of this work, it is possible to gain insight into the ^{59}Cu(p,γ) reaction as gamma decays are observed from states above the proton emission threshold. Properties of proton-unbound states in ^{60}Zn can be used to evaluate the ^{59}Cu(p,γ) reaction rate in order to better understand the shape and structure of X-ray burst light curves. Specifically, low-spin states which correspond to low-l proton captures (i.e. where a proton with a small amount of angular momentum captures onto a nucleus) on the 3/2$^-$ ground state of ^{59}Cu are expected to play a decisive role.

The reaction rate, r_{aX}, of a nuclear reaction $a+X \rightarrow Y+b$, or $X(a,b)Y$, in a stellar environment can be expressed by,

$$r_{\mathrm{aX}} = N_{\mathrm{a}} N_{\mathrm{X}} \left(\frac{8}{\pi\mu}\right)^{\frac{1}{2}} \frac{1}{(kT)^{\frac{3}{2}}} \int_0^{\infty} \sigma(E)\cdot E \cdot \exp\left(-\frac{E}{kT}\right) dE \tag{6.3}$$

where N_{a} and N_{X} are the number of particles of a and X, respectively, μ is the reduced mass of the system, $\mu = m_{\mathrm{a}} m_{\mathrm{X}}/(m_{\mathrm{a}}+m_{\mathrm{X}})$, k is the Boltzmann constant, T is the temperature of the stellar environment, E is the energy and $\sigma(E)$ is the energy dependent cross section.

Resonant reactions occur through an excited state of a compound nucleus, C^*, such that $a+X \rightarrow C^* \rightarrow Y+b$ where C^* is at energy E_{x}. At astrophysical temperatures, $X(p,\gamma)Y$ reactions are dominated by captures to resonances close to the proton emission threshold. These resonances can only occur if conservation of angular momentum and parity are maintained. For $X(p,\gamma)Y$ resonances, the spin of the resonant state $J_{\mathrm{C}} = J_{\mathrm{X}} + J_{\mathrm{p}} + l$, where J_{X} is the spin of the ground state of X, J_{p} is the spin of a proton (1/2) and l is the angular momentum for proton capture. Similarly, the parity of the resonant state $\pi(J_C) = \pi(J_X)\cdot\pi(J_p)\cdot(-1)^l$, where $\pi(J_X)$ is the parity of a and $\pi(J_p)$ is the parity of a proton (+1). In the ^{59}Cu(p,γ) reaction, resonance states must satisfy spin condition $J_{\mathrm{C}} = 3/2 + 1/2 + l = l + 2$, hence why low-spin states in ^{60}Zn correspond to low-l proton captures.

The reaction rate, r_{pX}, for $X(p,\gamma)Y$ where narrow isolated resonances dominate, can be given by,

$$r_{\mathrm{pX}} = N_{\mathrm{p}} N_{\mathrm{X}} \left(\frac{2\pi}{\mu kT}\right)^{\frac{3}{2}} \hbar^2 \sum_i (\omega\gamma)_i \exp\left(-\frac{E_i}{kT}\right) \tag{6.4}$$

where new variables $\omega\gamma_i$ and E_{i} are the resonance strength (defined in Equation 6.5) and resonance energy ($E_{\mathrm{x}} - S(p)_{\mathrm{C}}$) of each resonance contributing to the stellar reaction rate. For Equation 6.5, Γ_p and Γ_γ are the proton and γ-ray partial widths.

$$\omega\gamma = \frac{2J_C+1}{(2J_x+1)(2J_p+1)} \frac{\Gamma_p \Gamma_\gamma}{\Gamma_p + \Gamma_\gamma} \tag{6.5}$$

The low-energy resonant states which are relevant to the reaction rate will typically have large γ-decay branches such that $\Gamma_p \ll \Gamma_\gamma$. One can thus simplify Equation 6.5 such that $\omega\gamma = \omega\Gamma_p$. The proton partial width, Γ_p, is dependent on the spectroscopic factor, C^2S, and the single particle width, Γ_{sp}, as given in Equation 6.6. Γ_{sp} is defined in Equation 6.7, where m is the mass of the particle, R is the nuclear radius (as described in Section 2.2.1), P_C is the proton penetrability and θ_{sp} is the dimensionless single-particle width.

$$\Gamma_p = C^2 S \Gamma_{sp} \tag{6.6}$$

$$\Gamma_{sp} = 2\frac{\hbar^2}{mR^2} P_C \theta_{sp}^2 \tag{6.7}$$

It is clear from this brief discussion that the astrophysical reaction rate is dependent on properties of proton-unbound states in ^{60}Zn including excitation energy and relevant resonance energy, spin-parity and spectroscopic factor. While this study has discovered multiple new states above the proton emission threshold at S_p = 5105.0(4) keV [179] (listed in Table 6.6), in general, definitive spin-parity assignments are not possible, therefore the ^{59}Cu(p,γ) reaction rate cannot be evaluated to the level of precision required for X-ray burst nucleosynthesis

models. Given the high level density in this energy region, the imprecise spin assignments of the majority of these levels as seen in this work would lead to proton penetrabilities varying by several orders of magnitude based on the different potential spin assignments of all these states. This, together with the unknown proton spectroscopic factors, would lead to resonant strengths that are uncertain by several orders of magnitude. Furthermore, the unconfirmed potential for shape coexistence in this nuclei leads to further uncertainty in the reaction rate, since bands built upon potential shape coexisting states will further increase the level density in the astrophysical burning region. As well as this, low-lying 0^+ states are potential isomers and thus potentially extra states to which proton capture can occur.

Table 6.6 Properties of proton-unbound resonant states in ^{60}Zn observed in this work. J^π is the spin-parity assignment based on this work, E_x the level energy, E_γ the transition energy for decays from the state and E_r the resonance energy relative to the ^{59}Cu+p threshold at 5105 keV [179].

J^π	E_x (keV)	E_r (keV)	E_γ (keV)
2^+,6^+	5127.0(16)	22(2)	2934.4(14)
0^+,4^+	5177(2)	73(3)	2618(2)
(2^+)	5186(2)	81(3)	2627(2)
1,3	5239(3)	134(4)	2680(3)
(7^-)	5289.5(21)	184(3)	937.5(15)
3,5	5444(3)	339(4)	3251(3)
2,4	5462(3)	357(4)	1951(3)
2^+,6^+	5489.6(17)	385(2)	3297.0(15)
2	5504.0(17)	399(2)	3311.4(15)
2,4	5510(2)	405(3)	1998(2)
4,6	5748(3)	643(4)	1396(2)
3,5	5782(3)	677(4)	3589(3)
6^+	5858(3)	753(4)	1506(2)
			3665(5)
5^+	6271(4)	1166(5)	4076.3(19)
			2761.4(17)

Nevertheless, the first observation of these gamma decays enables some conclusions to be drawn on the level density beyond the proton emission threshold, with the level density observed in this work roughly in agreement with the recent work of Soltesz et al. [199]. This

paves the way for future work, such as an angle-integrated ^{59}Cu(d,n) measurement which can identify the states with large spectroscopic factors, C^2S, that play a key role in the astrophysical ^{59}Cu(p,γ) reaction rate. Such a study could be performed with the GRETINA + S800 setup at the National Superconducting Cyclotron Laboratory (NSCL)/FRIB. Studies of this type have been successfully used in the past to identify key resonances in several reactions of astrophysical interest [200–203], once the key gamma rays have been identified.

In addition, the data and analysis reported here are being combined with a further study of ^{60}Zn performed with Gammasphere at ANL using the microball and neutron wall ancillary detectors. These data are in the final stages of analysis and a publication combining both sets of data that will likely significantly reduce the uncertainty in the ^{59}Cu(p,γ) reaction rate will be prepared shortly. This work relies, critically, on the additional information on the low-lying structure of ^{60}Zn revealed in this thesis.

Chapter 7

Conclusion and Outlook

7.1 Conclusions and Outlook: Low-Energy Coulomb Excitation of ^{72}Se

A low-energy Coulomb-excitation experiment was performed at the HIE-ISOLDE facility at CERN using a beam of radioactive ^{72}Se ions, with the goal of obtaining a detailed set of nuclear matrix elements to describe its low-lying structure. This experiment was performed with two targets, ^{208}Pb and ^{196}Pt, with the majority of data expected to be collected with the ^{208}Pb target. However, due to technical difficulties with the zirconium oxide production target, the radioactive beam intensity delivered was only a fraction of what was expected. As a result, the total statistics collected with the ^{208}Pb target was significantly less than anticipated, with only a single transition in ^{72}Se observed.

Information that could be obtained on the matrix elements connecting low-lying states in ^{72}Se from this experiment was more limited than first expected. No model-independent measurement was possible using the ^{208}Pb target data, but using the data from the ^{196}Pt target, it was possible to deduce the quadrupole moment of the 2_1^+ state with just a single ^{72}Se transition observed, via the target normalisation method. This was achievable as ^{196}Pt has

well-established low-lying structure and precisely known spectroscopic data. Furthermore, 3 transitions from this nucleus were observed in the experiment. Quadrupole moments are attainable from these experiments given the angular dependence of the cross section due to the reorientation effect, with the gamma-ray yield measured for different angular ranges of the scattered particle. All values for matrix elements and quadrupole moments reported in this work are in units of eb.

The quadrupole moment for the 2_1^+ state in ^{72}Se was found to be $Q_s(2_1^+) = -0.24^{+0.13}_{-0.22}$, implying a prolate configuration, in agreement, at the 1σ level, with the other experimentally reported value by Henderson et al of $-0.57^{+0.29}_{-0.29}$ [167], but with a significantly reduced uncertainty. This outcome confirms that the shape change between prolate and oblate shapes does not occur until at least ^{70}Se in the selenium isotopic chain. The transitional matrix element deduced from this experiment, $\langle 2_1^+ | E2 | 0_1^+ \rangle = 0.510^{+0.055}_{-0.025}$, is also within the 1σ limit of the literature value [170].

As well as the single transition in ^{72}Se, a transition from a beam contaminant, deduced to be ^{68}Ge, is observed. This represents the first post-acceleration of a radioactive neutron-deficient Ge isotope at an ISOL facility and is due to its extraction from the ion source as a 68GeS molecule. The quadrupole moment of the 2_1^+ state in ^{68}Ge is deduced in a similar fashion to that for ^{72}Se. The first experimentally-deduced value, $Q_s(2_1^+) = -0.39^{+0.33}_{-0.17}$, again implies prolate configuration, as in the ^{72}Se case.

Theoretical predictions made for the quadrupole moment for the 2_1^+ state in ^{72}Se using several different models are in contradiction, with the prolate configuration for this state reported in this work in agreement with calculations utilising beyond mean-field approaches but in disagreement with interacting boson model (IBM) calculations. This result reinforces the suitability of beyond mean-field approaches for regions of the nuclear chart where shape transitions are anticipated to occur.

The analysis reported here has resulted in an accepted follow-up Coulomb-excitation experiment, with a view to obtaining a greater set of E2 matrix elements connecting low-lying states in selenium isotopes - ideal for the further testing of theoretical models. Outlook into the nuclear structure and shape coexistence in neutron-deficient selenium isotopes can also be provided by neutron transfer reactions, specifically two-neutron transfer reactions, which can allow for the determination of the shape evolution for 0^+ states across the isotopic chain. A ^{74}Se(p,t)^{72}Se reaction study could provide valuable additional information and serve as an interesting follow-up to this work and to future Coulomb excitation studies. In such a study, a high-energy ^{74}Se beam would be directed onto a target containing protons, such as CH_2, and tritons produced from the resulting two-neutron transfer (p,t) reaction would be detected by silicon detectors at forward lab angles. Such reactions have proven difficult in the past for several reasons. For example, the Q-value tends to be quite high (Q = -11.979106 MeV / nucleon for this specific reaction). But with the development of higher energy and intensity accelerators and advancements in technology, performing these reactions are a more realistic possibility. A feasibility study into this potential experiment, where the reaction is simulated, is presented in Appendix A.

7.2 Conclusions and Outlook: Gamma-Ray Spectroscopy of the (N = Z) Nucleus ^{60}Zn

The light-ion fusion-evaporation reaction reported in this work allowed for the observation of a multitude of new states and transitions in the previously poorly known low-lying structure of ^{60}Zn. Previously unknown structures built above the second 2^+ state and yrast 3^+ are discovered, as well as several new states with transitions decaying to the 2^+ state of the ground state band. While the 0_2^+ was not observed here, the firm assignment for the second 2^+ state will provide critical information for further experiments to test the predicted shape changes and coexistence of prolate- and oblate-deformed structures in this region of the nuclear chart.

Limited statistics prohibited a comprehensive angular distribution analysis where the intensity of the observed gamma rays at given angles is plotted as a function of emission angle. Therefore, an alternative analysis where the ratio of counts seen for a particular transition at the most forward and the most backward angles is conducted. This analysis has lead to more precise spin-parity assignments of previously known states, as well as precise assignments for some of the newly-observed states.

The results presented in this work generally agree with the limited information from previous work and is able to enhance and build upon this previously reported data in most cases. Not all states and transitions detailed in other studies are observed in this work. However, it is wort noting that these states are only reported in one previous study which was performed with gamma-ray detectors with limited resolution and without enriched target material. Shell-model predictions are able to tentatively predict parts of the low-lying structure of ^{60}Zn observed in experiment, with some newly observed states being paired with states predicted by theory. These calculations are not fully in agreement with experiment, however, bringing into question the ability for these type of theoretical models to make predictions for nuclei in this region.

In addition to the extension of the low-lying level structure of ^{60}Zn, several gamma decays were observed from states above the proton-emission threshold. Some of these states could correspond to resonances in the ^{59}Cu(p,γ) reaction rate, which play a key role in the shape of X-ray burst light curves. With this in mind, a dedicated experiment performed at ANL with Gammasphere coupled to the neutron shell and microball ancillary detectors was recently performed to obtain further information on these proton-unbound gamma-decay states, such as more precise resonance energies and spin-parity assignments. This work is in the final stages of analysis and will be combined with the (^{3}He,n) study reported here to provide the most comprehensive experimental description of ^{60}Zn up to the region relevant for explosive hydrogen burning. Furthermore, a ^{59}Cu(d,n) integrated cross section measurement was recently accepted to be performed at the FRIB facility. This will be conducted with a view to constraining spectroscopic factors in this energy region of ^{60}Zn, allowing for a more precise estimation of the astrophysical ^{59}Cu(p,γ) reaction rate. Studies of this type rely on existing knowledge of gamma rays from the unbound states of interest, such as those reported here.

References

[1] G. Gamow. Mass defect curve and nuclear constitution. *Proceedings of the Royal Society of London. Series A*, 126(803):632–644, 1930.

[2] C. F. Weizsäcker. Examination of the possibility of a fluid-mechanics treatment of dense granular flows. *Zeitschrift für Physik*, 96(7–8):431–458, 1935.

[3] James Rainwater. Nuclear energy level argument for a spheroidal nuclear model. *Phys. Rev.*, 79:432–434, Aug 1950.

[4] S.G. Nilsson. Binding states of individual nucleons in strongly deformed nuclei. *Kgl. Danske Videnskab. Selskab., Mat.-fys Medd.*, 29(16):3–48, 1955.

[5] Gertrude Scharff-Goldhaber and J. Weneser. System of even-even nuclei. *Phys. Rev.*, 98:212–214, Apr 1955.

[6] Toshio Marumori, Toshihide Maskawa, Fumihiko Sakata, and Atsushi Kuriyama. Self-Consistent Collective-Coordinate Method for the Large-Amplitude Nuclear Collective Motion. *Progress of Theoretical Physics*, 64(4):1294–1314, 10 1980.

[7] J. C. Slater. Note on Hartree's method. *Phys. Rev.*, 35:210–211, Jan 1930.

[8] V. Fock. Näherungsmethode zur lösung des quantenmechanischen mehrkörperproblems. *Zeitschrift für Physik*, 61(1):126–148, Jan 1930.

[9] Douglas Rayner Hartree and W. Hartree. Self-consistent field, with exchange, for beryllium. *Proceedings of the Royal Society of London. Series A - Mathematical and Physical Sciences*, 150(869):9–33, 1935.

[10] N. N. Bogoljubov. On a new method in the theory of superconductivity. *Il Nuovo Cimento (1955-1965)*, 7(6):794–805, Mar 1958.

[11] J. H. Hamilton, A. V. Ramayya, W. T. Pinkston, R. M. Ronningen, G. Garcia-Bermudez, H. K. Carter, R. L. Robinson, H. J. Kim, and R. O. Sayer. Evidence for coexistence of spherical and deformed shapes in ^{72}Se. *Phys. Rev. Lett.*, 32:239–243, Feb 1974.

[12] J. P. Delaroche. Private Communication, 2014.

[13] Nobuo Hinohara, Takashi Nakatsukasa, Masayuki Matsuo, and Kenichi Matsuyanagi. Microscopic description of oblate-prolate shape mixing in proton-rich se isotopes. *Phys. Rev. C*, 80:014305, Jul 2009.

[14] K. Kaneko, M. Hasegawa, and T. Mizusaki. Shape transition and oblate-prolate coexistence in $n = z$ fpg-shell nuclei. *Phys. Rev. C*, 70:051301, Nov 2004.

[15] V. Elomaa, T. Eronen, U. Hager, and et al. Light-ion-induced reactions in mass measurements of neutron-deficient nuclides close to A = 100. *Eur. Phys. A*, 40:1–9, Mar 2009.

[16] I. Angeli and K.P. Marinova. Table of experimental nuclear ground state charge radii: An update. *Atomic Data and Nuclear Data Tables*, 99(1):69 – 95, 2013.

[17] W. L. Bragg. The arrangement of atoms in crystals. *The London, Edinburgh, and Dublin Philosophical Magazine and Journal of Science*, 40(236):169–189, 1920.

[18] E. Rutherford. Lxxix. the scattering of α and β particles by matter and the structure of the atom. *The London, Edinburgh, and Dublin Philosophical Magazine and Journal of Science*, 21(125):669–688, 1911.

[19] W. Bothe and H. Becker. Künstliche erregung von kern-γ-strahlen. *Zeitschrift für Physik*, 66(5):289–306, May 1930.

[20] J. Chadwick. Possible existence of a neutron. *Nature*, 129:312, 1932.

[21] J. J. Thomson. Xl. cathode rays. *The London, Edinburgh, and Dublin Philosophical Magazine and Journal of Science*, 44(269):293–316, 1897.

[22] R. A. Millikan. On the elementary electrical charge and the avogadro constant. *Phys. Rev.*, 2:109–143, Aug 1913.

[23] G. L. Greene, E. G. Kessler, R. D. Deslattes, and H. Börner. New determination of the deuteron binding energy and the neutron mass. *Phys. Rev. Lett.*, 56:819–822, Feb 1986.

[24] James Clark Maxwell. *A Treatise on Electricity and Magnetism*, volume 2, pages 128–437. Clarendon Press, Oxford, 1873.

[25] Charles-Augustin de Coulomb. Premier mémoire sur l'électricité et le magnétisme. *Histoire de l'Académie Royale des Sciences*, page 569–577, 1785.

[26] A. Einstein and M. Grossmann. Covariance properties of the field equations of the theory of gravitation based on the generalized theory of relativity. *Zeitschrift für Mathematik und Physik*, 64:215–225, 1915.

[27] E. Fermi. Versuch einer theorie der β-strahlen. I. *Zeitschrift für Physik*, 88(3):161–177, Mar 1934.

[28] S. Glashow. The renormalizability of vector meson interactions. *Nucl. Phys.*, 107, 1959.

[29] Abdus Salam and J. C. Ward. Weak and electromagnetic interactions. *Il Nuovo Cimento (1955-1965)*, 11(4):568–577, Feb 1959.

[30] Steven Weinberg. A model of leptons. *Phys. Rev. Lett.*, 19:1264–1266, Nov 1967.

[31] Murray Gell-Mann. Symmetries of baryons and mesons. *Phys. Rev.*, 125:1067–1084, Feb 1962.

[32] Bruno R. Stella and Hans-Jürgen Meyer. Υ(9.46 Gev) and the gluon discovery (a critical recollection of pluto results). *The European Physical Journal H*, 36(2):203, Oct 2011.

[33] Ch. Berger, W. Lackas, F. Raupach, W. Wagner, G. Alexander, L. Criegee, H.C. Dehne, K. Derikum, R. Devenish, G. Flügge, G. Franke, Ch. Gerke, E. Hackmack, P. Harms, G. Horlitz, Th. Kahl, G. Knies, E. Lehmann, B. Neumann, R.L. Thompson, U. Timm, P. Waloschek, G.G. Winter, S. Wolff, W. Zimmermann, O. Achterberg, V. Blobel, L. Boesten, H. Daumann, A.F. Garfinkel, H. Kapitza, B. Koppitz, W. Lührsen, R. Maschuw, H. Spitzer, R. Van Staa, G. Wetjen, A. Bäcker, S. Brandt, J. Bürger, C. Grupen, H.J. Meyer, G. Zech, H.J. Daum, H. Meyer, O. Meyer, M. Rössler, and K. Wacker. Jet analysis of the Υ(9.46) decay into charged hadrons. *Physics Letters B*, 82(3):449 – 455, 1979.

[34] H. Yukawa. *Proc. Phys.-Math. Soc. Jpn.*, 17:48, 1935.

[35] C. M. G. Lattes, H. Muirhead, G. P. S. Occhialini, and C. F. Powell. Processes inolving charged mesons. *Nature*, 159:694–697, 1947.

[36] Xiangdong Ji. Qcd analysis of the mass structure of the nucleon. *Phys. Rev. Lett.*, 74:1071–1074, Feb 1995.

[37] Hans F. Ehrenberg, Robert Hofstadter, Ulrich Meyer-Berkhout, D. G. Ravenhall, and Stanley E. Sobottka. High-energy electron scattering and the charge distribution of Carbon-12 and Oxygen-16. *Phys. Rev.*, 113:666–674, Jan 1959.

[38] J. Heisenberg, R. Hofstadter, J. S. McCarthy, I. Sick, B. C. Clark, R. Herman, and D. G. Ravenhall. Elastic electron scattering by ^{208}Pb and new information about the nuclear charge distribution. *Phys. Rev. Lett.*, 23:1402–1405, Dec 1969.

[39] Roger C Barrett and Daphne F Jackson. *Nuclear sizes and structure*. Clarendon Press, Oxford, 1977.

[40] Kenneth S Krane. *Introductory nuclear physics*. Wiley, New York; Chichester, 1988.

[41] T. Suzuki, H. Geissel, O. Bochkarev, L. Chulkov, M. Golovkov, N. Fukunishi, D. Hirata, H. Irnich, Z. Janas, H. Keller, T. Kobayashi, G. Kraus, G. Münzenberg, S. Neumaier, F. Nickel, A. Ozawa, A. Piechaczeck, E. Roeckl, W. Schwab, K. Sümmerer, K. Yoshida, and I. Tanihata. Nuclear radii of Na and Mg isotopes. *Nuclear Physics A*, 630(3):661 – 677, 1998.

[42] G. Royer. On the coefficients of the liquid drop model mass formulae and nuclear radii. *Nuclear Physics A*, 807(3):105 – 118, 2008.

[43] C. Mazzocchi, Z. Janas, and J et al. Döring. First measurement of β-decay properties of the proton drip-line nucleus 60Ga. *Eur. Phys. A*, 12:269–277, Nov 2001.

[44] P J Nolan and J F Sharpey-Schafer. The measurement of the lifetimes of excited nuclear states. *Reports on Progress in Physics*, 42(1):1–86, jan 1979.

[45] David C. Camp. Energy levels in 72Ge from the decays of 72Ga and 72As. *Nuclear Physics A*, 121(3):561 – 591, 1968.

[46] AZ Schwarzschild and EK Warburton. The measurement of short nuclear lifetimes. *Annual review of nuclear science*, 18(1):265–290, 1968.

[47] P. A. M. Dirac. A new notation for quantum mechanics. *Mathematical Proceedings of the Cambridge Philosophical Society*, 35(3):416–418, 1939.

[48] V. F. Weisskopf. Radiative transition probabilities in nuclei. *Phys. Rev.*, 83:1073–1073, Sep 1951.

[49] Kurt Alder and Aage Winther. *Electromagnetic excitation : theory of Coulomb excitation with heavy ions*. North-Holland Publishing Co. (etc.), Amsterdam ; Oxford, 1975.

[50] Sir Ernest Rutherford F.R.S. and E.N. da C. Andrade B.Sc. Ph.D. XCIV. The wave-length of the soft γ rays from radium B. *The London, Edinburgh, and Dublin Philosophical Magazine and Journal of Science*, 27(161):854–868, 1914.

[51] P. Villard. Sur la reflexion et la refraction de rayons cathodiques et des rayons deviables du radium. *Comptes rendus*, 130:1010–1011, 1900.

[52] M. M. Villard. Sur le rayonnement du radium. *C. R. Acad. Sci. Paris*, 130:1178, 1900.

[53] E. Rutherford M.A. D.Sc. XV. The magnetic and electric deviation of the easily absorbed rays from radium. *The London, Edinburgh, and Dublin Philosophical Magazine and Journal of Science*, 5(26):177–187, 1903.

[54] J. Tinsley Oden. Electromagnetic waves. In *An Introduction to Mathematical Modeling*, pages 73–92. John Wiley & Sons, Inc., Hoboken, NJ, USA, 2011.

[55] J. O. Hirschfelder, J. L. Magee, and M. H. Hull. The penetration of gamma-radiation through thick layers I. Plane geometry, Klein-Nishina scattering. *Phys. Rev.*, 73:852–862, Apr 1948.

[56] H. Hertz. Ueber einen einfluss des ultravioletten lichtes auf die electrische entladung. *Annalen der Physik*, 267(8):983–1000, 1887.

[57] A. Einstein. On a heuristic point of view concerning the production and transformation of light. *Annalen der Physik*, 17:132–148, 1905.

[58] R. A. Millikan. A direct determination of "*h*.". *Phys. Rev.*, 4:73–75, Jul 1914.

[59] Arthur H. Compton. A quantum theory of the scattering of x-rays by light elements. *Phys. Rev.*, 21:483–502, May 1923.

[60] Patrick Maynard Stuart Blackett, Giuseppe Paolo Stanislao Occhialini, and Ernest Rutherford. Some photographs of the tracks of penetrating radiation. *Proceedings of the Royal Society of London. Series A, Containing Papers of a Mathematical and Physical Character*, 139(839):699–726, 1933.

[61] J. Chadwick, P. M. S. Blackett, and G. Occhialini. New evidence for the positive electron. *Nature*, 131:473, 1933.

[62] John M. (John Markus) Blatt. *Theoretical nuclear physics*. Wiley ; Chapman & Hall, New York : London, 1952.

[63] John M. (John Markus) Blatt and Victor F. Weisskopf. *Theoretical nuclear physics*. Springer-Verlag, New York, 1979.

[64] E. U Condon. *Theory of atomic spectra*. Cambridge University Press, Cambridge, 1935.

[65] M. E. Rose. *"Theory of Internal Conversion", in Alpha-, beta- and gamma-ray spectroscopy*, pages 887–905, ed. by K. Siegbahn. North-Holland, Amsterdam, 1968.

[66] William D Myers and W.J Swiatecki. Average nuclear properties. *Annals of Physics*, 55(3):395–505, 1969.

[67] Jm Wang, Hf Zhang, and Jq Li. Predictions for alpha-decay half-lives of heavy and superheavy elements with a generalized liquid drop model. *Journal Of Physics G-Nuclear And Particle Physics*, 41(7):075109, 2014.

[68] G. Brown, T. T. S Kuo, and J. W. Holt. *The nucleon-nucleon interaction and the nuclear many-body problem : selected papers of Gerald E. Brown and T. T. S. Kuo*. World Scientific Publishing Co Pte Ltd, 2010.

[69] E. Gapon and D. Iwanenko. Zur bestimmung der isotopenzahl. *Naturwissenschaften*, 20(43):792–793, Oct 1932.

[70] Elsasser, W.M. Sur le principe de pauli dans les noyaux - III. *J. Phys. Radium*, 5(12):635–639, 1934.

[71] Maria G. Mayer. On closed shells in nuclei. *Phys. Rev.*, 74:235–239, Aug 1948.

[72] Maria Goeppert Mayer. On closed shells in nuclei II. *Phys. Rev.*, 75:1969–1970, Jun 1949.

[73] Otto Haxel, J. Hans D. Jensen, and Hans E. Suess. On the "magic numbers" in nuclear structure. *Phys. Rev.*, 75:1766–1766, Jun 1949.

[74] M. G. Mayer and J. H. D. Jensen. *Elementary theory of nuclear shell structure*. Wiley, 1955.

[75] A.H. Wapstra and K. Bos. The 1977 atomic mass evaluation: in four parts. *Atomic Data and Nuclear Data Tables*, 19(3):175 – 297, 1977.

[76] W. Pauli. Über den zusammenhang des abschlusses der elektronengruppen im atom mit der komplexstruktur der spektren. *Zeitschrift für Physik*, 31(1):765–783, Feb 1925.

[77] W. Pauli. The connection between spin and statistics. *Phys. Rev.*, 58:716–722, Oct 1940.

[78] W. N. Cottingham and D. A. Greenwood. *An Introduction to Nuclear Physics*. Cambridge University Press, 2 edition, 2001.

[79] H. A. Bethe and R. F. Bacher. Nuclear physics A. stationary states of nuclei. *Rev. Mod. Phys.*, 8:82–229, Apr 1936.

[80] Roger D. Woods and David S. Saxon. Diffuse surface optical model for nucleon-nuclei scattering. *Phys. Rev.*, 95:577–578, Jul 1954.

[81] N. Schwierz, I. Wiedenhover, and A. Volya. Parameterization of the Woods-Saxon potential for shell-model calculations. *arXiv:0709.3525 [nucl-th]*, Oct 2018.

[82] T. Potter. 'Structure of nuclei'. [Online] Accessible: https://www.hep.phy.cam.ac.uk/~chpotter/particleandnuclearphysics/Lecture_14_StructureOfNuclei.pdf.

[83] '22.02 introduction to applied nuclear physics - 5. nuclear structure'. [Online] Accessible: https://ocw.mit.edu/courses/nuclear-engineering/22-02-introduction-to-applied-nuclear-physics-spring-2012/lecture-notes/MIT22_02S12_lec_ch5.pdf.

[84] T. D. Newton. On the spherical oscillator nucleus. *Canadian Journal of Physics*, 37(8):944–964, 1959.

[85] T. D. Newton. Energy levels of a completely anisotropic oscillator. *Canadian Journal of Physics*, 38:700, 1960.

[86] R. F. (Richard F.) Casten. *Nuclear structure from a simple perspective*. Oxford studies in nuclear physics. Oxford University Press, New York ; Oxford, 1990.

[87] 'Deformed (Nilsson) shell model'. [Online] Accessible: hhttps://web-docs.gsi.de/~wolle/TELEKOLLEG/KERN/LECTURE/Fraser/L9.pdf.

[88] B.R. Mottelson and S.G. Nilsson. The intrinsic states of odd-A nuclei having ellipsoidal equilibrium shape. *Kgl. Danske Videnskab, Selskab. Mat.-fys. Skrifter*, 1(8), 1959.

[89] Niels Bohr and Fritz Kalckar. On the transmutation of atomic nuclei by impact of material particles. *Kgl. Danske Videnskab. Selskab., Mat.-fys Medd.*, 14(10), 1937.

[90] Aage Bohr. The coupling of nuclear surface oscillations to the motion of individual nucleons. *Kgl. Danske Videnskab. Selskab., Mat.-fys Medd.*, 26(14), 1952.

[91] Aage Niels Bohr and Benjamin Roy Mottelson. Collective and individual-particle aspects of nuclear structure. *Kgl. Danske Videnskab. Selskab., Mat.-fys Medd.*, 27(16):1–174, 1953.

[92] Aage Bohr and Ben Mottelson. *Nuclear structure - Volume II: Nuclear Deformations*. World Scientific, Singapore ; London, 1998.

[93] C. E. Svensson, A. O. Macchiavelli, A. Juodagalvis, A. Poves, I. Ragnarsson, S. Åberg, D. E. Appelbe, R. A. E. Austin, G. C. Ball, M. P. Carpenter, E. Caurier, R. M. Clark, M. Cromaz, M. A. Deleplanque, R. M. Diamond, P. Fallon, R. V. F. Janssens, G. J. Lane, I. Y. Lee, F. Nowacki, D. G. Sarantites, F. S. Stephens, K. Vetter, and D. Ward. Lifetimes of superdeformed rotational states in ^{36}Ar. *Phys. Rev. C*, 63:061301, May 2001.

[94] Melvin Alexander Preston. *Structure of the nucleus*. Addison-Wesley Pub. Co., Reading, Mass. ; London, 1975.

[95] 'Rotational model'. [Online] Accessible: https://www.kth.se/social/upload/5176d9b0f276543c2c2bd4db/CH5.pdf.

[96] Einar Wold. The centrifugal stretching model and the deviation from the L(L+1) rule for rare-earth nuclei. *Nuclear Physics A*, 130(3):650 – 656, 1969.

[97] A. Johnson, H. Ryde, and S.A. Hjorth. Nuclear moment of inertia at high rotational frequencies. *Nuclear Physics A*, 179(3):753 – 768, 1972.

[98] Carlos A Bertulani. *Nuclear physics in a nutshell*, volume 2. Princeton University Press, 2007.

[99] K. Kitao, Y. Tendow, and A. Hashizume. Nuclear data sheets for A = 120. *Nuclear Data Sheets*, 96(2):241 – 390, 2002.

[100] J. R. Vanhoy, R. T. Coleman, K. A. Crandell, S. F. Hicks, B. A. Sklaney, M. M. Walbran, N. V. Warr, J. Jolie, F. Corminboeuf, L. Genilloud, J. Kern, J.-L. Schenker, and P. E. Garrett. Structure of ^{120}Te from the ^{118}Sn$(\alpha, 2n\gamma)$ reaction and ^{120}I decay. *Phys. Rev. C*, 68:034315, Sep 2003.

[101] A. Deltuva and A. C. Fonseca. Ab initio four-body calculation of n-^{3}He, p-^{3}H, and d-d scattering. *Phys. Rev. C*, 76:021001, Aug 2007.

[102] L. Coraggio, A. Covello, A. Gargano, N. Itaco, T. T. S. Kuo, and R. Machleidt. Nuclear structure calculations and modern nucleon-nucleon potentials. *Phys. Rev. C*, 71:014307, Jan 2005.

[103] G. Hagen, T. Papenbrock, D. J. Dean, and M. Hjorth-Jensen. Ab initio coupled-cluster approach to nuclear structure with modern nucleon-nucleon interactions. *Phys. Rev. C*, 82:034330, Sep 2010.

[104] A. Kievsky, M. Viviani, L. Girlanda, and L. E. Marcucci. Comparative study of three-nucleon force models in A=3,4 systems. *Phys. Rev. C*, 81:044003, Apr 2010.

[105] P. Navrátil, V. G. Gueorguiev, J. P. Vary, W. E. Ormand, and A. Nogga. Structure of A=10-13 nuclei with two- plus three-nucleon interactions from chiral effective field theory. *Phys. Rev. Lett.*, 99:042501, Jul 2007.

[106] J. C. Slater. The theory of complex spectra. *Phys. Rev.*, 34:1293–1322, Nov 1929.

[107] D. R. Hartree. The wave mechanics of an atom with a non-Coulomb central field. part I. Theory and Methods. *Mathematical Proceedings of the Cambridge Philosophical Society*, 24(1):89–110, 1928.

[108] Björn O. Roos. *The Complete Active Space Self-Consistent Field Method and its Applications in Electronic Structure Calculations*, pages 399–445. John Wiley & Sons, Ltd, 2007.

[109] A. A. Hasanein and M. W. Evans. *The Hartree-Fock Self-Consistent Field Method*, pages 39–78. World Scientific, 1996.

[110] Charlotte Froese Fischer. General Hartree-Fock program. *Computer Physics Communications*, 43(3):355 – 365, 1987.

[111] A. Gorgen, E. Clément, W. Korten, E. Bouchez, A. Chatillon, A. Hürstel, Y. Le Coz, Ch. Theisen, J. N. Wilson, M. Zielinska, C. Andreoiu, F. Becker, P. Butler, J. M. Casandjian, W. N. Catford, T. Czosnyka, G. de France, J. Gerl, R.-D. Herzberg, J. Iwanicki, D. G. Jenkins, G. D. Jones, P. J. Napiorkowski, G. Sletten, and C. Timis. Shape coexistence in 74 Kr and 76 Kr. *The European Physical Journal Special Topics*, 150(1):117–120, 2007.

[112] A. Petrovici, K.W. Schmid, and Amand Faessler. Microscopic aspects of shape coexistence in 72Kr and 74Kr. *Nuclear Physics A*, 665(3):333 – 350, 2000.

[113] David Lawrence Hill and John Archibald Wheeler. Nuclear constitution and the interpretation of fission phenomena. *Phys. Rev.*, 89:1102–1145, Mar 1953.

[114] E. R. Gamba. *A Compton-background-correction method for fast-timing measurements using $LaBr_3(Ce)$ detectors: The case of ^{114}Pd*. PhD thesis, 2018.

[115] Nobuo Hinohara, Koichi Sato, Takashi Nakatsukasa, Masayuki Matsuo, and Kenichi Matsuyanagi. Microscopic description of large-amplitude shape-mixing dynamics with inertial functions derived in local quasiparticle random-phase approximation. *Phys. Rev. C*, 82:064313, Dec 2010.

[116] K.E.G. Loebner, M. Vetter, and V. Hoenig. Nuclear intrinsic quadrupole moments and deformation parameters. *Nucl. Data, Sect. A*, 7:495–564, May 1970.

[117] Andreas Gorgen and Wolfram Korten. Coulomb excitation studies of shape coexistence in atomic nuclei. *Journal of Physics G: Nuclear and Particle Physics*, 43(2):024002, jan 2016.

[118] Krishna Kumar. Intrinsic quadrupole moments and shapes of nuclear ground states and excited states. *Phys. Rev. Lett.*, 28:249–253, Jan 1972.

[119] Douglas Cline. Nuclear shapes studied by coulomb excitation. *Annual Review of Nuclear and Particle Science*, 36(1):683–716, 1986.

[120] T. Schmidt, K. Heyde, A. Blazhev, and J. Jolie. Shell model based deformation analysis of light Cadmium isotopes. *arXiv:1706.02544 [nucl-th]*, Sep 2007.

[121] Kris Heyde and John L. Wood. Shape coexistence in atomic nuclei. *Rev. Mod. Phys.*, 83:1467–1521, Nov 2011.

[122] H. Morinaga. Interpretation of some of the excited states of 4*n* self-conjugate nuclei. *Phys. Rev.*, 101:254–258, Jan 1956.

[123] G.E. Brown and A.M. Green. Nuclear coexistence in the oxygen region and realistic nucleon-nucleon forces. *Nuclear Physics*, 85(1):87 – 96, 1966.

[124] F. Hoyle. On Nuclear Reactions Occuring in Very Hot STARS.I. the Synthesis of Elements from Carbon to Nickel. *ApJS*, 1:121, September 1954.

[125] P A Butler. Octupole collectivity in nuclei. *Journal of Physics G: Nuclear and Particle Physics*, 43(7):073002, Jun 2016.

[126] S. Takami, K. Yabana, and M. Matsuo. Tetrahedral and triangular deformations of z=n nuclei in mass region a,à°60,Äì80. *Physics Letters B*, 431(3):242–248, 1998.

[127] K. Wimmer, W. Korten, T. Arici, P. Doornenbal, P. Aguilera, A. Algora, T. Ando, H. Baba, B. Blank, A. Boso, S. Chen, A. Corsi, P. Davies, G. de Angelis, G. de France, D.T. Doherty, J. Gerl, R. Gernhser, D. Jenkins, S. Koyama, T. Motobayashi, S. Nagamine, M. Niikura, A. Obertelli, D. Lubos, B. Rubio, E. Sahin, T.Y. Saito, H. Sakurai, L. Sinclair, D. Steppenbeck, R. Taniuchi, R. Wadsworth, and M. Zielinska. Shape coexistence and isospin symmetry in a,ÄØ=,ÄØ70 nuclei: Spectroscopy of the tz,ÄØ=,ÄØ,àí1 nucleus 70kr. *Physics Letters B*, 785:441–446, 2018.

[128] D. Lunney, J. M. Pearson, and C. Thibault. Recent trends in the determination of nuclear masses. *Rev. Mod. Phys.*, 75:1021–1082, Aug 2003.

[129] J. C. Hardy and I. S. Towner. Superallowed 0+ $\rightarrow$ 0+ nuclear $/beta$ decays: 2020 critical survey, with implications for vud and ckm unitarity. *Physical Review C*, 102(4), 10 2020.

[130] R. P. Feynman and M. Gell-Mann. Theory of the fermi interaction. *Phys. Rev.*, 109:193–198, Jan 1958.

[131] Jenkins, D. and Courtin, S. Weighing the evidence for clustering in nuclei. *J. Phys. G*, 42(3), 2015.

[132] K. Alder, A. Bohr, T. Huus, B. Mottelson, and A. Winther. Study of nuclear structure by electromagnetic excitation with accelerated ions. *Rev. Mod. Phys.*, 28:432–542, Oct 1956.

[133] F.P. Slater B.A. M.Sc. Xcix. the excitation of γ radiation by α particles from radium emanation. *The London, Edinburgh, and Dublin Philosophical Magazine and Journal of Science*, 42(252):904–923, 1921.

[134] Clyde L. McClelland and Clark Goodman. Excitation of heavy nuclei by the electric field of low-energy protons. *Phys. Rev.*, 91:760–761, Aug 1953.

[135] J. O. Newton and F. S. Stephens. Experimental observation of double coulomb excitation. *Phys. Rev. Lett.*, 1:63–65, Jul 1958.

[136] F. S. Stephens, R. M. Diamond, and I. Perlman. Multiple coulomb excitation in th^{232} and u^{238}. *Phys. Rev. Lett.*, 3:435–438, Nov 1959.

[137] K. M. Lynch, S. G. Wilkins, J. Billowes, C. L. Binnersley, M. L. Bissell, K. Chrysalidis, T. E. Cocolios, T. Day Goodacre, R. P. de Groote, G. J. Farooq-Smith, D. V. Fedorov, V. N. Fedosseev, K. T. Flanagan, S. Franchoo, R. F. Garcia Ruiz, W. Gins, R. Heinke, Á. Koszorús, B. A. Marsh, P. L. Molkanov, P. Naubereit, G. Neyens, C. M. Ricketts, S. Rothe, C. Seiffert, M. D. Seliverstov, H. H. Stroke, D. Studer, A. R. Vernon, K. D. A. Wendt, and X. F. Yang. Laser-spectroscopy studies of the nuclear structure of neutron-rich radium. *Phys. Rev. C*, 97:024309, Feb 2018.

[138] M. Matejska-Minda, P. Bednarczyk, B. Fornal, F. R. Xu, W. Y. Liang, G. de Angelis, S. Aydin, S. Brambilla, M. Ciemała, E. Farnea, T. Hüyük, G. Jaworski, M. Kmiecik, M. Krzysiek, S. Leoni, A. Maj, R. Menegazzo, W. Męczyński, C. Michelagnoli, M. Palacz, F. Recchia, E. Sahin, J. Styczeń, B. Szpak, C. A. Ur, R. Wadsworth, and M. Zięblíński. Lifetime measurements of short-lived excited states, and shape changes in ^{69}As and ^{66}Ge nuclei. *Phys. Rev. C*, 100:054330, Nov 2019.

[139] B. S. Nara Singh, V. Nanal, and R. G. Pillay. Hexadecapole deformation studies in ^{148}Nd and ^{150}Nd. *Pramana*, 61:507–515, Sep 2003.

[140] I Bergstrom. How should we investigate nuclides far off the stability line. *Nuclear Instruments and Methods*, 43(1):129–145, 1966. Proceedings of the Tenth Summer Meeting of Nuclear Physicists.

[141] D. C. Radford, C. Baktash, J. R. Beene, B. Fuentes, A. Galindo-Uribarri, C. J. Gross, P. A. Hausladen, T. A. Lewis, P. E. Mueller, E. Padilla, D. Shapira, D. W. Stracener, C.-H. Yu, C. J. Barton, M. A. Caprio, L. Coraggio, A. Covello, A. Gargano, D. J. Hartley, and N. V. Zamfir. Coulomb excitation of radioactive ^{132,134,136}Te beams and the low $B(E2)$ of ^{136}Te. *Phys. Rev. Lett.*, 88:222501, May 2002.

[142] O. Niedermaier, H. Scheit, V. Bildstein, H. Boie, J. Fitting, R. von Hahn, F. Köck, M. Lauer, U. K. Pal, H. Podlech, R. Repnow, D. Schwalm, C. Alvarez, F. Ames, G. Bollen, S. Emhofer, D. Habs, O. Kester, R. Lutter, K. Rudolph, M. Pasini, P. G. Thirolf, B. H. Wolf, J. Eberth, G. Gersch, H. Hess, P. Reiter, O. Thelen, N. Warr, D. Weisshaar, F. Aksouh, P. Van den Bergh, P. Van Duppen, M. Huyse, O. Ivanov, P. Mayet, J. Van de Walle, J. Äystö, P. A. Butler, J. Cederkäll, P. Delahaye, H. O. U. Fynbo, L. M. Fraile, O. Forstner, S. Franchoo, U. Köster, T. Nilsson, M. Oinonen, T. Sieber, F. Wenander, M. Pantea, A. Richter, G. Schrieder, H. Simon, T. Behrens, R. Gernhäuser, T. Kröll, R. Krücken, M. Münch, T. Davinson, J. Gerl, G. Huber, A. Hurst, J. Iwanicki, B. Jonson, P. Lieb, L. Liljeby, A. Schempp, A. Scherillo, P. Schmidt, and G. Walter. "safe" coulomb excitation of ^{30}Mg. *Phys. Rev. Lett.*, 94:172501, May 2005.

[143] E. Clément, A. Görgen, W. Korten, E. Bouchez, A. Chatillon, J.-P. Delaroche, M. Girod, H. Goutte, A. Hürstel, Y. Le Coz, A. Obertelli, S. Péru, Ch. Theisen, J. N. Wilson, M. Zielińska, C. Andreoiu, F. Becker, P. A. Butler, J. M. Casandjian, W. N. Catford, T. Czosnyka, G. de France, J. Gerl, R.-D. Herzberg, J. Iwanicki, D. G. Jenkins, G. D. Jones, P. J. Napiorkowski, G. Sletten, and C. N. Timis. Shape coexistence in neutron-deficient krypton isotopes. *Phys. Rev. C*, 75:054313, May 2007.

[144] C. Chandler, P. H. Regan, C. J. Pearson, B. Blank, A. M. Bruce, W. N. Catford, N. Curtis, S. Czajkowski, W. Gelletly, R. Grzywacz, Z. Janas, M. Lewitowicz, C. Marchand, N. A. Orr, R. D. Page, A. Petrovici, A. T. Reed, M. G. Saint-Laurent, S. M. Vincent, R. Wadsworth, D. D. Warner, and J. S. Winfield. Evidence for a highly deformed oblate 0^+ state in $^{74}_{36}$Kr. *Phys. Rev. C*, 56:R2924–R2928, Dec 1997.

[145] E. Bouchez, I. Matea, W. Korten, F. Becker, B. Blank, C. Borcea, A. Buta, A. Emsallem, G. de France, J. Genevey, F. Hannachi, K. Hauschild, A. Hürstel, Y. Le Coz, M. Lewitowicz, R. Lucas, F. Negoita, F. de Oliveira Santos, D. Pantelica, J. Pinston, P. Rahkila, M. Rejmund, M. Stanoiu, and Ch. Theisen. New shape isomer in the self-conjugate nucleus ^{72}Kr. *Phys. Rev. Lett.*, 90:082502, Feb 2003.

[146] W. Nazarewicz, J. Dudek, R. Bengtsson, T. Bengtsson, and I. Ragnarsson. Microscopic study of the high-spin behaviour in selected A $\neq$ 80 nuclei. *Nuclear Physics A*, 435(2):397 – 447, 1985.

[147] A. M. Hurst, P. A. Butler, D. G. Jenkins, P. Delahaye, F. Wenander, F. Ames, C. J. Barton, T. Behrens, A. Bürger, J. Cederkäll, E. Clément, T. Czosnyka, T. Davinson,

G. de Angelis, J. Eberth, A. Ekström, S. Franchoo, G. Georgiev, A. Görgen, R.-D. Herzberg, M. Huyse, O. Ivanov, J. Iwanicki, G. D. Jones, P. Kent, U. Köster, T. Kröll, R. Krücken, A. C. Larsen, M. Nespolo, M. Pantea, E. S. Paul, M. Petri, H. Scheit, T. Sieber, S. Siem, J. F. Smith, A. Steer, I. Stefanescu, N. U. H. Syed, J. Van de Walle, P. Van Duppen, R. Wadsworth, N. Warr, D. Weisshaar, and M. Zielińska. Measurement of the sign of the spectroscopic quadrupole moment for the 2_1^+ state in ^{70}Se: No evidence for oblate shape. *Phys. Rev. Lett.*, 98:072501, Feb 2007.

[148] J. Ljungvall, A. Görgen, M. Girod, J.-P. Delaroche, A. Dewald, C. Dossat, E. Farnea, W. Korten, B. Melon, R. Menegazzo, A. Obertelli, R. Orlandi, P. Petkov, T. Pissulla, S. Siem, R. P. Singh, J. Srebrny, Ch. Theisen, C. A. Ur, J. J. Valiente-Dobón, K. O. Zell, and M. Zielińska. Shape coexistence in light Se isotopes: Evidence for oblate shapes. *Phys. Rev. Lett.*, 100:102502, Mar 2008.

[149] A. Obertelli, T. Baugher, D. Bazin, J. P. Delaroche, F. Flavigny, A. Gade, M. Girod, T. Glasmacher, A. Goergen, G. F. Grinyer, W. Korten, J. Ljungvall, S. McDaniel, A. Ratkiewicz, B. Sulignano, and D. Weisshaar. Shape evolution in self-conjugate nuclei, and the transitional nucleus ^{68}Se. *Phys. Rev. C*, 80:031304, Sep 2009.

[150] E. A. McCutchan, C. J. Lister, T. Ahn, R. J. Casperson, A. Heinz, G. Ilie, J. Qian, E. Williams, R. Winkler, and V. Werner. Shape coexistence in ^{72}Se investigated following the β decay of ^{72}Br. *Phys. Rev. C*, 83:024310, Feb 2011.

[151] Jorrit de Boer and Jörg Eichler. *The Reorientation Effect*, pages 1–65. Springer US, Boston, MA, 1968.

[152] Probing shape coexistence in neutron deficient 72 Se via low energy Coulomb excitation - Proposal, Oct 2014.

[153] N. Bree, K. Wrzosek-Lipska, A. Petts, A. Andreyev, B. Bastin, M. Bender, A. Blazhev, B. Bruyneel, P. A. Butler, J. Butterworth, M. P. Carpenter, J. Cederkäll, E. Clément, T. E. Cocolios, A. Deacon, J. Diriken, A. Ekström, C. Fitzpatrick, L. M. Fraile, Ch. Fransen, S. J. Freeman, L. P. Gaffney, J. E. García-Ramos, K. Geibel, R. Gernhäuser, T. Grahn, M. Guttormsen, B. Hadinia, K. Hadyńska-Klęk, M. Hass, P.-H. Heenen, R.-D. Herzberg, H. Hess, K. Heyde, M. Huyse, O. Ivanov, D. G. Jenkins, R. Julin, N. Kesteloot, Th. Kröll, R. Krücken, A. C. Larsen, R. Lutter, P. Marley, P. J. Napiorkowski, R. Orlandi, R. D. Page, J. Pakarinen, N. Patronis, P. J. Peura, E. Piselli, P. Rahkila, E. Rapisarda, P. Reiter, A. P. Robinson, M. Scheck, S. Siem, K. Singh Chakkal, J. F. Smith, J. Srebrny, I. Stefanescu, G. M. Tveten, P. Van Duppen, J. Van de Walle, D. Voulot, N. Warr, F. Wenander, A. Wiens, J. L. Wood, and M. Zielińska. Shape coexistence in the neutron-deficient even-even $^{182-188}$Hg isotopes studied via coulomb excitation. *Phys. Rev. Lett.*, 112:162701, Apr 2014.

[154] D. Cline, H.S. Gertzman, H.E. Gove, P.M.S. Lesser, and J.J. Schwartz. The static quadrupole moment of the first excited state of 60Ni. *Nuclear Physics A*, 133(2):445 – 464, 1969.

[155] P.M.S. Lesser, D. Cline, Philip Goode, and R.N. Horoshko. Static electric quadrupole moments of the first excited states of 56Fe and the even titanium nuclei. *Nuclear Physics A*, 190(3):597 – 634, 1972.

[156] P. B. Vold, D. Cline, P. Russo, J. K. Sprinkle, R. P. Scharenberg, and R. J. Mitchell. Quadrupole moment of the first excited 2^+ state of ^{18}O. *Phys. Rev. Lett.*, 39:325–328, Aug 1977.

[157] D. Cline. *"Physics of Medium-light Nuclei", in Proceeding [sic] of the Topical Conference on Physics of Medium Light Nuclei*, pages 89, ed. R. A. Ricci and P. Blasi. Compositori, 1978.

[158] 'The ISOLDE facility'. [Online] Accessible: https://isolde.cern/isolde-facility.

[159] U. Koster, U.C. Bergmann, D. Carminati, R. Catherall, J. Cederkall, J.G. Correia, B. Crepieux, M. Dietrich, K. Elder, V.N. Fedoseyev, L. Fraile, S. Franchoo, H. Fynbo, U. Georg, T. Giles, A. Joinet, O.C. Jonsson, R. Kirchner, Ch. Lau, J. Lettry, H.J. Maier, V.I. Mishin, M. Oinonen, K. Perajarvi, H.L. Ravn, T. Rinaldi, M. Santana-Leitner, U. Wahl, and L. Weissman. Oxide fiber targets at isolde. *Nuclear Instruments and Methods in Physics Research Section B: Beam Interactions with Materials and Atoms*, 204:303–313, 2003. 14th International Conference on Electromagnetic Isotope Separators and Techniques Related to their Applications.

[160] L. Gaffney and J. Konki. 'Miniball'. [Online] Accessible: http://isolde.web.cern.ch/experiments/miniball.

[161] N Warr. 'The miniball cluster'. [Online] Accessible: https://www.ikp.uni-koeln.de/~warr/doc/miniball_detectors.pdf.

[162] R. H. Pehl. Germanium gamma-ray detectors. *Physics Today*, 30(11):50, 1977.

[163] 'Double Sided Strip Detectors', November 2018. [Online] Accessible: http://www.micronsemiconductor.co.uk/strip-detectors-double-sided.

[164] James B. Cumming and Noah R. Johnson. Decay of selenium-72. *Phys. Rev.*, 110:1104–1108, Jun 1958.

[165] L.P. Gaffney. 'MiniballCoulexSort '. [Online] Accessible: https://github.com/Miniball/MiniballCoulexSort.

[166] D. Radford. 'Radware '. [Online] Accessible: https://radware.phy.ornl.gov/.

[167] J. Henderson, C. Y. Wu, J. Ash, P. C. Bender, B. Elman, A. Gade, M. Grinder, H. Iwasaki, E. Kwan, B. Longfellow, T. Mijatović, D. Rhodes, M. Spieker, and D. Weisshaar. Localizing the shape transition in neutron-deficient selenium. *Phys. Rev. Lett.*, 121:082502, Aug 2018.

[168] GOSIA User Group. 'GOSIA: Coulomb Excitation Codes'. [Online] Accessible: http://www.pas.rochester.edu/~cline/Gosia/.

[169] L. P. Gaffney. 'chisqsurface'. [Online] Accessible: https://github.com/lpgaff/chisqsurface.

[170] D. Abriola and A.A. Sonzogni. Nuclear data sheets for a = 72. *Nuclear Data Sheets*, 111(1):1–140, 2010.

[171] E.A. McCutchan. Nuclear data sheets for a = 68. *Nuclear Data Sheets*, 113(6):1735–1870, 2012.

[172] K. Nomura, R. Rodríguez-Guzmán, and L. M. Robledo. Structural evolution in germanium and selenium nuclei within the mapped interacting boson model based on the gogny energy density functional. *Phys. Rev. C*, 95:064310, Jun 2017.

[173] G. F. Bertsch, M. Girod, S. Hilaire, J.-P. Delaroche, H. Goutte, and S. Péru. Systematics of the first 2^+ excitation with the gogny interaction. *Phys. Rev. Lett.*, 99:032502, Jul 2007.

[174] P.-G. Reinhard, D. J. Dean, W. Nazarewicz, J. Dobaczewski, J. A. Maruhn, and M. R. Strayer. Shape coexistence and the effective nucleon-nucleon interaction. *Phys. Rev. C*, 60:014316, Jun 1999.

[175] J O Newton. Nuclear spectroscopy with heavy ions. *Progr. Nucl. Phys. 11: 53-144(1970).*, 1 1970.

[176] E.K. Warburton, J.J. Kolata, J.W. Olness, A.R. Poletti, and Ph. Gorodetzky. Gamma rays from fusion-evaporation reactions in 32,â§a<46 nuclei. *Atomic Data and Nuclear Data Tables*, 14(2):147 – 160, 1974.

[177] Peter Dendooven. The development and status of the igisol technique. *Nuclear Instruments and Methods in Physics Research Section B: Beam Interactions with Materials and Atoms*, 126(1):182 – 189, 1997. International Conference on Electromagnetic Isotope Separators and Techniques Related to Their Applications.

[178] C. E. Svensson, D. Rudolph, C. Baktash, M. A. Bentley, J. A. Cameron, M. P. Carpenter, M. Devlin, J. Eberth, S. Flibotte, A. Galindo-Uribarri, G. Hackman, D. S. Haslip, R. V. F. Janssens, D. R. LaFosse, T. J. Lampman, I. Y. Lee, F. Lerma, A. O. Macchiavelli, J. M. Nieminen, S. D. Paul, D. C. Radford, P. Reiter, L. L. Riedinger, D. G. Sarantites, B. Schaly, D. Seweryniak, O. Thelen, H. G. Thomas, J. C. Waddington, D. Ward, W. Weintraub, J. N. Wilson, C. H. Yu, A. V. Afanasjev, and I. Ragnarsson. Decay out of the doubly magic superdeformed band in the $N = Z$ nucleus ^{60}zn. *Phys. Rev. Lett.*, 82:3400–3403, Apr 1999.

[179] M. Wang, G. Audi, A. H. Wapstra, F. G. Kondev, M. MacCormick, X. Xu, and B. Pfeiffer. The ame2012 atomic mass evaluation (ii). tables, graphs and references. *Chin.Phys.C*, 36:1603, 2012.

[180] D. T. Doherty, G. Lotay, P. J. Woods, D. Seweryniak, M. P. Carpenter, C. J. Chiara, H. M. David, R. V. F. Janssens, L. Trache, and S. Zhu. Key resonances in the $^{30}\mathrm{P}(p,\gamma)^{31}\mathrm{S}$ gateway reaction for the production of heavy elements in one novae. *Phys. Rev. Lett.*, 108:262502, Jun 2012.

[181] D. T. Doherty, P. J. Woods, G. Lotay, D. Seweryniak, M. P. Carpenter, C. J. Chiara, H. M. David, R. V. F. Janssens, L. Trache, and S. Zhu. Level structure of $^{31}\mathrm{S}$: From low excitation energies to the region of interest for hydrogen burning in novae through the $^{30}\mathrm{P}(p,\gamma)^{31}\mathrm{S}$ reaction. *Phys. Rev. C*, 89:045804, Apr 2014.

[182] D. G. Jenkins, A. Meadowcroft, C. J. Lister, M. P. Carpenter, P. Chowdhury, N. J. Hammond, R. V. F. Janssens, T. L. Khoo, T. Lauritsen, D. Seweryniak, T. Davinson, P. J. Woods, A. Jokinen, H. Penttila, G. Martínez-Pinedo, and J. José. Reevaluation of the ^{30}P$(p,\gamma)^{31}$S astrophysical reaction rate from a study of the $t = 1/2$ mirror nuclei, ^{31}S and ^{31}P. *Phys. Rev. C*, 73:065802, Jun 2006.

[183] John Markus Blatt and Victor Frederick Weisskopf. *Theoretical nuclear physics*. Courier Corporation, 1991.

[184] Daniel T. Doherty. *Experimental Studies for Explosive Nuclear Astrophysics*. PhD thesis, 2014.

[185] 'ATLAS'. [Online] Accessible: https://www.phy.anl.gov/atlas.

[186] Micheal P. Carpenter. 'Gammasphere'. [Online] Accessible: https://www.anl.gov/phy/gammasphere.

[187] M A Riley, J Simpson, and E S Paul. High resolution gamma-ray spectroscopy and the fascinating angular momentum realm of the atomic nucleus. *Physica Scripta*, 91(12):123002, nov 2016.

[188] Nicola M. Lumley. *High-K isomers in ^{180}Os*. PhD thesis, 2010.

[189] I-Yang Lee. The gammasphere. *Nuclear Physics A*, 520:c641 – c655, 1990. Nuclear Structure in the Nineties.

[190] 'GammaSphere ROOT sorter '. [Online] Accessible: https://www.phy.anl.gov/gammasphere/doc/GSSort/.

[191] E. Browne and J.K. Tuli. Nuclear data sheets for A = 60. *Nuclear Data Sheets*, 114(12):1849 – 2022, 2013.

[192] G. H. Dulfer, B. O. ten Brink, T. J. Ketel, A. W. B. Kalshoven, and H. Verheul. On the decay of ^{61}zn and ^{60}zn using mass separated sources. *Z.Phys.*, 251:416, 1972.

[193] R. B. Schubank, J. A. Cameron, and V. P. Janzen. Gamma-ray spectroscopy of ^{60,61}Zn and ^{59,60}Cu. *Phys. Rev. C*, 40:2310–2319, Nov 1989.

[194] D Pelte and Dirk Schwalm. In-beam gamma-ray spectroscopy with heavy ions. In *Heavy ion collisions*. 1982.

[195] D. Rudolph, I. Ragnarsson, C. Andreoiu, M. A. Bentley, M. P. Carpenter, R. J. Charity, R. M. Clark, J. Ekman, C. Fahlander, P. Fallon, W. Reviol, D. G. Sarantites, and D. Seweryniak. Single-particle and collective excitations in the $n = 28$ isotones ^{54}Fe and ^{53}Mn. *Phys. Rev. C*, 102:014316, Jul 2020.

[196] F. Pougheon, P. Roussel, P. Colombani, H. Doubre, and J.C. Roynette. Two-nucleon stripping reactions induced by 16o in 54fe and 58ni at 80 mev. *Nuclear Physics A*, 193(1):305 – 322, 1972.

[197] A. Boucenna, L. Kraus, I. Linck, and Tsan Ung Chan. Two-proton transfer reactions on even ni and zn isotopes. *Phys. Rev. C*, 42:1297–1311, Oct 1990.

[198] D. Evers, W. Assmann, K. Rudolph, S.J. Skorka, and P. Sperr. The (3he, n) reaction on even (f, p) shell nuclei at 15, 18 and 21 mev (ii). *Nuclear Physics A*, 230(1):109 – 140, 1974.

[199] D. Soltesz, M. A. A. Mamun, A. V. Voinov, Z. Meisel, B. A. Brown, C. R. Brune, S. M. Grimes, H. Hadizadeh, M. Hornish, T. N. Massey, and et al. Determination of the zn60 level density from neutron evaporation spectra. *Physical Review C*, 103(1), Jan 2021.

[200] A. Kankainen, P.J. Woods, and F. et al. Nunes. Angle-integrated measurements of the ^{26}Al(d,n)^{27}Si reaction cross section: a probe of spectroscopic factors and astrophysical resonance strengths. *Eur. Phys. A*, 40:1–6, Jan 2016.

[201] A. Kankainen, P.J. Woods, H. Schatz, T. Poxon-Pearson, D.T. Doherty, V. Bader, T. Baugher, D. Bazin, B.A. Brown, J. Browne, A. Estrade, A. Gade, J. Jose, A. Kontos, C. Langer, G. Lotay, Z. Meisel, F. Montes, S. Noji, F. Nunes, G. Perdikakis, J. Pereira, F. Recchia, T. Redpath, R. Stroberg, M. Scott, D. Seweryniak, J. Stevens, D. Weisshaar, K. Wimmer, and R. Zegers. Measurement of key resonance states for the ^{30}P(p,γ)^{31}S reaction rate, and the production of intermediate-mass elements in nova explosions. *Physics Letters B*, 769:549–553, 2017.

[202] D. Kahl, P.J. Woods, T. Poxon-Pearson, F.M. Nunes, B.A. Brown, H. Schatz, T. Baumann, D. Bazin, J.A. Belarge, P.C. Bender, B. Elman, A. Estrade, A. Gade, A. Kankainen, C. Lederer-Woods, S. Lipschutz, B. Longfellow, S.-J. Lonsdale, E. Lunderberg, F. Montes, W.J. Ong, G. Perdikakis, J. Pereira, C. Sullivan, R. Taverner, D. Weisshaar, and R. Zegers. Single-particle shell strengths near the doubly magic nucleus 56ni and the 56ni(p,γ)57cu reaction rate in explosive astrophysical burning. *Physics Letters B*, 797:134803, 2019.

[203] S. Hallam, G. Lotay, A. Gade, D. T. Doherty, J. Belarge, P. C. Bender, B. A. Brown, J. Browne, W. N. Catford, B. Elman, A. Estradé, M. R. Hall, B. Longfellow, E. Lunderberg, F. Montes, M. Moukaddam, P. O'Malley, W.-J. Ong, H. Schatz, D. Seweryniak, K. Schmidt, N. K. Timofeyuk, D. Weisshaar, and R. G. T. Zegers. Exploiting isospin symmetry to study the role of isomers in stellar environments. *Phys. Rev. Lett.*, 126:042701, Jan 2021.

[204] Kyle G. Leach. *Neutron Transfer Reactions on ^{64}Zn as a Probe for Testing Shell-Model Isospin-Symmetry-Breaking Theory*. PhD thesis, 2012.

[205] Norman K Glendenning. *Direct nuclear reactions*. World Scientific, Washington; London, 2004.

Appendix A

Feasibility Study of the ^{74}Se(p,t)^{72}Se Reaction

Here, the ^{74}Se(p,t)^{72}Se reaction is simulated, where a high-energy ^{74}Se beam would be directed onto a proton target and tritons produced from the resulting two-neutron transfer (p,t) reaction would be detected by silicon detectors at forward lab angles. Such reactions have proven difficult in the past for several reasons, for example, the Q-value tends to be quite high (Q = -11.979106 MeV / nucleon for this specific reaction). But with the development of higher energy and intensity accelerators and advancements in technology, performing these reactions are a more realistic possibility.

Given the complicated nature of performing this experiment and extracting worthwhile results, it seemed sensible to perform a feasibility study using simulations created by computer codes to analyse the kinematics of the reaction. A basic computer code using relativistic kinematics can be written and used to perform these simulations.

The reaction simulation will give indicators as to whether this experiment can realistically be conducted. Firstly, tritons reaching the detector can be estimated. If number of tritons that hit the detector is too low, the validity of the data produced from the experiment will be compromised. The simulation can also give an insight into the energy resolution of the

detector(s). After factoring in the beam uncertainty, if the chosen detector(s) cannot distinguish between tritons representing different nuclear states, the results obtained will be meaningless. Once hypothetical setups are constrained with these indicators, calculations can be made to see if Rutherford scattering of the beam will contaminate the data collected.

Overview

Neutron transfer reactions are reactions where a select number of neutrons are transferred to or away from the nucleus of interest. These are classified as direct reactions and "are generally used to explore the shell-structure of the nucleus, since they are sensitive to specific states through the insertion or removal of nucleons to/from a given orbital" [204].

Since direct reactions probe individual nucleons within the nucleus and leave the rest of the nuclear interior unchanged, the shell structure of the nucleus can be directly observed. Nucleon transfer reactions are an essential tool in this regard, since the angular distribution of the observed ejectile is a direct signature of the angular momentum transferred in the reaction [205]. The idea with this experiment is to use a two-nucleon transfer reaction as a spectroscopic probe, which, if successful, can provide novel information into the shell structure of ^{72}Se nuclei.

For two-nucleon transfer probes, the final state angular distribution is sensitive to the angular momentum transfer, however unlike in the single-nucleon case, this angular momentum is carried by a pair of particles, and therefore does not directly reflect the angular-momentum of the single-particle states where the nucleons are transferred [205]. The total angular momentum of the transferred pair can be shared in several ways. Therefore, all such possibilities are consistent with the structure of the connected states must contribute coherently to the reaction. Consequently, the two-nucleon transfer cross-sections are proportional to this constructive (or destructive) coherence, which depends explicitly on the correlation of the nucleon pair. The aim of experiments such as this is to populate the ground state of different bands (potentially up to

the 5th 0^+ state as in the case for ^{64}Zn [204]) which can test the accuracy of the isospin-mixing calculations within the shell model and give a better understanding of the shell model orbitals that drive nuclear reactions [204].

Reaction Simulation

Before the detector geometry is considered, the simulation is run in order to display at what angle (in the lab reference frame) and energy tritons would hypothetically hit a detector given a chosen beam intensity. The results for this are shown in Figure A.1. This is done in order to see if the energy resolution is acceptable at any angle. As this reaction is done in inverse kinematics, two solutions will always be visible for the tritons.

The level spacing for the excited states in this isotope is in the order of 800 keV. The code was implemented in such a way to simulate tritons being produced with a difference of 400 keV in energy, i.e. simulating two nuclear states with an energy spacing of 400 keV. The reasoning behind this is that if tritons produced from two nuclear states 400 keV apart are clearly distinguishable in a simulation, it can be said with confidence that tritons in the actual experiments produced from nuclear states with an energy spacing in the order of 800 keV could be definitely resolved. If it was possible to distinguish between the two at any range of angles in a plot created by the code, this would mean that the energy resolution at said angles for the chosen beam should be sufficient for the reaction to be a success.

With a Q value of 11.979 MeV/u, the minimum beam energy for the reaction to even occur is ~900 Mev. In order to obtain the ideal beam energy for this experiment, calculations of the distorted wave Born approximation (DWBA) are required. Given the supplementary nature of this study with respect to this thesis, these are not done here and are calculations which could be done in further works. Here, the experiment is simulated at two energies, 1100 MeV and 2200 MeV.

A beam energy of 1100 MeV was initially selected, with a beam uncertainty of 1%, in line with what can be obtained with typical high-energy cyclotrons. The code was executed with 10^5 triton events being simulated. The results from this are shown in Figure A.1a. It is not immediately clear, but distinction could be made between the tritons produced by the two nuclear states at the lower energy solution. This area is focused on in Figure A.1c and the distinction between the two types of triton is much easier to see. The simulation is also done with beam energy of 2200 MeV and beam uncertainty 1%; similar results can be seen in figures A.1b and A.1d. From these results, it is clear that there is the potential for this reaction to yield worthwhile results, should the geometry required be feasible.

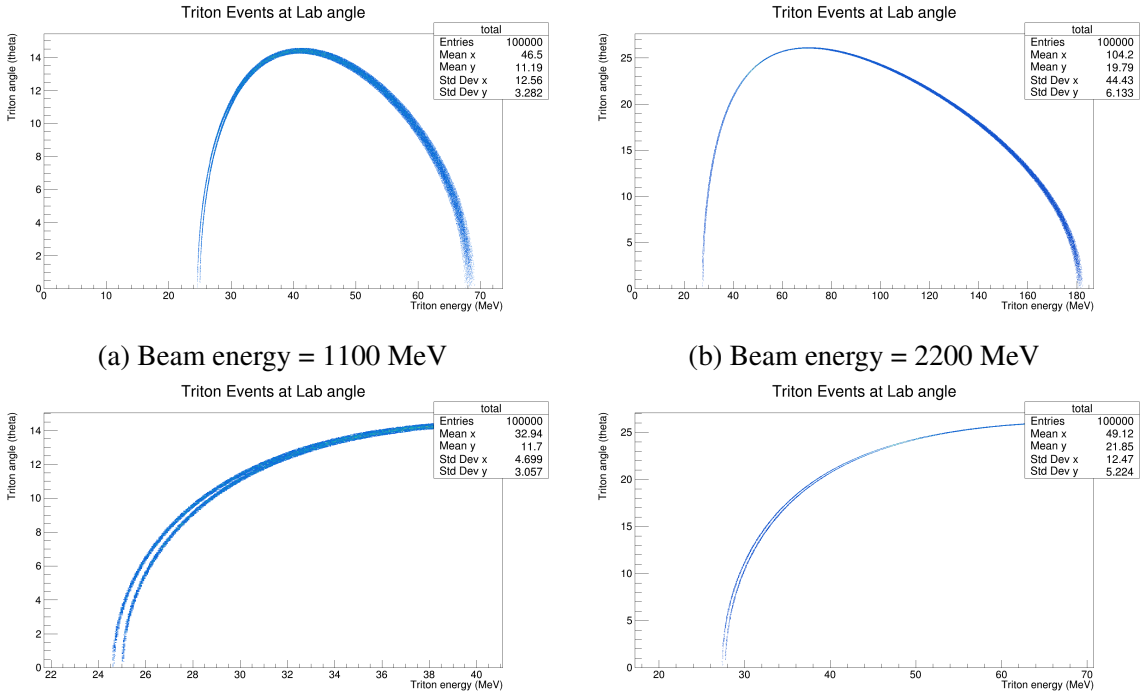

(a) Beam energy = 1100 MeV

(b) Beam energy = 2200 MeV

(c) Clearer resolution (1100 MeV)

(d) Clearer resolution (2200 MeV)

Fig. A.1 The angles and energies detected for tritons produced from two different nuclear states

The next step in this study was to determine what kind of detector to use and it was decided that a W1 type detector with active area of 5cm x 5cm and a strip width of 3.1 mm [163] would be used. Given the "acceptable" resolution produced previously was still not appropriate, it was

clear that each detector strip could not cover a wide range of angles or they would not be able to resolve between the different tritons.

It was also noted, as can be seen in figures A.1c and A.1d, that the resolution was certainly not good enough at angles above 11°and 23°for 1100 MeV beam and 2200 MeV beam respectively, so geometrical setups at these angles could be dismissed. Angles below 1°were also dismissed with the assumption the the efficiency of the detector at these angles would be far too low.

The geometry modelled in the simulation is visualised in Figure A.2, where d1 is the linear distance to the plane of the detector and d2 is the distance from the beam line axis to the detector. Varying these distances allows the manipulation of the angles spanned by the detector as the detector will cover the distance from d2 to d2 + 49.6 mm.

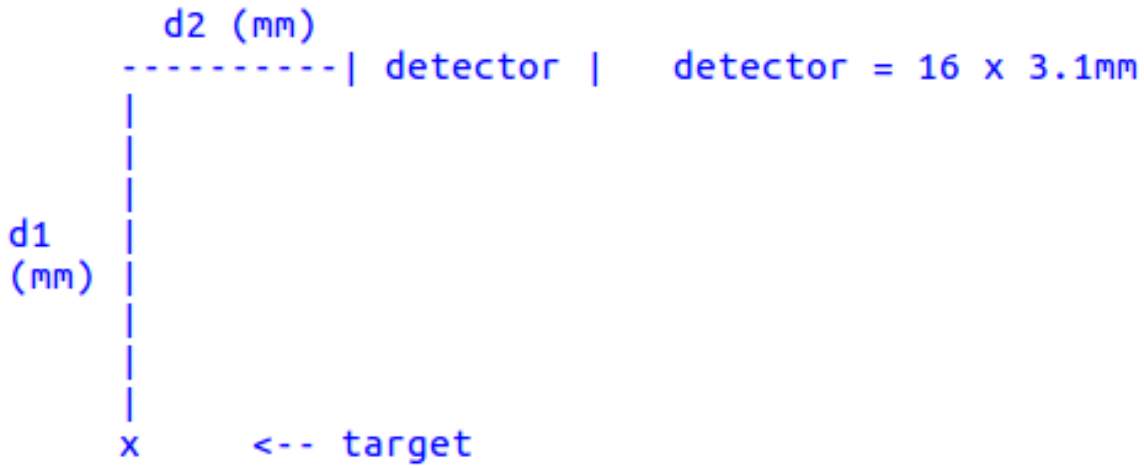

Fig. A.2 Simple representation of the prospective geometry for the experiment, used for the simulation

The detectors properties were factored into the code and several plots were created exploring different geometrical setups obeying the constraints mentioned above, with beam energy of both 1100 and 2200 MeV. Some of these are presented in figures A.3, A.4, A.5 and A.6. These plots give give an insight into what the 16 strips of this W1 type detector would see given a specific experimental setup.

Figures A.3a and A.3b show results for very small angle detection. It is likely at these angles that the results would be affected by Rutherford scattering, but this area is investigated first to see if it produces a favourable setup. If this were the case, precise Rutherford cross-section calculations can be made to see if the angle range is affected or not. However, in this case, it is not worth going this far. While the resolution for both beam energies is very good, the efficiency is very poor, with <1% of tritons actually being detected. This means that in order to extract worthwhile results, an unfeasibly long run time or beam intensity would be required.

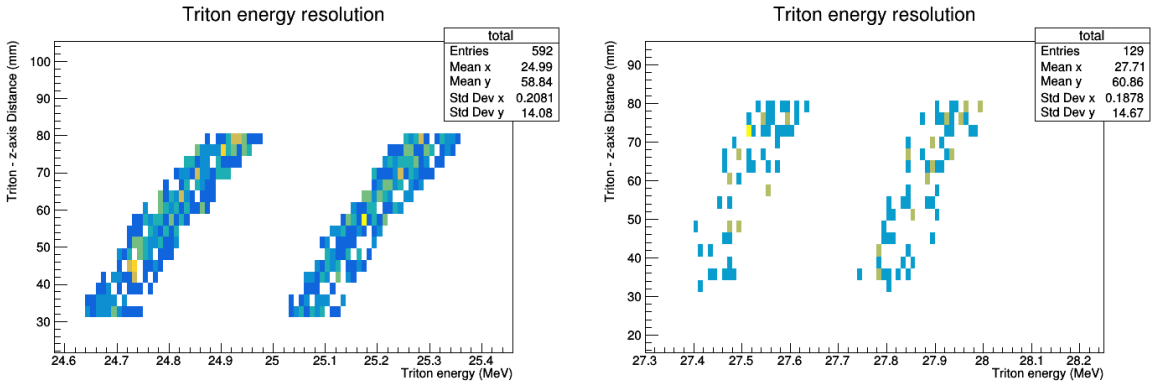

(a) Beam energy = 1100 MeV

(b) Beam energy = 2200 MeV

Fig. A.3 Detector hits at low angle for the reaction where d1 = 1500mm and d2 = 31mm, spanning $\theta \approx 1°$- $3°$

The plots that can be seen in Figure A.4 are for two different geometrical setups which have the detector starting its angular range at a value of around 6°. In plots A.4a and A.4b, the value of d1 is kept the same as in the simulation rum at small angles, with d2 moved across to reflect the change in angle that is desired. The resolution in both cases is still very good, but the triton efficiency is still quite poor, especially for the 2200MeV beam energy case, where it is still <1%, with respect to ≈ 2% for 1100 MeV. Plots A.4c and A.4d reduce both d1 and d2 by a factor of 2.5, meaning the angular range spanned by the detector is greater thus the efficiency is increased. The drawback of smaller distances is that each detector strip covers a larger chunk of theta, increasing the risk of poor energy resolution. This problem is visible in Figure A.4c, where the resolution is still okay at the lower angles and energies but is lost as

these increase and it no longer becomes possible to distinguish between the two solutions. This is not a problem in the 2200 MeV case in Figure A.4d, but the efficiency is still low at around 2%.

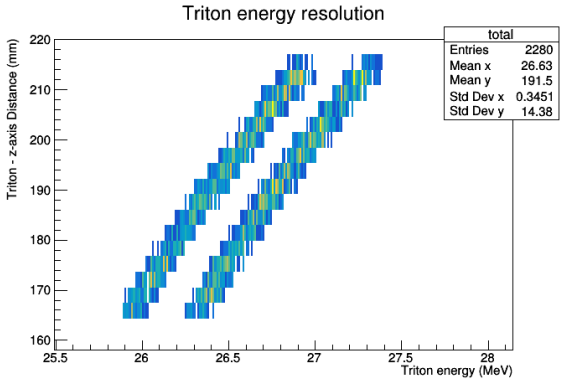

(a) 1100 MeV; d1 = 1500mm, d2 = 165m

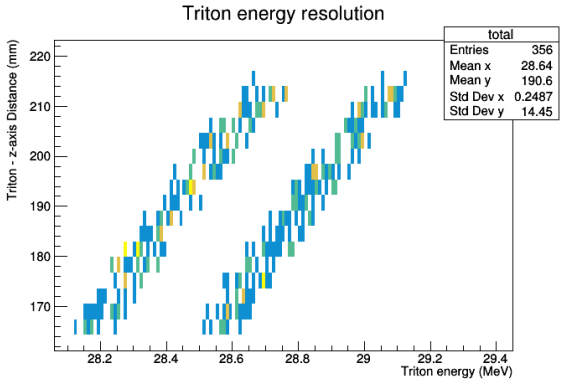

(b) 2200 MeV; d1 = 1500mm, d2 = 165mm

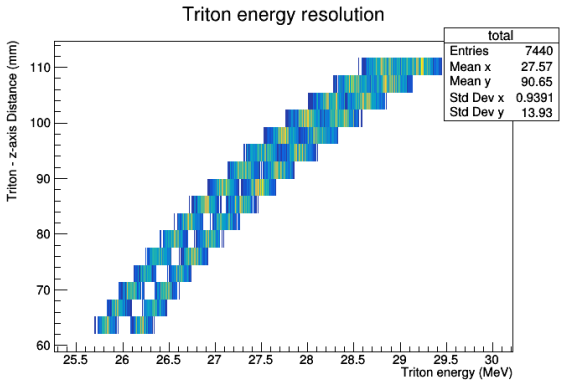

(c) 1100 MeV; d1 = 600mm, d2 = 62mm

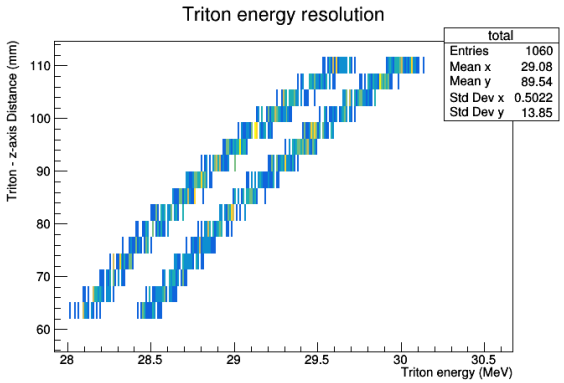

(d) 2200 MeV; d1 = 600mm, d2 = 62mm

Fig. A.4 Detector hits spanning $\theta \approx 6°$- $8°$for (a) and (b), spanning $\theta \approx 6°$- $11°$for (c) and (d)

Some different geometrical setups for the detector in the beam energy = 1100 MeV case are explored in A.5. Figure A.5a shows an adjustment to the setup in A.4c, with d2 reduced in order to span lower angles in an attempt to regain good energy resolution. This is successful, but with a cost in efficiency, falling to around 4%. This is not bad, but with such low angles in question, further and more precise Rutherford scattering calculations may be needed. The d1= 1500mm case is re-explored in Figure A.5b, with a d2 value to make the detector span the highest possible angles where we could expect to see any resolution as deducted from

Figure A.1c. In this case, the energy resolution of the detectors is borderline, with the two solutions just about distinguishable. Again, the efficiency is around 4%. Comparing this plot with the one in Figure A.4c shows the resolution is dependent on how much angle each detector strip subtends, with the resolution is very poor in A.4c but workable in A.5b.

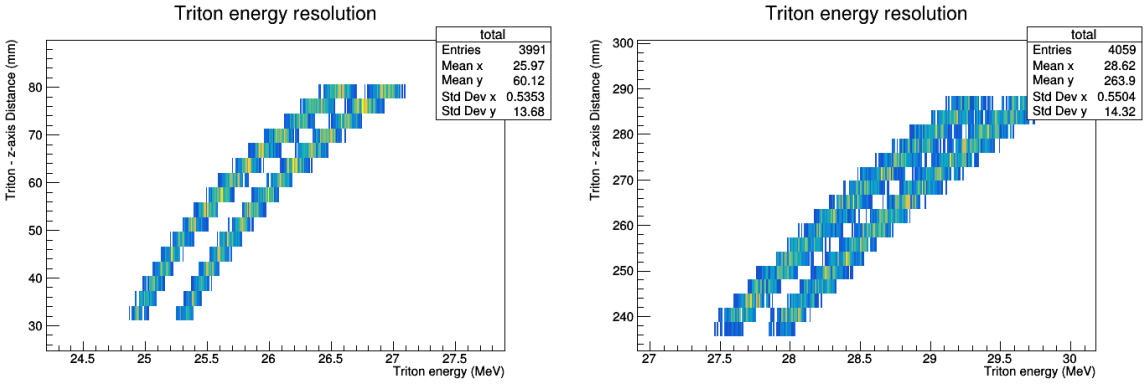

(a) d1=600mm, d2=31mm, $\theta \approx 3°$- $7°$ (b) d1=1500mm, d2=237.5mm, $\theta \approx 9°$-$11°$

Fig. A.5 Some other geometrical setups for beam energy = 1100 MeV

With the efficiency of any simulation shown so far with beam energy = 2200 MeV not being above 2%, Figure A.6 displays plots with setups attempting to improve this. The first thing that is striking about these plots compared others with beam energy = 2200 MeV is that the energy resolution is nowhere near as optimised. In Figure A.6d, the two solutions are totally indistinguishable and problematically, this is the setup that provides the highest efficiency $\approx$ 5%. Unfortunately, each detector strip subtends to large an amount of theta to be able to resolve between energies at a high enough level. The other 3 setups with greater d1 values (i.e. with detector spanning small angle ranges) all have an efficiency of around 2-3%. This is still quite low and as mentioned previously, none of these have a suitable energy resolution. Given this evidence, it seems the reaction is less feasible when performed with a beam energy of 2200 MeV.

It has to be noted that the simulation as it was run here provides very rough and basic results given time constraints. Going forward with this work, as well as incorporating DWBA calculations for finding the best beam energy, accurate spectroscopic factors could be factored

into the code, giving a complete insight into the resolution of the detectors in a more realistic fashion. The intrinsic resolution of Silicon could also be included, modelled with a Gaussian distribution in a similar way done for the beam uncertainty. These changes would provide more credible results and simulations incorporating these may be done going forward. Nonetheless, the simulation as described above give a reasonable insight into whether this reaction is even remotely feasible and whether it is worth investigating further.

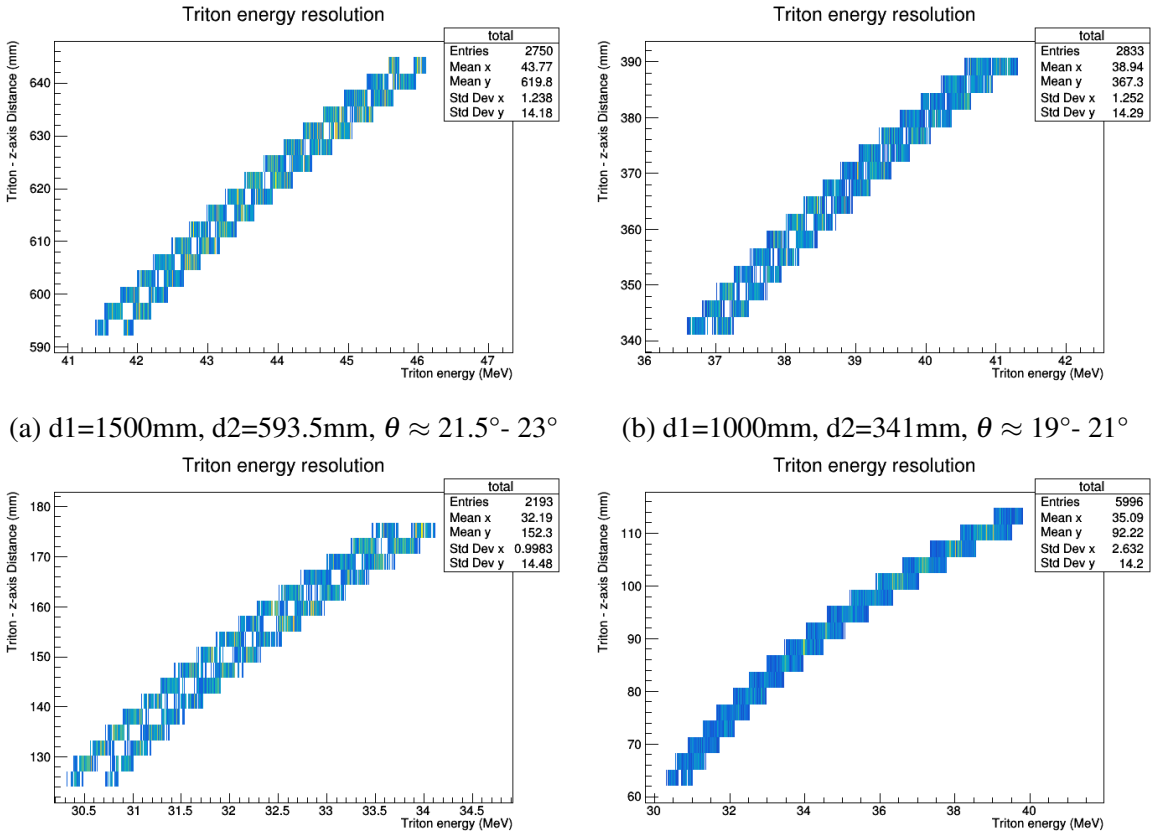

(a) d1=1500mm, d2=593.5mm, $\theta \approx 21.5°$- 23°

(b) d1=1000mm, d2=341mm, $\theta \approx 19°$- 21°

(c) d1=600mm, d2=126mm, $\theta \approx 11°$- 16°

(d) d1=300mm, d2=63mm, $\theta \approx 11°$- 21°

Fig. A.6 Some other geometrical setups for beam energy = 2200 MeV

Potential Future Experiment

The evidence in this section points to the fact that this reaction is feasible, though possibly requiring a well-optimised setup to produce useful results. This has not been perfectly constrained here for the reasons just mentioned, therefore making it tough to make a definitive statement on its feasibility at this moment in time. From the simulations performed so far, it would appear that placing the detector in such a way that d1 $\approx$ 600mm and d2 $\approx$ 40mm (as displayed in Figure A.2 with a beam energy of 1100 MeV is a setup that could potentially provide worthwhile results. Future investigation into the feasibility of this reaction can be done using this setup as a starting point to be further improved with more precise calculations.

Appendix B

Input Files used for Coulomb Excitation Analysis

As discussed in Section 4.2, GOSIA is used to extract matrix elements of interest via a multidimensional fit to the data. The data required is also detailed in this section and the input files used to define this data for this thesis work are presented here. An extension of the GOSIA code, GOSIA2, is used in this work, where the extraction of projectile matrix elements is realised by normalising to the target data. In this case, the required input data specified is required for the both beam and target. The χ^2 minimum is found for the target data and the set of normalisation factors deduced is used to minimise the beam data. This is achieved using the 'chisqsurface' code alongside GOSIA. This code is run from the command line using the following command, with flags as defined in Table B.1:

chisqsurface -m 72Se_196Pt.inp -i 72Se_196Pt_INTI.inp –np=4 –nt=20 –x-low=-1.5 –x-upp=1.5 –nx=301 –y-low=0.3 –y-upp=0.8 –ny=51 –x-index=3 –y-index=1

The minimisation file, '72Se_196Pt.inp', is shown in Figure B.1. The very first line of this file is a flag ("1") to tell GOSIA2 that this is the file for the projectile. The first section titled "OP,FILE" introduces all of the extra files (both input and output) that will be used by the code. Key input files introduced here are the target input file, "196Pt.inp" (shown in Figure B.2),

Table B.1 Flags used in the chisqsurface code. For the 'total number of data points', this is the total sum of the number of yields and the number of literature values for spectroscopic data

Flag	Input
-m	Minimisation file
-i	Integration file
–np	Number of projectile data points
–nt	Number of target data points
–x-low	Lower limit for x-axis matrix element value
–x-upp	Upper limit for x-axis matrix element value
–nx	Number of steps in the x-axis matrix element
–y-low	Lower limit for y-axis matrix element value
–y-upp	Upper limit for y-axis matrix element value
–ny	Number of steps in the y-axis matrix element
–x-index	Index of x-axis matrix element (from input file)
–y-index	Index of y-axis matrix element (from input file)

the projectile yields file, "72Se_196Pt.yie" (shown in Figure B.5) and the two miniball files which define the size and geometry of the gamma-ray detector array. Other files defined here are output file, such as "72Se_196Pt.out" where results from the minimisation are written, and the ".bst" files, where best fit matrix element values are written. Defining these bst files means further input files, ".bst.lit" files are required, detailing the corresponding matrix elements' literature values. These files are shown in Figures B.3 and B.4 for ^{72}Se and ^{196}Pt respectively.

The "OP,GOSI" section of the input file defines the specifics of the experiment you wish to analyse results from, as well as introducing basic data for the nucleus of interest. In this case, this is the projectile, and the first part of this section, "LEVE", details the energetic levels of interest, where a given line reads (index, parity, spin, energy in MeV). Next, under "ME", the matrix elements to be varied are introduced, with the first line defining the multipolarity of the matrix elements ($E2$), and the following lines reading as follows: (index of final state, index of initial state, starting value, lower bound, upper bound). An identical value of lower and upper bound indicates this matrix element is fixed, and this is necessary for all projectile matrix elements for the target normalisation technique. "EXPT" defines the experimental conditions, with the first line representing the number of different experiments (different angular ranges),

follow by the atomic number and mass number of the the nucleus of interest. The following lines represent the remaining details for each individual "experiment", such as the atomic number and mass number of the other nucleus, beam energy and average angle of particle detection. The rest of the "OP,GOSI" section defines flags for the presentation of output.

The "OP,YIEL" section defines known values of relevance to the fit, such as the internal conversion coefficients, the number of individual gamma-ray detectors and their angles (θ and ϕ) with respect to the beam axis, normalisation coefficients and known spectroscopic data for the nucleus of interest (gamma-decay branching ratios, lifetimes of states, mixing ratios and matrix element values). If no spectroscopic data is known, then "0,0" is written for the appropriate line. The final section of the input file is "OP,RAW", which is used to convert raw yields into efficiency-corrected yields. In this work, this function of GOSIA is not used as the yields inputted are already efficiency corrected. To negate this function, the standard line seen is implemented throughout, and the Figure displaying the file is cropped accordingly.

The target input file, "196Pt.inp" (shown in Figure B.2), introduced in the projectile input file, follows the same format. One can see the key differences, such as the LEVE and ME sections containing information about the target, as well as the EXPT section being defined slightly differently to make the target the nucleus of "interest". Furthermore, some new output files are introduced in "OP,FILE", as well as the first-line flag being "2" telling GOSIA2 that this is the file for the target. The yield input file for target yields, "196Pt.yie" (shown in Figure B.6), is introduced. Finally, one can see in "OP,YIEL" that the previously reported spectroscopic data for the target is specified, which is used to fit the target yield data to matrix element values. A set of normalisation factors is then deduced by the code is used to minimise the beam data, with the combined chi-squared minimum for a set of 2 projectile matrix elements (in this case those in index 1 and 3) found.

72Se_196Pt.inp | 72Se_196Pt.yie | 72Se.bst.lit | 196Pt.inp | 196Pt.bst.lit | 196Pt.yie

```
1
OP,FILE
22,3,1
72Se_196Pt.out
25,3,1
72Se_196Pt.inp
26,3,1
196Pt.inp
8,3,1
miniball.f8
9,3,1
miniball.f9
3,3,1
72Se_196Pt.yie
4,3,1
72Se.cor
7,3,1
72Se.map
27,3,1
196Pt.map
11,3,2
crf.dat
12,3,1
72Se.bst
32,3,1
196Pt.bst
15,3,1
72Se.err
13,3,1
cnor.dat
99,3,1
72Se.amp
0,0,0
OP,TITL
Beam Excitation 72Se
OP,GOSI
LEVE
 1,  1,  0,  0.0
 2,  1,  2,  0.862
 3,  1,  4,  1.637
 4,  1,  0,  0.937
 5,  1,  2,  1.317
0,0,0,0
ME
2,0,0,0,0
 1 2 0.46 1 1
 1 5 0.06 2 2
 2 2 -0.76 3 3
 2 3 0.93 4 4
 2 4 0.54 5 5
 4 5 0.8 6 6
0,0,0,0,0
EXPT
4, 34, 72
-78, 196, 305, -84.15, 3,1,0,0,360,0,1
-78, 196, 305, -59.85, 3,1,0,0,360,0,2
-78, 196, 305, -97.50, 3,1,0,0,360,0,3
-78 ,196, 305, 32.75, 3,1,0,0,360,0,4
CONT
INT,4
1 1000
2 1000
3 1000
4 1000
LCK,
0,0
SPL,1.
INR,
PRT,
2,1
3,1
4,1
5,1
7,1
8,1
12,1
13,1
14,1
16,1
18,1
19,1
20,1
0,0
END,

OP,YIEL
0
9,1    ! number of energy meshpoints and multipolarities
0.2, 0.4, 0.6, 0.8, 0.9, 1.0, 1.3, 1.6, 2.0    ! energy meshpoints
2   ! multipolarity
0.0637, 0.00560, 0.001600, 0.000729, 0.000542, 0.000421, 0.000262, 0.000279, 0.000410    ! conversion coeff. for given multipolarity
24,24,24,24 ! number of detectors per experiment
1,2,3,4,5,6,7,8,9,10,11,12,13,14,15,16,17,18,19,20,21,22,23,24
136.33 136.33 136.33 45.79 45.79 45.79 42.95 42.95 42.95 136.98 136.98 136.98 131.17 131.17 131.17 40.31 40.31 40.31 136.72 136.72 136.72 32.23 32.23 32.23
130.82 130.82 130.82 54.99 54.99 54.99 133.56 133.56 133.56 51.45 51.45 51.45 235.24 235.24 235.24 233.11 233.11 233.11 311.46 311.46 311.46 319.63 319.63 319.63
1,2,3,4,5,6,7,8,9,10,11,12,13,14,15,16,17,18,19,20,21,22,23,24
136.33 136.33 136.33 45.79 45.79 45.79 42.95 42.95 42.95 136.98 136.98 136.98 131.17 131.17 131.17 40.31 40.31 40.31 136.72 136.72 136.72 32.23 32.23 32.23
130.82 130.82 130.82 54.99 54.99 54.99 133.56 133.56 133.56 51.45 51.45 51.45 235.24 235.24 235.24 233.11 233.11 233.11 311.46 311.46 311.46 319.63 319.63 319.63
1,2,3,4,5,6,7,8,9,10,11,12,13,14,15,16,17,18,19,20,21,22,23,24
136.33 136.33 136.33 45.79 45.79 45.79 42.95 42.95 42.95 136.98 136.98 136.98 131.17 131.17 131.17 40.31 40.31 40.31 136.72 136.72 136.72 32.23 32.23 32.23
130.82 130.82 130.82 54.99 54.99 54.99 133.56 133.56 133.56 51.45 51.45 51.45 235.24 235.24 235.24 233.11 233.11 233.11 311.46 311.46 311.46 319.63 319.63 319.63
1,2,3,4,5,6,7,8,9,10,11,12,13,14,15,16,17,18,19,20,21,22,23,24
136.33 136.33 136.33 45.79 45.79 45.79 42.95 42.95 42.95 136.98 136.98 136.98 131.17 131.17 131.17 40.31 40.31 40.31 136.72 136.72 136.72 32.23 32.23 32.23
130.82 130.82 130.82 54.99 54.99 54.99 133.56 133.56 133.56 51.45 51.45 51.45 235.24 235.24 235.24 233.11 233.11 233.11 311.46 311.46 311.46 319.63 319.63 319.63
2,1
1
1000
1
1
1000
1
1
1000
1
1
1000
1
4 ! flag (map/inti/mini)
0,0
0,0
0,0
0,0
OP,RAW
1
0 0 0 0 0 0 -50 0
0 0 0 0 0 0 -50 0
```

Fig. B.1 Input file for ^{72}Se

*72Se_196Pt.inp | 72Se_196Pt.yie | 72Se.bst.lit | 196Pt.inp | 196Pt.bst.lit | 196Pt.yie

```
2
OP,FILE
22,3,1
196Pt.out
26,3,1
196Pt.inp
25,3,1
72Se_196Pt.inp
8,3,1
miniball.f8
9,3,1
miniball.f9
3,3,1
196Pt.yie
4,3,1
196Pt.cor
27,3,1
196Pt.map
7,3,1
72Se.map
11,3,2
crf.dat
32,3,1
196Pt.bst
12,3,1
72Se.bst
15,3,1
196Pt.err
13,3,1
cnor.dat
99,3,1
196Pt.amp
0,0,0
OP,TITL
Target Excitation 196Pt
OP,GOSI
LEVE
 1, 1, 0, 0.0
 2, 1, 2, 0.356
 3, 1, 4, 0.877
 4, 1, 2, 0.689
0,0,0,0
ME
2,0,0,0,0
 1 2 1.172 0.1 2
 2 2 0.83 0.1 2
 2 3 1.91 0.1 3
 2 4 1.36 0.1 2
 3 3 1.37 0.1 2
 4 4 -0.515 -1.5 -0.1
7,0,0,0,0
 2 4 0.38 0.1 2
0,0,0,0,0
EXPT
4, 78, 196
34, 72, 305, -84.15, 3,1,0,0,360,0,1
34, 72, 305, -59.85, 3,1,0,0,360,0,2
34, 72, 305, -97.50, 3,1,0,0,360,0,3
34, 72, 305, 32.75, 3,1,0,0,360,0,4
CONT
INT,4
1 1000
2 1000
3 1000
4 1000
LCK,
0,0
SPL,1.
INR,
PRT,
2,1
3,1
4,1
5,1
7,1
8,1
12,1
13,1
14,1
16,1
18,1
19,1
20,1
0,0
END,

OP,YIEL
0
13,2    ! number of energy meshpoints and multipolarities
0.1, 0.2, 0.3, 0.33333, 0.35, 0.4, 0.45, 0.5, 0.55, 0.6, 0.7, 0.8, 1.0   ! energy meshpoints
2   ! multipolarity
4.88, 0.359, 0.098, 0.072, 0.063, 0.044, 0.032, 0.025, 0.0197, 0.0161, 0.0114, 0.0086, 0.00547  ! cnv coeff. for given multiplrty
7
6.67, 0.934, 0.305, 0.229, 0.201, 0.141, 0.103, 0.078, 0.0607, 0.0484, 0.0325, 0.0231, 0.0131
24,24,24,24 ! number of detectors per experiment
1,2,3,4,5,6,7,8,9,10,11,12,13,14,15,16,17,18,19,20,21,22,23,24
136.33 136.33 136.33 45.79 45.79 45.79 42.95 42.95 42.95 136.98 136.98 136.98 131.17 131.17 131.17 40.31 40.31 40.31 136.72 136.72 136.72 32.23 32.23 32.23
130.82 130.82 130.82 54.99 54.99 54.99 133.56 133.56 133.56 51.45 51.45 51.45 235.24 235.24 235.24 233.11 233.11 233.11 311.46 311.46 311.46 319.63 319.63 319.63
1,2,3,4,5,6,7,8,9,10,11,12,13,14,15,16,17,18,19,20,21,22,23,24
136.33 136.33 136.33 45.79 45.79 45.79 42.95 42.95 42.95 136.98 136.98 136.98 131.17 131.17 131.17 40.31 40.31 40.31 136.72 136.72 136.72 32.23 32.23 32.23
130.82 130.82 130.82 54.99 54.99 54.99 133.56 133.56 133.56 51.45 51.45 51.45 235.24 235.24 235.24 233.11 233.11 233.11 311.46 311.46 311.46 319.63 319.63 319.63
1,2,3,4,5,6,7,8,9,10,11,12,13,14,15,16,17,18,19,20,21,22,23,24
136.33 136.33 136.33 45.79 45.79 45.79 42.95 42.95 42.95 136.98 136.98 136.98 131.17 131.17 131.17 40.31 40.31 40.31 136.72 136.72 136.72 32.23 32.23 32.23
130.82 130.82 130.82 54.99 54.99 54.99 133.56 133.56 133.56 51.45 51.45 51.45 235.24 235.24 235.24 233.11 233.11 233.11 311.46 311.46 311.46 319.63 319.63 319.63
1,2,3,4,5,6,7,8,9,10,11,12,13,14,15,16,17,18,19,20,21,22,23,24
136.33 136.33 136.33 45.79 45.79 45.79 42.95 42.95 42.95 136.98 136.98 136.98 131.17 131.17 131.17 40.31 40.31 40.31 136.72 136.72 136.72 32.23 32.23 32.23
130.82 130.82 130.82 54.99 54.99 54.99 133.56 133.56 133.56 51.45 51.45 51.45 235.24 235.24 235.24 233.11 233.11 233.11 311.46 311.46 311.46 319.63 319.63 319.63
1,2,3,4,5,6,7,8,9,10,11,12,13,14,15,16,17,18,19,20,21,22,23,24
136.33 136.33 136.33 45.79 45.79 45.79 42.95 42.95 42.95 136.98 136.98 136.98 131.17 131.17 131.17 40.31 40.31 40.31 136.72 136.72 136.72 32.23 32.23 32.23
130.82 130.82 130.82 54.99 54.99 54.99 133.56 133.56 133.56 51.45 51.45 51.45 235.24 235.24 235.24 233.11 233.11 233.11 311.46 311.46 311.46 319.63 319.63 319.63
2,1
1
1000
1
1
1000
1
1
1000
1
1
1000
1
4 ! flag (map/intl/mini)
0,0
3,1 ! Lifetimes
 2, 34.15, 0.15
 3, 3.55, 0.05
 4, 33.8, 0.7
0,0 ! mixing ratios
7,1 ! Known ME
 2 1 2 1.172 0.003
 2 2 2 0.83 0.09
 2 2 3 1.91 0.02
 2 2 4 1.36 0.02
 7 2 4 0.38 0.02
 2 3 3 1.37 0.17
 2 4 4 -0.52 0.32
OP,RAW
1
```

Fig. B.2 Input file for ^{196}Pt

72Se_196Pt.inp × 72Se_196Pt.yie × 72Se.bst.lit ×

```
1 0.46
2 0.06
3 -0.76
4 0.93
5 0.54
6 0.8
```

Fig. B.3 Input file used to specify the literature values for matrix elements in ^{72}Se to be used in the GOSIA fit. Matrix elements are listed in order according to their definiton in the input file.

196Pt.inp × 196Pt.bst.lit × 196Pt.yie ×

```
1 1.172
2 0.83
3 1.91
4 1.36
5 1.37
6 -0.515
7 0.38
```

Fig. B.4 Input file used to specify the literature values for matrix elements in ^{196}Pt to be used in the GOSIA fit. Matrix elements are listed in order according to their definiton in the input file.

72Se_196Pt.inp × 72Se_196Pt.yie × 72Se.bst.lit ×

```
1 1  1 34 72 305 1 1.0
2 2  1 7300 1500
3 2  1 34 72 305 1 1.0
4 2  1 3400 1100
5 3  1 34 72 305 1 1.0
6 2  1 3100 800
7 4  1 34 72 305 1 1.0
8 2  1 5800 1300
```

Fig. B.5 Input file used to specify experimental yields for transitions in ^{72}Se to be used in the GOSIA fit

196Pt.inp × 196Pt.bst.lit × 196Pt.yie ×

```
 1 1  1 34 72 305 3 1.0
 2 2  1 16900 2800
 3 4  2 2400 500
 4 3  2 3000 600
 5 2  1 34 72 305 3 1.0
 6 2  1 10000 1700
 7 4  2 1250 410
 8 3  2 1200 400
 9 3  1 34 72 305 3 1.0
10 2  1 6900 1200
11 4  2 1150 400
12 3  2 1800 500
13 4  1 34 72 305 1 1.0
14 2  1 14300 2500
```

Fig. B.6 Input file used to specify experimental yields for transitions in ^{196}Pt to be used in the GOSIA fit

Both yield files are formatted in a similar way to the input files and indexes are defined from the input files. Each individual experiment as defined in the input files has its own yields, with the first line dedicated to defining which experiment the subsequent yields appertain to, detailing the experiment number as defined in the respective input file, atomic number of projectile, mass number of projectile and beam energy. The yields are then specified, with index of initial and final energy levels of the respective nuclei, yield value and uncertainty written on each line in that order.